

Investigations of Multiferroic Materials

A Thesis
Submitted for the Degree of

Doctor of Philosophy

by

Jyoti Ranjan Sahu



**JAWAHARLAL NEHRU CENTRE FOR ADVANCED
SCIENTIFIC RESEARCH
(A Deemed University)
BANGALORE, INDIA**

April 2010

DECLARATION

I hereby declare that the matter embodied in this thesis entitled “**Investigations of Multiferroic Materials**” is the result of investigations carried out by me under the supervision of **Prof. C. N. R. Rao, FRS** at the Chemistry and Physics of Materials Unit, Jawaharlal Nehru Centre for Advanced Scientific Research, Bangalore, India, and that it has not been submitted elsewhere for the award of any degree or diploma.

In keeping with the general practice in reporting scientific observations, due acknowledgement has been made whenever the work described is based on the findings of other investigators. Any omission that might have occurred by oversight or error of judgement is regretted.

Jyoti Ranjan Sahu

CERTIFICATE

I hereby certify that the matter embodied in this thesis entitled “**Investigations of Multiferroic Materials**” has been carried out by **Mr. Jyoti Ranjan Sahu** at the Chemistry and Physics of Materials Unit, Jawaharlal Nehru Centre for Advanced Scientific Research, Bangalore, India under my supervision and that it has not been submitted elsewhere for the award of any degree or diploma.

Prof. C. N. R. Rao, FRS

(Research Supervisor)

CONTENTS

Acknowledgements	v
Preface	ix
1. MULTIFERROICS: AN OVERVIEW	
1.1 Introduction	1
1.2 Ferromagnets	2
1.2.1 Theories of ferromagnetism	4
1.3 Ferroelectrics	9
1.3.1 Symmetry	12
1.3.2 Theories of ferroelectricity	13
1.4 Multiferroics	18
1.4.1 Symmetry	21
1.4.2 Magnetoelectric effect	22
1.4.3 Types of multiferroics	
Bismuth-based compounds: Lone-pair effect	28
Rare-earth manganites, LnMnO_3 : Polyhedral tilting and spiral magnetic ordering	30
LnMn_2O_5 : Frustrated magnetism	36
Relaxor ferroelectric and magnetoelectric RCr_2X_4 [$\text{R}=\text{Cd},\text{Hg}$; $\text{X}=\text{S},\text{Se}$]	39
Frustrated multiferroic MnWO_4 system	41
Magnetic ferroelectricity due to charge-ordering	44
Bibliography	49

2. SCOPE OF THE PRESENT INVESTIGATIONS65

2.1 Studies of multiferroic nature in manganites of $YMnO_3$ family	
2.1.1 Single crystal studies of $ErMnO_3$	66
2.1.2 A Raman study on multiferroic $LuMnO_3$	69
2.2 Raman evidence for orbiton-mediated multiphonon scattering in multiferroic $TbMnO_3$	71
2.3 Multiferroic nature of rare-earth chromites	
2.3.1 Rare-earth chromites, $LnCrO_3$ ($Ln = Y, Ho, Er, Yb, Lu$).....	76
2.3.2 $YCr_{1-x}Mn_xO_3$ and $LuCr_{1-x}Mn_xO_3$ Solid solutions	79
2.4 Beneficial modification of the properties of multiferroic $BiFeO_3$ by cation substitution.....	80
2.5 Charge-ordered multiferroic rare-earth ferrites, $LnFe_2O_4$	82
2.6 Charge-ordered manganites	
2.6.1 $Ln_{1-x}A_xMnO_3$	86
2.6.2 Magnetoelectric effect in binary rare-earth manganite systems.....	91
Bibliography.....	94

3. EXPERIMENTAL DETAILS

3.1 Synthesis of materials	115
3.1.1 Solid state reaction route	115
Synthesis of $Bi_{1-x}La_xFeO_3$ and $BiFe_{1-x}Mn_xO_3$	116
Synthesis of $LnCrO_3$, $Y(Lu)Cr_{1-x}Mn_xO_3$, $LuMnO_3$	117
Synthesis of $Ln_{1-x}A_xMnO_3$ ($Ln = \text{rare earth}, A = \text{alkaline earth}$).....	117
Synthesis of the binary rare-earth manganite systems	118
3.1.2 Synthesis of rare-earth ferrites	
Synthesis of $YbFe_2O_4$ and $Lu_{0.5}Y_{0.5}Fe_2O_4$	119
Synthesis of YFe_2O_4 and $ErFe_2O_4$	119
3.1.3 Preparation of single-crystalline samples	119
Floating-zone melting technique	120

3.2 Structure and morphology

3.2.1 Structural analysis: Powder x-ray diffraction	123
3.2.2 Electron microscopy	124
Scanning electron microscopy	125
Energy dispersive x-ray analysis	127

3.3 Measurements of physical properties

3.3.1 Dielectric measurements.....	129
3.3.2 Ferroelectric hysteresis	134
3.3.3 DC magnetic measurements.....	135
3.3.4 Magneto-dielectric measurements.....	136
3.3.5 Heat Capacity measurement.....	138
3.3.6 Non-linear optical experiments.....	140
3.3.7 Raman spectroscopy.....	141
3.3.8 Differential thermal analysis.....	142

Bibliography.....	144
-------------------	-----

4. RESULTS AND DISCUSSION

4.1 Studies of multiferroic nature in manganites of $YMnO_3$ family

Summary.....	145
4.1.1 Single crystal studies of $ErMnO_3$	146
4.1.2 A Raman study on multiferroic $LuMnO_3$	153
Conclusions.....	161

4.2 Raman evidence for orbiton-mediated multiphonon scattering in multiferroic $TbMnO_3$

Summary.....	162
Raman evidence for orbiton-mediated multiphonon scattering in multiferroic $TbMnO_3$	163
Conclusions.....	169

4.3 Multiferroic nature of rare-earth chromites

4.3.1 Rare-earth chromites, $LnCrO_3$ ($Ln = Ho, Er, Yb, Lu$)	
Summary.....	170
Rare-earth chromites, $LnCrO_3$ ($Ln = Ho, Er, Yb, Lu$)	171
Conclusions.....	182
4.3.2 $YCr_{1-x}Mn_xO_3$ and $LuCr_{1-x}Mn_xO_3$ solid solutions	
Summary.....	183
$YCr_{1-x}Mn_xO_3$ and $LuCr_{1-x}Mn_xO_3$ solid solutions.....	184
Conclusions	194

4.4 Beneficial modification of the properties of multiferroic BiFeO ₃ by cation substitution	
Summary.....	195
Beneficial modification of the properties of multiferroic BiFeO ₃ by cation substitution.....	196
Conclusions.....	205
4.5 Charge-ordered multiferroic rare-earth ferrites, LnFe ₂ O ₄	
Summary.....	206
Charge-ordered multiferroic rare-earth ferrites, LnFe ₂ O ₄	207
Conclusions.....	215
4.6 Charge-ordered manganites	
4.6.1 Ln _{1-x} A _x MnO ₃ (Ln = rare earth, A = alkaline earth)	
Summary.....	217
Ln _{1-x} A _x MnO ₃ (Ln = rare earth, A = alkaline earth).....	218
Conclusions	233
4.6.2 Magnetoelectric effect in binary rare-earth manganite systems	
Summary.....	235
Magnetoelectric effect in binary rare-earth manganite systems.....	237
Conclusions.....	250
Bibliography.....	251

Acknowledgements

There are no words that can express my deep respect and sincere gratitude towards my research supervisor, Professor C. N. R. Rao, FRS. It was his invaluable guidance, immense support and constant encouragement that have been instrumental in developing me as a scientific researcher. I am also grateful to him for not only suggesting me the research problems but also for providing me constant guidance till their completion. I am ecstatic and also honored for getting the opportunity of working under him who is a great scientist as well as a noble human being. He is endowed with not only a very fertile brain with the most tenacious memory but also an extremely generous heart. I shall always remember his endless enthusiasm, dedication and commitment towards science and will try to imbibe these fantastic qualities in me as well. Moreover, his time-management skill, wit and quick-decision-making qualities will inculcate in me disciplinary attitude with an everlasting inspirational influence in me.

I am extremely thankful to Prof. A. R. Raju who had opened for me the door to JNCASR. Although my interaction with him was for less than a year, it was a very enjoyable and memorable experience. During that period, he had always helped me strengthen my pillar of science.

I am highly thankful to Prof. A. Sundaresan for his collaboration in many scientific works. He has always been helpful to me in carrying out experimental works with fruitful discussions on science. His sense of humility will certainly have a tremendous impact in my life ahead.

I am extremely thankful to Prof. Umesh V. Waghmare who had collaborated for my first scientific work. I will never forget his humble, caring nature for me.

I extend my sincere thanks to other collaborators, Prof. A. K. Sood, Dr. K. Ramesha, Mr. Claudy Rayan Serrao, Mr. Anirban Ghosh, Ms. Nirat Ray, Mr. Venkatprasad Bhat, Mr. Pradeep Kumar, Mr. Surajith Saha and Mr. D. V. S. Muthu for their collaboration works.

I would like to thank Prof. Chandrabhas Narayana for his amicable attitude to me and many valuable scientific discussions that he shared with me.

I would like to express my heart-felt gratitude to all my labmates and seniors: Claudy, Motin, Thiru, Anirban, Anne, Asish, Krishna, Saratbhai, Jogibhai, Minaxie, Prabha, Anupama, Raj, Kripa, Manu, Angshuman, Kalyan and Ajmala for their help and relationship with me giving me the realization of the lab as a family.

I would like to thank all the course-work teachers, Professors, A. R. Raju, A. Sundaresan, Umesh V. Waghmare, Chandrabhas Narayana, K. S. Narayan, S. B. Krupanidhi, K. B. R. Verma, G. U. Kulkarni, S. Balasubramanian, Shobhana Narasimhan, Amitabh Joshi.

I acknowledge Prof. T. N. Guru Row, Prof. P. K. Das and Mr. Ravindra Pandey for useful discussions and carrying out some experiments.

I would like to thank Mrs. Indumathi Rao and Mr. Sanjay for their hospitality and kindness for me.

I would like to thank Dr. A. Govindaraj and Dr. M. Eswaramoorthy, Prof. S.M. Shivaprasad for their help and humorous, friendly attitude to me.

I am very thankful to Mr. Anil, Mr. Basavaraj, Mr. Srinath, Mr. Vasu, Mr. Arokianathan, Mrs. Selvi, Mr. Moorthy, Mr. Srinivas for their help in measurements.

My special thanks are for Mr. Pranab, Dr. Mangalam and Mr. Nitesh for their help in measurements.

I would like to thank, Mrs. Shashi, Mr. Gowda, Mr. Xavier and Mr. Victor for their kind help.

I acknowledge all the present and past wardens especially Prof. A. Sundaresan, Prof. U.V. Waghmare and Prof. S. Balasubramanian for their in-time-help and pertinent responses.

I thank all the academic, computer lab, library and administrative staff members for their smooth functioning of the associated works.

I am thankful to the children in JNC campus, security staffs and hostel employees for pleasant interactions with me.

I acknowledge University Grants Commission (UGC), India for fellowship and contingency grants sanctioned to me.

I am indebted to all my friends: Pratyush, Khatei, Thiru, Chandu, Gopal, Prakash, Saumya, Jyotirmayee, Nirakar, Subhankarbhai, Sudhanshu, Hembrambhai, Diptibhai, Debakantabhai, Kirtibhai, Ramakanta, Pavan, Vijay, Bhat, Mangalam, Manu, Gomathi, Subbu, Manoj, Satish, Rashid, Imam, Dinesh, Prashant, Rakesh, Venkat, Leela, Basant, Sandeep, Varun, Urmi, Manjunath, Kalyani, Shipra, Kanishka, Vivek, Jitesh, Nagraj, Avinash, Sabya, Satya, Srinu, Prakash, Malleswar, Abhay, Narendra, Arif and many more whom I sadly could not acknowledge due to space limitation.

Finally, I express my deepest sense of love, thanks and gratitude for my family, my mother, my late sister, “MAAMI” and GOD who have never let me feel alone in the world.

Preface

This thesis presents the synthesis and investigations of physical properties of multiferroic materials. Multiferroics are materials in which two or all the three properties: ferroelectricity, ferromagnetism and ferroelasticity occur in the same phase. Such materials have alluring potential applications because of the existence of many order parameters. The thesis is organized into four sections. *Section 1* gives an overview of multiferroics, explaining the origin of multiferroicity, occurrence of magnetoelectric coupling, their possible technological applications and the challenges involved.

Section 2 gives the scope of the investigations. The specific objectives of the present research on hexagonal rare-earth manganites like ErMnO_3 and LuMnO_3 , Raman evidence of multiphonon scattering in TbMnO_3 , multiferroic heavy rare earth chromites, solid solutions of Y(Lu)CrO_3 with Y(Lu)MnO_3 , cationic-substituted BiFeO_3 , charge-ordered rare earth ferrites, LnFe_2O_4 and rare earth manganites doped with alkaline earth metals are outlined. Experimental aspects are described in *section 3*.

In *section 4*, results of the investigations are discussed. In 4.1, Single crystal ErMnO_3 and polycrystalline LuMnO_3 have been established to be multiferroic through magnetic and ferroelectric properties studies, where support by Raman Spectra has also been reported. In 4.2, orbiton–phonon mixed nature of the high frequency Raman mode has been suggested. One of the first-order phonon modes shows anomalous softening below T_N (~ 46 K), suggesting a strong spin–phonon coupling. Magnetic and dielectric properties of heavy rare earth chromites and $\text{Y(Lu)Cr}_{1-x}\text{Mn}_x\text{O}_3$ are reported in 4.3, where Néel temperature and ferroelectric transition temperatures are found to be influenced by ionic radii of rare-earth ions. In 4.4, we have investigated separately the impact of the substitution of manganese in the B-site and that of lanthanum in the A-site of BiFeO_3 on its multiferroic properties. In 4.5, we describe the results of charge-ordered rare earth ferrites which show appreciable magnetoelectric effect. Magnetic, dielectric and magneto-dielectric properties of $\text{Ln}_{1-x}\text{A}_x\text{MnO}_3$ and its many binary systems (Ln = rare earth, A = alkaline earth) are discussed in 4.6.

Dedicated to

My Beloved Late Sister,

“MAAMI”

1. MULTIFERROICS: AN OVERVIEW

1.1 Introduction

The term ‘ferroic’ has been coined from an analogy between domain-related hysteretic response of the magnetization to magnetic field in iron, and a similar hysteretic response in dielectric and elastic crystals. This term has been suggested by Aizu to describe all types of mimetically twinned crystals in which one or more twin components may be switched to other equivalent states by the application of suitable external driving forces. These forces are magnetic field, electric field and mechanical stress for the domains which differ with respect to a given coordinate system in orientation of spontaneous magnetization M_s , spontaneous polarization P_s and spontaneous deformation ε_s respectively [1,2]. In a thermodynamic classification of ferroics, ferroelectrics, ferromagnetics and ferroelastics are considered as *primary ferroics*, whereas six kinds of *secondary ferroics* have been defined, namely ferrobielectrics, ferrobimagnetics, ferrobielastics, ferroelastoelectrics, ferromagnetoelastics and ferromagnetoelastics, the domain states of which differ in electric susceptibility, magnetic susceptibility, elastic compliance, piezoelectric co-efficients, piezomagnetic coefficients and magnetoelectric coefficients respectively.

1.2 Ferromagnets

Around 600 B.C., magnetism was observed in loadstone or magnetite by its inherent property of attracting iron [3]. However, the claim for the discovery of magnetism dates back to 2500 B.C. when Chinese were using magnetic compass. Socrates mentioned that magnetite was used to induce iron to get the attractive power (magnetism). Thus permanent and induced magnetism were human's earliest scientific discoveries. The science behind operation of magnetic compass enlightened only after the realization of the fact that the earth itself is a huge magnet by Gilbert. Later, Coulomb's investigations in 16th century form the starting point in the research to understand magnetism.

The magnetic effects, except diamagnetism, observed in inorganic materials are due to the presence of unpaired electrons. Thus magnetism is mainly observed in compounds having transition metals and lanthanides due to the presence of unpaired *d* and *f* electrons respectively. The random orientations of unpaired electrons on the different atoms lead the material to be paramagnetic. Parallel alignment of these unpaired electrons makes the material ferromagnetic. If they align in antiparallel, then the material becomes antiferromagnetic. The term “weak ferromagnetism” is used to describe antiferromagnets with a small canting of the spins away from antiparallel alignment. In case of unequal magnetic moment of the spins in antiparallel alignment, it will lead to ferrimagnetic behavior. However, among the different magnetic behaviors, materials having ferromagnetism are widely used in application.

A ferromagnetic material undergoes a phase transition from a high temperature phase that does not have a macroscopic magnetic moment to a low-temperature phase that has a spontaneous magnetization even in the absence of an applied magnetic field. This can be explained on the basis of the parallel alignment of the magnetic dipoles which are randomly distributed at high-temperature paramagnetic regime. In fact, the dipoles constitute domains each of which has a net magnetization and separated by domain walls. The subsequent alignment and reorientation of the domains upon the application of magnetic field, \mathbf{H} , results in a hysteresis loop. The ferromagnetic material starts in an unmagnetised state and as we keep on increasing the magnetic field, the magnetization increases non-linearly upto a saturated value of magnetization M_s . When the field is gradually reduced to zero, the $M \sim H$ curve traces a different path to a non-zero value of magnetization called residual or remnant magnetization. This property is termed as retentivity. In order to reduce the magnetization to zero, we need to apply a reverse field which is called as coercive field, H_c .

Depending upon the characteristics of the hysteresis loop a ferromagnetic material is classified under the category of soft or hard ferromagnet which have respectively small and large values of coercive field. Soft magnetic materials are used in applications requiring frequent reversals of the directions of magnetization such as cores of transformer motors, inductors and generators. Hard magnetic materials, on the other hand, are used to produce permanent magnets.

1.2.1 Theories of ferromagnetism:

Many of the properties of ferromagnets have successfully been explained by two phenomenological theories: the Curie-Weiss localized-moment theory and the Stoner band theory of ferromagnetism [4].

The ferromagnetic nature of a material is characterized by its constituent electrons which must be having a net angular momentum. This can arise from either the orbital component of the angular momentum or the spin component contributed from unpaired electrons.

The Weiss theory of ferromagnetism [4,5] is based on the concept of ferromagnetic domains which are spontaneously magnetized due to the presence of an internal molecular field called Weiss field or the exchange field B_E . The Weiss field cannot be simply due to magnetic dipole-dipole interaction between the neighboring dipoles as this would generate fields of the order of 10^3 G only whereas the actual field strengths are observed to be quite high. For example, the Weiss field for iron is of the order of 10^7 G. It was Heisenberg who first proposed in 1928 that the Weiss field was the consequence of the quantum-mechanical exchange interaction between the atoms. This interaction arises due to the Pauli's exclusion principle according to which any change in the relative orientation of the two spins would disturb the spatial distribution of charge, thus producing interaction between the two atoms. Apparently, the strength of the interaction between the adjacent atoms depends upon the extent of overlap of their wave functions as well as the relative orientation of the electron spins but not on the spin magnetic moments. Thus, this is an electrostatic and non-magnetic type of interaction.

Using Heitler-London theory of chemical bonding, it can be shown that the total energy of a system of two atoms contains an exchange energy term given by

$$U_{ij} = -2 J_e \mathbf{S}_i \cdot \mathbf{S}_j$$

Where \mathbf{S}_i and \mathbf{S}_j represent the spins of the two atoms and J_e is the exchange integral which is assumed to be the same for any pair of atoms. Its value depends upon the overlap of the charge distributions of the two atoms i.e. on the interatomic distance. In general, J_e is positive for large interatomic distances and negative for smaller ones. The above expression is known as the Heisenberg model of exchange energy. It also follows that if J_e is positive, the parallel alignment of spins exhibits lower-energy and hence is more stable as compared to the antiparallel arrangement, thereby producing magnetization. In a similar way, it can be concluded that the negative value of J_e does not favor magnetism.

Below the Curie temperature, T_C , the molecular field is so strong that it magnetizes the substance even in the absence of an external applied field. At high enough temperatures, the thermal energy kT and associated entropic effects overcome the alignment energy of the molecular field resulting in random orientation of the magnetic moments and paramagnetic behavior. The Weiss picture leads to the experimentally observed Curie-Weiss law behavior for the susceptibility χ of many magnetic materials

$$\chi = C / (T - T_C)$$

However, the Weiss theory fails to hold good in one important aspect. It is unable to interpret the measured values of the magnetic moment per atom in some ferromagnetic materials, particularly in ferromagnetic transition metals, where two significant discrepancies were observed. First, according to the Weiss theory, the magnetic dipole moment on each atom or ion should be the same in both the ferromagnetic and paramagnetic phases which is not the case as revealed through experiments. Second, the magnetic dipole moment on each atom or ion should correspond to an integer number of electrons which is again not the observed result. The treatment with metals could be successfully approached by Stoner band theory of ferromagnetism.

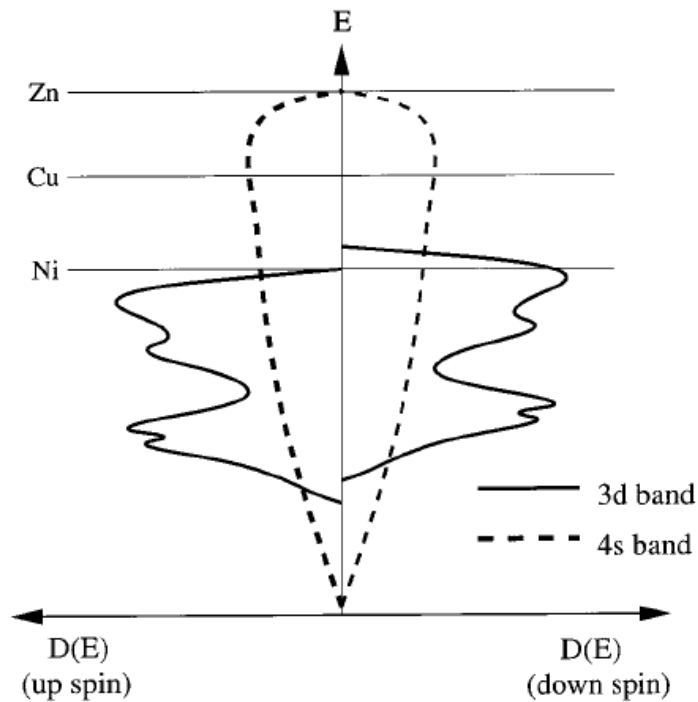


Fig. 1.1: 3d and 4s up- and down-spin densities of states in first-row transition metals, with exchange interaction included.

In the Stoner theory [6], the fundamental driving force for ferromagnetism is again the exchange energy, which is minimized if all of the electrons have the same spin. It is useful to visualize the exchange interaction as shifting the energy of the 3d band for electrons with one spin direction relative to the band for electrons with the opposite spin direction. Fig. 1.1 shows the 4s and 3d densities of states within this picture. The magnitude of the shift is independent of the wave vector, giving a rigid displacement of the states in a band with one spin direction relative to the states with the opposite spin direction. If the Fermi energy lies within the 3d band, then the displacement will lead to more electrons of the lower-energy spin direction and, hence, a spontaneous magnetic moment in the ground state. In Ni, for example, the exchange interaction displacement is so strong that one 3d subband is filled with five electrons, and the other contains all 0.54 holes. Thus, the saturation magnetization of Ni is $M = 0.54N\mu_B$, where N is the total number of Ni atoms in the sample. We now see why the magnetic moments of the transition metals do not correspond to integer numbers of electrons! This model also explains why the later transition metals, Cu and Zn, are not ferromagnetic. In Cu, the Fermi level lies above the 3d bands. Because both of the 3d bands are filled and the 4s band has no exchange splitting, the numbers of up- and down- spin electrons are equal. In Zn, both the 3d and 4s bands are filled and so do not contribute a magnetic moment.

When electrons have their spins parallel to each other, exchange energy is minimized [7]. In practice, however, there are many other contributions to the electronic energy and the net result, particularly in insulators, is often an antiferromagnetic arrangement. For example, the superexchange interaction in which the magnetic ordering

between cations is determined by chemical-bonding considerations with intervening anions often leads to antiferromagnetism (or ferrimagnetism if the ions are different). Superexchange is illustrated in Fig. 1.2, for example, of Mn^{2+} ions in which an oxygen atom lies between two filled manganese d orbitals and has some covalent bond formation with both of them.

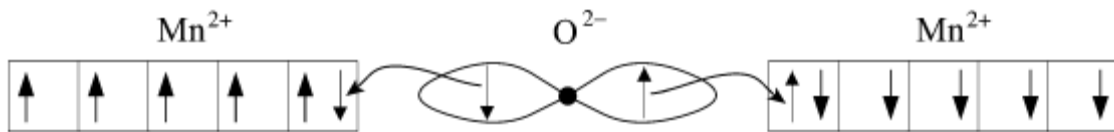


Fig. 1.2: Schematic of the superexchange mechanism in MnO (Ref. 7).

Superexchange interactions can lead to parallel alignment of magnetic moments for certain bonding configurations – for example, if an oxygen atom bonds with two manganese d orbitals, one of which is empty and the other of which is filled – as illustrated in Fig. 1.3.

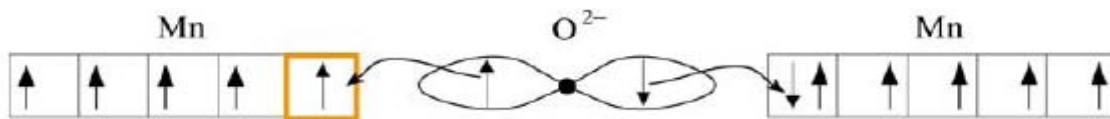


Fig. 1.3: Superexchange mechanism between one empty (*marked in red*) and one occupied Mn *d* orbital (Ref. 7).

Therefore, many magnetic materials contain a combination of ferro- and antiferromagnetically coupled ions. The details of the long-range magnetic ordering are then determined by strain, since ferro- and antiferromagnetically coupled ions have

different bond lengths. Minimizing the strain energy usually results in a net antiferromagnetism, for example in LaMnO_3 , planes of ferromagnetically coupled Mn ions couple antiferromagnetically to each other [8].

Most of the ferromagnetic materials known are metallic and there are considerable number of insulating ferromagnetic compounds. The ferromagnetism observed in those insulating compounds are explained on the basis of superexchange interaction. Even though superexchange interaction has been explained earlier, a considerably more satisfactory system of semi-empirical rules was developed over a period of years by Goodenough [8] and Kanamori [9]. These rules have the important features of the occupation of various d levels as dictated by ligand field theory. They are related to the prescriptions of Andersons' work about the sign of superexchange [10]. The exchange interaction in magnetic insulators is predominantly caused by the so-called superexchange which is due to the overlap of the localized orbitals of the magnetic electrons with those of intermediate ligands. The main features of the superexchange interactions are usually explained in terms of the so-called Goodenough- Kanamori- Anderson rules [9,11,12]. According to these rules, a 180° superexchange (the magnetic ion-ligand-magnetic ion angle is 180°) of two magnetic ions with partially filled d shells is strongly antiferromagnetic, whereas a 90° superexchange interaction is ferromagnetic and much weaker.

1.3 Ferroelectrics

The “ferro” part in the name “ferroelectric” can be assumed to be a misnomer, as it does not refer to the presence of iron in ferroelectric materials. Rather, it arises from the

many similarities in behavior between ferroelectrics, with their spontaneous electric polarization, and ferromagnets, with their spontaneous magnetization. In fact, the earliest observation of ferroelectricity [13] describes the electric hysteresis in Rochelle salt, $\text{KNa}(\text{C}_4\text{H}_4\text{O}_6) \cdot 4\text{H}_2\text{O}$ as “analogous to the magnetic hysteresis in the case of iron.”

A ferroelectric material is defined as one that undergoes a phase transition from a high-temperature phase that behaves as an ordinary dielectric (so that an applied electric field induces an electric polarization, which goes to zero when the field is removed) to a low-temperature phase that has a spontaneous polarization whose direction can be switched by an applied field. Many properties of ferroelectric materials are analogous to those of ferromagnets, but with the electric polarization, \mathbf{P} , corresponding to the magnetization, \mathbf{M} ; the electric field, \mathbf{E} , corresponding to the magnetic field, \mathbf{H} ; and the electric displacement, \mathbf{D} , corresponding to the magnetic flux density, \mathbf{B} . For example, ferroelectric materials also have domains and show a hysteretic response of both polarization and electric displacement to an applied electric field. As a result, they also find applications in data storage. The onset of spontaneous electric polarization coincides with a divergence in the static dielectric permeability, ϵ , because at T_c , an infinitesimally small external electric field will cause a large polarization. They find application as capacitors because their concentration of electric flux density results in high dielectric permeabilities. They are also used in electromechanical transducers and actuators (because the change in electric polarization is accompanied by a change in shape [14]).

Although studies of Rochelle salt were pivotal in establishing many of the basic properties of ferroelectric materials, the complex structure and large number of ions per

unit cell made it difficult to elucidate a coherent theory of ferroelectricity from the results of experiments on this material. The most widely studied and widely used ferroelectrics today are perovskite-structure oxides, ABO_3 , which have the prototypical cubic structure shown in Fig. 1.4. The cubic perovskite structure is characterized by a small cation, B, at the center of an octahedron of oxygen anions, with large cations, A, at the unit cell corners. Below the Curie temperature, there is a structural distortion to a lower-symmetry phase accompanied by the off-center shift of the small cation. The spontaneous polarization derives largely from the electric dipole moment created by this shift. The comparatively simple perovskite structure and the small number of atoms per unit cell have made detailed theoretical studies of perovskite ferroelectrics possible and resulted in a good understanding of the fundamentals of ferroelectricity.

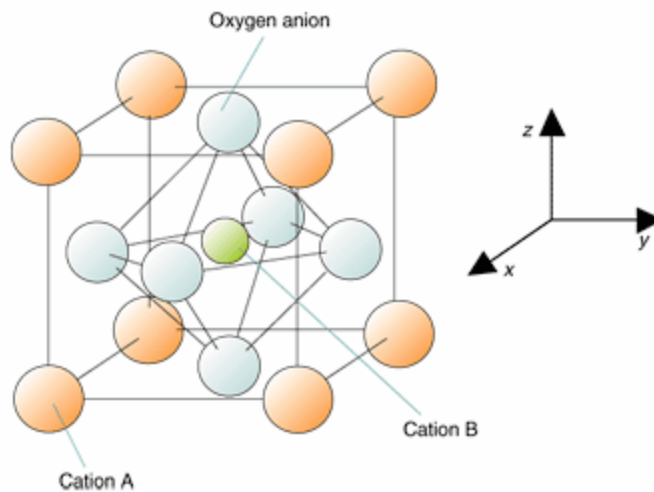


Fig. 1.4: Perovskite Structure

1.3.1 Symmetry

Absence of inversion symmetry and polar nature of ferroelectric crystals cause a spontaneous polarization along one or more crystal axes. Thus the symmetry plays a key role in these materials.

The symmetry of the crystals is governed by their lattice structure. Though there are thousands of crystals in nature, they all can be grouped together into 230 space groups based on the symmetry elements. The space groups in three dimensions are made from combinations of 32 crystallographic point groups with 14 Bravais lattices which belong to one of 7 crystal systems. The 32 point groups can be further classified into (a) crystals having center of symmetry and (b) crystals which do not possess center of symmetry. Crystals with center of symmetry include 11 point groups and are labeled as centrosymmetric and they do not show polarity. The remaining 21 point groups do not have center of symmetry (i.e. noncentrosymmetric). All non-centrosymmetric point groups, except the point group 432, show piezoelectric effect along the unique directional axes. A crystal having no center of symmetry possesses one or more crystallographically unique directional axes. Space groups lacking an inversion center (non-centrosymmetric) are further divided into polar and chiral types. A chiral space group is one without any rotoinversion symmetry elements. Rotoinversion (also called an 'inversion axis') is rotation followed by inversion; for example, a mirror reflection corresponds to a two-fold rotoinversion. Chiral space groups must therefore only contain (purely) rotational and translational symmetry. These arise from the crystal point groups 1, 2, 3, 4, 6, 222, 422, 622, 32, 23, and 432. Chiral molecules such as proteins crystallize in chiral space groups. The term 'polar' is often used for those space groups which are neither centrosymmetric

nor chiral. However the term 'polar' is more correctly used for any space group containing a unique anisotropic axis. These occur in point groups 1, 2, 3, 4, 6, m , $mm2$, $3m$, $4mm$, and $6mm$. Thus some chiral space groups are also polar. Out of the twenty point groups which show the piezoelectric effect, the ten polar point groups have only one unique direction axis and such crystals show spontaneous polarization.

Thus considering symmetry restrictions, all ferroelectric materials are pyroelectric, however not all pyroelectric materials are ferroelectric. Since all pyroelectric materials are piezoelectric, this means ferroelectric materials are inherently piezoelectric.

1.3.2 Theories of ferroelectricity

If the bonding in an ideal cubic perovskite were entirely ionic and the ionic radii were of the correct size to ensure ideal packing, then the short range repulsions between adjacent electron clouds makes the structure stable, the structure would remain centrosymmetric and therefore, not ferroelectric. The existence or absence of ferroelectricity is determined by a balance between these short-range repulsions that favor the non-ferroelectric symmetric structure and additional bonding considerations which act to stabilize the distortions necessary for the ferroelectric phase [15]. Even in ferroelectric materials, the short-range repulsions dominate at high temperature, resulting in the symmetric unpolarized state. As the temperature is decreased, the stabilizing forces associated with the polarization of the ions as they are displaced becomes stronger than the short-range repulsive ion-ion interactions and the polarized state becomes stable even

in the absence of an applied field. The changes in the chemical bonding that stabilize distorted structures have long been recognized in the field of coordination chemistry and are classified as second-order Jahn-Teller effects [16,17] or sometimes pseudo-Jahn-Teller effects [18] in the chemistry literature.

Cochran was the first to introduce and treat in detail the concept of soft phonons as the mechanism for displacive ferroelectric transitions [19]. A soft mode means a mode whose frequency decreases and vanishes (for a second order phase transition) at T_c . The displacements, which can be thought of as the order parameter of the transition, increase and ultimately saturate as the temperature is lowered well below T_c . The decrease and ultimate vanishing of the frequency of the soft mode as the transition is approached is caused by cancellation between competing forces (short-range and long-range Coulombic forces).

Although continuum and soft mode theories have been very successful in the analysis and interpretation of FE properties and in identifying the mechanism for the FE transition in soft-mode systems, the atomic-level origin of ferroelectricity, particularly in the ABO_3 perovskites, remained unclear [20]. Most perplexing was the vastly different FE behavior for seemingly very similar compounds. Examples include the following: Despite the fact that the Ta and Nb ions have comparable sizes and the same valence, $KTaO_3$ remains cubic paraelectric down to the lowest temperatures, whereas isomorphous $KNbO_3$ exhibits on cooling a sequence of three FE phase transitions, cubic to tetragonal to orthorhombic to rhombohedral; $SrTiO_3$ exhibits a subtle antiferrodistortive transition driven by a soft-zone boundary phonon at 110 K, whereas

BaTiO₃ exhibits the aforementioned three FE transitions. Understanding these differences is a challenge for first-principles electronic structure and total energy calculations.

Prior to approximately 1990, there was very little such work and the theoretical techniques were not adapted to treat ferroelectric and electromechanically coupled phenomena. In 1990, Boyer et al. [21] envisioned that first-principles theory could lead to a deeper understanding of FE properties and could ultimately be used to design ferroelectrics with desired properties. Among the significant theoretical advances made since have been an understanding of the role of covalency and hybridization in driving ferroelectricity in the perovskites and the ability to provide a good description of the ground state and to calculate the transition temperature, polarization and piezoelectric and elastic constants [22].

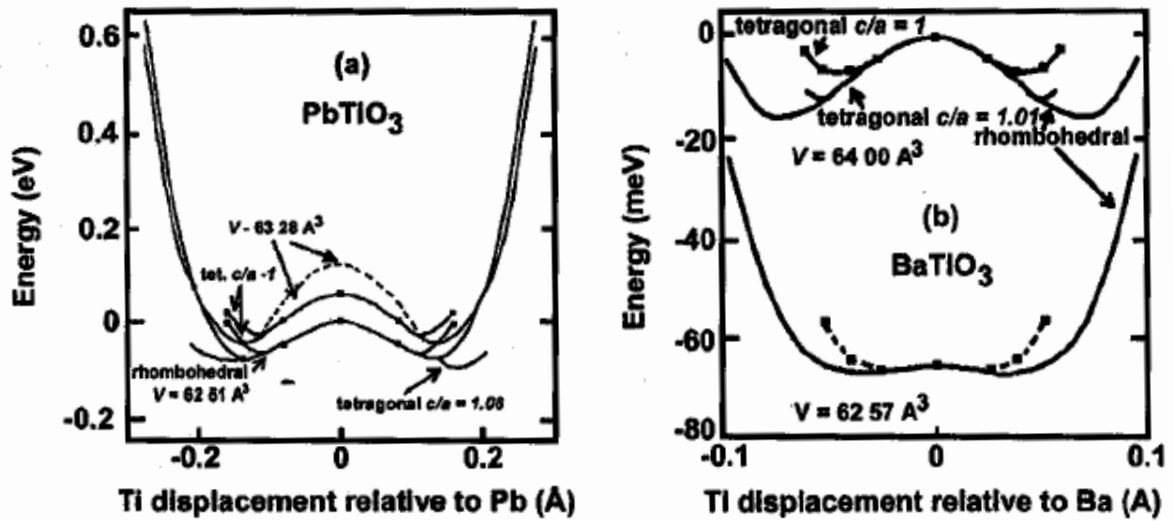


Fig. 1.5: Potential Energy vs soft-mode distortion for PbTiO₃ and BaTiO₃ calculated using first principles theory showing the influence of strain (expressed in terms of tetragonal c/a ratio) and unit cell volume. Note the different energy scales for (a) and (b). [Ref. 20]

One of the first successes of first-principles theory was an understanding of the difference between BaTiO_3 and PbTiO_3 . Using the all-electron, full-potential, linearized augmented plane-wave (LAPW) method within the local density approximation (LDA) for the exchange and correlations between electrons, Cohen and Krakauer performed lattice dynamics and electronic structure calculations for the two materials. The results revealed several new insights into the physics. Fig. 1.5 shows the calculated potential as a function of soft-mode distortion for the two crystals [20,23]. Several features should be noted. The wells for PbTiO_3 are much deeper than for BaTiO_3 . In the absence of tetragonal lattice strain (i.e. $c/a = 1.0$), the rhombohedral phase is the ground state for both crystals. However, tetragonal strain stabilizes the tetragonal phase in the case of PbTiO_3 but not in BaTiO_3 , where the rhombohedral phase remains more stable. Fig. 1.5 also shows the strong influence of decreasing volume (or increasing pressure) on the two potentials. In both cases, pressure decreases the well depth, which is in agreement with the experimentally observed decreases in transition temperatures and ultimate vanishing of the FE state at sufficiently high pressure.

A second significant finding from these calculations is that the ferroelectric instability is due to hybridization between the oxygen 2p and titanium 3d states. If this hybridization is inhibited, the ferroelectric instability is suppressed and the cubic phase is stable. Additionally, in BaTiO_3 , the Ba is ionic and spherical, whereas the Pb in PbTiO_3 is highly nonspherical in the FE phase and its polarization helps stabilize the tetragonal ground state.

Density functional electronic structure calculations on several other perovskites including KTaO_3 , KNbO_3 , [24,25] and PbZrO_3 have now established that the strong transition metal-oxygen covalency is a general feature of the ABO_3 perovskites. The absence of ferroelectricity in KTaO_3 , as contrasted in KNbO_3 , has been identified as due to extreme sensitivity of the soft mode to this covalency and to the slight chemical differences between Ta and Nb, particularly the higher d binding energy of Nb. The calculated energies of the soft FE modes of KTaO_3 and KNbO_3 at their experimental volumes are shown in Fig. 1.6. In the figure, the energy per formula unit is plotted as a function of the relative displacement of the transition-metal ion with respect to the oxygen octahedra. Consistent with these results, the LDA calculations yield a stable (real frequency) FE mode for KTaO_3 and an unstable (imaginary frequency) FE mode for KNbO_3 as observed experimentally.

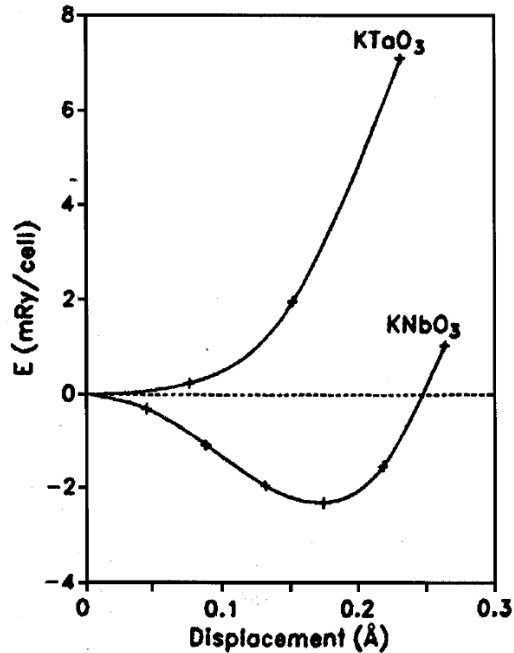


Fig. 1.6: Potential energy vs. soft-mode displacement for KTaO_3 and KNbO_3 calculated using first principles theory.

1.4 Multiferroics

The term multiferroics was coined by Schmid [2] to encompass materials which exhibit two or more of the primary ferroic properties observed in the same phase. Ferroelectricity, ferromagnetism, ferroelasticity and ferrotoroidicity form the four basic primary ferroic order parameters and ferrotoroidicity is still being under debate. This implies that they have a spontaneous magnetization that can be reoriented by an applied magnetic field, a spontaneous polarization that can be reoriented by an applied electric field and a spontaneous deformation that can be reoriented by an applied stress. It is, however, customary to exclude ferroelasticity and consider only magnetic and ferroelectric characteristics. Materials which exhibit both magnetic and electrical orderings have invited much attention in the past few years not only because of their fascinating aspects in fundamental science, but because of their technological potential in possible device applications. For example, they have high dielectric permittivity and high magnetic permeability and could therefore replace the inductor and capacitor in resonant circuits with a single component, further miniaturizing portable cellular technologies. Strong coupling between the polarization and magnetization would allow ferroelectric data storage combined with a magnetic read and the ability to tune or switch the magnetic properties with an electric field and vice versa could lead to as-yet-unanticipated developments in conventional devices such as transducers.

As of now, not many multiferroic compounds are known. Most of them are antiferromagnetic ferroelectrics and the preferred combination of ferromagnetism and ferroelectricity is only achieved in the form of weak ferromagnetism or weak

ferroelectricity accompanying the otherwise antiferroic order [4,26,27]. There are 20 point groups that allow a spontaneous electric polarization, \mathbf{P} , and 31 that allow a spontaneous magnetic polarization, \mathbf{M} . Thirteen point groups (1, 2, 2', m , m' , 3, 3 m' , 4, 4 m' , $m'm'2'$, $m'm'2'$, 6, and 6 m') are found in both sets, allowing both properties to exist in the same phase. However, symmetry restrictions cannot explain the low number of magnetic ferroelectrics because even in compounds permitting the coexistence it is usually absent. Furthermore, the dearth of magnetic ferroelectrics may find a reason as due to the less number of magnetic insulators because ferroelectrics are essentially insulators and magnets are often metals. However, there are many ferrimagnets or weak ferromagnets (showing canted antiferromagnetic ordering) which are insulators, but do not develop ferroelectricity. Therefore, a lack of magnetic insulators cannot account for the low number of magnetic ferroelectrics.

The common perovskite oxide ferroelectrics have a formal charge corresponding to the d^0 electron configuration on the B cation. Clearly, if there are no d electrons creating localized magnetic moments, then there can be no magnetic ordering of any type, either ferro-, ferri-, or antiferromagnetic. It appears however that, in most cases, as soon as the d shell on the small cation is partially occupied, the tendency for it to make a distortion that removes the center of symmetry is eliminated. This could be the result of a number of effects, including size, structural distortion. The Shannon ionic radii of some common d^0 small cations found in ferroelectric perovskite oxides are: Ti^{4+} , 74.5 pm; Nb^{5+} , 78 pm; and Zr^{4+} , 86 pm. Some representative d^n cations that are found as the small cations in nonferroelectric perovskite oxides include Mn^{3+} (d^4), Ti^{3+} (d^1), and V^{4+} (d^1) with radii of 78.5, 81, and 72 pm, respectively. Therefore, typical B-site cations with d

electron occupation do not have considerably larger radii than typical d^0 B-site cations. So, it can be concluded that the size of the B cation is not the deciding factor in the existence or absence of ferroelectricity. In perovskite compounds, the transition metal ion can trigger two types of Jahn–Teller distortion: (i) A first-order distortion which retains the centre of symmetry by elongation of the oxygen octahedra observed in the case of LaMnO_3 and YTiO_3 having partially filled 3d orbitals in transition metal ions [28]. (ii) A second-order distortion which breaks the centrosymmetry by off-centre movement of the transition-metal ion, the well-known examples being BaTiO_3 and PZT and this requires an empty 3d shell. Since only a partially filled 3d orbital can lead to magnetic ordering, whereas the breaking of centrosymmetry is a necessary condition for the formation of a spontaneous polarization, the conditions for ferroelectricity and (anti)ferromagnetism are mutually exclusive. In spite of this incompatibility, multiferroism has been achieved in various compounds where some mechanisms like structural anisotropy, paramagnetic doping, lone-pair asymmetry etc. come into play.

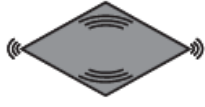
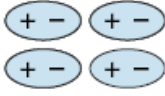
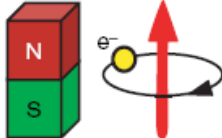
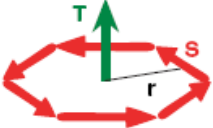
The first ferromagnetic ferroelectric material to be discovered [29] was nickel iodine boracite, $\text{Ni}_3\text{B}_7\text{O}_{13}\text{I}$ which is widely believed as the Rochelle salt for magnetic ferroelectrics. Magnetoelectric switching has been known to occur in $\text{Ni}_3\text{B}_7\text{O}_{13}\text{I}$. This was followed by the synthesis of many more multiferroic boracite compounds with the general formula $\text{M}_3\text{B}_7\text{O}_{13}\text{X}$ ($\text{M} = \text{Cr, Mn, Fe, Co, Cu, Ni}$ as the bivalent ion and $\text{X} = \text{Cl, Br, I}$) which are ferroelectric ferroelastic antiferromagnets, in some cases accompanied by a weak ferromagnetic moment. Many of them possess a ferroelectric Curie temperature above room temperature, whereas the magnetic ordering temperature never

exceeds 100 K [30]. The search for multiferroic material started in the late nineteen fifties in Russia, with the transition metal ion in a perovskite oxide configuration partly replaced by paramagnetic ion. Using this approach, multiferroicity was acquired in solid solutions like $\text{PbFe}_{1/2}\text{Nb}_{1/2}\text{O}_3$ [31] and $[\text{PbFe}_{2/3}\text{W}_{1/3}\text{O}_3]_{1-x}[\text{PbMg}_{1/2}\text{W}_{1/2}\text{O}_3]_x$ [32]. Here, Mg and W ions are diamagnetic and cause the ferroelectricity and the formally d^5 Fe^{3+} ion is responsible for the magnetic ordering. Similar other examples include $\text{Pb}_2(\text{CoW})\text{O}_6$ and $\text{Pb}_2(\text{FeTa})\text{O}_6$ [33] which are both ferroelectric and ferromagnetic. Multiferroics of composition BaMF_4 with $M = \text{Mg, Mn, Fe, Co, Ni, Zn}$ were introduced and discussed in detail by Guggenheim and Scott [34,35]. These compounds are ferroelastic ferroelectric with an extrapolated Curie temperature above the melting point showing antiferromagnetic or weak ferromagnetic ordering at 25 – 70 K.

1.4.1 Symmetry

Any physical system can be characterized by its behavior under a reversal of space and time. These so-called parity operations possess only two eigen values, -1 and +1, which correspond to a change of sign or no change of sign, respectively, when the parity operation is applied [36]. The primary ferroic properties (Table 1.1) can be characterized by their behavior under space and time inversion. Space inversion, for example, will reverse the direction of polarization (P), while leaving the magnetization (M) invariant. Time reversal, in turn, will change the sign of M, while the sign of P remains invariant. Thus, multiferroics are space- and time-asymmetric because of the coexistence of two order parameters—one violating space reversal symmetry and one violating time-reversal symmetry.

Table 1.1 : Ferroics - symmetry

Time \ Space	Invariant	Change
Invariant	Ferroelastic 	Ferroelectric 
Change	Ferromagnetic 	Ferrotoroidic 

1.4.2 Magnetoelectric effect

The magnetoelectric (ME) effect, in its most general definition, indicates the coupling between electric and magnetic fields in matter [27]. Two independent events mark the birth of the ME effect. (i) In 1888, Rontgen observed that when a moving dielectric was placed in an electric field, it became magnetized, which was later followed by discovery of the reverse effect—polarization of a moving dielectric in a magnetic field. (ii) In 1894, the possibility of intrinsic ME behavior of (non-moving) crystals on the basis of symmetry considerations was pointed by Curie [37]. The term ‘magnetoelectric’ was coined by Debye [38] a few years after the first (unsuccessful) attempts to demonstrate the static ME effect experimentally. Although Curie’s early recognition of symmetry has been considered a key issue in the search for ME behavior, many decades passed until it was realized that the ME response is only allowed in time-asymmetric media. Such violation of time-reversal symmetry can extrinsically occur through application of an external magnetic field or movement as in the historic experiment conducted by Rontgen [39], or intrinsically in the form of long-range

magnetic ordering. Dzyaloshinskii [40] was the first to show violation of time-reversal symmetry explicitly for a particular system (antiferromagnetic Cr_2O_3), which was soon followed by experimental confirmation of an electric-field-induced magnetization and a magnetic field-induced polarization in Cr_2O_3 , both linear in the applied field. The experiments on Cr_2O_3 constituted a breakthrough in research on the ME effect. Nevertheless, it became immediately clear that technical applications, e.g. in the form of ME switches, were hampered by the small magnitude of the induced polarization or magnetization. The subsequent search for alternative ME materials revealed ME behaviour in Ti_2O_3 , GaFeO_3 , several boracite and phosphate compounds, solid solutions like $\text{PbFe}_{0.5}\text{Nb}_{0.5}\text{O}_3$ and garnet films among others. Soon, about 80 compounds displaying the ME effect had been identified. Wood and Austin had proposed 15 types of applications of ME materials [41]. Devices for (i) modulation of amplitudes, polarizations and phases of optical waves, (ii) ME data storage and switching, (iii) optical diodes, (iv) spin-wave generation, (v) amplification and (vi) frequency conversion were discussed. However, use of the ME effect as a tool in basic research was considered far more promising than engineering applications at that time. Because of its time-asymmetric nature, the ME effect was regarded as a complementary tool for neutron diffraction in the determination of magnetic symmetries and phase transitions and for the observation of antiferromagnetic domains and their manipulation [42].

The magnetoelectric effect in a single-phase crystal is traditionally explained [43,44] through Landau theory by writing the free energy F of the system in terms of an applied magnetic field H whose i^{th} component is denoted H_i and an applied electric field

E whose i^{th} component is denoted E_i . Note that this convention is unambiguous in free space, but that E_i within a material encodes the resultant field that a test particle would experience. Let us consider a non-ferroic material, where both the temperature-dependent electrical polarization $P_i(T)$ (μCcm^{-2}) and the magnetization $M_i(T)$ (μ_B per formula unit, where μ_B is the Bohr magneton) are zero in the absence of applied fields and there is no hysteresis. It may be represented as an infinite, homogeneous and stress-free medium by writing F under the Einstein summation convention in S.I. units as:

$$-F(E,H) = \frac{1}{2} \epsilon_0 \epsilon_{ij} E_i E_j + \frac{1}{2} \mu_0 \mu_{ij} H_i H_j + \alpha_{ij} E_i H_j + \frac{1}{2} \beta_{ijk} E_i H_j H_k + \frac{1}{2} \gamma_{ijk} H_i E_j E_k + \dots \quad (1)$$

The first term on the right hand side describes the contribution resulting from the electrical response to an electric field, where the permittivity of free space is denoted ϵ_0 , and the relative permittivity $\epsilon_{ij}(T)$ is a second-rank tensor that is typically independent of E_i in non-ferroic materials. The second term is the magnetic equivalent of the first term, where $\mu_{ij}(T)$ is the relative permeability and μ_0 is the permeability of free space. The third term describes linear magnetoelectric coupling via $\alpha_{ij}(T)$; the third-rank tensors $\beta_{ijk}(T)$ and $\gamma_{ijk}(T)$ represent higher-order (quadratic) magnetoelectric coefficients.

In the present scheme, all magnetoelectric coefficients incorporate the field independent material response functions $\epsilon_{ij}(T)$ and $\mu_{ij}(T)$. The magnetoelectric effects can then easily be established in the form $P_i(H_j)$ or $M_i(E_j)$. The former is obtained by differentiating F with respect to E_i and then setting $E_i = 0$. A complementary operation involving H_i establishes the latter. One obtains:

$$P_i = \alpha_{ij}H_j + \frac{1}{2} \beta_{ijk}H_jH_k + \dots \quad (2)$$

and
$$M_i = \alpha_{ij}E_j + \frac{1}{2} \gamma_{ijk}E_jE_k + \dots \quad (3)$$

In ferroic materials, the above analysis is less rigorous because $\epsilon_{ij}(T)$ and $\mu_{ij}(T)$ display field hysteresis. Moreover, ferroics are better parameterized in terms of resultant rather than applied fields [45]. This is because it is, then, possible to account for the potentially significant depolarizing/demagnetizing factors in finite media, and also because the coupling constants would then be functions of temperature alone, as in standard Landau theory.

The magnetoelectric behavior of a material can be fully understood if its magnetic point group symmetry is known. This is because the magnetoelectric coefficients α_{ij} , β_{ijk} and γ_{ijk} possess the symmetry of the material. For example, α_{ij} can only be nonzero for materials that do not have a centre of symmetry and are time-asymmetric. Conversely, information regarding the magnetoelectric coefficients based on electrical [46] or optical [47] experiments can aid the determination of magnetic point group symmetries. Magnetoelectric coupling can be measured indirectly by simply recording changes in either the magnetization near, say, a ferroelectric transition temperature or the dielectric constant near a magnetic transition temperature. The resulting effects are described using various terms such as ‘magnetocapacitance’ or ‘magnetodielectric response’. However, true magnetocapacitance measurements do not provide mechanistic insight nor yield coupling constants. Direct measurements are more challenging. They record either a magnetic response to an applied electric field or an electrical response to an applied

magnetic field. The former scenario typically requires electrically addressing the sample in a magnetometer. In the latter scenario, the electrical response can be measured in terms of either current or voltage. The time-integrated current per unit area directly represents the magnetically induced change of polarization in equation (2), that is, $\alpha = \partial P / \partial H$, ignoring higher-order terms.

Nonlinear Coupling: Most materials have small values of either ϵ_{ij} or μ_{ij} or both, so the linear magnetoelectric effect will also be small. However, no such restriction applies to higher-order couplings, such as those described by β_{ijk} and γ_{ijk} . For example, in some materials, terms such as $\beta_{ijk}H_jH_k$ can dominate the linear term $\alpha_{ij}H_j$ in equation (2), as first shown experimentally at low temperatures in the piezoelectric paramagnet $\text{NiSO}_4 \cdot 6\text{H}_2\text{O}$ [48]. In order to achieve large magnetoelectric effects at room temperature through higher-order terms, we suggest investigating magnetic materials with reduced dimensionality. Indeed, two-dimensional spin order associated with $\beta(T)$ can persist to a temperature T_{2D} that exceeds the temperature T_{3D} at which three-dimensional spin order associated with $\alpha(T)$ is destroyed. This scenario arises at low temperature in BaMnF_4 [49].

Indirect Coupling: So far, our discussion of linear and higher-order magnetoelectric coupling has ignored the effects of strain. Such effects could be significant or even dominant. For example, the inclusion of piezomagnetism (magnetostriction) would generate cross terms in equation (1) that are proportional to strain and vary linearly (quadratically) with H_i . Analogous expressions would arise from piezoelectricity or

electrostriction. Furthermore, mixed terms involving products of strain, H_i and E_j have been predicted [50]. In two-phase materials, magnetic and electrical properties are strain-coupled by design in the quest for large magnetoelectric effects. Indirect coupling with enhancements in strength of several orders of magnitude over single-phase systems have been achieved [51].

In summary, magnetoelectric coupling, which describes the influence of a magnetic (electric) field on the polarization (magnetization) of a material and vice versa, is an independent phenomenon which may not necessarily arise in materials that are both magnetically and electrically polarizable [Fig. 1.7, Ref. 43].

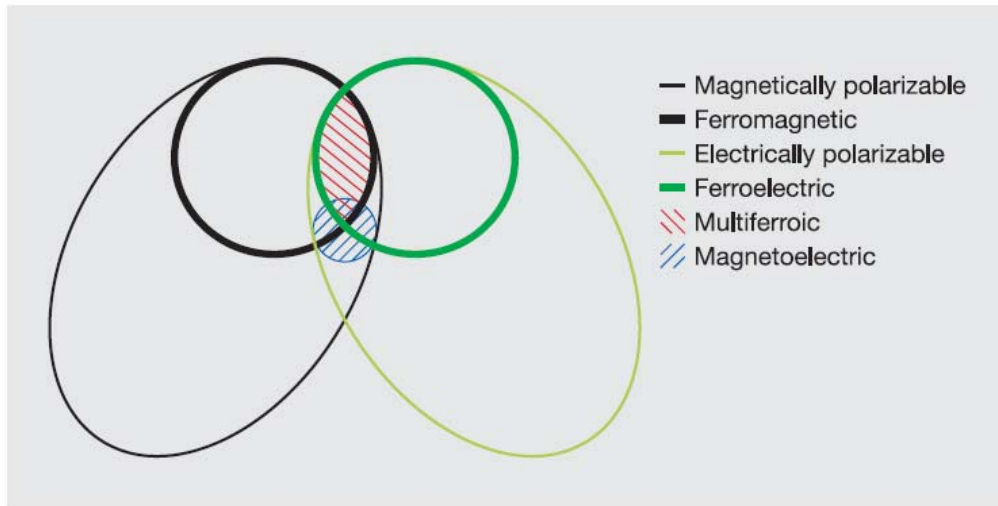


Fig. 1.7: The relationship between multiferroic and magnetoelectric materials. Ferromagnets (ferroelectrics) form a subset of magnetically (electrically) polarizable materials such as paramagnets and antiferromagnets (paraelectrics and antiferroelectrics). The intersection (red hatching) represents materials that are multiferroic. Magnetoelectric coupling (blue hatching) is an independent phenomenon that can, but need not, arise in any of the materials that are both electrically and magnetically polarizable. In practice, it is likely to arise in all such materials, either directly or via strain. [Ref. 43]

1.4.3 Types of multiferroics

Bismuth-based compounds: Lone pair effect

Properties of the Bismuth compounds are largely determined by the Bi 6s lone pair. The so called lone pairs, two valence electrons of Bi^{3+} , and also of Pb^{2+} , which could have participated in chemical bonds using (sp) hybridized states (usually sp^2 or sp^3), but which in these systems do not participate in such bonds. The Bi ion with two electrons on the 6s orbital moves away from the centrosymmetric position in its oxygen surrounding [52]. From the phenomenological point of view, this gives high polarizability of corresponding ions, which in classical theory of ferroelectricity is believed to lead, or at least strongly enhance, the instability towards ferroelectricity. From the microscopic point of view, we can simply say that the particular orientation of these lone pairs, or dangling bonds, may create local dipoles, which finally can order in a ferroelectricity or antiferroelectricity fashion. Because the ferroelectric and magnetic orders in these materials are associated with different ions, the coupling between them is weak. BiFeO_3 is an incommensurate antiferromagnet and a commensurate ferroelectric at room temperature [53, 54]. The spins are not collinear and take a long wavelength-spiral form and the magnetoelectric effect is, therefore, not linear and occurs in the presence of a large magnetic field [55] or by appropriate chemical substitution [56] and in epitaxial thin films [57].

BiMnO_3 is probably the only single-phase material which is truly multiferroic, but the observed polarization is small ($0.12 \mu\text{C}/\text{cm}^2$ at 87 K) [58]. In Fig. 1.8, we show the magnetic and ferroelectric properties of BiMnO_3 along with the magnetic field induced changes in the dielectric constant [58, 59]. Ferromagnetism in BiMnO_3 is due to orbital

ordering [60] and ferroelectric ordering is accompanied by a structural transition [58]. It has been shown recently that BiMnO₃ is centrosymmetric at room temperature with the centrosymmetric space group C2/c [61]. Theoretical calculations also seem to suggest a centrosymmetric structure. It is possible that this material is locally non-centrosymmetric and globally centrosymmetric. We shall discuss this aspect later in the framework of ferroelectricity of YCrO₃ [62]. BiCrO₃ exhibits a ferroelectric transition at 440 K and parasitic ferromagnetism below 114 K [63]. Bi₂Mn_{4/3}Ni_{2/3}O₆ is a polar oxide showing a magnetic response of a concentrated spin-glass below 35 K [64]. Bi₂MnNiO₆ shows both the ferroelectric and ferromagnetic properties [65].

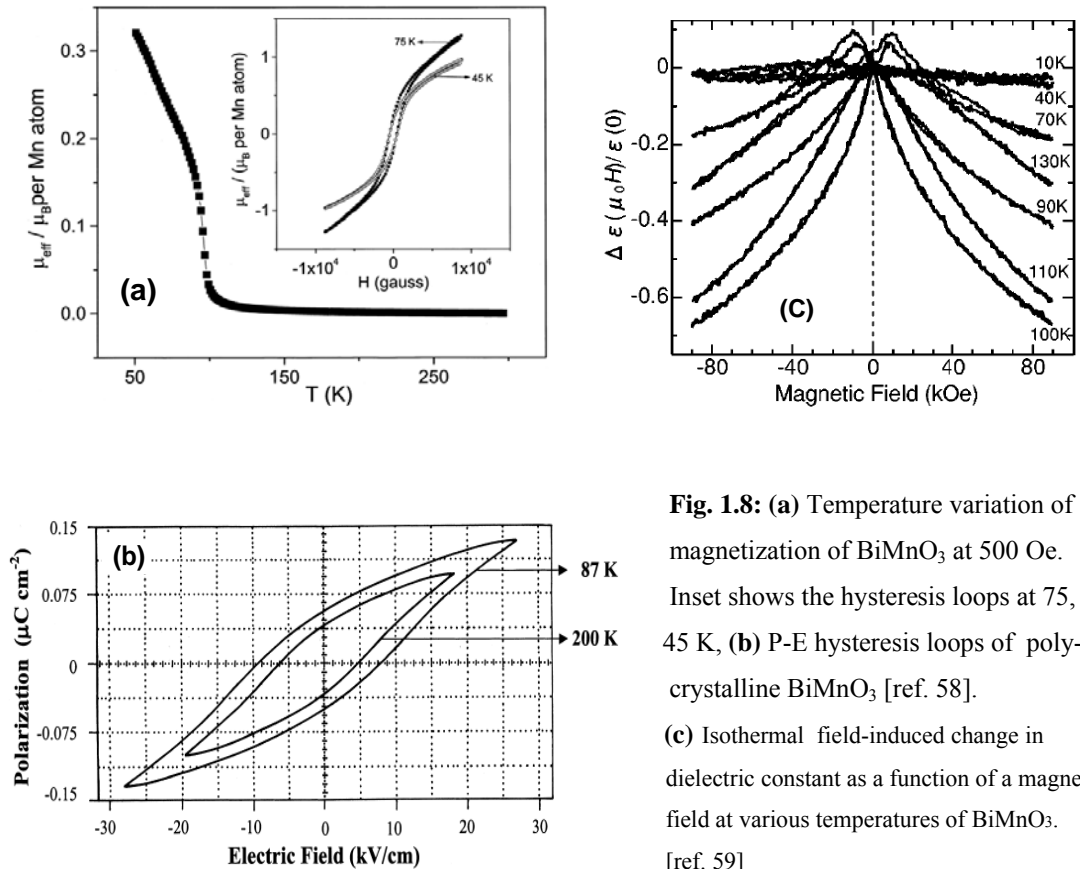


Fig. 1.8: (a) Temperature variation of magnetization of BiMnO₃ at 500 Oe. Inset shows the hysteresis loops at 75, 45 K, (b) P-E hysteresis loops of polycrystalline BiMnO₃ [ref. 58]. (c) Isothermal field-induced change in dielectric constant as a function of a magnetic field at various temperatures of BiMnO₃. [ref. 59]

Rare earth manganites, LnMnO_3 : Spiral magnetic ordering and polyhedral tilting

Rare-earth manganites RMnO_3 prepared under ordinary synthetic conditions crystallize in the orthorhombic perovskite structure ($o\text{-RMnO}_3$) for $R=\text{La-Dy}$ with large ionic radius (r_{ion}) and in the hexagonal structure ($h\text{-RMnO}_3$) for $R=\text{Ho-Lu}$ with smaller r_{ion} . $o\text{-RMnO}_3$ manganites show a rich variety of subtle interplay among charge, spin, orbital, and lattice degrees of freedom, for example, colossal magnetoresistance and charge ordering in hole-doped LaMnO_3 [66] and the recent discovery of multiferroicity in TbMnO_3 and DyMnO_3 [67,68]. Because of the orbital ordering of Mn^{3+} ions in orthorhombic RMnO_3 , the exchange between nearest neighbouring spins and the next-nearest neighboring spins is ferromagnetic (FM) in the ab planes. Therefore, spins in each ab plane of LaMnO_3 order ferromagnetically. But, the coupling between the planes is antiferromagnetic (AFM) [8]. The replacement of La by smaller ions such as Tb or Dy increases structural distortion, inducing next nearest-neighbour AFM exchange in the ab planes comparable to the nearest-neighbour FM exchange. This frustrates the FM ordering of spins in the ab planes and below ~ 42 K, Tb(Dy)MnO_3 shows an incommensurate magnetic ordering with a collinear sinusoidal modulation along the b axis, which is paraelectric. However, as temperature is lowered and magnetization grows in magnitude, a spiral state with rotating spins becomes energetically more favourable, sets in at ~ 28 K, and induces ferroelectricity. Thus, the perovskite compounds RMnO_3 ($R = \text{Eu, Gd, Tb and Dy}$) show a transition to an incommensurate lattice structure below their Ne'el temperature, and subsequently undergo a transition to A- type antiferromagnetic state for EuMnO_3 and GdMnO_3 and an incommensurate-commensurate (IC-C) phase transition for TbMnO_3 and DyMnO_3 at a lower temperature [69]

(Fig. 1.9 (a)). Although the ground state of GdMnO_3 with the largest ionic radius of R (r_R) is not ferroelectric in zero magnetic fields ($H = 0$), a ferroelectric phase with electric polarization (P) along the a axis appears by applying $H = 1$ T along the b axis. Both TbMnO_3 and DyMnO_3 show a ferroelectric order with P along the c axis even at $H = 0$ below a lock-in transition temperature where nonzero wave vectors for magnetic and lattice modulations become nearly constant [69]. The ferroelectric order arises at T_{lock} only in the compounds where the wave number of lattice modulation is fractional ($0 < \delta_l < 1$) at the commensurate (C) phase below T_{lock} [68]. This result confirms that the ferroelectricity in RMnO_3 can be discussed in the framework of improper ferroelectrics [68,70], where P is generated by secondary atomic displacements induced by anharmonic couplings to the primary lattice modulation with nonzero wave vector (i.e., $\delta_l \neq 0$). These systems also exhibit a flop of the ferroelectric polarization from $P \parallel c$ to $P \parallel a$, when H is applied along the a or b axis.

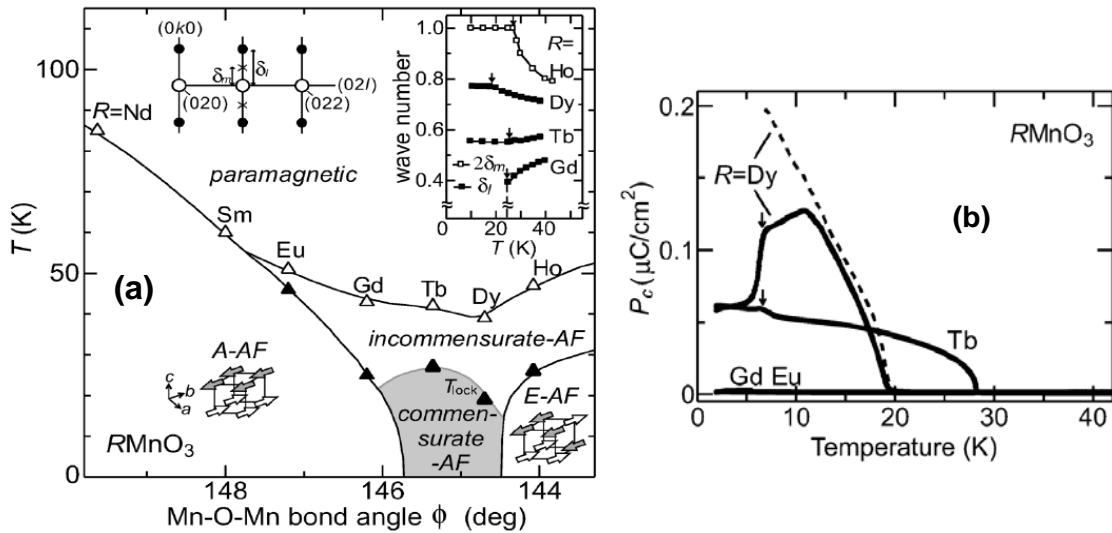


Fig. 1.9: (a) Magnetic phase diagram for RMnO_3 as a function of Mn-O-Mn bond angle ϕ . Open and closed triangles denote the Néel and lock-in transition temperatures, respectively. (b) Temperature profiles of electric polarization along the c axis for crystals of RMnO_3 . [Ref. 68]

Fig. 1.9 (b) shows the polarization along c -axis in ferroelectric TbMnO_3 and DyMnO_3 and the anomalies at T_{flop} or T_N (R) corresponding to the ordering of R -moment. The perovskite RMnO_3 ($R=\text{Ho, Er, Tm, Yb, and Lu}$) are prepared under high pressure [71]. Heat capacity studies show that the temperature interval between the antiferromagnetic transition and the first-order transition to the presumably E -type structure narrows with the decreasing ionic radius of R and almost closes for $R=\text{Lu}$. Ferroelectricity is observed in orthorhombic HoMnO_3 and YMnO_3 at the magnetic lock-in transitions into an E -type structure [72,73]. In HoMnO_3 , the ferroelectric polarization strongly depends on the external magnetic field, indicating the involvement of the rare earth moment order in this compound. Gigantic magnetoelectric phenomena has been observed in DyMnO_3 [68]. Fig. 1.10 (a) and (b) demonstrate gigantic magnetoelectric phenomena observed in DyMnO_3 which indicate the flop of ferroelectric polarization vector from the direction along the c to the a axis by the application of B . Fig. 1.10(c) shows the isothermal magnetocapacitance $\{\Delta\epsilon_a(B)/\epsilon_a(0)=[\epsilon_a(B) - \epsilon_a(0)]/\epsilon_a(0)\}$ curves at several temperatures marking the shift of B_{flop} towards higher B with increasing T and greater magnetocapacitance.

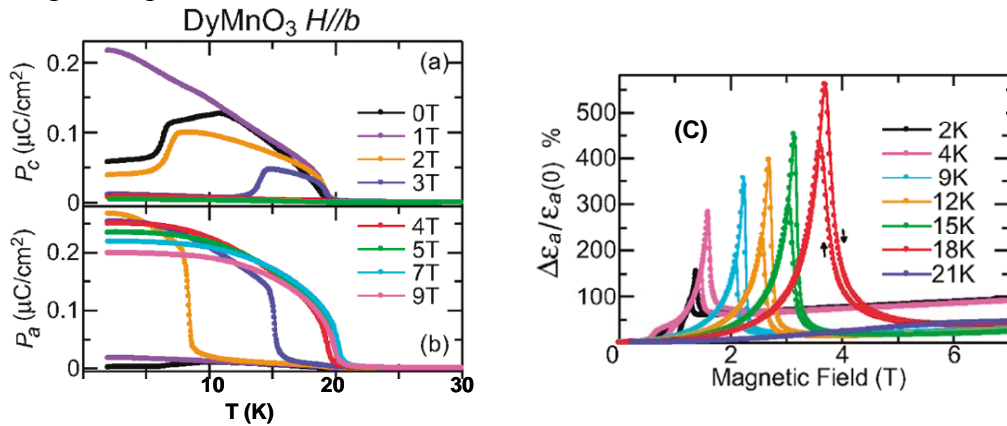


Fig. 1.10: (a), (b) Temperature dependence of electric polarization along the c and a axes at several magnetic fields for crystals of DyMnO_3 . (c) Isothermal magnetocapacitance effect at several temperatures with electric field parallel to the a axis. Magnetic field was applied along the b axis [Ref. 68].

The $RMnO_3$ ($R = Ho, \dots Lu, Y$ or Sc) compounds prepared by standard solid-state reaction at ambient pressure crystallize in the hexagonal structure [74]. The hexagonal structure adopted by $YMnO_3$ and the manganites of the small rare earths consists of non-connected layers of MnO_5 trigonal bipyramids corner-linked by in-plane oxygen ions (O_P), with apical oxygen ions (O_T) forming close-packed planes separated by a layer of R^{3+} ions [75]. It is markedly different from the cubic perovskite structure, which features MnO_6 octahedra corner-linked to form a three-dimensional (3D) network. Early work in the 1960s established $YMnO_3$ to be ferroelectric [76,77], with space group $P6_3cm$ and revealed an A-type antiferromagnetic ordering with non-collinear Mn spins oriented in a triangular arrangement. Recent reports [78,79] of coupling between the magnetic and ferroelectric ordering in $YMnO_3$ provide compelling motivation for understanding the origin of its ferroelectric behavior. In the 1970s, the high-temperature crystal structure of $YMnO_3$ was investigated [80] and a change in symmetry above the ferroelectric ordering temperature was observed.

We find that the main difference between the paraelectric $P6_3/mmc$ and ferroelectric $P6_3cm$ structures is that in the paraelectric phase, all ions are constrained to planes, parallel to the ab plane, whereas below the ferroelectric transition temperature, the mirror planes perpendicular to the hexagonal c axis are lost [75]. There are two major atomic displacements in the crystal structure from the centrosymmetric $P6_3/mmc$ to the ferroelectric $P6_3cm$. The first change is the buckling of R-planes and the tilting of MnO_5 bipyramids, which results in a shorter c axis. Furthermore, due to the tilting, O_T ions are shifted in-plane towards the two longer Y- O_P bonds. The second change is the vertical shift of the Y ions away from the high-temperature mirror plane, while keeping the

distance to O_T constant. Both the bond lengths within the MnO_5 bipyramids and the $Y-O_T$ bond lengths within the six-fold coordination remain unchanged. As a result, one of the two ~ 2.8 Å $Y-O_P$ bond lengths is reduced to ~ 2.3 Å, the other is enlarged to 3.4 Å, leading to a net electric polarization. Just like $YMnO_3$, hexagonal $HoMnO_3$ also exhibits a dielectric anomaly at T_N (75 K) [81]. An electrically driven magnetic phase transition has also been observed in $HoMnO_3$. Hexagonal $LuMnO_3$ also shows a dependence of the dielectric constant in the T_N region with a weak magnetoelectric coupling [82].

Concerning the magnetism of hexagonal $RMnO_3$, there are several neutron-scattering measurements [83–86] to investigate the magnetic ordering of Mn moments. According to those studies, the ordering pattern of the Mn moments in hexagonal $RMnO_3$ is the so-called 120° structure, where the Mn moments lie within a triangular-lattice layer. The Neél temperature (T_N) ranges from 70 K to 130 K upon changing the rare earth R and this is much lower than a Weiss temperature (θ), typically $|\theta| \sim 10T_N$. This substantial reduction of T_N compared with $|\theta|$ is attributed to strong geometrical frustration of the triangular lattice of the Mn ions [87]. This ratio is close to unity in the perovskite phase, where there is no geometric frustration of the spin-spin interactions [88]. T_N in the hexagonal phase is about twice that of the perovskite phase, and the absolute value of the Weiss constant $|\theta|$ is enhanced by an order of magnitude in the hexagonal phase relative to its value in the perovskite phase.

The coupled electric and magnetic ordering in ferroelectromagnets is accompanied by the formation of domains and domain walls [89]. The spatial maps of

coupled antiferromagnetic and ferroelectric domains in YMnO_3 are obtained by imaging with optical second harmonic generation. The coupling originates from an interaction between magnetic and electric domain walls, which leads to a configuration that is dominated by the ferroelectromagnetic product of the order parameters.

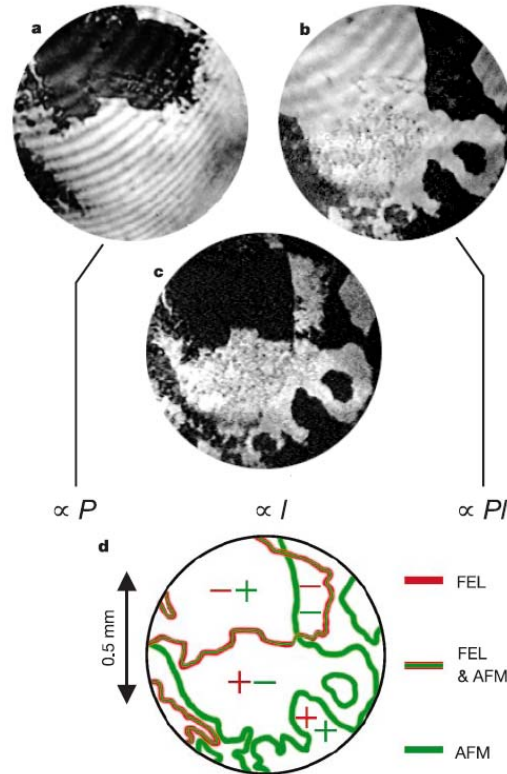


Fig. 1.11: Coexisting electric and magnetic domains of an YMnO_3 sample at 6 K imaged with second harmonic light at 2.46 eV. **(a)** Exposed with second harmonic light from $\chi(P)$. Dark and bright areas correspond to opposite FEL domains. **(b)** Exposed with FEM-second harmonic light from $\chi(Pl)$. Bright and dark regions are distinguished by an opposite sign of the product Pl so that states with $(+P, +l)$ and $(-P, -l)$, or $(+P, -l)$ and $(-P, +l)$ are indistinguishable. The resulting two domain configurations may therefore be termed FEM (pseudo-) domains. **(c)** Exposed with interfering second harmonic contributions from $\chi(P)$ and $\chi(Pl)$. Dark and bright areas correspond to opposite AFM domains. **(d)** Topology of FEL (red) walls and AFM (green) walls in the sample with \pm signs of the corresponding color indicating the orientation of the FEL and AFM order parameters in selected domains. Solely red walls are absent because any FEL wall is accompanied by an AFM wall coupled to it. This is why the sign of the FEM product Pl is conserved upon crossing a FEL domain border, and FEL walls are invisible in **(b)**. [Ref. 89]

LnMn₂O₅ : Frustrated magnetism

The current revolution in the field of multiferroics began with the discovery of the high magnetic tenability of electric polarization and dielectric constant in the orthorhombic rare-earth Manganites RMnO₃ [69] and RMn₂O₅ [90]. Compounds with the general formula RMn_2O_5 (R =rare earth or Bi) crystallize in the orthorhombic structure (space group $Pbam$), where Mn⁴⁺O₆ octahedra share edges to form infinite chains along the c axis, and these chains are linked by pairs of Mn³⁺O₅ pyramids in the ab planes [91-93]. Successive phase transitions of magnetic and dielectric ordering were found to occur simultaneously in this system. The characteristic magnetic ordering of the system exhibits an incommensurate–commensurate phase transition, and again transitions to an incommensurate phase. Special attention is given to the magnetic structure in order to discuss the mechanism for the introduction of ferroelectric polarization. They show sequential magnetic transitions: incommensurate sinusoidal orderings of magnetic Mn spins at $T_1 = 42-45$ K, commensurate antiferromagnetic ordering at $T_2 = 38-41$ K, re-entrant transition into the incommensurate sinusoidal state at $T_3 = 20-25$ K and finally an ordering of rare-earth spins below $T_4 = 10$ K [94-99]. These manganites exhibit electric polarization induced by a collinear spin order in a frustrated magnetic system. Ferroelectricity occurs with the onset of commensurate magnetic ordering which is characterized by a peak in the dielectric curve [90]. The commensurate and incommensurate magnetic structures of the magnetoelectric system YMn₂O₅, as determined from neutron diffraction, were found to be spin-density waves lacking a global center of symmetry. The concept of magnetoelastic coupling to the lattice enables us to predict the polarization based entirely on the observed magnetic structure and sign

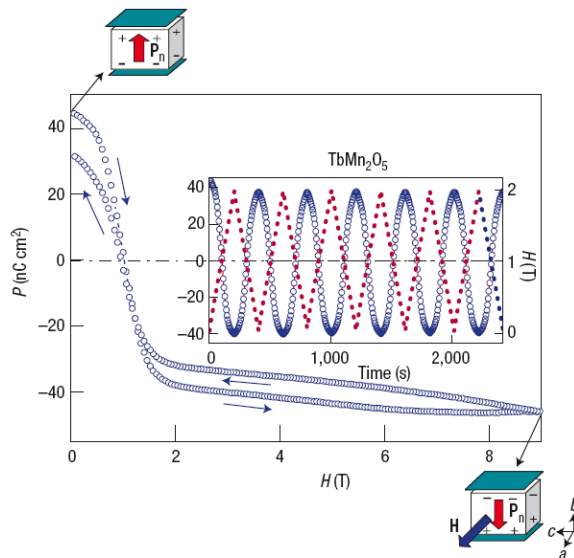
reversal of the spontaneous polarization at the commensurate-incommensurate transition [100]. Magnetically induced changes in bond lengths between Mn ions with different formal valence, adding up to a net ferroelectric moment is the most plausible explanation for the microscopic mechanism of ferroelectricity in this system [101].

Complex magnetic structures and phase diagrams are observed in all multiferroics showing strong interplay between magnetic and dielectric phenomena [101]. All these materials are ‘frustrated’ magnets, in which competing interactions between spins preclude simple magnetic orders. The disordered paramagnetic phase in frustrated magnets extends to unusually low temperatures. For example, the Curie–Weiss temperature, T_{cw} , of YMn_2O_5 , obtained by fitting its magnetic susceptibility χ with the high-temperature asymptotic $\chi \approx [C/(T+T_{cw})]$, is ~ 250 K. The temperature T_{CW} reflects the strength of interaction between spins, and in usual magnets it gives a good estimate of the spin ordering temperature. The fact that the long-range magnetic order sets in at $T_1 \approx 45$ K, which is about five times smaller than T_{cw} , is clear indication for the presence of significant magnetic frustration in YMn_2O_5 .

An external magnetic field induces and/or modifies ferroelectric states in a magnetic material, $DyMn_2O_5$ indicating coupling between magnetic and dielectric properties [102]. Measurements of the temperature dependence of hysteretic polarization curves, pyroelectric current, specific heat, optical second harmonic generation and x-ray superlattice peaks have revealed successive phase transitions between 43 and 4 K, accompanying three ferroelectric phases. The zero-field lowest-temperature phase (< 8 K) induced by the Dy-moment ordering is a reentrant paraelectric state, but is turned into a ferroelectric state with increasing magnetic field. The phenomenon is closely

related to the metamagnetic transitions of the Dy f moment, indicating that all the ferroelectric phases of this material are strongly tied to the antiferromagnetic Mn spin structure affected by the f - d exchange interaction. Similarly, HoMn_2O_5 undergoes a transition to a ferroelectric state around 35 K [103]. With further decreasing temperature (T), HoMn_2O_5 shows the second dielectric transition to the lowest- T phase, where spontaneous polarization is almost zero. The application of H up to 14 T stabilizes the ferroelectric phase in HoMn_2O_5 . The electric polarization in TbMn_2O_5 shows a startling magnetic-field induced reversal at low T , shown in fig. 1.12 [104]. At 3 K, the direction of P is completely reversed with a rather low H , corresponding to a change in P of $\sim 80 \text{ nC cm}^{-2}$ at 2 T. This change in P for H below 2 T is considerably large and nonlinear, suggesting that this behavior stems from H -induced phase transitions, possibly associated with the H -induced change of Tb magnetism. However, the P change for high H is rather linear with H , indicating that the linear magnetoelectric effect becomes active above 2 T. A strikingly reversible and reproducible variation of the polarization by varying H linearly from 0 to 2 T was observed without any noticeable decay in its magnitude, as displayed in inset of Fig. 1.12 envisioning a ferroelectric memory device that can be magnetically recorded.

Fig. 1.12: Change of total electric polarization by applied magnetic fields at 3 K. Polarization flipping at 3 K by linearly varying magnetic field from 0 to 2 T is shown in inset. These results clearly display highly reproducible polarization switching by magnetic fields. [Ref. 101,104]



Relaxor ferroelectric and magnetoelectric spinel RCr_2X_4 [R=Cd, Hg; X=S, Se]

CdCr_2S_4 crystallizes in the normal cubic spinel structure (space group $\text{Fd}\bar{3}\text{m}$, lattice constant $a = 1.024$ nm), with Cr^{3+} octahedrally surrounded by sulphur ions, yielding a half-filled lower t_{2g} triplet with spin $S = 3/2$. It behaves like a typical soft ferromagnet exhibiting ferromagnetic hysteresis and a saturation magnetization of $6 \mu_B$ [105-107]. The observed enhancement of dielectric constant just below the ferromagnetic ordering transition temperature $T_C = 85$ K is strongly correlated with ferromagnetic ordering indicating strong magnetoelectric coupling effect [Fig. 1.13(a)]. A very broad peak appears in the curves for $\epsilon'(T)$ between 150 and 250 K, shifting to lower temperatures and increasing in amplitude with decreasing frequency [105]. It exhibits the characteristic behavior of a relaxor ferroelectric, the typical strong dispersion effects often being ascribed to the freezing-in of ferroelectric clusters [108,109]. Broad peak maxima are revealed, typical of relaxational behavior in the plots for $\epsilon''(\nu)$ for a series of temperatures. The peak frequency decreases when the temperature is lowered, indicating the freezing-in of polar moments. Exchange striction, which mechanically induces the strain, is associated with the ferromagnetic ordering around T_C and local lattice distortion takes place inducing the enhancement of dielectric constant. A ferroelectric ordering occurs near $T_p = 56$ K, which is enhanced by externally applying electric field. The ferroelectricity in CdCr_2S_4 results from an off-centre position of the Cr^{3+} ions [110]. A strong reduction in magnetization is observed well below $T_C = 85$ K with increasing external dc electric field [Fig. 1.13(b)] [107]. A new and remarkable feature is that the external electric field induces a dip in the $M(T)$ curve at a temperature corresponding to

ferroelectric ordering which gradually grows deeper and clearer as the electric field increases. Below this temperature, a detectable suppression of magnetization by electric field occurs. These two phenomena can be thought to be due to the strong correlation among magnetic spin, electric dipole, and the lattice in CdCr_2S_4 .

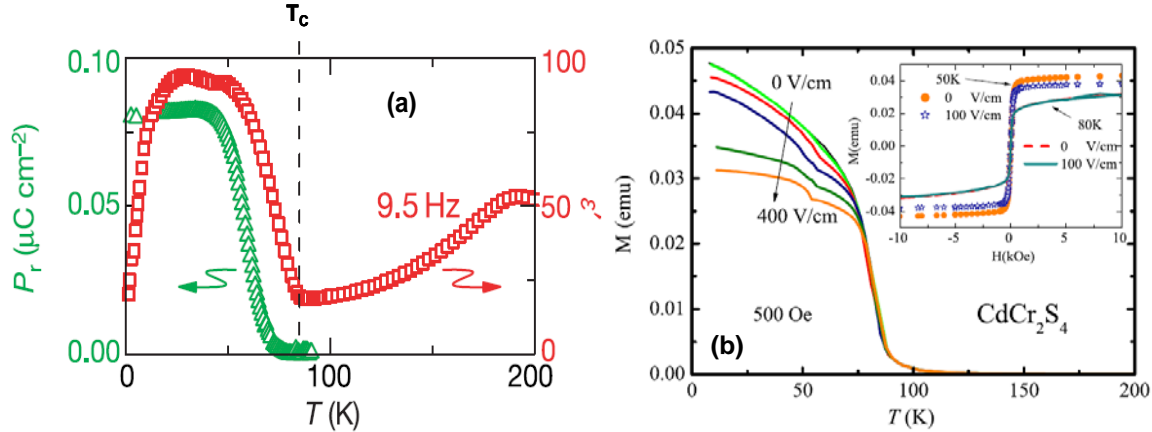


Fig. 1.13 (a) Right scale: dielectric constant versus temperature measured at a frequency of 9.5 Hz. Left scale: thermo-remnant polarization versus temperature measured after cooling in an electric field of 50 kV m^{-1} [Ref. 105]. (b) Temperature-dependent magnetization is measured at 500 Oe. A dip near T_p becomes gradually clearer with increasing external dc electric field. The inset shows the isothermal $M \sim H$ at 80 and 50 K at electric fields of 0 and 100 V/cm. Suppression of $M \sim H$ by electric field is seen at $T = 50 \text{ K}$ (below T_p), but not observed at $T = 80 \text{ K}$ (below T_c) [Ref. 107].

The magnetocapacitive coupling in CdCr_2S_4 is indeed extremely strong and can be termed colossal [107]. For example, the magnetocapacitive ratio at magnetic field 5 T comes out to be 500 % for a frequency of 20 Hz. However, the ferroelectric ordering near T_p under magnetic field shows a much higher ratio than that of the corresponding ferromagnetic state. This colossal magnetocapacitive behavior might be due to the fact that under magnetic field, spins are more ordered and the exchange striction is further enhanced. Raman scattering experiments on CdCr_2S_4 single crystals show pronounced anomalies in intensity and frequency of optical phonon modes with an onset temperature $T = 130 \text{ K}$ that coincides with the regime of giant magnetocapacitive effects [111]. A loss

of inversion symmetry and Cr off-centering are deduced from the observation of longitudinal optical and formerly infrared active modes for $T < T_c = 84$ K. For CdCr_2Se_4 , the magnetic transition is shifted to higher temperatures [112]. The magnetic order sets in at $T_c = 125$ K. At this temperature, an increase of $\epsilon'(T)$ towards lower temperatures is detected too. Thus, similar to CdCr_2S_4 , the closely related CdCr_2Se_4 also exhibits a strong magnetodielectric coupling. The typical relaxor peaks in the real part of the permittivity at $T > T_c$ are shifted to higher temperatures and only can be detected for the lowest frequencies within the examined temperature regime below 300 K. Similarly, the dielectric constant of HgCr_2S_4 becomes strongly enhanced in the region below 60–80 K, triggered by the onset of ferromagnetic correlations. In addition, the observation of polarization hysteresis curves indicates the development of ferroelectric order below about 70 K [113].

Frustrated multiferroic MnWO_4 system

MnWO_4 is one of the multiferroic materials in which the cycloidal spin structure induces ferroelectricity. This material is crystallized in a wolframite structure, which belongs to the monoclinic space group $P2/c$ with $\beta \sim 91^\circ$ at room temperature. The crystal structure is characterized by alternative stacking of manganese and tungsten layers along the a axis. Edge-sharing MnO_6 and WO_6 octahedra are aligned in zigzag chains along the c axis. MnWO_4 is known as a frustrated magnet with only one kind of magnetic ion, Mn^{2+} ($S=5/2$). The ratio of the Weiss temperature (θ) to the Néel temperature (T_N) is reported to be ~ 6 indicating that the magnetic interactions are moderately frustrated in this system [114]. With decreasing temperature, MnWO_4 undergoes successive magnetic phase transitions to three long-wavelength antiferromagnetic (AF) ordering states, AF3

($T_2 < T < T_N$), AF2 ($T_1 < T < T_2$) and AF1 ($T < T_1$), T_1 , T_2 and T_N being 7.6 K, 12.3 K and 13.5 K respectively. According to neutron diffraction results at 0 T [115], AF1, AF2, and AF3 are a commensurate collinear-antiferromagnetic phase, an incommensurate cycloidal-spiral-spin phase, and an incommensurate collinear-antiferromagnetic phase, respectively. In AF1 and AF3, Mn^{2+} magnetic moments collinearly align in the ac plane, forming an angle of about 35° with the a axis, whereas in AF2 an additional component along the b axis exists. Among the three magnetic phases (AF1–AF3), only the AF2 phase with the spiral spin structure shows ferroelectricity [114,116–118]. According to the microscopic model proposed by Katsura et al. [119], the spin moments on two neighboring sites, S_i and S_j , should induce a local dipole moment \mathbf{p} given by $\mathbf{p} = A\mathbf{e}_{ij} \times (\mathbf{S}_i \times \mathbf{S}_j)$, where \mathbf{e}_{ij} is the unit vector connecting the two sites and A is a constant. This formula, which can also be regarded as the inverse Dzyaloshinskii-Moriya interaction [120], predicts the macroscopic uniform \mathbf{P} in a magnetic structure with cycloidal-spiral-spin components, and explains the relationship between magnetic structure and \mathbf{P} observed in the AF2 phase. In addition, the correlation between the vector spin chirality ($\mathbf{C} \equiv \mathbf{S}_j \times \mathbf{S}_i$) of the spiral-spin structure and \mathbf{P} direction has recently been confirmed by spin-polarized neutron diffraction measurement.

The magnetic-field dependence of electric polarization indicates that the noncollinear spin configuration plays a key role for the appearance of the ferroelectric phase [114,121]. A small anomaly of M_b is observed around 10.7 T, which emerges as a peak of the derivative dM_b/dH_b . At this H , FE \mathbf{P} rotates from along b axis to a axis suggesting that the \mathbf{P} flop is caused by an H -induced magnetic phase transition [121]. Since $MnWO_4$ contains no rare-earth element, the present results indicate that the H -

induced P flop can take place without help from $4f$ moments unlike in perovskite RMnO_3 .

Memory effect has been studied through the temperature dependence of P along the b axis (P_b) at 0 T [122]. First, a single crystal sample was cooled from above T_N and P_b was measured by applying a poling electric field along the b axis (open circles), $E = +500$ kV/m [Fig. 1.14(a)]. Below 7.6 K, where the PE AF1 phase appears, the poling field was removed. Then the P_b was measured by warming the sample (filled circles). As shown in the figure, the P_b value in the warming process without a poling E (II) is the same as that obtained in the cooling process with a poling E (I). These results indicate that the domain states of the FE AF2 phase are memorized even in the PE AF1 phase without vector spin chirality, and this “memory effect” makes it possible to reproduce the FE single-domain states without a poling E in the phase transition from the PE (AF1) to the FE (AF2) phase.

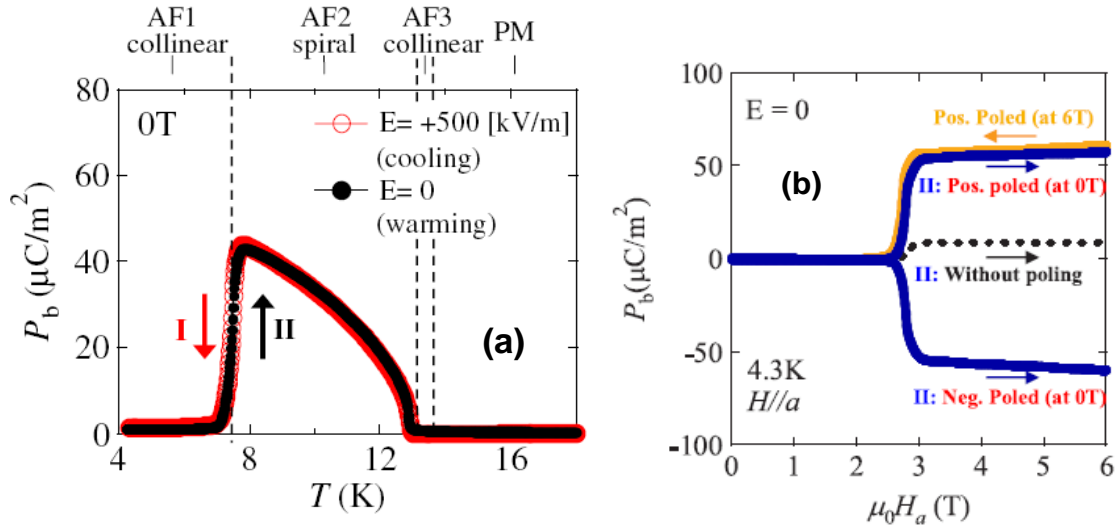


Fig. 1.14 Magnetoelectric memory effect: (a) Temperature dependence of electric polarization along the b axis (P_b). (b) Magnetic-field dependence of electric polarization along the b axis (P_b) at 4.3 K. [Ref. 122]

It has been found that an H can also reproduce the FE single-domain state through the memory effect of the AF1 phase [122]. Fig. 1.14(b) shows the H dependence of P_b . Before each measurement, the sample was cooled from above T_N in an electric field E (-500, 0, or 500 kV/m) at 0 T (I). At 4.3 K (PE AF1), the poling field E was removed, and then P_b was measured while increasing H in the a direction up to 6 T (II). As displayed in Fig. 1.14(b), the H-induced FE phase transition occurs around 3 T. The noticeable point is that the sign of the H-induced FE P depends on the direction of the poling E at 0 T. In addition, the H-induced P value is as large as that of the FE single-domain state, which is shown by an orange (light grey) line in Fig. 1.14(b). These results mean “ME memory effect,” which means we can magnetically read out the electrically written information of the FE single-domain state from the PE state.

Magnetic ferroelectricity due to charge-ordering

It has been pointed out recently by Khomskii and coworkers [123] and later, by Ederer et al. [124] that coupling between magnetic and charge-ordering in charge-ordered and orbital-ordered perovskites like $\text{Ln}_{1-x}\text{A}_x\text{MnO}_3$ and in charge-ordered rare-earth ferrites, LnFe_2O_4 [125,126], can give rise to magneto-ferroelectricity. The essential mechanism by which charge ordering can lead to the appearance of ferroelectricity is easily explained with the help of the schematic picture shown in figures 1.15 and 1.16. In Fig. 1.15(a), a homogeneous crystal (a one-dimensional chain in this case) with equal (say zero) charge on each site is shown. Fig. 1.15(b) shows the same chain after a charge ordering at which the sites become inequivalent: one set of sites has charge $+e$ and the other $-e$, as in NaCl. This process does not break spatial inversion symmetry so that the

resulting state cannot have a net dipole moment. This is made explicit in figure 1.15(b) by marking mirror planes of the charge ordered structure [127].

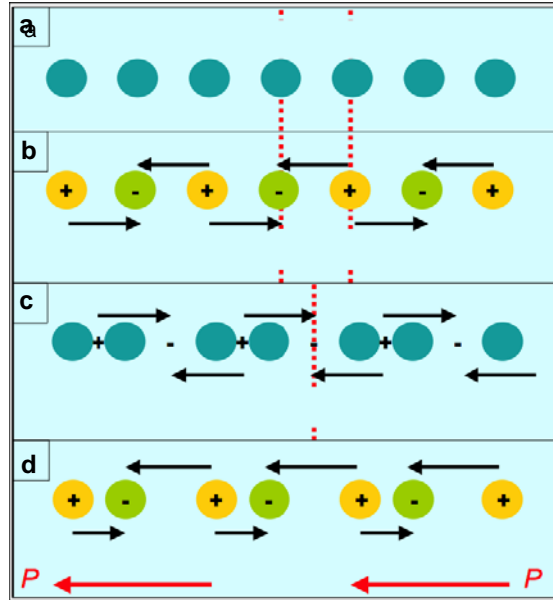


Fig. 1.15: (a) Example of a neutral one-dimensional chain exhibiting (b) site-centered charge ordering, (c) bond-centered charge ordering, and (d) a linear combination of these two that is ferroelectric. The arrows indicate the polarization, which is in total zero in (b) and (c), but develops a macroscopic moment, indicated by the red arrow in (d). The red dashed lines in (a), (b) and (c) indicate mirror planes of the system (ref. [127]).

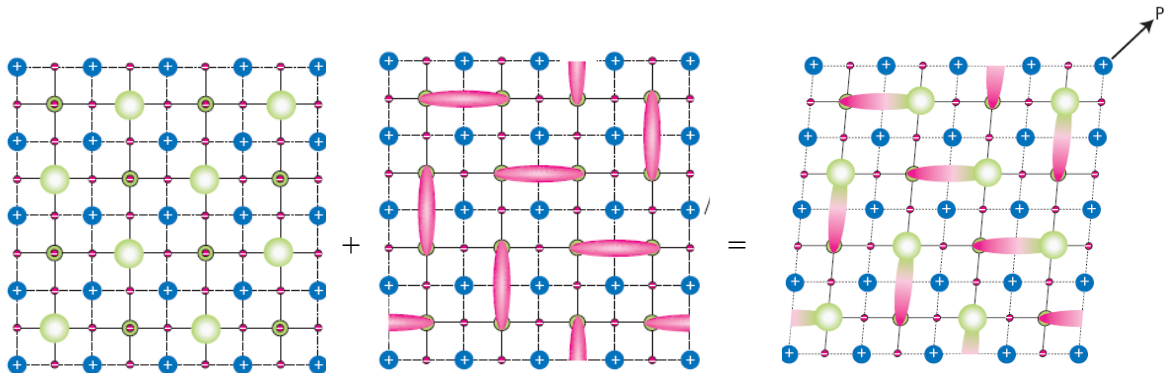


Fig. 1.16: (a) Mn- or site-centred ordering, in which formally 3+ and 4+ Mn ions (green) orbitally order in a checkerboard pattern. The additional charge (green circles) is localized on the Mn sites. (b) The bond-ordering model in which the Mn sites have equal charge and the variation in charge is localized on the Mn-Mn bonds (pink ellipses). (c) The intermediate state proposed by Efremov and colleagues (ref. [123]) combines both Mn-centred and bond-centred ordering, and leads to ferroelectric polarization. (ref. [124])

Another type of charge ordering occurs when a system dimerizes, where the charge is localized not on sites but on bonds, see figures 1.15 (c) and 1.16 (b). The existence of such dimers has also been suggested by Aladine et al. [128] coining the name “Zener Polaron” to the pair of Mn-ions associated with delocalization. One can use the terminology of a site-centered charge ordering (SCO) or site-centered charge density wave (S-CDW) in the case of figure 1.15 (b) and 1.16 (a) and a bond-centered CO (BCO) or bond-centered charge density wave (B-CDW) in the case of figure 1.15 (c) and 1.16 (b). Also the B-CDW structure is centrosymmetric and thus cannot be ferroelectric [127].

If one now combines both types of charge ordering in one system, the situation changes drastically. The situation with simultaneous site- and bond-centered CO is schematically shown in figures 1.15 (d) and 1.16 (c). In this region, the character of the CO actually changes in a regular way, it evolves from a pure site-centered ground state with magnetic CE-type order at $x = 0.5$ to an admixture of bond-centered state increasing with decreasing x , and finally to a pure bond-centered one around $x = 0.4$. From the figures, it is immediately clear that the charge-ordering pattern of this state lacks inversion symmetry. Each molecule [short bond in Fig. 1.15 (d)] develops a net dipole moment so that as a result, the whole system becomes ferroelectric. Thus solids can become ferroelectric if on top of site-centered charge ordering also a bond dimerization occurs [123]. These different charge ordered states are, in general, very close in energy. This observation is confirmed independently by density functional calculations [129, 130].

It is important to note some of the important characteristics of the charge-ordered manganites in order to fully understand their ferroic properties. The most important feature is that all these manganites exhibit electronic phase separation at low temperatures ($T < T_{CO}$) [131]. They exhibit a decrease in resistivity on application of large magnetic fields (> 4 T) [131, 132]. Application of electric fields also causes a significant decrease in the resistivity of the manganites [132, 133]. On the application of electric fields, the manganites show magnetic response [134]. Such electric field-induced magnetization may also be taken as evidence for coupling between the electric and magnetic order parameters in the manganites. It is likely that grain boundaries between the different electronic phases have a role in determining the dielectric behavior. The importance of grain boundaries in giving rise to high dielectric constants has indeed been recognized [135, 136].

Even though the field has been in existence since 1960 or earlier, a huge leap in multiferroic research occurred only after 2000. Recently, many compounds with spiral spin structure like $Ni_3V_2O_8$ [137], $CuFeO_2$ [138] have been found to be multiferroic with strong magnetoelectric coupling. There has been a common practice of realizing the enhanced multiferroic properties through approaches like forming the solid solutions and composites of parent ferroelectric and magnetic materials [139-141].

Recent research on multiferroic systems gives an optimistic scenario wherein alternative mechanisms bring about magnetic ferroelectricity in a variety of materials. Some of the important mechanisms that have emerged relate to tilting of metal-oxygen polyhedra, spiral magnetic ordering and stereochemical activity of the Bi lone pair. In

many of the multiferroic oxides, magnetic frustration appears to give rise to novel magnetic properties which then induce ferroelectricity. The role of local non-centrosymmetry and charge ordering of mixed valent ions are two new ideas that have come to the fore. It appears that many ferroelectric materials formally possessing centrosymmetric structure may indeed have local non-centrosymmetry. In principle, non-centrosymmetry can also be achieved by making use of strain, defects and other factors. Multiferroics also offer theoretical challenges besides attractive experimental possibilities. In particular, there is considerable scope for investigations of the large family of charge-ordered manganites and related materials. It is likely that a large number of materials in this family are not only multiferroic but also magnetoelectric, considering the known effects of electric and magnetic fields on these materials. There is every possibility that magnetoelectric effects in the manganites can be exploited technologically in memory devices, recording and other applications. The recent work of Gajek et al. [142] on thin films of $\text{La}_{0.1}\text{Bi}_{0.9}\text{MnO}_3$ promises their use in memory devices. For experimental materials scientists, the challenge of discovering materials exhibiting both magnetism and ferroelectricity with coupling between them makes the subject exciting. Some of the important aspects are related to united theoretical development, study of spectroscopic properties and discovery of monophasic multiferroic materials showing magnetoelectric coupling.

Bibliography

1. K. Aizu, Possible species of ferromagnetic, ferroelectric, and ferroelastic crystals, *Phys. Rev. B* **2**, 754 (1970)
2. H. Schmid, Multiferroics magnetoelectrics, *Ferroelectrics*, **162**, 317 (1994)
3. A.H. Morrish, *The physical principles of magnetism*, Wiley, New York, (1965).
4. N.A. Hill, Why are there so few magnetic ferroelectrics? *J. Phys. Chem. B*, **104**, 6694 (2000)
5. P. Weiss, Lhypothese du champ moleculaire et la propriete ferromagnetique, *J. Phys.*, **6**, 661 (1907)
6. E.C. Stoner, Atomic moments in ferromagnetic metals and alloys with nonferromagnetic elements, *Philos. Mag.* **15**, 1080 (1933)
7. N.A. Spaldin, Analogies and differences between ferroelectrics and ferromagnets, *Physics of Ferroelectrics*, **105**, 175 (2007)
8. J.B. Goodenough: Theory of the role of covalence in the perovskite-type manganites $[La,M(II)]MnO_3$, *Phys. Rev.* **100**, 564 (1955)
9. J. Kanamori, Superexchange interaction and symmetry properties of electron orbitals, *J. Phys. Chem. Solids* **10**, 87 (1959)
10. P.W. Anderson, New approach to the theory of superexchange interactions, *Phys. Rev.* **115** (1), 2 (1959)
11. P.W. Anderson, *Theory of magnetic exchange interactions*. Academic Press, New York (1963)

12. J.B. Goodenough, Magnetism and the chemical bond. Interscience Publisher, New York (1963).
13. J. Valasek: Piezoelectric and allied phenomena in rochelle salt, Phys. Rev. **17**, 475 (1921)
14. L.E. Cross, Mater. Chem. Phys., Ferroelectric materials for electromechanical transducer applications **43**, 108 (1996)
15. H. D. Megaw: Origin of ferroelectricity in barium titanate and other perovskite-type crystals, Acta Crystallogr. **5**, 739 (1952)
16. P.S. Halasyamani, K.R. Poeppelmeier: Non-centrosymmetric oxides, Chem. Mater. **10**, 2753 (1998)
17. U. Opik, M.L.H. Pryce: Studies of the Jahn–Teller effect I: A survey of the static problem, Proc. Roy. Soc. A **238**, 425 (1957)
18. I.B. Bersuker: Modern aspects of the Jahn–Teller theory and applications to molecular problems, Chem. Rev. **101**, 1067 (2001)
19. W. Cochran, Crystal stability and the theory of ferroelectricity, Phys. Rev. Lett. **3**, 412 (1959)
20. G. A. Samara, Ferroelectricity Revisited – Advances in materials and physics, solid state physics, vol. **56**, Academic Press.
21. L.L. Boyer, R.E. Cohen, H. Krakauer and W.A. Smith, First principles calculations for ferroelectrics — a vision, Ferroelectrics **111**, 1 (1990)
22. R. E. Cohen, Theory of ferroelectrics: a vision for the next decade and beyond, J. Phys. Chem. Solids **61**, 139 (2000)
23. R. E. Cohen, Origin of ferroelectricity in perovskite oxides, Nature **358**, 136 (1992)

24. R. Yu and H. Krakauer, First-principles determination of chain-structure instability in KNbO_3 , *Phys. Rev. Lett.* **74**, 4067 (1995)
25. D.J. Singh, Stability and phonons of KTaO_3 , *Phys. Rev. B* **53**, 176 (1996)
26. C.N.R. Rao and C.R. Serrao, New routes to multiferroics, *J. Mater. Chem.*, **17**, 4931 (2007)
27. M. Fiebig, Revival of the magnetoelectric effect, *J. Phys. D: Appl. Phys.* **38**, R123 (2005)
28. T. Mizokawa, D. I. Khomskii and G.A. Sawatzky, Interplay between orbital ordering and lattice distortions in LaMnO_3 , YVO_3 , and YTiO_3 , *Phys. Rev. B*, **60**, 7309 (1999)
29. E. Ascher, H. Rieder, H. Schmid and H. Stossel, Some properties of ferromagneto electric nickel-iodine boracite, $\text{Ni}_3\text{B}_7\text{O}_{13}\text{I}$, *J. Appl. Phys.*, **37**, 1404 (1966).
30. Y.N. Venevtsev, V.V. Gagulin and I.D. Zhitomirsky, Material science aspects of seignette-magnetism problem *Ferroelectrics* **73**, 221 (1987)
31. G.A. Smolenskii, A.I. Agranovskaya and V.A. Isupov, *Sov. Phys.—Solid State* **1**, 149 (1959)
32. G. Srinivasan, R. Hayes and M.I. Bichurin, Low frequency and microwave magnetoelectric effects in thick film heterostructures of lithium zinc ferrite and lead zirconate titanate, *Solid State Commun.* **128**, 261 (2003)
33. W. Brixel, J.-P. Rivera, A. Steiner, H. Schmid, Magnetic field induced magnetoelectric effects, $(\text{ME})_{\text{H}}$, in the perovskites Pb_2CoWO_6 and $\text{Pb}_2\text{FeTaO}_6$, *Ferroelectrics* **79**, 201, (1988)

34. J.F. Scott, Spectroscopy of incommensurate ferroelectrics, *Ferroelectrics* **24**, 127 (1980)
35. M. Eibschutz and H.J. Guggenheim, Antiferromagnetic-piezoelectric crystals: BaMF_4 ($M = \text{Mn, Fe, Co and Ni}$), *Solid State Communications*, **6**, 737 (1968)
36. B. B. Van Aken, J.-P. Rivera, H. Schmid & M. Fiebig, Observation of ferrotoroidic domains, **449**, 702 (2007)
37. P. Curie, *J. Physique* **3**, 393 (1894)
38. P. Debye, *Z. Phys.* **36**, 300 (1926)
39. W. C. Rontgen, *Ann. Phys.* **35**, 264 (1888)
40. I. E. Dzyaloshinskii, *Sov. Phys.—JETP* **10**, 628 (1959)
41. V. E. Wood and A. E. Austin, *Int. J. Magn.* **5**, 303 (1973)
42. H. Schmid, Introduction to the proceedings of the 2nd international conference on magnetoelectric interaction phenomena in crystals, MEIPIC-2, *Ferroelectrics* **161**, 1 (1994)
43. W. Eerenstein, N.D. Mathur and J.F. Scott, Multiferroic and magnetoelectric materials, *Nature* **442**, 759 (2006)
44. J.P. Rivera, On definition, units, measurements, tensor forms of the linear magnetoelectric effect and on a new dynamic method applied to Cr-Cl boracite, *Ferroelectrics* **161**, 165 (1994).
45. M.E. Lines and A.M. Glass, Principles and applications of ferroelectrics and related materials (Clarendon Press, Oxford, 1977).
46. P. Sciau, M. Clin, J. -P. Rivera and H. Schmid, Magnetoelectric measurements on BaMnF_4 , *Ferroelectrics* **105**, 201 (1990).

47. M. Fiebig, et al., Determination of the magnetic symmetry of hexagonal manganites by second harmonic generation, *Phys. Rev. Lett.* **84**, 5620 (2000).
48. S.L. Hou and N. Bloembergen, Paramagnetoelectric effects in $\text{NiSO}_4 \cdot 6\text{H}_2\text{O}$, *Phys. Rev.* **138**, A1218 (1965).
49. J.F. Scott, Mechanisms of dielectric anomalies in BaMnF_4 , *Phys. Rev. B* **16**, 2329 (1977).
50. H. Grimmer, The piezomagnetoelectric effect, *Acta Crystallogr. A* **48**, 266 (1992).
51. J. Ryu, A. Va'squez Carazo, K. Uchino and H.-E. Kim, Magnetoelectric properties in piezoelectric and magnetostrictive laminate composites. *Jpn. J. Appl. Phys.* **40**, 4948 (2001).
52. R. Seshadri, and N.A. Hill, Visualizing the role of Bi 6s "lone pairs" in the off-center distortion in ferromagnetic BiMnO_3 , *Chem. Mater.* **13**, 2892 (2001).
53. J. R. Teague, R. Gerson and W. J. James, Dielectric hysteresis in single crystal BiFeO_3 , *Solid State Commun.* **8**, 1073 (1970).
54. I. Sosnowska, T. P. Neumaier and E. Steichele, Spiral magnetic ordering in bismuth ferrite, *J. Phys. C: Solid State Phys.* **15**, 4835 (1982).
55. Y.F. Popov, A.M. Kadomtseva, G.P. Vorobev and A.K. Zvezdin, Discovery of the linear magnetoelectric effect in magnetic ferroelectric BiFeO_3 in a strong magnetic field, *Ferroelectrics* **162**, 135 (1994).
56. V.A. Murashov, D.N. Rakov, V.M. Ionov, I.S. Dubenko, Y.V. Titov and V.S. Gorelik, Magnetoelectric $(\text{Bi,Ln})\text{FeO}_3$ compounds: Crystal growth, structure and properties, *Ferroelectrics* **162**, 11 (1994).

57. F. Bai, J. Wang, M. Wuttig, J. Li, N. Wang, A.P. Pyatakov, A. K. Zvezdin, L. E. Cross and D. Viehland, Destruction of spin cycloid in (111) c-oriented BiFeO₃ thin films by epitaxial constraint: Enhanced polarization and release of latent magnetization, *Appl. Phys. Lett.* **86**, 032511 (2005).
58. A. M. dos Santos, S. Parashar, A.R. Raju, Y.S. Zhao, A.K. Cheetham and C. N. R. Rao, Evidence for the likely occurrence of magnetoferroelectricity in the simple perovskite, BiMnO₃, *Solid State Commun.* **122**, 49 (2002).
59. T. Kimura, S. Kawamoto, I. Yamada, M. Azuma, M. Takano and Y. Tokura, Magnetocapacitance effect in multiferroic BiMnO₃, *Phys. Rev. B* **67**, 180401 (2003).
60. A. M. dos Santos, A. K. Cheetham, T. Atou, Y. Syono, Y. Yamaguchi, K. Ohoyama, H. Chiba, and C. N. R. Rao, Orbital ordering as the determinant for ferromagnetism in biferroic BiMnO₃, *Phys. Rev. B* **66**, 644251 (2002).
61. A. Belik, S. Iikubo, T. Yokosawa, K. Kodama, N. Igawa, S. Shamoto, M. Azuma, M. Takano, K. Kimoto, Y. Matsui and E. T.- Muromachi, Origin of the monoclinic-to-monoclinic phase transition and evidence for the centrosymmetric crystal structure of BiMnO₃, *J. Am. Chem. Soc.* **129**, 971 (2007).
62. K. Ramesha, A. Llobet, Th. Proffen, C.R. Serrao and C.N.R. Rao, Observation of local non-centrosymmetry in weakly biferroic YCrO₃, *J. Phys: Condens. Matter* **19**, 102202 (2007).
63. S. Niitaka, M. Azuma, M. Takano, E. Nishibori, M. Takata and M. Sakata, Crystal structure and dielectric and magnetic properties of BiCrO₃ as a ferroelectromagnet, *Solid State Ionics* **172**, 557 (2004).

64. H. Hughes, M.M.B. Allix, C.A. Bridges, J.B. Claridge, X. Kuang, H. Niu, S. Taylor, W. Song, and M. J. Rosseinsky, A polar oxide with a large magnetization synthesized at ambient pressure, *J. Am. Chem. Soc.* **127**, 13790 (2005).
65. M. Azuma, K. Takata, T. Saito, S. Ishiwata, Y. Shimakawa and M. Takano, Designed ferromagnetic, ferroelectric $\text{Bi}_2\text{NiMnO}_6$, *J. Am. Chem. Soc.* **127**, 8889 (2005).
66. Colossal Magnetoresistance, Charge Ordering, and Related properties of Manganese Oxides, edited by C. N. R. Rao and B. Raveau (World Scientific, Singapore, 1998)
67. T. Kimura, T. Goto, H. Shintani, K. Ishizaka, T. Arima, Y. Tokura, Magnetic control of ferroelectric polarization. *Nature* **426**, 55 (2003)
68. T. Goto, T. Kimura, G. Lawes, A.P. Ramirez, Y. Tokura, Ferroelectricity and giant magnetocapacitance in perovskite rare-earth manganites, *Phys. Rev. Lett.* **92**, 257201 (2004)
69. T. Kimura, G. Lawes, T. Goto, Y. Tokura, A. P. Ramirez, Magnetoelectric phase diagrams of orthorhombic RMnO_3 ($R = \text{Gd, Tb, and Dy}$). *Phys. Rev. B* **71**, 224425 (2005)
70. A. P. Levanyuk and D.G. Shannikov, Improper Ferroelectrics, *Sov. Phys. Usp.* **17**, 199 (1974)
71. M. Tachibana, T. Shimoyama, H. Kawaji, T. Atake and E.T.- Muromachi, Jahn-Teller distortion and magnetic transitions in perovskite RMnO_3 ($R = \text{Ho, Er, Tm, Yb, and Lu}$), *Phys. Rev. B* **75**, 144425 (2007)

72. B. Lorenz, Y.-Q. Wang and C.-W. Chu, Ferroelectricity in perovskite HoMnO_3 and YMnO_3 , *Phys. Rev. B* **76**, 104405 (2007)
73. B. Lorenz, Y.Q. Wang, Y.Y. Sun and C.W. Chu, Large magnetodielectric effects in orthorhombic HoMnO_3 and YMnO_3 , *Phys. Rev. B* **70**, 212412 (2004)
74. S.C. Abrahams, Ferroelectricity and structure in the YMnO_3 family, *Acta Cryst. B* **57**, 485 (2001).
75. B.B. Van Aken, T.T.M. Palstra, A. Filippetti and N.A. Spaldin, The origin of ferroelectricity in magnetoelectric YMnO_3 , *Nature Materials*, **3**, 164 (2004)
76. H.L. Yakel, W.C. Koehler, E.F. Bertaut and E.F. Forrat, On the crystal structure of the manganese (III) trioxides of the heavy lanthanide and yttrium. *Acta Crystallogr.* **16**, 957 (1963).
77. G. A. Smolenskii & V. A. Bokov, Coexistence of magnetic and electric ordering in crystals. *J. Appl.Phys.* **35**, 915 (1964).
78. M. Fiebig, T. Lottermoser, D. Fröhlich, A. V. Goltsev and R. V. Pisarev, Observation of coupled magnetic and electric domains. *Nature* **419**, 818 (2002).
79. T. Lottermoser, M. Fiebig, D. Fröhlich, S. Kallenbach and M. Maat, Coupling of ferroelectric and antiferromagnetic order parameters in hexagonal RMnO_3 . *Appl. Phys. B* **74**, 759 (2002).
80. K. Lukaszewicz and J. Karut-Kalicinska, X-ray investigations of the crystal structure and phase transitions of YMnO_3 . *Ferroelectrics* **7**, 81 (1974).
81. T. Lottermoser, T. Lonkai, U. Amann, D. Hohlwein, J. Ihringer and M. Fiebig, Magnetic phase control by an electric field, *Nature* **430**, 541 (2004).

82. B.B. Van Aken and T.T.M. Palstra, Influence of magnetic on ferroelectric ordering in LuMnO_3 , *Phys. Rev. B: Condens. Matter* **69**, 134113 (2004).
83. A. Muñoz, J.A. Alonso, M.J. Martí'nez-Lope, M.T. Casa'is, J.L. Martí'nez and M. T. Ferna'ndez-Dí'az and Magnetic structure of hexagonal RMnO_3 ($R = \text{Y, Sc}$): thermal evolution from neutron powder diffraction, *Phys. Rev. B* **62**, 9498 (2000)
84. T. Katsufuji, M. Masaki, A. Machida, M. Moritomo, K. Kato, E. Nishibori, M. Takata, M. Sakata, K. Ohoyama, K. Kitazawa and H. Takagi, Crystal structure and magnetic properties of hexagonal RMnO_3 ($R = \text{Y, Lu and Sc}$) and the effect of doping. *Phys. Rev. B* **66**, 134434 (2002).
85. M. Bieringer and J. E. Greedan, Magnetic structure and spin reorientation transition in ScMnO_3 , *J. Solid State Chem.* **143**, 132 (1999)
86. W. C. Koehler, H. L. Yakel, E. O. Wollan and J. W. Cable, A note on the magnetic structures of rare earth manganese oxides, *Physics Letters*, **9**, 93 (1964)
87. T. Katsufuji, S. Mori, M. Masaki, Y. Moritomo, N. Yamamoto and H. Takagi, Dielectric and magnetic anomalies and spin frustration in hexagonal RMnO_3 ($R=\text{Y, Yb, and Lu}$), *Phys. Rev. B* **64**, 104419 (2001)
88. J.-S. Zhou, J.B. Goodenough, J.M. Gallardo-Amores, E. Morán, M.A. Alario-Franco and R. Caudillo, Hexagonal versus perovskite phase of manganite RMnO_3 ($R=\text{Y, Ho, Er, Tm, Yb, Lu}$), *Phys. Rev. B* **74**, 014422 (2006)
89. M. Fiebig, T. Lottermoser, D. Frohlich, A. V. Goltsev and R. V. Pisarev, Observation of coupled magnetic and electric domains, *Nature* **419**, 818 (2002).

90. Y. Noda, H. Kimura, M. Fukunaga, S. Kobayashi, I. Kagomiya and K. Kohn, Magnetic and ferroelectric properties of multiferroic RMn_2O_5 , *J. Phys.: Condens. Matter* **20**, 434206 (2008)
91. S. C. Abrahams and J. L. Bernstein, Crystal Structure of Paramagnetic DyMn_2O_5 at 298°K , *J. Chem. Phys.* **46**, 3776 (1967)
92. J A Alonso, M T Casais, M J Martinez-Lope, J L Martinez and M T Fernandez-Diaz, A structural study from neutron diffraction data and magnetic properties of RMn_2O_5 ($R = \text{La}$, rare earth), *J. Phys.: Condens. Matter* **9**, 8515 (1997).
93. G. R. Blake, L. C. Chapon, P. G. Radaelli, S. Park, N. Hur, S-W. Cheong and J. Rodríguez-Carvajal, Spin structure and magnetic frustration in multiferroic RMn_2O_5 ($R=\text{Tb, Ho, Dy}$), *Phys. Rev. B* **71**, 214402 (2005)
94. S. Quezel-Ambrunaz, F. Bertaut and G. Buisson, Structure of TMn_2O_5 compounds of rare earth and manganese oxides. *Compt. Rend.* **258**, 3025 (1964).
95. M. Schieber, A. Grill, I. Nowik, B. M. Y. Wanklyn, R. C. Sherwood and L. G. Van Uitert, Magnetocrystalline anisotropy of rare-earth Manganites, *J. Appl. Phys.* **44**, 1864 (1973).
96. E. I. Golovenchits, N. V. Morozov, V. A. Sanina and L. M. Sapozhnikova, Correlation of magnetic and dielectric properties in EuMn_2O_5 single crystals, *Sov. Phys. Solid State* **34**, 56 (1992).
97. K. Saito and K. Kohn, Magnetoelectric effect and low-temperature phase transitions of TbMn_2O_5 , *J. Phys. Condens. Matter* **7**, 2855–2863 (1995).

98. A. Inomata and K. Kohn, Pyroelectric effect and possible ferroelectric transition of helimagnetic GdMn_2O_5 , TbMn_2O_5 and YMn_2O_5 . *J. Phys. Condens. Matter* **8**, 2673 (1996).
99. P. P. Gardner, C. Wilkinson, J. B. Forsyth and B. M. Wanklyn, The magnetic structures of the rare earth manganates ErMn_2O_5 and TbMn_2O_5 . *J. Phys. C: Solid State Phys.* **21**, 5653–5661 (1998).
100. L. C. Chapon, P.G. Radaelli, G.R. Blake, S. Park and S.-W. Cheong, Ferroelectricity induced by acentric spin-density waves in YMn_2O_5 , *Phys. Rev. Lett.* **96**, 097601 (2006)
101. S. W. Cheong and M. Mostovoy, Multiferroics: a magnetic twist for ferroelectricity, *Nature Mater.*, **6**, 13 (2007)
102. D. Higashiyama, S. Miyasaka, N. Kida, T. Arima and Y. Tokura, Control of the ferroelectric properties of DyMn_2O_5 by magnetic fields, *Phys. Rev. B* **70**, 174405 (2004)
103. D. Higashiyama, S. Miyasaka and Y. Tokura, Magnetic-field-induced polarization and depolarization in HoMn_2O_5 and ErMn_2O_5 , *Phys. Rev. B* **72**, 064421 (2005)
104. N. Hur, S. Park, P. A. Sharma, J. S. Ahn, S. Guha and S-W. Cheong, Electric polarization reversal and memory in a multiferroic material induced by magnetic fields, *Nature*, **429**, 392 (2004)
105. J. Hemberger, P. Lunkenheimer, R. Fichtl, H.-A. Krug von Nidda, V. Tsurkan and A. Loidl, Relaxor ferroelectricity and colossal magnetocapacitive coupling in ferromagnetic CdCr_2S_4 , *Nature*, **434**, 364 (2005)

106. P. Lunkenheimer, R. Fichtl, J. Hemberger, V. Tsurkan and A. Loidl, Relaxation dynamics and colossal magnetocapacitive effect in CdCr_2S_4 , *Phys. Rev. B* **72**, 60103 (R) (2005)
107. C. P. Sun, C. C. Lin, J. L. Her, C. J. Ho, S. Taran, H. Berger, B. K. Chaudhuri and H. D. Yang, Field-dependent dielectric and magnetic properties in multiferroic CdCr_2S_4 , *Phys. Rev. B* **79**, 214116 (2009)
108. G. A. Samara, The relaxational properties of compositionally disordered ABO_3 Perovskites, *J. Phys.: Condens. Matter* **15**, R367 (2003)
109. L. E. Cross, Relaxor ferroelectrics, *Ferroelectrics* **76**, 241 (1987).
110. N. W. Grimes, Off-centre ions in compounds with spinel structure, *Phil. Mag.* **26**, 1217 (1972).
111. V. Gnezdilov, P. Lemmens, Yu. G. Pashkevich, P. Scheib, Ch. Payen, K. Y. Choi, J. Hemberger, A. Loidl, V. Tsurkan, Evidence for local lattice distortions in giant magnetocapacitive CdCr_2S_4 , arXiv:cond-mat/0702362v1 (2007)
112. J. Hemberger, P. Lunkenheimer, R. Fichtl, S. Weber, V. Tsurkan and A. Loidl, Multiferroic behavior in CdCr_2X_4 ($X = \text{S}; \text{Se}$), *Physica B* **378**, 363 (2006)
113. S. Weber, P. Lunkenheimer, R. Fichtl, J. Hemberger, V. Tsurkan, and A. Loidl, Colossal Magnetocapacitance and Colossal Magnetoresistance in HgCr_2S_4 , *Phys. Rev. Lett.* **96**, 157202 (2006)
114. K. Taniguchi, N. Abe, T. Takenobu, Y. Iwasa and T. Arima, Ferroelectric polarization flop in a frustrated magnet MnWO_4 induced by a magnetic field, *Phys. Rev. Lett.* **97**, 097203 (2006)

115. G. Lautenschläger, H. Weitzel, T. Vogt, R. Hock, A. Böhm, M. Bonnet, and H. Fuess, Magnetic phase transitions of MnWO_4 studied by the use of neutron diffraction, *Phys. Rev. B* **48**, 6087 (1993).
116. H. Sagayama, K. Taniguchi, N. Abe, T. Arima, M. Soda, M. Matsuura and K. Hirota, Correlation between ferroelectric polarization and sense of helical spin order in multiferroic MnWO_4 , *Phys. Rev. B* **77**, 220407(R) (2008)
117. A. H. Arkenbout, T. T. M. Palstra, T. Siegrist and T. Kimura, Ferroelectricity in the cycloidal spiral magnetic phase of MnWO_4 , *Phys. Rev. B* **74**, 184431 (2006).
118. K. Taniguchi, N. Abe, H. Sagayama, S. Ohtani, T. Takenobu, Y. Iwasa, and T. Arima, Magnetic-field dependence of the ferroelectric polarization and spin-lattice coupling in multiferroic MnWO_4 , *Phys. Rev. B* **77**, 064408 (2008)
119. H. Katsura, N. Nagaosa, and A. V. Balatsky, Spin current and magnetoelectric effect in noncollinear magnets, *Phys. Rev. Lett.* **95**, 057205 (2005)
120. I. A. Sergienko and E. Dagotto, Role of the Dzyaloshinskii-Moriya interaction in multiferroic perovskites, *Phys. Rev. B* **73**, 094434 (2006).
121. K. Taniguchi, N. Abe, H. Umetsu, H.A. Katori and T. Arima, Control of the magnetoelectric domain-wall stability by a magnetic field in a multiferroic MnWO_4 , *Phys. Rev. Lett.* **101**, 207205 (2008).
122. K. Taniguchi, N. Abe, S. Ohtani and T. Arima, Magnetoelectric memory effect of the nonpolar phase with collinear spin structure in multiferroic MnWO_4 , *Phys. Rev. Lett.* **102**, 147201 (2009).
123. D.V. Efremov, J. van den Brink and D.I. Khomskii, Bond- Versus site-centred ordering and possible ferroelectricity in manganites, *Nat. Mater.* **3**, 853 (2004).

124. C. Ederer and N.A. Spaldin, Magnetolectrics: A new route to magnetic ferroelectrics, *Nat. Mater.*, **3**, 849 (2004)
125. N. Ikeda, H. Ohsumi, K. Ohwada, K. Ishii, T. Inami, K. Kakurai, Y. Murakami, K. Yoshii, S. Mori, Y. Horibe, and H. Kito, Ferroelectricity from iron valence ordering in the charge-frustrated system LuFe_2O_4 , *Nature* **436**, 1136 (2005).
126. N. Ikeda, S. Mori and K. Kohn, Charge Ordering and dielectric dispersion in mixed valence oxides RFe_2O_4 , *Ferroelectrics* **314**, 41 (2005).
127. J. van den Brink and D.I. Khomskii, Multiferroicity due to charge ordering, *J. Phys.: Condens. Matter* **20**, 434217 (2008).
128. A.D.-Aladine, J.R.-Carvajal, L.P.-Gaudart, M.T.F.-Di'az and A. Revcolevschi, Zener polaron ordering in half-doped manganites, *Phys. Rev. Lett.* **89**, 097205 (2002)
129. D.V. Efremov, and D.I. Khomskii, Orbital ordering in manganites in the band approach, *Phys. Rev. B: Condens. Matter* **72**, 012402 (2005).
130. C. Wang, G. Guo and L. He, Ferroelectricity driven by the noncentrosymmetric magnetic ordering in multiferroic TbMn_2O_5 : A first-principles study, *Phys. Rev. Lett.* **99**, 177202 (2007).
131. V.B. Shenoy, D.D. Sarma, and C.N.R. Rao, Electronic phase separation in correlated oxides: The phenomenon, its present status and future prospects, *ChemPhysChem* **7**, 2053 (2006).
132. C.N.R. Rao, Charge, spin, and orbital ordering in the perovskite manganates, $\text{Ln}_{1-x}\text{A}_x\text{MnO}_3$ (Ln = Rare Earth, A = Ca or Sr), *J. Phys. Chem. B* **104**, 5877 (2000).

133. S. Parashar, L. Sudheendra, A.R. Raju, and C.N.R. Rao, Current-induced phase control in charged-ordered $\text{Nd}_{0.5}\text{Ca}_{0.5}\text{MnO}_3$ and $\text{Pr}_{0.6}\text{Ca}_{0.4}\text{MnO}_3$ crystals, *J. Appl. Phys.* **95**, 2181 (2004).
134. A. Guha, N. Khare, A.K. Raychaudhuri and C.N.R. Rao, Magnetic field resulting from nonlinear electrical transport in single crystals of charge-ordered $\text{Pr}_{0.63}\text{Ca}_{0.37}\text{MnO}_3$, *Phys. Rev. B: Condens. Matter* **62**, R11941 (2000).
135. P. Lunkenheimer, V. Bobnar, A.V. Pronin, A.I. Ritus, A.A. Volkov and A. Loidl, Origin of apparent colossal dielectric constants, *Phys. Rev. B: Condens. Matter* **66**, 521051 (2002).
136. L. Sudheendra, and C.N.R. Rao, Electronic phase separation in the rare-earth manganates $(\text{La}_{1-x}\text{Ln}_x)_{0.7}\text{Ca}_{0.3}\text{MnO}_3$ ($\text{Ln} = \text{Nd, Gd and Y}$), *J. Phys.: Condens. Matter* **15**, 3029 (2003).
137. G. Lawes, M. Kenzelmann and C. Broholm, Magnetically induced ferroelectricity in the buckled Kagome antiferromagnet $\text{Ni}_3\text{V}_2\text{O}_8$, *J. Phys.: Condens. Matter* **20**, 434205 (2008)
138. T. Kimura, J.C. Lashley, A.P. Ramirez, Inversion symmetry breaking in the noncollinear magnetic phase of the triangular-lattice antiferromagnet CuFeO_2 , *Phys. Rev. B* **73**, 220401 (2006)
139. J. Cheng, S. Yu, J. Chen, and Z. Meng and L. E. Cross, Dielectric and magnetic enhancements in $\text{BiFeO}_3\text{-PbTiO}_3$ solid solutions with La doping, *Appl. Phys. Lett.* **89**, 122911 (2006)

140. A. Singh, V. Pandey, R. K. Kotnala and D. Pandey, Direct Evidence for Multiferroic magnetoelectric coupling in $0.9\text{BiFeO}_3\text{-}0.1\text{BaTiO}_3$, *Phys. Rev. Lett.* **101**, 247602 (2008)
141. S. Y. Tan, S. R. Shannigrahi, S. H. Tan and F. E. H. Tay, Synthesis and characterization of composite $\text{MgFe}_2\text{O}_4\text{-BaTiO}_3$ multiferroic system, **103**, 094105 (2008)
142. M. Gajek, M. Bibes, S. Fusil, K. Bouzehouane, J. Fontcuberta, A. Barthlmy and A. Fert, Tunnel junctions with multiferroic barriers, *Nat. Mater.* **6**, 296 (2007).

2. SCOPE OF THE PRESENT INVESTIGATIONS

In the present world, magnetic and electronic materials permeate every aspect of modern life [1]. For example, the vast amount of data generated by consumer electronic products is often stored as regions of opposite magnetic polarization in ferromagnets, while the sensors industry relies on ferroelectrics. Ferromagnetic-ferroelectric multiferroics are particularly appealing not only because they have the properties of both parent compounds, but also because interactions between the magnetic and electric polarizations lead to additional functionalities [1]. There is great interest in the study of multiferroics in recent years, and a few novel materials with multiferroic properties have indeed been discovered. Multiferroics which exhibit coupling between the magnetic and electrical order parameters are of vital interest both academically and technologically [2-5]. Multiferroics provide a rich source for exploring the fundamental science of phase control and magnetoelectric interactions. Magnetoelectric effects have been observed in the form of ferroelectric phase transitions induced by magnetic fields in perovskite manganites [6] and ferromagnetism induced by electric fields in hexagonal manganites [7]. Magnetoelectric memory effects and magnetic switching of ferroelectric domains (and the converse process) have been demonstrated.

2.1 Studies of multiferroic nature of the manganites of YMnO_3 family

2.1.1 Single crystal studies of ErMnO_3

Multiferroic compounds of heavy rare-earth hexagonal manganites, RMnO_3 ($R = \text{Sc, Y, Ho-Lu}$), also called the YMnO_3 family, represent an exciting family of ferroic materials. The simultaneous presence of electric and magnetic ordering [8,9], the unusual strong magnetic two-dimensional (2D) short-range order [10] the existence of ferroelectromagnetic domains [11] and the coupling of electric and magnetic order parameters [12] attracted interest of experimentalists, engineers and theoreticians. Possible applications as random access memory devices are proposed according to the ferromagnetic and ferroelectric behaviors of epitaxial thin films [13,14]. Though systematic studies on this class of manganites started in the 1960s [10,15] and the publications are numerous, (e.g., Refs. 16–19), the magnetic structure remained controversial until optical measurements were carried out [20].

In the 1970s, the high-temperature crystal structure of YMnO_3 was investigated [21] and a change in symmetry above the ferroelectric ordering temperature was observed. However, Raman and infra-red spectroscopy of the high-temperature paraelectric and low-temperature ferroelectric phases showed only weak bands in the ferroelectric phase due to the non-centrosymmetry, indicating that the structural differences between the ferroelectric and paraelectric phases are very small [22]. Experimentally, the phase transition from ferroelectric to paraelectric state has been confirmed by pyroelectric measurement [23]. The unit cell parameters show discontinuity

of the values at this temperature corresponding to T_{FE} . Dielectric anomaly is observed at T_{FE} in the temperature dependence of resistivity curves in the single crystal studies on this family of compounds [16].

Magnetic susceptibility, specific heat and dielectric constant measurements on hexagonal manganites reveal the onset of magnetic ordering of the frustrated Mn^{3+} spins ($S = 2$) on a triangular Mn lattice (YMnO₃: $T_N = 71$ K; LuMnO₃: $T_N = 90$ K and ScMnO₃: $T_N = 130$ K). The transition is characterized by a sharp kink in the magnetic susceptibility at T_N below which it continues to increase due to the frustration on the triangular lattice. The specific heat shows one clear continuous phase transition at T_N , which is independent of external magnetic field up to 9 T with an entropy content as expected for Mn^{3+} ions. The temperature-dependent dielectric constant displays a distinct anomaly at T_N [17]. ScMnO₃ undergoes a second magnetic transition below 75 K, corresponding to a spin reorientation [19]. The bulk measurements as well as elastic and inelastic neutron scattering experiments of YMnO₃ show clearly that above T_N , there is very diffusive magnetic scattering in both space and time, indicating short range dynamic correlations which are a signature of a spin liquid phase. This spin liquid phase forms out of geometrically frustrated Mn moments. Even when they become ordered below T_N , surprisingly enough, there are short range spatial correlations. The analysis of the spin wave spectrum in the ordered phase shows that the spin waves can be well described in terms of a Heisenberg Hamiltonian with a small easy plane anisotropy [24]. The optical second harmonic intensity for light incident along the optical axis ($k \parallel z$) of HoMnO₃ single crystal shows that beyond Néel temperature, the SH signal vanishes, which confirms its purely magnetic origin [20]. In the temperature range between $T_N = 72$ K and

the spin reorientation temperature $T_R = 41$ K, the SH signal exhibits a sixfold symmetry with maximum intensity for $P(2\omega) \parallel E(\omega) \parallel x$ and zero intensity for $P(2\omega) \parallel E(\omega) \parallel y$. The corresponding magnetic symmetry is thus $P\bar{6}_3cm$ with magnetic SHG susceptibility tensor components $\chi^{(c)}_{xxx} \neq 0$ and $\chi^{(c)}_{yyy} = 0$. Below T_R , $\chi^{(c)}_{xxx} = 0$ and $\chi^{(c)}_{yyy} \neq 0$ with corresponding magnetic space group $P\bar{6}_3cm$. The change of magnetic structure goes along with a 90° spin rotation and a change of the antiferromagnetic domain structure. For Ho, Er, Tm, and Yb, there are additional contributions to the magnetic properties from the rare-earth ions with the possibility of 4f spin ordering below ~ 6 K [25].

Temperature dependence of magnetisation data on $ErMnO_3$ indicates a weak antiferromagnetic transition at 80 K which is more noticeable in the χT curve [26]. The same feature is reflected in the thermal expansion measurements with the appearance of a shoulder-like structure which is not very sensitive to magnetic field. Raman measurements on $ErMnO_3$ as a function of temperature shows that the E_2 phonon frequencies ($234, 297 \text{ cm}^{-1}$) which involve motions of O_3 and O_4 oxygen atoms within the xy plane exhibit anomalies at 80 K [27]. This can be interpreted by extra hardening deviations below 80 K that could not be modeled by anharmonicity alone, suggesting a spin-phonon coupling below T_N .

In the present work, we have investigated the multiferroic properties of $ErMnO_3$ through magnetic, specific heat and dielectric measurements. Furthermore, we have studied the anisotropic dependence of its dielectric constant on magnetic field through the magnetocapacitance measurements on single crystal.

2.1.2 A Raman study on multiferroic LuMnO₃

LuMnO₃ belongs to the YMnO₃ family and exhibits structure and physical properties similar to ErMnO₃. LuMnO₃ shows magnetic ordering of triangular lattice at 90 K manifested by the sharp kinks in the magnetic susceptibility and specific heat at T_N [17]. It has a much higher paramagnetic Curie-Weiss temperature θ_{CW} of value 519 K which is discernibly smaller than that reported for single crystal [16,17]. This large ratio of θ_{cw} / T_N is a measure of the geometrical frustration of the antiferromagnetic system [28]. Anomaly has been observed at 86 K in the dielectric constant curve for LuMnO₃ measured parallel to ab plane [16] similar to YMnO₃ [9] confirming the coupling between magnetic and ferroelectric orderings. Magnetic phase can be controlled by an external electric field as ferromagnetic ordering in hexagonal HoMnO₃ is reversibly switched on and off by the applied field via magnetoelectric interactions which is monitored using magneto-optical techniques [7].

The thermal conductivity of the magnetically frustrated, ferroelectric LuMnO₃ exhibits an isotropic suppression in the paramagnetic state, followed by a sudden increase upon magnetic ordering [29]. This unprecedented behavior without an associated static structural distortion probably originates from the strong dynamic coupling between acoustic phonons and low-energy spin fluctuations in geometrically frustrated magnets. Inelastic neutron scattering measurements performed on YMnO₃ provides evidence for a strong coupling between magnons and phonons, evidenced by the opening of a gap below T_N in the dispersion of the transverse acoustic phonon mode polarized along the ferroelectric axis [30]. High-resolution neutron diffraction data taken on LuMnO₃ show

that all the atoms belonging to the same unit cell exhibit significantly large atomic displacements at T_N : as large as approximately 0.05 Å, which is almost comparable to those reported for archetypal ferroelectric materials [31]. This phenomenon of magneto-elastic coupling can be stressed with the fact that for the hexagonal manganites there are no orbital degrees of freedom, which could otherwise induce similarly large atomic displacements for compounds having Mn^{3+} ions, through the familiar Jahn–Teller mechanism. Also, these manganites undergo this isostructural transition well below their ferroelectric transition points. The evidence of magneto-elastic coupling has further been supported by high-resolution neutron diffraction studies on other family members [32] and thermal expansion measurement on $HoMnO_3$ [33]. An assignment of the Raman and infra-red phonon lines to definite atomic vibrations has been made on the basis of their symmetries in close comparison with results of lattice dynamical calculations for $YMnO_3$ in its ferroelectric ($P6_3cm$, $Z=6$) and high-temperature paraelectric ($P6_3/mmc$, $Z=2$) phases [22]. The phonon spectra observed for $YMnO_3$ through Raman scattering show anomalous temperature variation at the Néel temperature, suggesting a coupling between the spin and phonon systems below T_N . Furthermore, a sudden change of the spectra at the Curie temperature $T_C > 900$ K suggests an abrupt structural phase change from the ferroelectric to the paraelectric phase [34]. Coherent acoustic phonons in the hexagonal manganite $LuMnO_3$ have been observed using two-color femtosecond optical pump-probe spectroscopy [35]. A pronounced phase change occurs in the vicinity of the Néel temperature (T_N), which is related to the temperature dependent red-shift of the on-site Mn d–d optical transition at 1.7 eV that is coupled to the AFM ordering as recently observed in optical conductivity measurements [36].

In the present study, we have confirmed the multiferroic nature of LuMnO₃ through magnetic and dielectric measurements. Raman spectra of LuMnO₃ have been recorded in the 77–800 K range covering both the antiferromagnetic transition at 90 K and the ferroelectric–paraelectric transition at 750 K.

2.2 Raman evidence for orbiton-mediated multi-phonon scattering in multiferroic TbMnO₃

In 2003, ferroelectric activity was found in TbMnO₃, for the first time in a rare-earth manganite with orthorhombically distorted perovskite structure, which shows antiferromagnetic orders with long wavelengths owing to competing magnetic interactions [6,37]. At lower temperatures, the system shows successive magnetic phase transitions: the Mn moments in TbMnO₃ undergo an antiferromagnetic transition at $T_N \sim 41$ K, the Mn moments are aligned along the b axis and show sinusoidal order with a propagation wave vector $(0, k_{Mn}, 1)$ with k_{Mn} decreasing from 0.295 below T_N (Fig. 2.1). This is followed by incommensurate-commensurate magnetic transition T_N at 27 K with magnetic modulation wave vector becoming locked at 0.28. These orderings are characterized by the anomalies in magnetization and specific heat. Ferroelectric order with spontaneous polarization along the c axis develops at $T_C \sim 27$ K. Upon further decrease in temperature, the temperature dependence of the specific heat shows the third anomaly at ~ 7 K, where the Tb³⁺ moments show long-range ordering with a propagation vector $(0, \sim 0.42, 1)$ different from that of Mn moments. At approximately this

temperature, the electric polarization also exhibits a small anomaly. These results suggest an intimate connection between magnetism and ferroelectricity in TbMnO_3 .

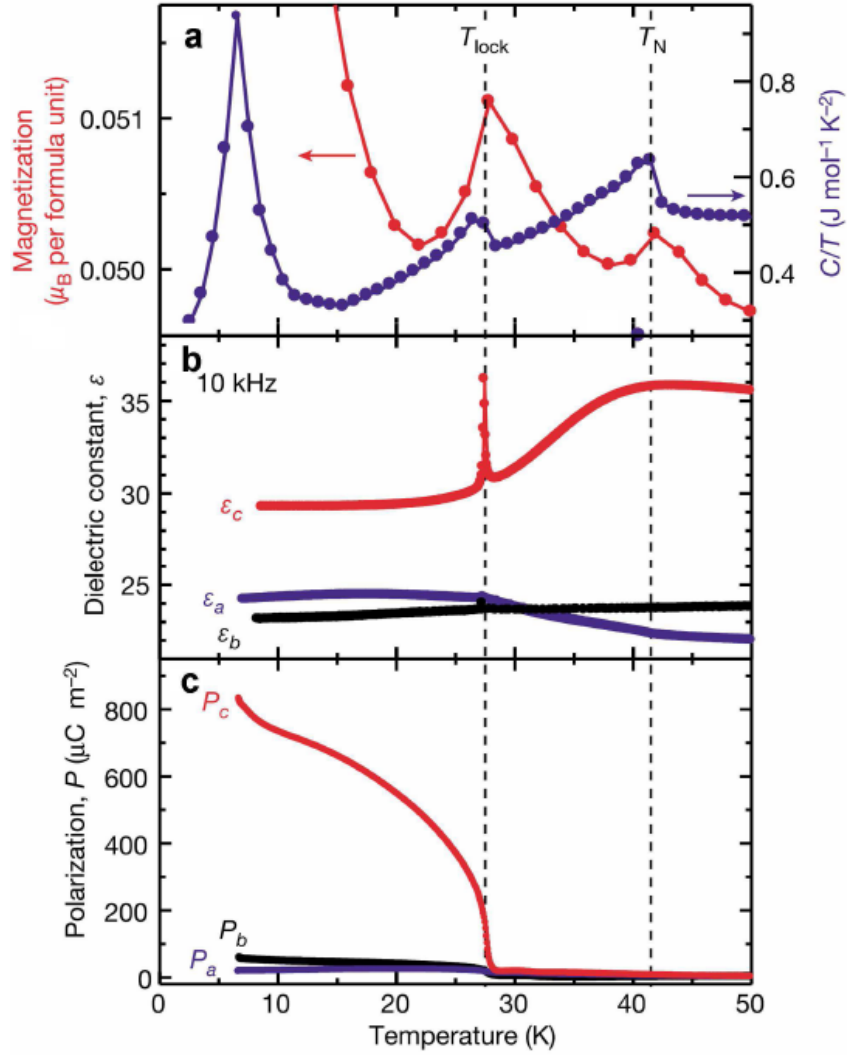


Fig. 2.1: Temperature profiles of (a) magnetization and specific heat divided by temperature C/T , (b) dielectric constant ϵ at 10 kHz and (c) electric polarization P along the principal axes in single crystals of TbMnO_3 . [Ref. 6]

The collinear sinusoidally modulated magnetic structure model was formerly proposed by Quezel et al. [38] for both the antiferromagnetic paraelectric phase ($T_C \leq T \leq T_N$). A recent neutron diffraction measurement [39] suggests that the magnetic structure

below T_C is a transversely modulated spiral spin structure which is responsible for the origin for ferroelectricity along c - axis (Fig. 2.2). Accompanying the magnetic ordering, there is a lattice modulation with $\delta_l = 2\delta_m$ (second harmonic).

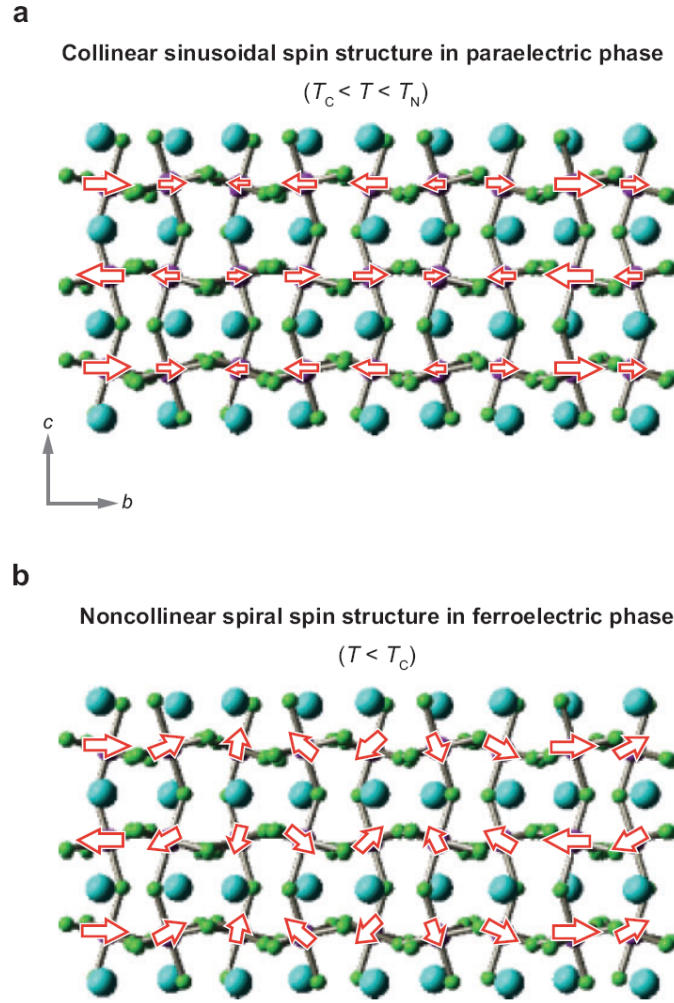


Fig. 2.2: Schematic drawings of proposed magnetic structures at Mn sites in the (a) paraelectric antiferromagnetic phase ($T_C \leq T \leq T_N$) and (b) ferroelectric antiferromagnetic phase ($T \leq T_C$) of TbMnO_3 [Ref. 37]

Although the magnitude of electric polarization P in TbMnO_3 is much smaller than that in conventional perovskite ferroelectrics, the ferroelectricity of TbMnO_3 can be controlled by a magnetic field H [6,40]. Namely, the direction of the spontaneous

polarization in ferroelectric TbMnO₃ can be switched by 90° by tuning the magnitude of magnetic field (electric polarization flop). The flop of the ferroelectric polarization in TbMnO₃ with applied magnetic field is caused from the flop of the Mn cycloidal plane [41].

In recent years, the focus in multiferroics has been on the electromagnons i.e. magnons with an electric dipole excited by an applied ac electric field, observed below 100 cm⁻¹ [42-46]. The effect of orbital ordering on the Raman spectra of perovskite manganites, RMnO₃ has been investigated both theoretically [47–50] and experimentally [49, 51–54]. Three broad bands near 1000, 1170 and 1290 cm⁻¹ in the Raman spectra of LaMnO₃ were attributed to orbiton excitations [49,55], an assignment still being debated and alternative proposals made [47,48,50,56]. Although in centrosymmetric LaMnO₃, Raman modes are not infrared active, infrared absorption [56] shows bands similar to those in the Raman spectra, attributing these features to multiphonon scattering instead of orbital excitations. Allen et al. [47] have proposed that, as a result of strong electron–phonon coupling, orbitons in LaMnO₃ are self-trapped by the local rearrangement of the lattice and hence multiphonon Raman scattering with intensities comparable to those of the one-phonon Raman modes has been predicted. This arises from the Franck–Condon (FC) process via the self-trapped orbitons, suggesting a mixed character of phonons and orbitons for the high frequency modes. This mixed character has also been shown theoretically by other calculations considering the effects of super-exchange and electron–phonon interactions [57,50]. The high intensity ratio (~0.1–0.4) of the second-order modes to their first-order counterparts has been observed experimentally for LaMnO₃ [51] and RMnO₃ (R = La, Pr, Ho and Y) [52], supporting the theoretical

proposal for the mixed nature of the multiphonon bands. On the other hand, a recent room temperature Raman study of RMnO_3 ($\text{R} = \text{Pr, Eu, Dy, Ho}$ and Y) and O^{18} isotopically substituted EuMnO_3 [58] suggests that the high frequency modes are due to second-order scattering involving only Brillouin-zone boundary phonons. All these experimental studies have been carried out at room temperature and above. Our present Raman study looks at multiferroic TbMnO_3 as a function of temperature from 5 to 300 K, covering the spectral range from 200 to 1525 cm^{-1} and focuses mainly on the temperature dependence of the two high energy excitations observed at 1157 and 1328 cm^{-1} .

As far as first-order phonons are concerned, it has been shown that in RMnO_3 ($\text{R} = \text{La, Nd, Sm, Gd, Dy, Pr}$ and Tb), a few Raman and IR phonons involving oxygen vibrations are anomalous, i.e. the phonon frequency decreases as temperature is lowered below T_N [59–62] arising from spin–phonon coupling. There have been reports of Raman studies on multiferroic TbMnO_3 dealing with only first-order Raman scattering [59,63–65], but to our knowledge, there is no report of the high frequency excitations in TbMnO_3 . In our work, we present Raman scattering data from an unoriented single crystal of TbMnO_3 as a function of temperature in the range 5–300 K. We show that the intensity ratio of the second-order mode to the corresponding first-order one is very high and remains constant with temperature as predicted by Allen et al. [47,48] for coupled multiphonon–orbiton modes. In addition, the first order mode involving oxygen vibrations ($\omega \sim 616 \text{ cm}^{-1}$) shows anomalous softening below T_N , possibly due to strong spin–phonon coupling.

2.3 Multiferroic nature of rare-earth chromites

2.3.1 Rare-earth chromites, LnCrO_3 ($\text{Ln} = \text{Ho, Er, Yb and Lu}$)

The ac conductivity data on polycrystalline samples of a few chromites reveal that LaCrO_3 exhibits the maximum conductivity among the chromites with an activation energy of 2.2 eV [66]. Furthermore, there are no breaks in the $\log \sigma \sim 1/T$ plot for LaCrO_3 perhaps indicating the absence of the phase transformation. Similar is the case for DyCrO_3 . The appearance of breaks in the $\log \sigma \sim 1/T$ plots of YCrO_3 , DyCrO_3 , HoCrO_3 , YbCrO_3 , and LuCrO_3 and the fact that since no magnetic transitions are found in these compounds at these high temperatures [67] consolidated the speculation that these breaks may correspond to ferroelectric-paraelectric transitions [68]. This led to investigations of the dielectric properties of the heavy rare earth chromites, which were found to be ferroelectric just as the corresponding manganites [69]. The E_a values of chromites in the low temperature region show an increasing trend from Dy to Lu: the electrical conductivity at a given temperature decreases in the rare earth series from LaCrO_3 to YbCrO_3 . The optical spectra of the LnCrO_3 compounds show that the Ln-O covalency increases while the Cr-O covalency decreases down the rare earth series [70]. The decrease in the magnitude of conductivity of LnCrO_3 down the rare earth series may possibly be related to the decrease in the overlap of the cationic orbitals associated with the decrease in the Cr-O covalency and increased covalency of the Ln-O bond. A decrease in the probability of hopping of the charge carriers would be expected to accompany these changes in the bonding [66].

Rare earth chromites are *p*-type semiconductors with conductivities larger than the parent rare earth oxide but comparable to that of the corresponding transition metal

oxide [66]. The electrical transport properties of these solids can be explained in terms of the localized behavior of the d-electrons; in all the systems investigated, there is evidence for small polarons. Among the three series of rare earth compounds, namely chromites, manganites and ferrites, chromites exhibit the highest conductivity, lowest E_a and largest drift mobility, the conductivity of the chromites depending markedly on the Ln ion [66].

$YCrO_3$ and $ErCrO_3$ are canted antiferromagnets just below the ordering temperature T_N in which a ferromagnetic component occurs in the crystallographic c-direction due to canting of the two antiferromagnetic sublattices [71]. $YCrO_3$ has been found to exhibit weak ferromagnetism with spontaneous magnetic moment appearing along c-axis [72]. Sharp peaks in the perpendicular ac magnetic susceptibilities have been observed for frequencies from 10 Hz to 100 kHz at T_N (140 K for $YCrO_3$ and 133 K for $ErCrO_3$) and found to exhibit dependence on dc magnetic field which is well described by the thermodynamic theory of magnetic phase transition in a weak ferromagnet [71]. As a function of magnetic field, the value of the susceptibility varies at the peak with $H^{-2/3}$ power law. Below T_N , where magnetic domain effects are expected, viscous damped wall motion appears to explain the susceptibility behavior versus frequency in $ErCrO_3$.

Cr^{53} nuclear magnetic resonance (NMR) has been observed in the rare earth orthochromites, $YCrO_3$, $LuCrO_3$ and $EuCrO_3$. In each compound, two quadrupolar split resonances are observed and tentatively identified as arising from spins in the wall and domain. The major contributor to the electric field gradient is lattice and this contribution is correlated with the anisotropic part of the hyperfine field [73]. NMR studies on $YCrO_3$

shows a fast relaxation mechanism in the wall center. Comparison of the results of wall NMR with the data on wall mobility indicates that orthochromites are highly damped materials [74].

The A_{1g} and B_{2g} phonon frequencies in the Raman spectra of $YCrO_3$ show large blue shifts from T_N to lower temperatures. Such temperature dependence is understood by the magnetic ordering of Cr^{3+} ions because these phonon modes are related only to the motion of Cr and O ions [75]. Specific heat measurement on $YCrO_3$ single crystal in a temperature range from 30 to 360 K is done using high sensitive microcalorimeter ($1 \mu J/K$) [76]. $YCrO_3$ shows a sharp peak in the specific heat at $T_N \sim 140$ K due to a canted antiferromagnetic ordering.

$BiMnO_3$ is found to be ferroelectric below 770 K (T_E) and ferromagnetic below 105 K (T_C) [77]. $BiCrO_3$ is reported to exhibit a ferroelectric transition at 440 K and parasitic ferromagnetism below 114 K [78]. In addition to $BiMnO_3$, hexagonal rare earth manganites $LnMnO_3$ (with $Ln = Y, Ho, Er, Tm, Yb$ and Lu) are known to be multiferroic with $T_E \gg T_N$ [8,79]. Considering that $BiCrO_3$ is multiferroic just like $BiMnO_3$, it occurred to Rao et al. that rare earth chromites such as $YCrO_3$ may exhibit interesting multiferroic properties which was later proved to be multiferroic with $T_N = 140$ K and ferroelectric transition temperature, $T_{FE} = 473$ K [80]. While it is not a genuine ferroelectric like $BaTiO_3$, the dielectric transition and the weak polarization somewhat resembling relaxor-like behavior, along with canted antiferromagnetism, makes it an unusual multiferroic. The unusual aspect of $YCrO_3$ compared with other ferroelectrics like $BaTiO_3$ or the series $PbZr_{1-x}Ti_xO_3$, to name a few, is that, with a crystal structure of

the ABO_3 type, it has always been described with centrosymmetric crystal symmetries: $P2_1/n$ [81], $P2_1/m$ [82] or $Pnma$ [83]. The question therefore arises as to how to reconcile the existence of ferroelectricity in this material with the centrosymmetric crystal structure, since the presence of ferroelectricity requires the displacement of the B cation relative to the oxygen cage to create an electric dipole moment. First-principles density functional calculations have shown that the polarization found in $YCrO_3$ arising from the weak ferromagnetic instability is small and cannot explain the ferroelectric behavior, and therefore, local non-centrosymmetry is suggested to investigate the origin of the ferroelectricity in $YCrO_3$ [80]. By employing the neutron pair distribution function (PDF) method (which is an excellent method for studying local phenomena and ferroelectricity [84,85]) and Rietveld analysis of high-resolution neutron powder diffraction data, it was later shown that local non-centrosymmetry is responsible for the ferroelectricity in $YCrO_3$ [86].

By extending the logic for other heavy rare-earth chromites and on the basis of the analogy with the multiferroic nature of the heavy rare-earth manganites $LnMnO_3$ ($Ln = Y, Ho, Er, Tm, Yb$ and Lu), we have investigated the magnetic and dielectric properties of several heavy rare-earth chromites $LnCrO_3$ ($Ln = Ho, Er, Yb$ and Lu) to explore their possible multiferroic nature.

2.3.2 $YCr_{1-x}Mn_xO_3$ and $LuCr_{1-x}Mn_xO_3$ solid solutions

Initially, $YCrO_3$ was shown to be multiferroic with weak ferromagnetism and ferroelectricity [80]. Analogously, all the heavy rare-earth chromites of the series $LnCrO_3$ ($Ln = Y, Ho, Er, Yb$ and Lu) exhibit canted antiferromagnetic behavior in the 113-140 K

(T_N) range and a dielectric transition in the 472-516 K (T_E) range. Such a multiferroic behavior of these chromites has been explained on the basis of local non-centrosymmetry since these chromites formally possess the centrosymmetric orthorhombic structures. $YMnO_3$ is a well-known multiferroic with the antiferromagnetic transition temperature 71 K (T_N) and the ferroelectric transition at 913 K (T_E) [17,87]. $LuMnO_3$ is also a multiferroic with T_N and T_E values of 90 K and 750 K respectively [17,8].

We have investigated the effect of substitution of manganese for chromium in the chromites, $LnCrO_3$ ($Ln = Y, Lu$), on their multiferroic properties.

2.4 Beneficial modification of the properties of multiferroic

$BiFeO_3$ by cation substitution

$BiFeO_3$ (BFO) is a promising multiferroic candidate for practical applications because it possesses high antiferromagnetic transition temperature ($T_N = 640$ K) and ferroelectric transition temperature ($T_C = 1100$ K), both above room temperature [87-89]. Single-phase insulating BFO ceramics synthesized by liquid phase sintering and quenching processing techniques reveals that the formations of Fe^{2+} and oxygen deficiency leading to the higher leakage current are greatly suppressed [90,91]. The O-Bi-O angle was found out to be about 163.633° showing the occurrence of distorted $R3c$ crystal structure [91]. A well-saturated ferroelectric hysteresis loop with a large remnant polarization ($2P_r=23.5 \mu C/cm^2$) is observed with an applied field of 155 kV/cm. It does not exhibit ferromagnetic hysteresis loop at room temperature. The temperature-dependent magnetization shows a decreasing trend from room temperature down to

100 K followed by an increase in the value at lower temperatures [88,91]. A remarkably high saturation magnetization of $\sim 0.4 \mu_B/\text{Fe}$ along with room temperature ferromagnetic hysteresis loop has been observed in nanoscale (4–40 nm) multiferroic BFO which in bulk form exhibits weak magnetization ($\sim 0.02 \mu_B/\text{Fe}$) and an antiferromagnetic order [92-94]. Density functional theory shows that weak ferromagnetism of the Dzyaloshinskii-Moriya type occurs in this material and also explores the possibility of electric-field-induced magnetization reversal [95]. It predicts a significantly large ferroelectric polarization of 90-100 $\mu\text{C}/\text{cm}^2$ in a leakage-free BFO sample [96]. Temperature-dependent Raman scattering investigation reveals that the loss of the Raman spectrum at the Curie temperature, T_c indicates a cubic Pm-3m structure for the paraelectric phase, where, interestingly, the transition is not soft-mode driven and strong phonon anomalies around the Néel temperature T_N for some particular phonons suggests the multiferroic character of BFO [97]. High resolution neutron powder diffraction on BFO reveals that cycloidal spiral spin modulation superimposed on G-type antiferromagnetic spin ordering [98,99] cancels out any possible net magnetization. One of the ways of suppressing spiral spin modulation in BFO is the chemical substitution in the A-sublattice of the ABO_3 perovskite. Spontaneous magnetization has been revealed both for $\text{Bi}_{1-x}\text{R}_x\text{FeO}_3$ ($\text{R} = \text{Nd}, \text{Sm}, \text{Gd}, \text{Tb}, \text{Dy}$) solid solutions doped by magnetically active rare-earth ions [100-104] and for diamagnetically substituted $\text{Bi}_{1-x}\text{A}_x\text{FeO}_3$ ($\text{A} = \text{La}, \text{Sr}, \text{Pb}, \text{Ba}$) compounds [105-109]. While the dependence between the kind of substituting element and the magnetization value might be natural for rare-earth substitution, which can induce additional magnetic contribution at sufficient concentrations (at low temperature), it is the A-site substitution with the biggest ionic radius ions in case of

diamagnetic dopants which has been found to effectively suppress the spiral spin structure of BFO giving rise to the appearance of weak ferromagnetism [110]. Another bismuth-based compound, BiMnO_3 , is shown to be ferroelectric below 750 K (T_{FE}) and ferromagnetic below 105 K (T_{C}) [77, 111-113]. Moreover, Mn doping to Fe site has been reported to transform the spirally modulated spin structure to collinear spin structure [114]. In the literature, there is a study of one composition of $\text{BiFe}_{1-x}\text{Mn}_x\text{O}_3$ reporting a near room-temperature dielectric anomaly around the antiferromagnetic transition [115]. There are a few papers on the $\text{Bi}_{1-x}\text{La}_x\text{FeO}_3$ system which suggest a structural change at a certain composition although there are differences among the literature reports and furthermore, there are indications of possible improvement in the dielectric properties on substituting Bi by La [105, 116-118].

In the present study, we have investigated the modification of the multiferroic properties of BiFeO_3 by appropriate cationic substitutions with the elements like La and Mn over the range of compositions $x = 0.0\text{--}0.3$.

2.5 Rare-earth ferrites, LnFe_2O_4

In line with the phenomenon of cationic charge-ordering and induction of ferroelectricity in doped-perovskite manganites [119,120], some of the rare earth ferrites of the type LnFe_2O_4 (Ho-Lu,Y) are found to be charge-ordered because of competing interactions between the charges of the nearest and the next nearest neighbor ions on the triangular lattice [121-123]. These ferrites also show magnetoelectric effect. The origin of ferroelectricity in the ferrites is related to the charge-ordering transition arising from strong electron correlations.

LnFe_2O_4 , crystallizing in rhombohedral structures (space group R-3m) consists of alternate stacking of triangular lattices of rare-earth, iron and oxygen ions along the c axis [124]. The double iron triangular layer is separated by a single rare earth triangular layer in the structure. The Fe-Fe distances within a layer (3.44 Å) is longer than the Fe-Fe distances between the layers (3.156 Å) [125]. The iron has five-fold oxygen coordination with a triangular bipyramid. The rare-earth ion is positioned in a distorted oxygen octahedron. The Fe ions are in a mixed-valent state with equal amounts of Fe^{2+} and Fe^{3+} .

All the rare earth ferrites show magnetic ordering around 250 K [126-128]. The spontaneous magnetic moment evaluated from the saturated magnetization measurement is approximately $1.4 \mu_B$ per formula unit. The magnetization has strong uniaxial anisotropy with the easy axis along the c direction [129]. This fact is interpreted as the ferrimagnetic ordering of Fe^{2+} and Fe^{3+} . Mossbauer spectroscopy studies under a magnetic field [130,131] yielded information about the spin configuration of Fe ions. Among three types of Fe^{3+} ions, two of them contribute to the minority spins and the rest to the majority spin in a domain. All Fe^{2+} ions contribute to the majority spins. In a comparison of these findings with saturated magnetization, it was concluded that LnFe_2O_4 has a ferrimagnetic ordering.

The members of the LnFe_2O_4 family form a superstructure from the ordering of Fe^{2+} and Fe^{3+} . This superlattice cell possesses both magnetic and electric spontaneous polarization. The superstructure formed by the Fe^{2+} and Fe^{3+} ions supports electric polarization consisting of distributed electrons of polar symmetry, since the centers of Fe^{2+} and Fe^{3+} ions do not coincide [132-134]. The direct detection of charge ordering can

be done by the application of resonant x-ray scattering experiments [135]. The resonant x-ray scattering experiment on single crystals of LuFe_2O_4 proves the presence of the charge stripe [132]. Because of the frustrated nature of the triangular iron lattice in each iron layer, the usual bipartite checker-board $\text{Fe}^{2+}/\text{Fe}^{3+}$ charge ordering is not favorable, and another option becomes preferred. A charge redistribution between layers takes place, so that in each bi-layer one layer, say the lower layer, has a 2:1 ratio of $\text{Fe}^{2+}/\text{Fe}^{3+}$ and its upper counterpart has the inverse 1:2 ratio. Because of this interlayer charge redistribution each triangular layer can have a perfect, unfrustrated charge ordering. Each triangular layer will have three sublattices, one sublattice being occupied by Fe^{3+} and two others by Fe^{2+} . The charge ordering is vice versa in the other layer. As a result, each bilayer acquires a dipole moment, as shown in Fig. 2.3, and the total system becomes ferroelectric [132,133,136,137].

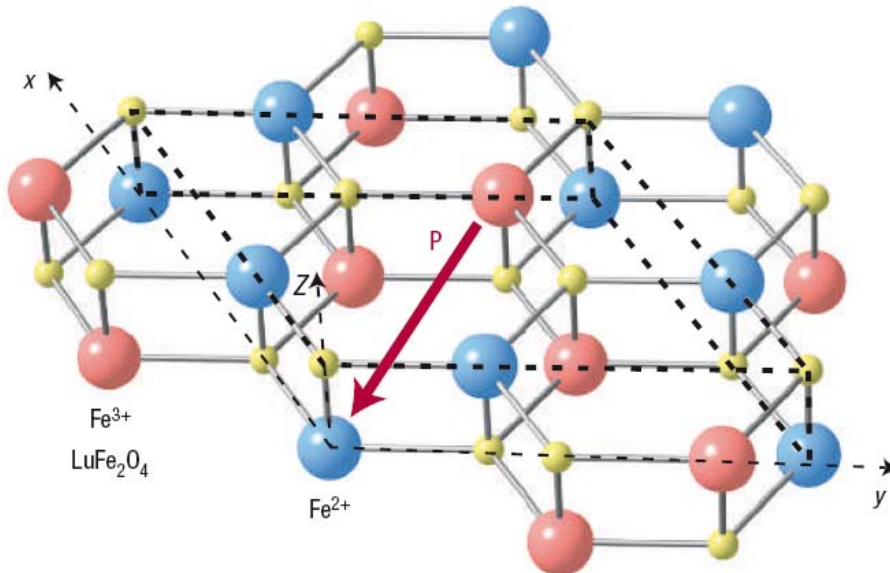


Fig. 2.3: Charge ordering in bilayered LnFe_2O_4 with a triangular lattice of Fe ions in each layer. The charge transfer from the top to bottom layer gives rise to net electric polarization (Ref. [137]).

Among all the rare earth ferrites, LuFe_2O_4 has been widely studied. Neutron diffraction studies of LuFe_2O_4 have shown that it undergoes successive phase transitions from a disordered state to a two-dimensional charge density wave (CDW) state and then to a three-dimensional CDW state [138,139]. In the two-dimensional CDW state, the CDW defined by the wave vector $(1/3,1/3)$ is formed in the hexagonal layer. From a dielectric viewpoint, this phase is viewed as random stacking of two-dimensional ferroelectric layers. In the three-dimensional CDW state, anti-phase stacking of the two-dimensional ordered layer develops. At the same time the in-plane charge order exhibits a doubly modulated long period structure. This phase is characterized by an incommensurate antiferroelectric phase [140]. In situ cooling transmission electron microscopy observations on LuFe_2O_4 show that the charges in the ground state are well crystallized in a charge-stripe phase and that charge concentration in this charge-stripe phase can be characterized by a non-sinusoidal CDW which gives rise to an electric polarization [141]. Magnetodielectric response was found in LuFe_2O_4 at room temperature indicating a coupling between the spins and electric dipoles [125]. The magnetocapacitance effect in LuFe_2O_4 is due to charge fluctuations arising from the interconversion between the two types of charge order, which are hindered by an applied magnetic field [142]. There was a report of experimental evidence for ferroelectricity in LuFe_2O_4 arising from electron correlations [132]. Later, magneto-dielectric response was discovered at room temperature indicating a coupling between the spins and electric dipoles [125,143].

Since most of the rare-earth ferrites have similar magnetic and dielectric behavior, we strongly believed that the similar magneto-dielectric properties would occur in these

materials. We have, therefore, synthesized $\text{Lu}_{0.5}\text{Fe}_{0.5}\text{Fe}_2\text{O}_4$, YFe_2O_4 , YbFe_2O_4 and ErFe_2O_4 and studied their magnetic, dielectric and magneto-dielectric properties in detail.

2.6 Charge-ordered manganites

2.6.1 $\text{Ln}_{1-x}\text{A}_x\text{MnO}_3$ (Ln = Lanthanide or Rare-earth, A = Alkaline earth)

Charge ordering occurs in some mixed-valent transition metal oxides. When differently charged cations in an oxide order on specific lattice sites, the hopping of electrons between the cations is no longer favored [144-147]. One, therefore, observes an increase in the electrical resistivity at the charge-ordering transition, often accompanied by a change in crystal symmetry. Because transition metal ions also carry spins, it is interesting to examine the magnetic (spin) ordering in the solids in relation to charge ordering. Charge ordering of Fe^{2+} and Fe^{3+} in Fe_3O_4 occurs at 120 K and below, where it coexists with the ferrimagnetic order that is established at a much higher temperature ($T = 858$ K). Around 120 K (T_V), Fe_3O_4 shows a sharp increase in resistivity, commonly referred to as the Verwey transition. Charge ordering occurs in perovskite manganites through a fairly wide range of compositions of $\text{Ln}_{1-x}\text{A}_x\text{MnO}_3$, (where Ln is a rare earth and A is a divalent cation), provided the Ln and A ions are not too large. Large Ln and A ions (e.g., La, Sr) favor ferromagnetism and metallicity, whereas the smaller ones (e.g., La, Ca, or Pr, Ca) favor charge ordering (see Fig. 2.4). It competes with the double-exchange interaction, which favors ferromagnetism and metallicity (charge ordering inhibits the electron transfer process that is associated with double exchange and therefore cannot coexist with ferromagnetism in manganites). Charge ordering occurs at a higher temperature than spin ordering in some of the manganites ($T_{CO} > T_N$), whereas in

some others $T_{CO} = T_N$. Orbital ordering occurs without charge ordering in the A-type antiferromagnetic manganites, but in the manganites where charge ordering occurs, antiferromagnetism of CE-type is found along with orbital ordering.

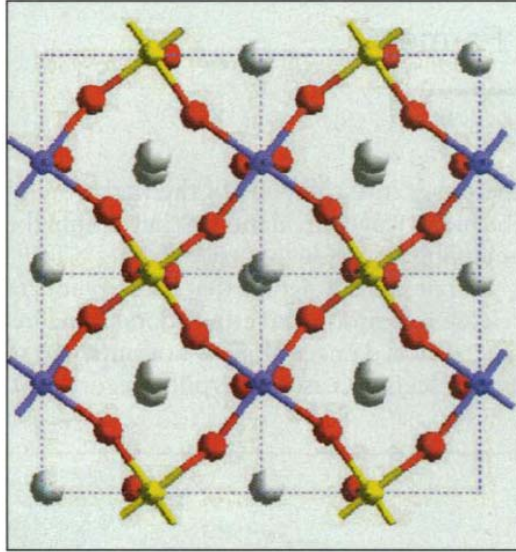


Fig. 2.4: Structure of a charge-ordered manganate. This view down the c axis of $\text{Nd}_{0.5}\text{Ca}_{0.5}\text{MnO}_3$ at 10 K shows charge ordering of the Mn^{3+} and Mn^{4+} cations. Mn^{3+} is shown in blue, Mn^{4+} in yellow, oxygen in red, and Nd/Ca in whitish gray. [Ref. 145]

Charge ordering in the manganites is strongly affected by the average radius of the A-site cation, $\langle r_A \rangle$. A simple way to vary $\langle r_A \rangle$ smoothly is to change the rare-earth element in $\text{Ln}_{1-x}\text{A}_x\text{MnO}_3$, because $\langle r_A \rangle$ decreases along the rare-earth series from La to Lu (known as the lanthanide-contraction) [145]. Changing the alkaline-earth element from Sr to Ca increases the range; thus, $\text{La}_{0.5}\text{Sr}_{0.5}\text{MnO}_3$ has $\langle r_A \rangle$ of 1.26 Å and $\text{Y}_{0.5}\text{Ca}_{0.5}\text{MnO}_3$ has $\langle r_A \rangle$ of only 1.13 Å. A small $\langle r_A \rangle$ gives rise to a significant deviation of the Mn–O–Mn bond angle from 180° and hence decreases the one-electron e_g bandwidth.

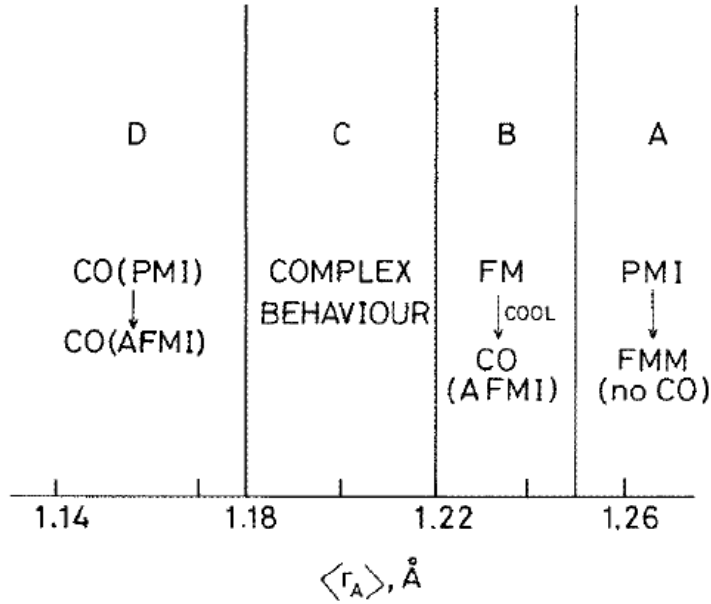


Fig. 2.5. Schematic phase diagram of rare-earth manganites showing different types of charge-ordering effect with the variation in the average radius of the A-site cations. FMM, ferromagnetic metal; PMI, paramagnetic insulator; AFMI, antiferromagnetic insulator; CO, charge-ordered state. [Ref. 148]

The diagram (Fig. 2.5) shows that when $\langle r_A \rangle$ is large (in region A), the ferromagnetic metallic state is stable [148]. Such manganites do not show charge-ordering (e.g., $\text{La}_{0.7}\text{Sr}_{0.3}\text{MnO}_3$ with $\langle r_A \rangle$ of 1.244 Å). With a slightly smaller $\langle r_A \rangle$, the ferromagnetic state becomes unstable and transforms to an antiferromagnetic charge-ordered (CO) state on cooling as in the region B of the figure (e.g. $\text{Nd}_{0.5}\text{Sr}_{0.5}\text{MnO}_3$ with $\langle r_A \rangle$ of 1.236 Å). When $\langle r_A \rangle$ is very small, as in region D, the oxide does not exhibit ferromagnetism and gives rise to an insulating charge-ordered ground state (e.g. $\text{Pr}_{0.7}\text{Ca}_{0.3}\text{MnO}_3$ with $\langle r_A \rangle$ of 1.179 Å).

We can also distinguish three different categories of manganites with respect to their sensitivity to magnetic fields: (a) manganites that are FM and become charge-ordered at low temperatures (e.g., $\text{Nd}_{0.5}\text{Sr}_{0.5}\text{MnO}_3$ when $T_{\text{CO}} = T_{\text{N}}$), with the CO state transforming to an FMM state on the application of a moderate magnetic field;

(b) manganites that are charge-ordered in the paramagnetic state ($T_N < T_{CO}$), and do not exhibit an FMM state, but transform to an FMM state under a magnetic field (e.g., $\text{Pr}_{1-x}\text{Ca}_x\text{MnO}_3$); and (c) those that are charge-ordered in the paramagnetic state ($T_N < T_{CO}$) as in b, but are not affected by magnetic fields up to 15 T or greater (e.g., $\text{Y}_{0.5}\text{Ca}_{0.5}\text{MnO}_3$ with $\langle r_A \rangle = 1.13 \text{ \AA}$). Category (c) is encountered when $\langle r_A \rangle \leq 1.17 \text{ \AA}$ [144]. The charge-ordered state can be melted by the application of electric field, even in $\text{Y}_{0.5}\text{Ca}_{0.5}\text{MnO}_3$ where the charge-ordered state is not affected by magnetic fields [149]. The insulator-metal (I-M) transition temperature decreases with increasing current. The hysteretic I-M transition is specially noteworthy in that there is a reproducible memory effect in the cooling and heating cycles. Application of external pressure suppresses charge-ordering; increases ferromagnetic T_C of $\text{Nd}_{0.5}\text{Sr}_{0.5}\text{MnO}_3$ and induces the metallicity in $\text{Pr}_{0.7}\text{Ca}_{0.3}\text{MnO}_3$ [150].

The formation of FM clusters in an AFM host matrix in the rare earth manganites has been noticed by many workers [144]. Thus, spin glass behavior has been encountered in the $\text{Ln}_{1-x}\text{A}_x\text{MnO}_3$ system at either extreme, corresponding to large or small x . Electronic phase separation is also evidenced in the manganites. Thus, an electron microscopic study of $\text{La}_{1-x-y}\text{Pr}_y\text{Ca}_x\text{MnO}_3$ ($x = 0.375$) has shown electronic phase separation into a submicrometer-scale mixture of CO insulator regions and FMM domains. Percolative transport could occur between the two states [151]. The coexistence of FM and CO states has been observed in $\text{La}_{0.5}\text{Ca}_{0.5}\text{MnO}_3$ and $\text{Nd}_{0.25}\text{La}_{0.25}\text{Ca}_{0.5}\text{MnO}_3$ [152,153]. In Cr-doped $\text{Nd}_{0.5}\text{Ca}_{0.5}\text{MnO}_3$, submicrometer scale FMM domains are embedded in an AFM CO state. So, the material shows a relaxor behavior [154]. $\text{Nd}_{0.5}\text{Sr}_{0.5}\text{MnO}_3$, which shows evidence for separation into three macroscopic phases, is

particularly interesting. These are the high-temperature FMM phase (Imma), the A-type AFM intermediate-temperature phase (Imma) and the CE-type AFM CO low-temperature phase ($P2_1/m$) [155]. The A-type AFM phase starts manifesting itself around 220 K, whereas the CE-type CO phase first appears at 150 K. There are three phases at the so-called CO transition at 150 K. The presence of the high-temperature FMM phase, even at very low temperatures, is noteworthy.

As we already discussed, one of the mechanisms to induce ferroelectricity and magnetoelectric effects in oxide materials is cation charge-ordering. Khomskii and coworkers have predicted recently that rare earth manganites of the formula $Ln_{1-x}A_xMnO_3$ should show charge-order driven magnetic ferroelectricity [119,120]. These rare earth manganites can exhibit two types of charge-ordering depending on the composition. Site-centered charge-order (SCO) is expected at $x = 0.5$ and bond-centered charge-order (BCO) at $x = 0.4$. The materials are expected to have a ferroelectric ground state between these two extremes. There is a report in the literature for the occurrence of a dielectric anomaly in $Pr_{0.6}Ca_{0.4}MnO_3$ around the charge-ordering transition temperature [156]. Although magnetic fields are noted to affect the dielectric properties of the manganites [157], there has been no definitive study of the effect of magnetic fields on the dielectric properties to establish whether there is coupling between the electrical and magnetic order parameters.

We have investigated the dielectric properties, magnetocapacitance and related features of rare earth manganite $Nd_{0.5}Ca_{0.5}MnO_3$ exhibiting SCO. We have also examined the manganite compositions of the type $Pr_{0.6}Ca_{0.4}MnO_3$ exhibiting BCO, which show canted antiferromagnetic or weak ferromagnetic behavior at low temperatures due to

electron phase separation. Besides these manganites, we have also studied $\text{Pr}_{0.7}\text{Ca}_{0.3}\text{MnO}_3$ and $\text{La}_{0.25}\text{Nd}_{0.25}\text{Ca}_{0.5}\text{MnO}_3$, which also have comparable radii of the A-site cations. Dielectric, magnetic and SHG measurements on the charge-ordered insulators, $\text{Y}_{1-x}\text{Ca}_x\text{MnO}_3$ ($x = 0.4, 0.45$ and 0.5) have also been carried out to explore their multiferroic nature.

2.6.2 Magnetoelectric effect in binary rare-earth manganite systems

One of the cognitive approaches of achieving multiferroic nature is by combining the ferroelectric and ferromagnetic properties through proper choice of compounds: ferroelectric compounds like BaTiO_3 , PbTiO_3 , $\text{Pb}(\text{Zr}_{1-x}\text{Ti}_x)\text{O}_3$ on one hand and BiFeO_3 , LaFeO_3 , LaMnO_3 on the other [158-163]. Through this route, not only the magnetic property has been enhanced, but it has also yielded high value of resistivity and low leakage current in BiFeO_3 making it favorable for appreciable polarization with well-saturated hysteresis loops [160,164].

Singh et al. [165] have shown that $0.9\text{BiFeO}_3\text{-}0.1\text{BaTiO}_3$ system shows a magnetoelectric coupling by magnetic, dielectric and calorimetric studies. The change in electric polarization with magnetization and the shift in position of Bi in the magnetic phase confirms the coupling of ferroelectric (P) and magnetic (M) order parameters. Furthermore, the polarization is not only found to increase in the ferromagnetic state, but also scales with magnetization (M) providing the direct evidence for the intrinsic magnetoelectric coupling of multiferroic origin. In case of $0.7\text{BiFeO}_3\text{-}0.3\text{BaTiO}_3$, the dielectric constant shows a broad ferro-para phase transition at around 175°C [166].

Magnetisation data shows a transition at 265 K which happens due to the presence of non-magnetic BaTiO₃ phase causing the reduction of the magnetic interaction and thus diminishing the Neel temperature to below room temperature. (Pb_{0.8}La_{0.2})(Ti_{0.8}Fe_{0.2})O₃ exhibits two prominent peaks observed at all the frequencies in the $\epsilon \sim T$ profile [162]. The first sharp peak at 434 K (T_C) is independent of frequencies and represents a pure FE to PE transition. Thus, doping of La (20 wt. %) at A-site is observed to decrease the FE transition temperature T_C to 434 K (as compared to 768 K for pure PbTiO₃). The second peak is found to be frequency dependent which corresponds to a magnetic transition around 640 K, thereby indicating magnetization-induced dielectric behavior.

It is reported that increasing proportions of LaMnO₃ in the BaTiO₃-LaMnO₃ system systematically decreases the dielectric constant and increases the loss, $\tan \delta$ [163]. Dielectric anomaly around 410 K and magnetic hysteresis at 293 K were clearly observed, which might imply the coexistence of ferroelectricity and ferromagnetism at room temperature. The magnetodielectric effect shows the increase of $[\{\epsilon(H) - \epsilon(0)\} / \epsilon(0)]$ with x and its proportionality to the square of the magnetization. Low-frequency magnetoelectric (ME) voltage coefficient α_E has been measured in bilayers and multilayers of La_{0.7}Sr_{0.3}MnO₃ (LSMO) - PZT and La_{0.7}Ca_{0.3}MnO₃ (LCMO) - PZT oxide films [167]. The effect is stronger in LSMO-PZT than in LCMO-PZT and is weaker in multilayers compared to bilayers. A maximum α_E of 60 mV/cm Oe is measured for the transverse ME effect and is a factor of 2 to 3 higher than the longitudinal effect. The bias magnetic-field dependence of α_E shows hysteresis and remanence. A general increase in α_E is observed with increasing frequency or decreasing temperature. BiFeO₃-PLZT

$[(\text{Pb}_{0.9}\text{La}_{0.1})(\text{Zr}_{0.65}\text{Ti}_{0.35})\text{O}_3]$ system gives the highest value of spontaneous magnetization corresponding to 30 wt. % composition of PLZT, indicating the presence of weak ferromagnetism which is considered to be due to structural distortion of BiFeO_3 from rhombohedral to cubic structure in the solid solutions and originating from Dzyaloshinskii-Moriya interaction [168].

We have studied magnetoelectric properties of a combination of two rare earth manganites with different properties; one showing ferromagnetism and the other exhibiting charge-ordering and possibly phase separation. The systems studied are $\text{La}_{0.7}\text{Ca}_{0.3}\text{MnO}_3$ - $\text{Y}_{0.5}\text{Ca}_{0.5}\text{MnO}_3$, $\text{La}_{0.5}\text{Sr}_{0.5}\text{MnO}_3$ - $\text{Y}_{0.5}\text{Ca}_{0.5}\text{MnO}_3$ and $\text{Pr}_{0.5}\text{Sr}_{0.5}\text{MnO}_3$ - $\text{Pr}_{0.6}\text{Ca}_{0.4}\text{MnO}_3$. $\text{Y}_{0.5}\text{Ca}_{0.5}\text{MnO}_3$ is very robust site-centered charge-ordered insulator while $\text{Pr}_{0.6}\text{Sr}_{0.4}\text{MnO}_3$ is a bond-centered charge-ordered insulator. Both seem to exhibit evidence for electronic phase separation at low temperatures while $\text{La}_{0.7}\text{Ca}_{0.3}\text{MnO}_3$ is a prototype manganite showing colossal magneto resistance around the ferromagnetic transition temperatures. $\text{La}_{0.5}\text{Sr}_{0.5}\text{MnO}_3$ and $\text{Pr}_{0.5}\text{Sr}_{0.5}\text{MnO}_3$ are ferromagnetic metals at room temperatures.

Bibliography

1. N.A. Spaldin, and M. Fiebig, The renaissance of magnetoelectric multiferroics, *Science* **309**, 391 (2005).
2. C.N.R. Rao and C.R. Serrao, New routes to multiferroics, *J. Mater. Chem.*, **17**, 4931 (2007)
3. W. Prellier, M.P. Singh and P. Murugavel, The single-phase multiferroic oxides: From bulk to thin film, *J. Phys.: Condens. Matter* **17**, R803 (2005).
4. W. Eerenstein, N. D. Mathur and J.F. Scott, Multiferroic and magnetoelectric materials, *Nature* **442**, 759 (2006).
5. S.W. Cheong and M. Mostovoy, Multiferroics: A magnetic twist for ferroelectricity, *Nat. Mater.* **6**, 13 (2007).
6. T. Kimura, T. Goto, H. Shintani, K. Ishizaka, T. Arima, and Y. Tokura, Magnetic control of ferroelectric polarization, *Nature* **426**, 55 (2003).
7. T. Lottermoser, T. Lonkai, U. Amann, D. Hohlwein, J. Ihringer, and M. Fiebig, Magnetic phase control by an electric field, *Nature* **430**, 541 (2004).
8. T. Lonkai, D. G. Tomuta, U. Amann, J. Ihringer, R. W. A. Hendrikx, D. M. Tobbens and J. A. Mydosh, Development of the high-temperature phase of hexagonal manganites, *Phys. Rev. B* **69**, 134108 (2004)
9. Z.J. Huang, Y. Cao, Y.Y. Sun, Y.Y. Xue, and C.W. Chu, Coupling between the ferroelectric and antiferromagnetic orders in YMnO_3 , *Phys. Rev. B* **56**, 2623 (1997)

10. T. Lonkai, D.G. Tomuta, J.U. Hoffmann, R. Schneider, D. Hohlwein and J. Ihringer, Magnetic two-dimensional short-range order in hexagonal manganites *J. Appl. Phys.* **93**, 8191 (2003).
11. M. Fiebig, T. Lottermoser, D. Frohlich, A.V. Goltsev and R.V. Pisarev, Observation of coupled magnetic and electric domains, *Nature (London)* **419**, 818 (2002).
12. A.V. Goltsev, R.V. Pisarev, T. Lottermoser, and M. Fiebig, Structure and Interaction of Antiferromagnetic Domain Walls in Hexagonal YMnO₃, *Phys. Rev. Lett.* **90**, 177204 (2003).
13. N.F.D. Ito, T. Yoshimura, and T. Ito, Ferroelectric properties of YMnO₃ epitaxial films for ferroelectric-gate field-effect transistors, *J. Appl. Phys.* **93**, 5563 (2003).
14. N. Fujimura, H. Sakata, D. Ito, T. Yoshimura, T. Yokota, and T. Ito, Ferromagnetic and ferroelectric behaviors of A-site substituted YMnO₃-based epitaxial thin films, *J. Appl. Phys.* **93**, 6990 (2003).
15. W.C. Koehler, H.L. Yakel, E.O. Wollan and J.W. Cable, A note on the magnetic structures of rare earth manganese oxides, *Physics Letters*, **9**, 93 (1964).
16. T. Katsufuji, S. Mori, M. Masaki, Y. Moritomo, N. Yamamoto and H. Takagi, Dielectric and magnetic anomalies and spin frustration in hexagonal RMnO₃ (R=Y, Yb, and Lu), *Phys. Rev. B* **64**, 104419 (2001).
17. D. G. Tomuta, S. Ramakrishnan, G. J. Nieuwenhuys and J. A. Mydosh, The magnetic susceptibility, specific heat and dielectric constant of hexagonal YMnO₃, LuMnO₃ and ScMnO₃, *J. Phys.: Condens. Matter* **13**, 4543 (2001)
18. K. Yoshii and H. Abe, Magnetic properties of LnMnO₃ (Ln=Ho, Er, Tm, Yb, and Lu), *J. Solid State Chem.* **165**, 131 (2002).

19. A. Munoz, J.A. Alonso, M.J. Martinez-Lope, M.T. Casias, J.L. Martinez, and M.T. Fernandez-Diaz, Magnetic structure of hexagonal RMnO_3 ($\text{R}=\text{Y}, \text{Sc}$): Thermal evolution from neutron powder diffraction data, *Phys. Rev. B* **62**, 9498 (2000).
20. M. Fiebig, D. Frohlich, K. Kohn, S. Leute, T.L.V.V. Pavlov, and R.V. Pisarev, Determination of the Magnetic Symmetry of Hexagonal Manganites by Second Harmonic Generation, *Phys. Rev. Lett.* **84**, 5620 (2000).
21. K. Lukaszewicz and J.K.-Kalicinska, X-ray investigations of the crystal structure and phase transitions of YMnO_3 , *Ferroelectrics* **7**, 81 (1974).
22. M.N. Iliev, H.-G. Lee, V. N. Popov, M. V. Abrashev, A. Hamed, R. L. Meng, and C. W. Chu, Raman- and infrared-active phonons in hexagonal YMnO_3 : Experiment and lattice dynamical calculations. *Phys. Rev. B* **56**, 2488 (1997).
23. I.G. Ismailzade and S.A. Kizhaev, Determination of the Curie-point of the ferroelectrics YMnO_3 and YbMnO_3 , *Sov. Phys.- Solid State* **7**, 236 (1965)
24. J. Park, J.-G. Park, G. S. Jeon, H.-Y. Choi, C. Lee, W. Jo, R. Bewley, K.A. McEwen and T. G. Perring, Magnetic ordering and spin-liquid state of YMnO_3 , *Phys. Rev. B* **68**, 104426 (2003)
25. N. Iwata and K. Kohn, Dielectric anomalies at magnetic transitions of hexagonal rare-earth manganese oxides RMnO_3 , *J. Phys. Soc. of Japan* **67** (9), 3318 (1998).
26. J. Park, U. Kong, S.I. Choi, J.-G. Park, C. Lee, W. Jo, Magnetic structure studies of ErMnO_3 , *Appl. Phys. A* **74** [Suppl.], S802 (2002)
27. J. Vermette, S. Jandl and M.M. Gospodinov, Raman study of spin-phonon coupling in ErMnO_3 , *J. Phys.: Condens. Matter* **20**, 425219 (2008).

28. A. P. Ramirez, in Handbook of Magnetic Materials, edited by K. H. J. Buschow (North-Holland, Amsterdam, 2001), Vol. **13**.
29. P. A. Sharma, J. S. Ahn, N. Hur, S. Park, S. B. Kim, S. Lee, J.-G. Park, S. Guha and S.-W. Cheong, Thermal Conductivity of Geometrically Frustrated, Ferroelectric YMnO₃: Extraordinary Spin-Phonon Interactions, Phys. Rev. Lett. **93**, 177202 (2004)
30. S. Petit, F. Moussa, M. Hennion, S. Pailhe's, L. Pinsard-Gaudart, and A. Ivanov, Spin phonon coupling in hexagonal multiferroic YMnO₃, Phys. Rev. Lett. **99**, 266604 (2007)
31. S. Lee, A. Pirogov, M. Kang, K.-H. Jang, M. Yonemura, T. Kamiyama, S.-W. Cheong, F. Gozzo, N. Shin, H. Kimura, Y. Noda and J.-G. Park, Giant magnetoelastic coupling in multiferroic hexagonal manganites, Nature **451**, 805 (2008)
32. X. Fabreges, S. Petit, I. Mirebeau, S. Pailhes, L. Pinsard, A. Forget, M.T. Fernandez-Diaz and F. Porcher, Spin-lattice coupling, frustration, and magnetic order in multiferroic RMnO₃, Phys. Rev. Lett. **103**, 067204 (2009)
33. C. dela Cruz, F. Yen, B. Lorenz, Y.Q. Wang, Y.Y. Sun, M.M. Gospodinov and C. W. Chu, Strong spin-lattice coupling in multiferroic HoMnO₃: Thermal expansion anomalies and pressure effect, Phys. Rev. B **71**, 060407(R) (2005)
34. H. Fukumura, S. Matsui, H. Harima, K. Kisoda, T. Takahashi, T. Yoshimura and N. Fujimura, Raman scattering studies on multiferroic YMnO₃, J. Phys.: Condens. Matter **19**, 365239 (2007).
35. D. Lim, R.D. Averitt, J. Demsar, and A.J. Taylor, N. Hur and S.W. Cheong, Coherent acoustic phonons in hexagonal manganite LuMnO₃, Appl. Phys. Lett. **83**, 4800 (2003)

36. A.B. Souchkov, J.R. Simpson, M. Quijada, H. Ishibashi, N. Hur, J.S. Ahn, S.W. Cheong, A.J. Millis, and H.D. Drew, Exchange interaction effects on the optical properties of LuMnO_3 , *Phys. Rev. Lett.* **91**, 027203 (2003)
37. T. Kimura, Spiral magnets as magnetoelectrics, *Annu. Rev. Mater. Res.* **37**, 387413 (2007)
38. S. Quezel, F. Tcheou, J. Rossat-Mignod, G. Quezel, E. Roudaut.. Magnetic structure of the perovskite-like compound TbMnO_3 , *Physica B* **86–88**, 916 (1977)
39. M. Kenzelmann, A.B. Harris, S. Jonas, C. Broholm, J. Schefer, S.B. Kim, C.L. Zhang, S.-W. Cheong, O.P. Vajk and J.W. Lynn, Magnetic inversion symmetry breaking and ferroelectricity in TbMnO_3 , *Phys. Rev. Lett.* **95**, 087206 (2005)
40. T. Kimura, G. Lawes, T. Goto, Y. Tokura, A. P. Ramirez, Magnetoelectric phase diagrams of orthorhombic RMnO_3 ($R = \text{Gd, Tb, and Dy}$). *Phys. Rev. B* **71**, 224425 (2005)
41. N. Aliouane, K. Schmalzl, D. Senff, A. Maljuk, K. Prokes, M. Braden, and D. N. Argyriou, Flop of Electric Polarization Driven by the Flop of the Mn Spin Cycloid in Multiferroic TbMnO_3 , *Phys. Rev. Lett.* **102**, 207205 (2009)
42. A. Pimenov, A.A. Mukhin, V.Y. Ivanov, V.D. Travkin, A.M Balbashov and A. Loidl, Possible evidence for electromagnons in multiferroic manganites, *Nat. Phys.* **2**, 97 (2006)
43. R.V. Aguilar, A.B. Sushkov, C.L. Zhang, Y.J. Choi, S.W. Cheong and H.D. Drew, Colossal magnon-phonon coupling in multiferroic $\text{Eu}_{0.75}\text{Y}_{0.25}\text{MnO}_3$, *Phys. Rev. B* **76**, 060404 (2007)

44. Y. Takahashi, N. Kida, Y. Yamasaki, J. Fjioka, T. Arima, R. Shimano, S. Miyahara, M. Mochizuki, N. Furukawa and Y. Tokura, Evidence for an electric-dipole active continuum band of spin excitations in multiferroic TbMnO₃, Phys. Rev. Lett. **101**, 187201 (2008)
45. R.V. Aguilar, M. Mostovoy, A.B. Sushkov, C.L. Zhang, Y.J. Choi, S.W. Cheong and H.D. Drew, Origin of electromagnon excitations in multiferroic RMnO₃, Phys. Rev. Lett. **102**, 047203 (2009)
46. A. Pimenov, A. Shuvaev, A. Loidl, F. Schrettle, A. A. Mukhin, V.D. Travkin, V.Yu Ivanov and A.M. Balbashov, Magnetic and magnetoelectric excitations in TbMnO₃, Phys. Rev. Lett. **102**, 107203 (2009)
47. P.B. Allen and V. Perebeinos, Self-trapped exciton and Franck-Condon spectra predicted in LaMnO₃, Phys. Rev. Lett. **83**, 4828 (1999)
48. V. Perebeinos and P.B. Allen, Multiphonon resonant Raman scattering predicted in LaMnO₃ from the Franck-Condon process via self-trapped excitons, Phys. Rev. B **64**, 085118 (2001)
49. E. Saito, S. Okamoto, K.T. Takahashi, K. Kobe, K. Yamamoto, T. Kimura, S. Ishihara, S. Maekawa and Y. Tokura, Observation of orbital waves as elementary excitations in a solid, Nature **410**, 180 (2001)
50. J. van den Brink, Orbital Excitations in LaMnO₃, Phys. Rev. Lett. **87**, 217202 (2001)
51. R. Kruger, B. Schulz, S. Naler, R. Rauer, D. Budelmam, J. Backstrom, K. H. Kim, S. W. Cheong, V. Perebeinos and M. Rubhausen, Orbital ordering in LaMnO₃ Investigated by Resonance Raman Spectroscopy, Phys. Rev. Lett. **92**, 097203 (2004)

52. L. Martin-Carron and A. de Andres, Excitations of the orbital order in RMnO₃ manganites: light scattering experiments, *Phys. Rev. Lett.* **92**, 175501 (2004)
53. K.Y. Choi, P. Lemmens, T. Sahaouri, G. Guntherodt, Y.G. Pashkevich, V.P. Gnezdilov, P. Reutler, L. Pinsard-Gaudart, B. Bucher and A. Revcolevschi, Existence of orbital polarons in ferromagnetic insulating La_{1-x}Sr_xMnO₃ (0.11≤x≤0.14) revealed by giant phonon softening, *Phys. Rev. B* **71**, 174402 (2005)
54. K.Y. Choi, P. Lemmens, G. Guntherodt, Y.G. Pashkevich, V.P. Gnezdilov, P. Reutler, L.P. Gaudart, B. Bucher and A. Revcolevschi, Orbiton-mediated multiphonon scattering in La_{1-x}Sr_xMnO₃, *Phys. Rev. B* **72**, 024301 (2005)
55. P.B. Allen and V. Perebeinos, Condensed-matter physics: First glimpse of the orbiton, *Nature* **410**, 155 (2001)
56. M. Gruninger, R. Ruckamp, M. Windt, P. Reutler, C. Zobel, T. Lorenz, A. Freimuth and A. Revcolevschi, Orbital physics (Communication arising): Experimental quest for orbital waves, *Nature* **418**, 39 (2002)
57. J. Bala, A.M. Oles and G.A. Sawatzky, Orbital-lattice polarons in ferromagnetic LaMnO₃, *Phys. Rev. B* **65**, 184414 (2002)
58. M.N. Iliev, V.G. Hadjiev, A.P. Litvinchuk, F. Yen, Y.Q. Wang, Y.Y. Sun, S. Jandl, J. Laverdiere, V.N. Popov and M.M. Gospodinov, Multiple-order Raman scattering from rare-earth manganites: Oxygen isotope and rare-earth substitution effects, *Phys. Rev. B* **75**, 064303 (2007)
59. J. Laverdiere, S. Jandl, A.A. Mukhin, V. Yu Iyanov, V.G. Iyanov and M.N. Iliev, Spin-phonon coupling in orthorhombic RMnO₃ (R = Pr, Nd, Sm, Eu, Gd, Tb, Dy, Ho, Y): A Raman study, *Phys. Rev. B* **73**, 214301 (2006)

60. E. Granado, A. Garcia, J.A. Sanjurjo, C. Rettori, I. Torriani, F. Prado, R.D. Sanchez, A. Caneiro and S.B. Oseroff, Magnetic ordering effects in the Raman spectra of $\text{La}_{1-x}\text{Mn}_{1-x}\text{O}_3$, *Phys. Rev. B* **60**, 11879 (1999)
61. W.S. Ferreira, J.A. Moreira, A. Almeida, M.R. Chaves, J.P. Araujo, J.B. Oliveira, J. M.M.D. Silva, T.M. Sa, T.M. Mendonca, P.S. Carvalho, J. Kreisel, J.L. Riberio, L.G. Vieira, P.B. Tavares and S. Mendonca, Spin-phonon coupling and magnetoelectric properties: EuMnO_3 versus GdMnO_3 , *Phys. Rev. B* **79**, 054303 (2009)
62. P. Kumar, S. Saha, C.R. Serrao, A.K. Sood and C.N.R. Rao, Temperature-dependent infrared reflectivity studies of multiferroic TbMnO_3 : Evidence for spin-phonon coupling, *Pramana-J. Phys.* **74**, 281 (2010)
63. L. Martin-Carron, A. de Andres, M.J. Martinez-Lope, M.T. Casais and J.A. Alonso, Raman phonons as a probe of disorder, fluctuations, and local structure in doped and undoped orthorhombic and rhombohedral manganites, *Phys. Rev. B* **66**, 174303 (2002)
64. M.N. Iliev, M.V. Abrashev, J. Laverdiere, S. Jandl, M.M. Gospodinov, Y.Q. Wang and Y.Y. Sun, Distortion-dependent Raman spectra and mode mixing in RMnO_3 perovskites ($R = \text{La, Pr, Nd, Sm, Eu, Gd, Tb, Dy, Ho, Y}$), *Phys. Rev. B* **73**, 064302 (2006)
65. L. Martin-Carron, J.S. Benitz and A. de Andres, High-pressure dependence of Raman phonons of RMnO_3 ($R = \text{Pr, Tb}$), *J. Solid State Chem.* **171**, 313 (2003)
66. G. V. S. Rao, B. M. Wanklyn and C. N. R. Rao, Electrical transport in rare earth ortho-chromites, -manganites and -ferrites, *J. Phys. Chem. Solids* **32**, 345 (1971)

67. R. Aleonard, R. Pauthenet, J. P. Rebouillat, and C. Veyret, Interpretation of the Magnetic Properties of the Rare Earth Chromites and the Rare Earth Manganites, *J. Appl. Phys.* **39**, 379 (1968)
68. G. V .S. Rao, G. V. Chandrashekhar, and C. N. R. Rao, Are rare earth orthochromites ferroelectric ?, *Solid State Commun.* **6**, 177 (1968).
69. H. L. Yakel, W. C. Koehler, E. F. Bertaut and E. F. Forrat, On the crystal structure of the manganese (III) trioxides of the heavy lanthanide and yttrium. *Acta Crystallogr.* **16**, 957 (1963).
70. G. V. S. Rao, C.N.R Rao, J.R. Ferraro, Infrared and electronic spectra of rare earth perovskites: ortho-chromites, -manganites and -ferrites, *Appl. Spec.* **24**, 436 (1970)
71. T. Morishita and K. Tsushima, Susceptibility of the weak ferromagnets ErCrO_3 and YCrO_3 near the critical anomaly, *Phys. Rev. B* **24**, 341 (1981)
72. V. M. Judin, and A. B. Sherman, Weak ferromagnetism of YCrO_3 , *Solid State Commun.* **4**, 661 (1966)
73. M. A. Butler, M. Eibschutz, and L. G. van Uitert, Cr^{53} Nuclear magnetic resonance in the rare earth orthochromites., *Phys. Rev. B: Condens. Matter* **6**, 51 (1972).
74. E. Jedryka, S. Nadolski and M. Wojcik, Wall NMR in the weak ferromagnets YCrO_3 and LuCrO_3 , *J. Magn. Magn. Mater.* **40**, 303 (1984).
75. M. Udagawa, K. Kohn, N. Koshizuka, T. Tsushima and K. Tsushima, Influence of magnetic ordering on the phonon Raman spectra in YCrO_3 and GdCrO_3 , *Solid State Commun.* **16**, 779 (1975).

76. J. W. Kim, Y. S. Oh, K. S. Suh, Y. D. Park, and K. H. Kim, Specific heat of a YCrO_3 single crystal as investigated by a SiN membrane based microcalorimeter, *Therm. Acta* **455**, 2 (2007).
77. T. Kimura, S. Kawamoto, I. Yamada, M. Azuma, M. Takano and Y. Tokura, Magnetocapacitance effect in multiferroic BiMnO_3 , *Phys. Rev. B: Condens. Matter* **67**, 180401 (2003).
78. S. Niitakaa, M. Azumaa, M. Takanob, E. Nishiboric, M. Takatad and M. Sakata, Crystal structure and dielectric and magnetic properties of BiCrO_3 as a ferroelectromagnet, *Solid State Ionics* **172**, 557 (2004).
79. M. Fiebig, T. Lottermoser and R. V. Pisarev, Spin-rotation phenomena and magnetic phase diagrams of hexagonal RMnO_3 , *J. Appl. Phys.* **93**, 8194 (2003)
80. C.R. Serrao, A.K. Kundu, S. B. Krupanidhi, U.V. Waghmare and C.N.R. Rao, Biferroic YCrO_3 , *Phys. Rev. B* **72**, 220101(R) (2005)
81. Katz, L. On the unit cell of YCrO_3 , *Acta Cryst.* **8**, 121 (1955).
82. J. T. Looby and L. Katz, Yttrium chromium oxide, a new compound of the perovskite type, *J. Am. Chem. Soc.* **76**, 6029 (1954).
83. S. Geller, and E. A. Wood, Crystallographic studies of perovskite-like compounds. I. Rare earth orthoferrites and YFeO_3 , YCrO_3 , YAlO_3 , *Acta Crystallogr.* **9**, 563 (1956).
84. G. H. Kwei, S. J. L. Billinge, S. Cheong and J. G. Saxton, Pair-distribution functions of ferroelectric perovskites: Direct observation of structural ground states, *Ferroelectrics* **164**, 57 (1995).
85. T. Egami, and S. J. L. Billinge, *Underneath the Bragg Peaks: Structural Analysis of Complex Materials*, (Amsterdam: Elsevier Science) (2003).

86. K. Ramesha, Llobet, T Proffen, C.R. Serrao and C.N.R. Rao, Observation of local non-centrosymmetry in weakly biferroic YCrO_3 , *J. Phys.: Condens. Matter* **19**, 102202 (2007)
87. G.A. Smolenskii and I.E. Chupis, Ferroelectromagnets, *Sov. Phys. Usp.* **25**, 475 (1982)
88. A.K. Pradhan, K. Zhang, D. Hunter, J.B. Dadson, G.B. Loutts, P. Bhattacharya, R. Katiyar, J. Zhang, D.J. Sellmyer, U. N. Roy, Y. Cui, and A. Burger, Magnetic and electrical properties of single-phase multiferroic BiFeO_3 , *J. Appl. Phys.* **97**, 093903 (2005)
89. V.R. Palkar, J. John, and R. Pinto, Observation of saturated polarization and dielectric anomaly in magnetoelectric BiFeO_3 thin films, *Appl. Phys. Lett.* **80**, 1628 (2002)
90. Y.P. Wang, L. Zhou, M.F. Zhang, X.Y. Chen, J.-M. Liu, and Z.G. Liu, Room-temperature saturated ferroelectric polarization in BiFeO_3 ceramics synthesized by rapid liquid phase sintering, *Appl. Phys. Lett.* **84**, 1731 (2004)
91. S.T. Zhang, M.H. Lu, D. Wu, Y.F. Chen, and N. B. Ming, Larger polarization and weak ferromagnetism in quenched BiFeO_3 ceramics with a distorted rhombohedral crystal structure, *Appl. Phys. Lett.* **87**, 262907 (2005)
92. R. Mazumder, P.S. Devi, D. Bhattacharya, P. Choudhury, and A. Sen and M. Raja, Ferromagnetism in nanoscale BiFeO_3 , *Appl. Phys. Lett.* **91**, 062510 (2007)
93. S. Vijayanand, H.S. Potdar, and P.A. Joy, Origin of high room temperature ferromagnetic moment of nanocrystalline multiferroic BiFeO_3 , *Appl. Phys. Lett.* **94**, 182507 (2009)

94. X. Yu and X. An, Enhanced magnetic and optical properties of pure and (Mn, Sr) doped BiFeO₃ nanocrystals, *Solid State Commun.* **149**, 711 (2009)
95. C. Ederer and N.A. Spaldin, Weak ferromagnetism and magnetoelectric coupling in bismuth ferrite, *Phys. Rev. B* **71**, 060401(R) (2005)
96. J.B. Neaton, C. Ederer, U.V. Waghmare, N.A. Spaldin and K.M. Rabe, First-principles study of spontaneous polarization in multiferroic BiFeO₃, *Phys. Rev. B* **71**, 014113 (2005)
97. R. Haumont, J. Kreisel, P. Bouvier and F. Hippert, Phonon anomalies and the ferroelectric phase transition in multiferroic BiFeO₃, *Phys. Rev. B* **73**, 132101 (2006)
98. I. Sosnowska, T.P.- Neumaier and E. Steichele, Spiral magnetic ordering in bismuth ferrite, *J. Phys. C: Solid State Phys.* **15**, 4835 (1982)
99. R. Przeniosło, A. Palewicz, M. Regulski, I. Sosnowska, R.M. Ibberson and K.S. Knight, Does the modulated magnetic structure of BiFeO₃ change at low temperatures?, *J. Phys.: Condens. Matter* **18**, 2069 (2006)
100. G.L. Yuan, S.W. Or, J.M. Liu and Z.G. Liu, Structural transformation and ferromagnetic behavior in single-phase Bi_{1-x}Nd_xFeO₃ multiferroic ceramics, *Appl. Phys. Lett.* **89**, 052905 (2006)
101. G.L. Yuan and S.W. Or, Multiferroicity in polarized single-phase Bi_{0.875}Sm_{0.125}FeO₃ ceramics, *J. Appl. Phys.* **100**, 024109 (2006)
102. V.R. Palkar, D.C. Kundaliya, S.K. Malik and S. Bhattacharya, Magnetoelectricity at room temperature in the Bi_{0.9-x}Tb_xLa_{0.1}FeO₃ system, *Phys. Rev. B* **69**, 212102 (2004)

103. P. Uniyal and K.L. Yadav, Study of dielectric, magnetic and ferroelectric properties in $\text{Bi}_{1-x}\text{Gd}_x\text{FeO}_3$, *Materials Letters* **62**, 2858 (2008)
104. Z.V. Gabbasova, M.D. Kuzmin, A.K. Zvezdin, I.S. Dubenko, V.A. Murashov, D.N. Rakov and I.B. Krynetsky, $\text{Bi}_{1-x}\text{R}_x\text{FeO}_3$ (R= rare earth): a family of novel magnetoelectrics, *Physics Letters A* **158**, 491 (1991)
105. S.-T. Zhang, Y. Zhang, M.-H. Lu, C.-L. Du, Y.-F. Chen, Z.-G. Liu, Y.-Y. Zhu, N.-B. Ming and X. Q. Pan, Substitution-induced phase transition and enhanced multiferroic properties of $\text{Bi}_{1-x}\text{La}_x\text{FeO}_3$ ceramics, *Appl. Phys. Lett.* **88**, 162901 (2006)
106. D.H. Wang, W.C. Goh, M. Ning, and C.K. Ong, Effect of Ba doping on magnetic, ferroelectric, and magnetoelectric properties in multiferroic BiFeO_3 at room temperature, *Appl. Phys. Lett.* **88**, 212907 (2006)
107. V.A. Khomchenko, D.A. Kiselev, J.M. Vieira, A.L. Kholkin, M.A. Sá and Y.G. Pogorelov, Synthesis and multiferroic properties of $\text{Bi}_{0.8}\text{A}_{0.2}\text{FeO}_3$ (A=Ca,Sr,Pb) ceramics, *Appl. Phys. Lett.* **90**, 242901 (2007)
108. V.A. Khomchenko, D.A. Kiselev, J.M. Vieira, Li Jian, A.L. Kholkin, A.M.L. Lopes, Y.G. Pogorelov, J.P. Araujo and M. Maglione, Effect of diamagnetic Ca, Sr, Pb, and Ba substitution on the crystal structure and multiferroic properties of the BiFeO_3 perovskite, *J. Appl. Phys.* **103**, 024105 (2008)
109. L.Y. Wang, D.H. Wang, H.B. Huang, Z.D. Han, Q.Q. Cao, B.X. Gu and Y.W. Du, The magnetic properties of polycrystalline $\text{Bi}_{1-x}\text{Sr}_x\text{FeO}_3$ ceramics, *J. Alloys and Compounds* **469**, 1 (2009)

110. V.A. Khomchenko, M. Kopcewicz, A.M.L. Lopes, Y. G. Pogorelov, J.P. Araujo, J.M. Vieira and A.L. Kholkin, Intrinsic nature of the magnetization enhancement in heterovalently doped $\text{Bi}_{1-x}\text{A}_x\text{FeO}_3$ (A=Ca, Sr, Pb, Ba) multiferroics, *J. Phys. D: Appl. Phys.* **41**, 102003 (2008)
111. Z.H. Chi, C.J. Xiao, S.M. Feng, F.Y. Li, C.Q. Jin, X. H. Wang, R.Z. Chen, L.T. Li, Manifestation of ferroelectromagnetism in multiferroic BiMnO_3 , *J. Appl. Phys.* **98**, 103519 (2005)
112. Z.H. Chi, H. Yang, S.M. Feng, F.Y. Li, R.C. Yu, C.Q. Jin, Room-temperature ferroelectric polarization in multiferroic BiMnO_3 , *J. Magn. Magn Mater.* **310**, e358 (2007)
113. A.M. dos Santos, S. Parashar, A.R. Raju, Y.S. Zhao, A.K. Cheetham and C.N.R. Rao, Evidence for the likely occurrence of magnetoferroelectricity in the simple perovskite, BiMnO_3 , *Solid State Commun.* **122**, 49 (2002).
114. I. Sosnowska, W. Schäfer, W. Kockelmann, K.H. Andersen, I.O. Troyanchuk, Crystal structure and spiral magnetic ordering of BiFeO_3 doped with manganese, *Appl. Phys. A* **74** [Suppl.], S1040 (2002)
115. C.H. Yang, T.Y. Koo, Y.H. Jeong, How to obtain magnetocapacitance effects at room temperature: The case of Mn-doped BiFeO_3 , *Solid State Commun.* **134**, 299 (2005)
116. V.A. Murashov, D.N. Rakov, V.M. Ionov, I.S. Dubenko, Y.V. Titov, Magnetoelectric $(\text{Bi,Ln})\text{FeO}_3$ compounds: crystal growth, structure and properties, *Ferroelectrics* **162**, 11 (1994)

117. Y.H. Lee, J.M. Wu, C.H. Lai, Influence of La doping in multiferroic properties of BiFeO₃ thin films, *Appl. Phys. Lett.* **88**, 042903 (2006).
118. Q.H. Jiang, C.W. Nan, Z.J. Shen, Synthesis and Properties of Multiferroic La-modified BiFeO₃ Ceramics, *J. Am. Ceram. Soc.* **89**, 2123 (2006).
119. D. V. Efremov, J. van den Brink, and D. I. Khomskii, Bond- Versus site-centred ordering and possible ferroelectricity in manganites, *Nat. Mater.* **3**, 853 (2004).
120. J. van den Brink and D. I. Khomskii, Multiferroicity due to charge ordering, *J. Phys.: Condens. Matter* **20**, 434217 (2008).
121. N. Ikeda, H. Ohsumi, M. Mizumaki, S. Mori, Y. Horibe, and K. Kishimoto, Frustration and ordering of iron ions on triangular iron mixed valence system RFe₂O₄, *J. Magn. Magn. Mater.* **272-276**, E1037 (2004).
122. A. Nagano, and S. Ishihara, Spin-charge-orbital structures and frustration in multiferroic RFe₂O₄, *J. Phys.: Condens. Matter* **19**, 145263 (2007).
123. N. Ikeda, S. Mori and K. Kohn, Charge Ordering and dielectric dispersion in mixed valence oxides RFe₂O₄, *Ferroelectrics* **314**, 41 (2005).
124. N. Kimizuka, A. Takenaka, Y. Sasada and T. Katsura, A series of new compounds A³⁺Fe₂O₄ (A = Ho, Er, Tm, Yb, and Lu), *Solid State Commun.* **15**, 1321 (1974).
125. M.A. Subramanian, T. He, J. Chen, N.S. Rogado, T. G. Calvarese and A.W. Sleight, Giant room-temperature magnetodielectric response in the electronic ferroelectric LuFe₂O₄, *Adv. Mater.* **18**, 1737 (2006).

126. K. Yoshii, N. Ikeda, Y. Matsuo, Y. Horibe and S. Mori, Magnetic and dielectric properties of RFe_2O_4 , $RFeMO_4$, and $RGaCuO_4$ ($R=Yb$ and Lu , $M=Co$ and Cu), *Phys. Rev. B: Condens. Matter* **76**, 024423 (2007).
127. K. Yoshii, N. Ikeda and S. Mori, Magnetic and dielectric behavior of $TmFe_2O_4$ and $TmFeCuO_4$, *J. Magn. Magn. Mater.* **310**, 1154 (2007).
128. K. Yoshii, N. Ikeda, and A. Nakamura, Magnetic and dielectric properties of frustrated ferrimagnet $TmFe_2O_4$, *Physica B* **378**, 585 (2006).
129. J. Iida, M. Tanaka, Y. Nakagawa, S. Funahashi, N. Kimizuka and S. Takekawa, Magnetization and spin correlation of two-dimensional triangular antiferromagnet $LuFe_2O_4$, *J. Phys. Soc. Jpn.* **62**, 1723 (1993).
130. M. Tanaka, H. Iwasaki, K. Siratori, and I. Shindo, Mossbauer study on the magnetic structure of $YbFe_2O_4$: A two-dimensional antiferromagnet on a triangular lattice, *J. Phys. Soc. Jpn.* **58**, 1433 (1989).
131. S. Nakamura, H. Kito and M. Tanaka, An approach to specify the spin configuration in the RFe_2O_4 ($R=Y$, Ho , Er , Tm , Yb and Lu) family: ^{57}Fe Mossbauer study on a single crystal $LuFe_2O_4$, *J. Alloys and Compounds*, **275**, 574 (1998)
132. N. Ikeda, H. Ohsumi, K. Ohwada, K. Ishii, T. Inami, K. Kakurai, Y. Murakami, K. Yoshii, S. Mori, Y. Horibe, and H. Kito, Ferroelectricity from iron valence ordering in the charge-frustrated system $LuFe_2O_4$, *Nature* **436**, 1136 (2005).
133. A. Nagano, M. Naka, J. Nasu and S. Ishihara, Electric polarization, magnetoelectric effect and orbital state of a layered iron oxide with frustrated geometry, *Phys. Rev. Lett.* **99**, 217202 (2007).

134. N. Ikeda, S. Mori and K. Yoshii, Ferroelectricity from valence ordering in RFe_2O_4 , *Ferroelectrics* **348**, 38 (2007).
135. Y. Murakami, H. Kawada, H. Kawata, M. Tanaka, T. Arima, Y. Moritomo and Y. Tokura, Direct observation of charge and orbital ordering in $\text{La}_{0.5}\text{Sr}_{1.5}\text{MnO}_4$, *Phys. Rev. Lett.* **80**, 1932 (1998).
136. N. Ikeda, K. Kohn, N. Myouga, E. Takahashi, H. Kitoh, and S. Takekawa, Charge frustration and dielectric dispersion in LuFe_2O_4 , *J. Phys. Soc. Jpn.* **69**, 1526 (2000).
137. S.-W. Cheong and M. Mostovoy, Multiferroics: a magnetic twist for ferroelectricity, *Nat. Mater.* **6**, 13 (2007)
138. Y. Yamada, K. Kitsuda, S. Nohdo and N. Ikeda, Charge and spin ordering process in the mixed-valence system LuFe_2O_4 : Charge ordering, *Phys. Rev. B: Condens. Matter* **62**, 12167 (2000).
139. N. Ikeda, Y. Yamada, S. Nohdo, T. Inami and S. Katano, Incommensurate charge ordering in mixed valence system LuFe_2O_4 , *Physica B* **241-243**, 820 (1997).
140. Y. Yamada, S. Nohdo and N. Ikeda, Incommensurate charge ordering in charge-frustrated LuFe_2O_4 system, *J. Phys. Soc. Jpn.* **66**, 3733 (1997).
141. Y. Zhang, H. X. Yang, C. Ma, H. F. Tian and J. Q. Li, Charge-stripe order in the electronic ferroelectric LuFe_2O_4 , *Phys. Rev. Lett.* **98**, 247602 (2007).
142. H. J. Xiang and M. H. Whangbo, Charge order and the origin of giant magnetocapacitance in LuFe_2O_4 , *Phys. Rev. Lett.* **98**, 246403 (2007).
143. J. Y. Park, J. H. Park, Y. K. Jeong and H. M. Jang, Dynamic magnetoelectric coupling in "electronic ferroelectric" LuFe_2O_4 , *Appl. Phys. Lett.* **91**, 152903 (2007)

144. C. N. R. Rao, Charge, Spin, and Orbital Ordering in the perovskite manganites, $\text{Ln}_{1-x}\text{A}_x\text{MnO}_3$ (Ln = Rare Earth, A = Ca or Sr), *J. Phys. Chem. B* **104**, 5877 (2000).
145. C. N. R. Rao and A. K. Cheetham, Charge ordering in manganates, *Science* **276**, 911 (1997).
146. C. N. R. Rao and Anthony K. Cheetham, Giant magnetoresistance, charge-ordering and related aspects of manganites and other oxide systems, *Adv. Mater.* **9**, 1009 (1997).
147. M. Coey, Charge-ordering in oxides, *Nature* **430**, 155 (2004).
148. A. Arulraj, R. Gundakaram, A. Biswas, N. Gayathri, A.K. Raychaudhuri and C. N. R. Rao, The nature of the charge-ordered state in $\text{Y}_{0.5}\text{Ca}_{0.5}\text{MnO}_3$ with a very small average radius of the A-site cations, *J. Phys.: Condens. Matter* **10**, 4447 (1998)
149. C.N.R. Rao, A.R. Raju, V. Ponnambalam, S. Parashar, and N. Kumar, Electric-field-induced melting of the randomly pinned charge-ordered states of rare-earth manganates and associated effects, *Phys. Rev. B: Condens. Matter* **61**, 594 (2000).
150. Y. Moritomo, H. Kuwahara, Y. Tomioka and Y. Tokura, Pressure effects on charge-ordering transitions in perovskite manganites, *Phys. Rev. B* **55**, 7549 (1997)
151. M. Uehara, S. Mori, C. H. Chen and S.-W. Cheong, Percolative phase separation underlies colossal magnetoresistance in mixed-valent Manganites, *Nature (London)*, **399**, 560 (1999).
152. P.G. Radaelli, D.E. Cox, M. Marezio, S.W. Cheong, Charge, orbital, and magnetic ordering in $\text{La}_{0.5}\text{Ca}_{0.5}\text{MnO}_3$, *Phys. Rev. B* **55**, 3015 (1997)
153. A. Arulraj, A. Biswas, A.K. Raychaudhuri, C.N.R. Rao, P.M. Woodward, T. Vogt, D.E. Cox, A.K. Cheetham, Reentrant transition from an incipient charge-

- ordered state to a ferromagnetic metallic state in a rare-earth manganate, *Phys. Rev. B.* **57**, R8115 (1998).
154. T. Kimura, Y. Tomioka, R. Kumai, Y. Okimoto and Y. Tokura, Diffuse phase transition and phase separation in Cr-doped $\text{Nd}_{1/2}\text{Ca}_{1/2}\text{MnO}_3$: A Relaxor Ferromagnet, *Phys. Rev. Lett.* **83**, 3940 (1999)
155. P. M. Woodward, D. E. Cox, T. Vogt, C. N. R. Rao and A. K. Cheetham, Effect of compositional fluctuations on the phase transitions in $(\text{Nd}_{1/2}\text{Sr}_{1/2})\text{MnO}_3$, *Chem. Mater.* **11**, 3528 (1999)
156. N. Biskup, A.D. Andrees, J.L. Martinez, and C. Perca, Origin of the colossal dielectric response of $\text{Pr}_{0.6}\text{Ca}_{0.4}\text{MnO}_3$, *Phys. Rev. B: Condens. Matter* **72**, 024115 (2005).
157. R.S. Freitas, J.F. Mitchell and P. Schiffer, Magnetodielectric consequences of phase separation in the colossal magnetoresistance manganite $\text{Pr}_{0.7}\text{Ca}_{0.3}\text{MnO}_3$, *Phys. Rev. B: Condens. Matter* **72**, 144429 (2005).
158. K. Ueda, H. Tabata and T. Kawai, Coexistence of ferroelectricity and ferromagnetism in BiFeO_3 - BaTiO_3 thin films at room temperature, *Appl. Phys. Lett.* **75**, 555 (1999)
159. Y. Wu, J.-G. Wan, C. Huang, Y. Weng, S. Zhao, J.-M. Liu and G. Wang, Strong magnetoelectric coupling in multiferroic BiFeO_3 - $\text{Pb}(\text{Zr}_{0.52}\text{Ti}_{0.48})\text{O}_3$ composite films derived from electrophoretic deposition, *Appl. Phys. Lett.* **93**, 192915 (2008)
160. X.-H. Liu, Z. Xu, S.-B. Qu, X.-Y. Wei and J.-L. Chen., Ferroelectric and ferromagnetic properties of Mn-doped 0.7BiFeO_3 - 0.3BaTiO_3 solid solution Ceramics International **34**, 797 (2008)

161. J. S. Kim, C. Cheon, Y. N. Choi and P. W. Jang, Ferroelectric and ferromagnetic properties of $\text{BiFeO}_3\text{-PrFeO}_3\text{-PbTiO}_3$ solid solutions, *J. Appl. Phys.* **93**, 9263 (2003)
162. A. Singh and R. Chatterjee, Magnetization induced dielectric anomaly in multiferroic $\text{LaFeO}_3\text{-PbTiO}_3$ solid solution, *Appl. Phys. Lett.* **93**, 182908 (2008)
163. N. G. Kim, Y. S. Koo, C. J. Won, N. Hur, J. H. Jung, J. Yoon, Y. Jo and M. H. Jung, Magnetodielectric effect in $\text{BaTiO}_3\text{-LaMnO}_3$ composites, *J. Appl. Phys.* **102**, 014107 (2007)
164. P. Murugavel, J.-H. Lee, J.Y. Jo, H.Y. Sim, J.-S. Chung, Y. Jo and M.-H. Jung, Structure and ferroelectric properties of epitaxial $(1-x)\text{BiFeO}_3\text{-xBaTiO}_3$ solid solution films, *J. Phys.: Condens. Matter* **20**, 415208 (2008)
165. A. Singh, V. Pandey, R. K. Kotnala and D. Pandey, Direct Evidence for Multiferroic Magnetoelectric Coupling in $0.9\text{BiFeO}_3\text{-0.1BaTiO}_3$, *Phys. Rev. Lett.* **101**, 247602 (2008)
166. M. T. Buscaglia, L. Mitoseriu, V. Buscaglia, I. Pallecchi, M. Viviani, P. Nanni and A.S. Siri, Preparation and characterisation of the magneto-electric $x\text{BiFeO}_3\text{-(1-x)BaTiO}_3$ ceramics, *J. Euro. Cera. Soc.* **26**, 3027 (2006)
167. G. Srinivasan, E. T. Rasmussen, B. J. Levin, and R. Hayes, Magnetoelectric effects in bilayers and multilayers of magnetostrictive and piezoelectric perovskite oxides, *Phys. Rev. B* **65**, 134402 (2002)
168. T. Kanai, S. Ohkoshi, A. Nakajima, T. Watanabe and K. Hashimoto, A ferroelectric ferromagnet composed of $(\text{PLZT})_x(\text{BiFeO}_3)_{1-x}$ solid solution, *Adv. Mater.* **13**, 487 (2001)

3. EXPERIMENTAL DETAILS

This section of the thesis mainly deals with the experimental aspects of the work carried out. It covers a brief description of the synthesis procedures of the materials along with the basic operation principles of the instruments employed and various characterization techniques adopted.

3.1 Synthesis of materials

This part of the section deals with the different synthesis methods used to prepare various materials. It contains a brief discussion about the conventional solid state reaction, sealed tube reaction and reduction method through which polycrystalline samples were prepared. It also includes floating zone melting technique used for the growth of single crystals.

3.1.1 Solid state reaction route

Conventional solid state reaction method is a well-established technique for the preparation of bulk ceramic materials [1]. The technique is known for its versatility in synthesis of perovskite type of functional ceramics [2]. This method depends on the inter-diffusion between the rare earth and transition metal oxide powders and therefore, it becomes necessary to use fine powders. The reaction temperatures are usually as high as 700° C to 1500° C, in order to maximize the diffusion length so that the reaction will occur at an appreciable rate. Both thermodynamic and kinetic factors are important in

solid state reaction. Thermodynamic factors determine whether or not a particular reaction should occur by considering the change in free energy that is involved, whereas kinetic factors decide the rate of reaction. In solid state reaction between two solids (powder), the actual reaction to form the product occurs at the interface. Hence, the possible rate controlling steps in the reaction are transport of matter to the reaction interface, reaction at the interface and transfer of matter away from the reaction interface.

Synthesis of $\text{Bi}_{1-x}\text{La}_x\text{FeO}_3$ and $\text{BiFe}_{1-x}\text{Mn}_x\text{O}_3$

Polycrystalline samples of the ferrites were synthesized by the conventional solid state reaction method. MnO_2 and La_2O_3 were employed for $\text{BiFe}_{1-x}\text{Mn}_x\text{O}_3$ ($x = 0, 0.1, 0.2, 0.3$) and $\text{Bi}_{1-x}\text{La}_x\text{FeO}_3$ ($x = 0, 0.1, 0.2, 0.3$) respectively and Bi_2O_3 and Fe_2O_3 were common in both the cases. As bismuth evaporates around 800°C , 4% of Bi_2O_3 were taken in excess for the synthesis of $\text{BiFe}_{1-x}\text{Mn}_x\text{O}_3$. However, this step was not adopted for $\text{Bi}_{1-x}\text{La}_x\text{FeO}_3$ with $x = 0.1, 0.2, 0.3$ as bismuth starts reacting with lanthanum before the onset of its evaporation. After the overnight preheating at 500°C , the powders were taken in stoichiometric proportions, mixed together and ground with propanol in an agate mortar for around an hour separately for each compound. They were sintered for 30 h in the form of disc-shaped pellets at 50°C intervals upto 800°C for $\text{BiFe}_{1-x}\text{Mn}_x\text{O}_3$ and 850°C for $\text{Bi}_{1-x}\text{La}_x\text{FeO}_3$ compositions with intermediate grinding. Finally, the samples were reground and pressed into pellets of 13 mm diameter with the application of 25 kN. 2 % of polyvinyl alcohol in water is used as a binder for proper shaping of the pellets. The resulting pellets were sintered for 10 h at a slow heating rate of $1^\circ\text{C}/\text{min}$ at the above-mentioned temperatures with an intermediate stay for 2 h at 600°C for binder removal

and cooled down to the room temperature with cooling rate of 2 °C/min. Finally, the pellets were annealed in oxygen atmosphere at 700 °C for 24 h to minimize oxygen vacancies.

Synthesis of LnCrO₃, Y(Lu)Cr_{1-x}Mn_xO₃, LuMnO₃

In order to synthesize polycrystalline samples of LnCr_{1-x}Mn_xO₃ (Ln = Y, Lu; x = 0.0–0.3), stoichiometric quantities of Ln₂O₃, Cr₂O₃ and MnO₂ were mixed and ground for 1 h in an agate mortar with propanol. The mixture was dried and ground again. The resulting powder was pelletised and sintered at 900 °C for 24 h. The pellets were then sintered at 1300 °C with intermediate grinding followed by sintering at regular intervals of 100 °C. The resulting product was ground, pelletised with polyvinylalcohol and sintered in air at 1450 °C for 50 h. To improve the oxygen stoichiometry, the pellets were annealed in oxygen at 800 °C for 24 h in a tube furnace.

Synthesis of Ln_{1-x}A_xMnO₃ (Ln = rare earth, A = alkaline earth)

Polycrystalline samples of Y_{0.5}Ca_{0.5}MnO₃, Y_{0.55}Ca_{0.45}MnO₃, Y_{0.6}Ca_{0.4}MnO₃, Pr_{0.6}Ca_{0.4}MnO₃, Gd_{0.5}Ca_{0.5}MnO₃ and Nd_{0.5}Ca_{0.5}MnO₃ were prepared by the conventional solid state reaction method. Rare earth oxides were pre-heated at 700 °C. Stoichiometric quantities of Ln₂O₃, CaCO₃ and Mn₂O₃ compounds were mixed thoroughly in propanol for homogeneity. Initial sintering in air was carried out at 900 °C for 30 h, subsequently followed by grinding and sintering at the intervals of 100 °C up to the maximum temperature of 1400 °C except Gd_{0.5}Ca_{0.5}MnO₃ and Y_{0.55}Ca_{0.45}MnO₃ for which the final temperature was 1300 °C and 1450 °C respectively. The duration of the final sintering

was 50 h. In order to compensate for the oxygen vacancies, the pellets were annealed in high-purity oxygen at 800 °C and then 700 °C for 24 h each.

Synthesis of the binary rare-earth manganite systems

The binary systems $\text{La}_{0.7}\text{Ca}_{0.3}\text{MnO}_3$ - $\text{Y}_{0.5}\text{Ca}_{0.5}\text{MnO}_3$, $\text{La}_{0.5}\text{Sr}_{0.5}\text{MnO}_3$ - $\text{Y}_{0.5}\text{Ca}_{0.5}\text{MnO}_3$ and $\text{Pr}_{0.5}\text{Sr}_{0.5}\text{MnO}_3$ - $\text{Pr}_{0.6}\text{Ca}_{0.4}\text{MnO}_3$ were prepared through two different methods.

In method I, stoichiometric quantities of respective starting materials (Ln_2O_3 with $\text{Ln} = \text{La}, \text{Pr}$ and Y , CaCO_3 , SrCO_3 and Mn_2O_3) were thoroughly ground for 1 h in an agate mortar with propanol with an aim to synthesize $(\text{La}_{0.7}\text{Ca}_{0.3})_{1-x}(\text{Y}_{0.5}\text{Ca}_{0.5})_x\text{MnO}_3$ and $(\text{La}_{0.5}\text{Sr}_{0.5})_{1-x}(\text{Y}_{0.5}\text{Ca}_{0.5})_x\text{MnO}_3$. The resulting powder was pelletized and heated at 900° C for 30 h. The subsequent heating in air was carried out at 100° C intervals for 30 h up to maximum temperatures of 1400° C with an intermediate grinding except in the case of $\text{La}_{0.5}\text{Sr}_{0.5}\text{MnO}_3$ in which final heating was done at 1300° C. The resulting product was ground, pelletized using binder (2% solution of polyvinylalcohol) and sintered in air at 1400° C for 50 h (in the case of $\text{La}_{0.5}\text{Sr}_{0.5}\text{MnO}_3$ 1300° C). The sintered pellets are then annealed in oxygen atmosphere at 800° C for 24 h to improve the oxygen stoichiometry.

In method II, for the synthesis of $(\text{La}_{0.7}\text{Ca}_{0.3}\text{MnO}_3)_{1-x}(\text{Y}_{0.5}\text{Ca}_{0.5}\text{MnO}_3)_x$, $(\text{La}_{0.5}\text{Sr}_{0.5}\text{MnO}_3)_{0.75}(\text{Y}_{0.5}\text{Ca}_{0.5}\text{MnO}_3)_{0.25}$ and $(\text{Pr}_{0.5}\text{Sr}_{0.5}\text{MnO}_3)_{1-x}(\text{Pr}_{0.6}\text{Ca}_{0.4}\text{MnO}_3)_x$, the respective parent compounds were prepared independently and were mixed in suitable proportions. The mixture was thoroughly ground, pelletized and heated at 1000° C onwards as described above in method I.

3.1.2 Synthesis of rare-earth ferrites

YbFe₂O₄ and Lu_{0.5}Y_{0.5}Fe₂O₄

Polycrystalline YbFe₂O₄ and Lu_{0.5}Y_{0.5}Fe₂O₄ were prepared starting with a mixture of high purity (sigma-aldrich 99.9%) Ln₂O₃, Fe₂O₃ and Fe metal powder taken in stoichiometric quantities. The mixtures were ground thoroughly in an agate mortar and pelletized. The pellets were taken in 10 mm diameter quartz tubes. The tubes were evacuated upto 10⁻⁵ bar using a diffusion pump backing with a rotary pump. Then the quartz tubes were sealed using a flame torch. The evacuated quartz tubes were heated at 1100 °C at a rate of 2 °C/min. for 24 h and then quenched with liquid nitrogen.

ErFe₂O₄, YFe₂O₄

ErFe₂O₄, YFe₂O₄ samples were prepared from a stoichiometric mixture of Ln₂O₃ and Fe₂O₃. The mixture was thoroughly mixed and pelletized later. The pellets were heated in a reducing atmosphere of CO₂/H₂ at 1200 °C with a ramping rate of 2 °C/min. for 24 h. The oxygen partial pressure of CO₂/H₂ gas mixtures was kept in the ratio of almost 2:1 with 120 bubbles of CO₂ and 65 bubbles of H₂ passing per minute. After the heating was over, the samples were rapidly cooled to room temperature.

3.1.3 Preparation of single-crystalline samples

There has been a lot of interest in preparation of high quality single crystals devoid of impurities and defects. There are several methods to grow single crystals: the Czochralski method, flux method, skull melting and Bridgman and Stockbarger methods [1]. The most popular technique for rare earth manganites and cobaltites is the floating

zone melting technique. The advantage of this technique is that it does not require any container; therefore, the contamination from the container wall is completely avoided. Moreover, the uniform distribution of chemical constituents can be obtained by eliminating heterogeneous nucleation.

Floating zone melting technique

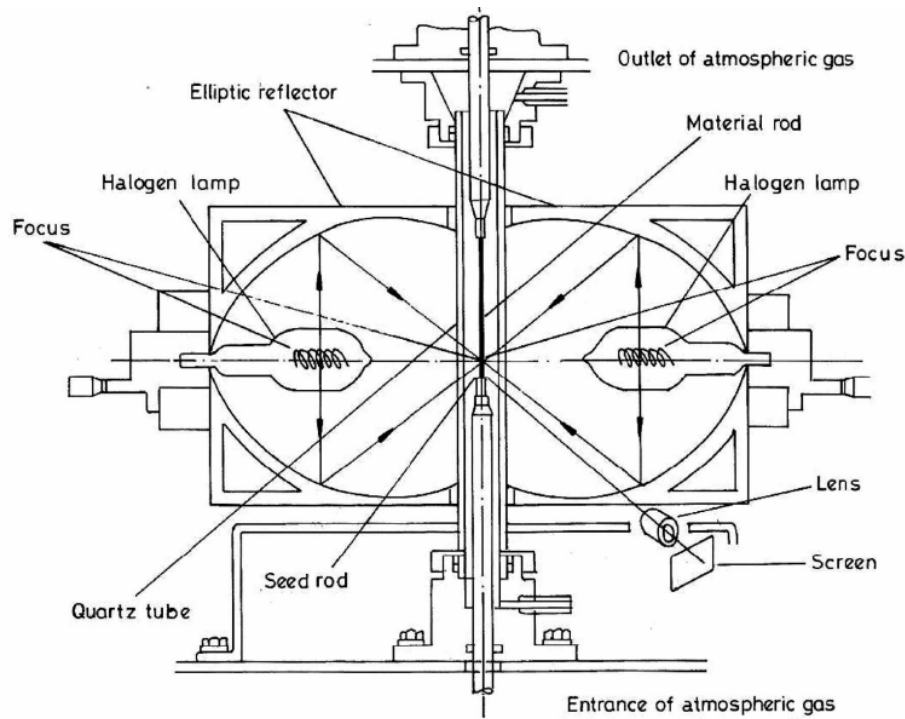


Fig. 3.1: The cross section of the floating zone melting furnace

Fig. 3.1 shows the schematic diagram of the floating zone image furnace. The furnace used in the present study was SC-M35HD, Nichiden Machinery Ltd., Japan. It consists of a pair of halogen lamps to generate infrared radiation, a pair of ellipsoidal mirror to focus the radiation onto the sample, a quartz tube enclosing the floating region

for maintaining the required atmosphere and two pulleys that can move independently or in a synchronized manner to control the growth rate. The growth rate can be varied from 0.1-99 mm/h. The maximum lamp temperature can be achieved upto 2200 °C and the corresponding maximum pressure inside the quartz tube is of six atmosphere pressure.

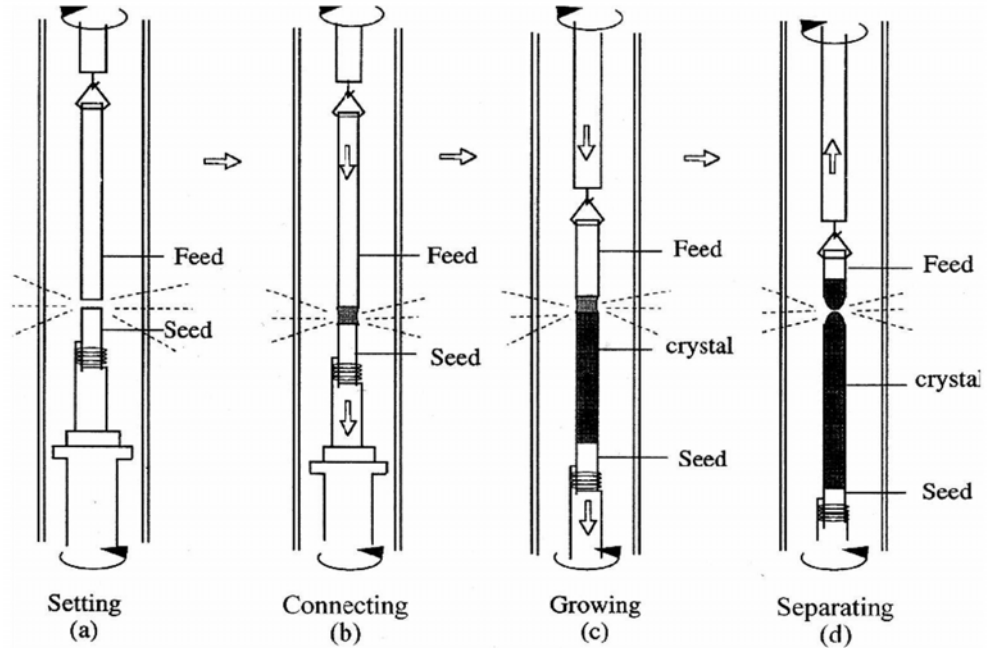


Fig. 3.2: Stages of crystal growths inside the furnace

Fig. 3.2 shows the schematic presentation of different stages of the crystal growth using the floating zone furnace. Infrared radiation coming from a pair of halogen lamps is focused onto the polycrystalline rods by using a pair of gold-coated concave ellipsoidal mirrors. At the focal point the rods melt. The melts between the two connecting feed and seed rods are held by surface tension force without any other support and hence the name floating zone melting technique. The stability of the molten zone can be controlled by changing the temperature, pressure, atmosphere, rod rotation speed and molten zone

pulling rate. In the presence of a seed, very slight supercooling (bringing a clean liquid many degrees below its freezing temperature without freezing) causes the crystal growth.

A floating-zone furnace fitted with two ellipsoidal halogen lamps with radiation heating was used to grow the single crystal of TbMnO_3 and ErMnO_3 . Polycrystalline rods (feed and seed) were prepared by conventional solid-state reaction method. Stoichiometric mixtures of the starting materials Tb_2O_3 and Mn_2O_3 were weighed in the desired proportions and ground for few hours in an agate mortar with propanol. The powder is heated at 900 °C, 1000 °C, 1200 °C with intermediate grinding. The powder was finally sintered at 1400 °C for 24 h in air. The sample was then reground and monophasic polycrystalline powder was hydrostatically pressed and sintered at 1400 °C for 24 h in air to obtain feed and seed rods with a diameter of 3-4 mm and a length of 90-100 mm. A single crystal was then grown under an air atmosphere at a growth rate of 4 mm/h. ErMnO_3 single crystal was also grown by a similar process. A mixture containing stoichiometric quantities of Er_2O_3 and MnO_2 was ground with propanol and the mixture was dried at 800 °C, followed by intermediate grinding and sintering at 100 °C intervals for 30 h up to 1200 °C. After final grinding, the resulting monophasic polycrystalline powder was hydrostatically pressed into rods and sintered at 1250 °C to obtain rods of around 4 mm in diameter and 90–100 mm in length. Single crystals were grown by the floating-zone method (SC-M35HD, Nichiden Machinery Ltd., Japan) fitted with two ellipsoidal halogen lamps. The rotation speed of the feed and seed was maintained at 15 rpm and single crystals were grown from the melt at a pulling rate of 3

mm/h. The single crystals were annealed at 900 °C for 12 h and at 800 °C for 24 h to improve the oxygen stoichiometry in the sample.

3.2 Structure and morphology

3.2.1 Structural analysis: Powder x-ray diffraction

The analytical techniques like x-ray diffraction and electron microscopy which reveal information about the crystallographic structure and chemical composition of materials are discussed in this section.

In powder x-ray diffraction (XRD) technique, the polycrystalline or powdered solid samples are analyzed to find the crystallographic structure, crystallite size (grain size) and preferred orientation [1]. This technique is used to identify unknown substances, by comparing diffraction data against the database maintained by the International Centre for Diffraction Data (ICDD). The basic principles of this x-ray diffraction and the analysis of the same is well known in the literature [3]. The observation of diffraction peaks is an indication of the crystalline behavior of a material under study. These peaks correspond to the basic Bragg reflection belonging to a particular family of planes, which is named after the scientists W.L. Bragg and W.H. Bragg who simplified the basic diffraction phenomena of x-rays by lattice planes present in a crystal. The Bragg equation which relates the lattice spacing and the observed 2θ in a diffraction pattern is given below.

$$2d_{hkl} \sin\theta = n\lambda \quad (3. 1)$$

where, d_{hkl} is the lattice spacing of a particular (hkl), θ is the glancing angle, λ is the wavelength of the X-ray source and n is the order of diffraction. Comparing the values of lattice spacing obtained from observed diffraction pattern of the synthesized powders with the JCPDS data, (hkl) values could be found out.

The phase purity of the polycrystalline samples was established by recording the X-ray diffraction patterns using a Seiferts 3000 TT diffractometer. The data were recorded in the 2θ range of 10° - 90° using $\text{Cu-K}\alpha$ radiation (1.5406 \AA). The lattice parameters were calculated from the XRD patterns using PROSZKI software package.

3.2.2 Electron Microscopy

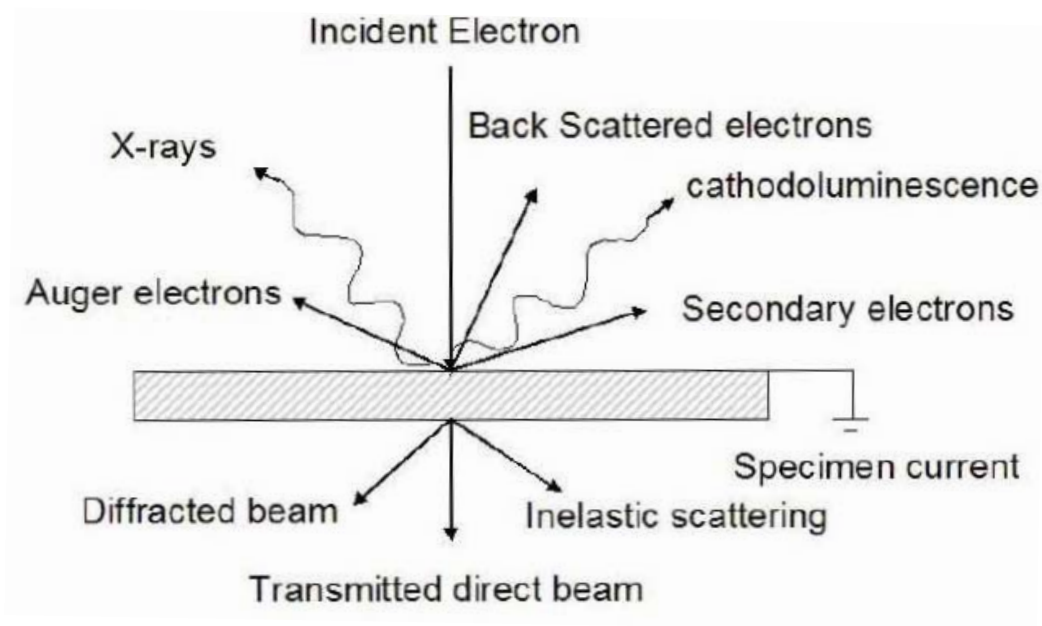


Fig. 3.3: Electron-specimen interactions

When a high energy electron beam is focused and allowed to interact with a solid medium, it undergoes several interesting phenomena. These phenomena are characteristic to the material of interest and can be utilized to characterize the material itself. Figure 3.4 shows the various possible phenomena that can occur when an electron beam is focused on the material. The wave particle duality exhibited by the electrons gives rise to a characteristic de Broglie wavelength depending on the acceleration voltage, which can be focused with the help of electromagnetic lenses and effectively used in electron microscope [4].

Scanning electron microscopy

Scanning electron microscope (SEM) is one of the most versatile and widely used tools of modern science as it allows the study of morphology and composition of the materials. By scanning an electron probe across a specimen, high resolution images of the morphology or topography of a specimen, with great depth of field, at very low or very high magnifications can be obtained. SEM uses a focused electron beam to scan small areas of solid samples. Secondary electrons emitted from the sample are collected to create an area map of the secondary emissions. Since the intensity of secondary emission is very dependent on local morphology, the area map is a magnified image of the sample. The SEM also produces images of high resolution, which means that closely spaced features can be examined at a high magnification.

SEM consists of an electron gun, electromagnetic lenses, a scanning system and an electron detector [5]. The electron gun provides a source of electrons. In a typical

SEM, an electron beam is thermionically emitted from an electron gun fitted with a tungsten filament cathode. Tungsten is normally used in thermionic electron guns because it has the highest melting point and lowest vapor pressure of all metals, thereby allowing it to be heated for electron emission. Other types of electron emitters include lanthanum hexaboride (LaB_6) cathodes and field emission guns. Field emission guns may be a cold-cathode type using tungsten single crystal emitters or a thermally-assisted Schottky type using emitters of zirconium oxide. Back-scattered electrons (BSE) are the electrons that are reflected from the sample by elastic scattering. BSE are often used in analytical SEM along with the spectra made from the characteristic x-rays. Because the intensity of the BSE signal is strongly related to the atomic number (Z) of the specimen, BSE images can provide information about the distribution of different elements in the sample. Characteristic x-rays are emitted when the electron beam removes an inner shell electron from the sample, causing a higher energy electron to fill the shell and release energy. These characteristic x-rays are used to identify the composition and measure the abundance of elements in the sample. For imaging in the conventional SEM, specimens must be electrically conductive, at least at the surface, and electrically grounded to prevent the accumulation of electrostatic charge at the surface. Nonconductive specimens tend to charge when scanned by the electron beam and especially in secondary electron imaging mode, this causes scanning faults and other image artifacts. They are, therefore, usually coated with an ultrathin electrically-conducting material, commonly gold. Coating prevents the accumulation of static electric charge on the specimen during electron irradiation.

A field-emission cathode in the electron gun of a SEM provides narrower probing beams at low as well as high electron energy, resulting in both improved spatial resolution and minimized sample charging and damage. Field-emission scanning electron microscope (FESEM) produces clearer, less electrostatically distorted images with spatial resolution down to 1 nm which is 3 to 6 times better than conventional SEM. Smaller-area contamination spots can be examined at electron accelerating voltages compatible with energy dispersive x-ray spectroscopy. Reduced penetration of low kinetic energy electrons probes closer to the immediate material surface. High quality and low voltage images are obtained with negligible electrical charging of samples (accelerating voltages range from 0.5 to 30 kV) and the need for placing conducting coatings on insulating materials is virtually eliminated.

Energy Dispersive X-ray analysis

The composition analysis of the powder sample was carried out by Energy Dispersive X-ray (EDX) analysis using a LEICA S440I scanning electron microscope fitted with a Si-Li detector. During EDX Analysis, the specimen is bombarded with an electron beam inside the scanning electron microscope. The bombarding electrons collide with the specimen atoms on electrons, knocking some of them off in the process. A position vacated by an ejected inner shell electron is eventually occupied by a higher-energy electron from an outer shell. To be able to do so, however, the transferring outer electron must give up some of its energy by emitting an X-ray photon. The amount of energy released by the transferring electron depends on which shell it is transferring from, as well as which shell it is transferring to. Furthermore, the atom of every element

releases X-rays with unique amounts of energy during the transferring process. Thus, by measuring the amounts of energy present in the X-rays being released by a specimen during electron beam bombardment, the identity of the atom from which the X-ray was emitted can be established.

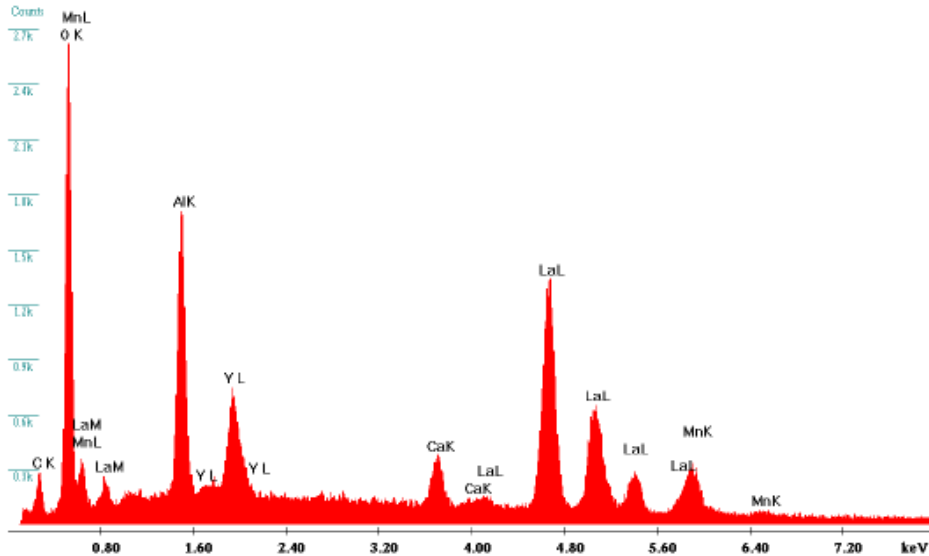


Fig. 3.4: A typical EDX spectrum

The output of an EDX analysis is an EDX spectrum (see Fig. 3.4). The EDX spectrum is just a plot of how frequently an X-ray is received for each energy level. An EDX spectrum normally displays peaks corresponding to the energy levels for which the most X-rays had been received. Each of these peaks are unique to an atom, and therefore corresponds to a single element. The higher a peak in a spectrum, the more concentrated the element is in the specimen.

3.3 Measurement of physical properties

3.3.1 Dielectric measurements

A material is classified as “dielectric” if it has the ability to store energy when an external electric field is applied [6]. The dielectric material increases the storage capacity of the capacitor by neutralizing charges at the electrodes, which ordinarily would contribute to the external field. The capacitance with the dielectric material is related to dielectric constant. If a DC voltage source V is placed across a parallel plate capacitor (Fig. 3.5), more charge is stored when a dielectric material is between the plates than if no material (a vacuum) is between the plates.

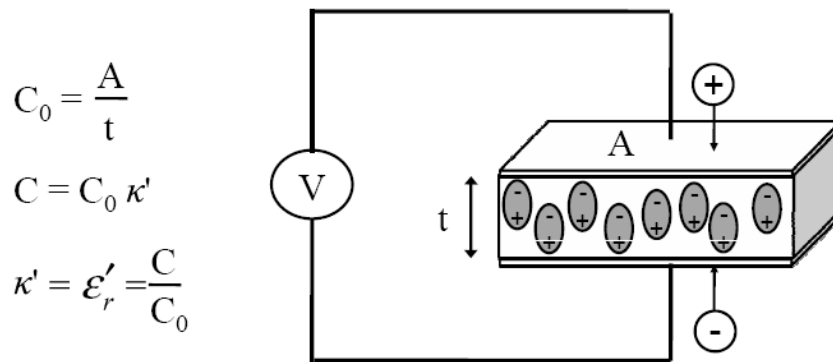


Fig. 3.5: Parallel plate capacitor, DC case

C and C_0 are capacitance with and without dielectric respectively. $\kappa' = \epsilon'_r$ is the real dielectric constant or permittivity and A and t are the area of the capacitor plates and the distance between them (Fig. 3.5). The capacitance of the dielectric material is related to the dielectric constant as indicated in the above equations. If an AC sinusoidal voltage source V is placed across the same capacitor (Fig. 3.6), the resulting current will be made up of a charging current I_c and a loss current I_l that is related to the dielectric constant.

The losses in the material can be represented as a conductance (G) in parallel with a capacitor (C).

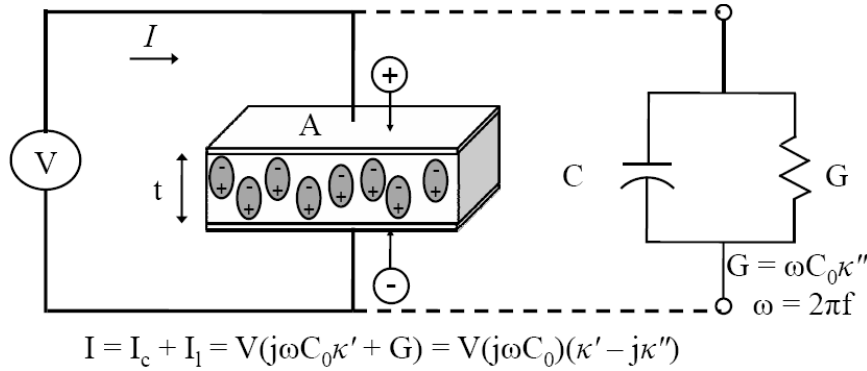


Fig. 3.6: Parallel plate capacitor, AC case

The following notations are used for the complex dielectric constant interchangeably:

$$\kappa = \kappa^* = \epsilon_r = \epsilon_r^* \quad (3.2)$$

From the point of view of electromagnetic theory, the definition of electric displacement (electric flux density) D_f is:

$$D_f = \epsilon E \quad (3.3)$$

where, $\epsilon = \epsilon^* = \epsilon_0 \epsilon_r$ is the absolute permittivity (or permittivity), ϵ_r is the relative permittivity, $\epsilon_0 = (1/36\pi) \times 10^{-9}$ F/m is the free space permittivity and E is the electric field. Permittivity describes the interaction of a material with an electric field, E and is a complex quantity.

$$\kappa = \epsilon / \epsilon_0 = \epsilon_r = \epsilon_r' - j\epsilon_r'' \quad (3.4)$$

Dielectric constant (κ) is equivalent to relative permittivity (ϵ_r) or the absolute permittivity (ϵ) relative to the permittivity of free space (ϵ_0). The real part of permittivity (ϵ_r') is a measure of how much energy from an external electric field is stored in a

material. The imaginary part of permittivity (ϵ_r'') is called the loss factor and is a measure of how dissipative or lossy a material is to an external electric field. The imaginary part of permittivity (ϵ_r'') is always greater than zero and is usually much smaller than (ϵ_r'). The loss factor includes the effects of both dielectric loss and conductivity. When complex permittivity is drawn as a simple vector diagram (Fig. 3.7), the real and imaginary components are 90° out of phase. The vector sum forms an angle δ with the real axis (ϵ_r'). The relative “lossiness” of a material is the ratio of the energy lost to the energy stored.

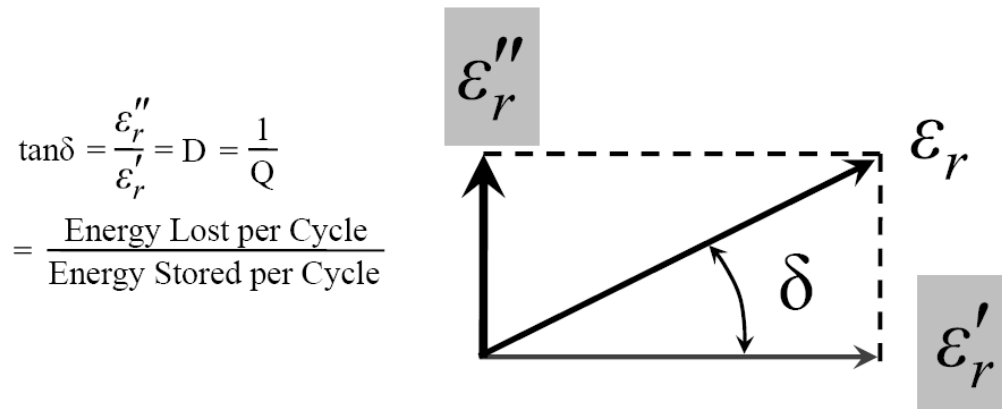


Fig. 3.7: Loss tangent vector diagram

The loss tangent or $\tan\delta$ is defined as the ratio of the imaginary part of the dielectric constant to the real part. D denotes dissipation factor and Q is quality factor. The loss tangent $\tan\delta$ is tangent loss or dissipation factor. Sometimes the term “quality factor or Q-factor” is used with respect to an electronic microwave material, which is the reciprocal of the loss tangent. For very low loss materials, since $\tan\delta = \delta$, the loss tangent can be expressed in angle units, milliradians or microradians.

A material may have several dielectric mechanisms or polarization effects that contribute to its overall permittivity (Fig. 3.8). A dielectric material has an arrangement of electric charge carriers that can be displaced by an electric field. The charges become polarized to compensate for the electric field such that the positive and negative charges move in opposite directions.

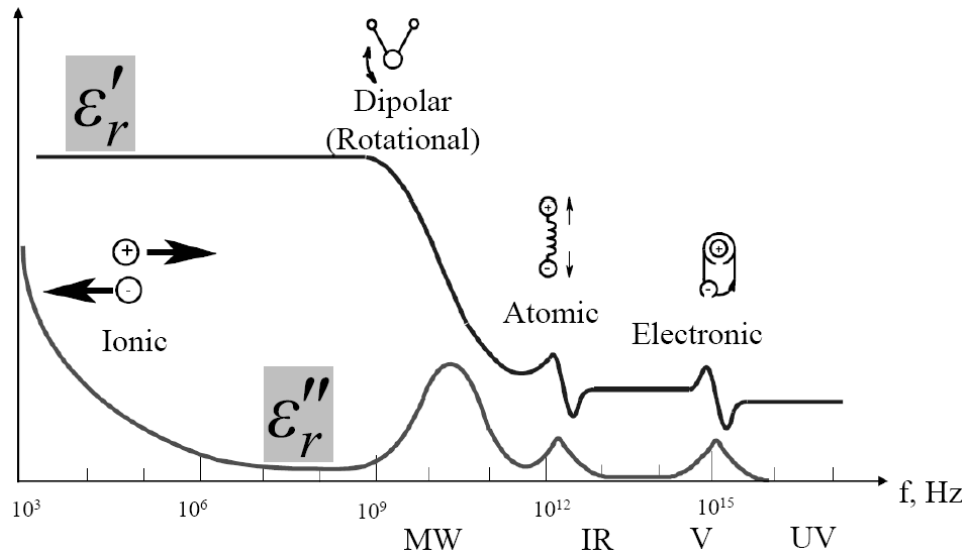


Fig. 3.8: Frequency response of dielectric mechanisms

At the microscopic level, several dielectric mechanisms can contribute to dielectric behavior. Dipole orientation and ionic conduction interact strongly at microwave frequencies. Water molecules, for example, are permanent dipoles, which rotate to follow an alternating electric field. These mechanisms are quite lossy - which explains why food heats in a microwave oven. Atomic and electronic mechanisms are relatively weak and usually constant over the microwave region. Each dielectric mechanism has a characteristic “cutoff frequency”. As frequency increases, the slow mechanisms drop out in turn, leaving the faster ones to contribute to ϵ_r' . The loss factor (ϵ_r'') will correspondingly peak at each critical frequency. The magnitude and cutoff frequency of

each mechanism is unique for different materials. Water has a strong dipolar effect at low frequencies - but its dielectric constant rolls off dramatically around 22 GHz. Teflon, on the other hand, has no dipolar mechanisms and its permittivity is remarkably constant well into the millimeter-wave region. A resonant effect is usually associated with electronic or atomic polarization. A relaxation effect is usually associated with orientation polarization.

For dielectric measurements, disc-shaped pellets were polished using emery paper. The pellets are then boiled in acetone and ultrasonically agitated for 5 minutes for a number of times. On these cleaned pellets, gold (200 nm) was sputtered on both sides in argon atmosphere to form a capacitor. The samples were, then, heated for 2 hours at 300 °C at a heating rate of 2 °C/min. The electrodes were made using copper wire and silver paste on these pellets. Dielectric measurements were carried out on such samples with a Precision Impedance Analyser (Agilent 4294 A).

Frequency Analysis:

The frequency domain measurements of the samples were carried out using the Precision Impedance Analyser (Agilent 4294 A). The instrument is interfaced to a computer for precise data acquisition. Frequency analysis was carried out in the range of 100 Hz - 1 MHz. The interference of the parasitic capacitance from the wire probe stations etc. were nullified using the calibration process. The sample in the form of a capacitor was connected in parallel with the impedance network inbuilt in the impedance analyzer and the variation in the effective impedance of the network was measured. Various other electrical parameters such as impedance, conductance, capacitance and

$\tan\delta$ etc. were also measured. The interface software Test point used for data acquisition is programmed in such a way that various measurement parameters like the amplitude of the applied signal, frequency range, background DC field etc. can be varied.

3.3.2 Ferroelectric hysteresis

Ferroelectric hysteresis is a measure of polarization induced due to the applied electric field. The hysteresis measurement is the most general and common tool for characterizing a ferroelectric sample [7].

The ferroelectric measurements of this thesis work have been carried out using Radiant Technologies Precision Workstation instrument. In this measurement, a voltage waveform is applied to the sample in a series of voltage steps. At each voltage step, the current induced in the sample by the voltage step is integrated and the integral value is captured and converted into polarization ($\mu\text{C}/\text{cm}^2$)

$$\frac{\mu\text{C}}{\text{cm}^2} = \frac{Q}{\text{Area}} = \frac{CV}{\text{Area}} = \frac{\text{Integrator Volts} \times \text{Sense Capacitor}}{\text{Sample Area}} \quad (3.5)$$

The voltage waveform is normally a standard bipolar triangular waveform that can be simply defined by providing the maximum voltage and the entire duration of the waveform in milliseconds. The sign of the voltage indicates the direction of the first leg of the waveform. The number of points is controlled primarily by the duration of the waveform, though it may also be adjusted by the voltage. The software automatically computes the number of points and provides the maximum number possible for the conditions specified. The waveform begins at 0 V and steps to a maximum value of the assigned voltage. It, then, proceeds to step to the negative of the assigned maximum.

Finally, it steps back to 0 V. A DC bias level may be assigned that will allow the entire waveform to be shifted from 0 V symmetry without losing the waveform symmetry. Note that care must be taken that at no time do the combination of the DC bias level and the step voltage exceed the capabilities of the Precision hardware configuration.

3.3.3 DC magnetic measurements

Various magnetometers have been devised to study magnetic materials. Vibrating sample magnetometer (VSM) is one among the instruments that are used relatively widespread for magnetic measurements. Since its invention forty years ago, it has become the workhorse in both laboratory and production environments for measuring the basic magnetic properties of materials as a function of magnetic field and temperature. Computer control and automation was introduced to the VSM two decades ago, but otherwise there have been no major advancements in performance until quite recently.

The VSM employs an electromagnet which provides the magnetizing field (DC), a vibrator mechanism to vibrate the sample in the magnetic field and detection coils which generate the signal voltage due to the changing flux emanating from the vibrating sample. The output measurement displays the magnetic moment M as a function of the field H . The magnetic field is usually generated by an electromagnet driven by a DC bipolar power supply. If extremely high magnetic fields are required (> 3 T), the electromagnet is replaced by a superconducting solenoid [8]. The voltage V measured across the sensing coils in a VSM can be expressed as the product of four contributing sources:

$$V = M \times A \times F \times S \quad (3.6)$$

where,

M = magnetic moment of the sample,

A = amplitude of vibration,

F = frequency of vibration and

S = sensitivity function of the sensing coils.

The magnetic measurements of this thesis work were carried out using a vibrating sample magnetometer in a Physical Property Measurement System (PPMS) of Quantum Design, USA. For the magnetic measurements in the PPMS, the samples are fixed to a quartz sample holder using low magnetic Brown Tape. The temperature dependence of the zero-field-cooled (ZFC) and field-cooled (FC) magnetization was measured in different applied magnetic fields. Hysteresis loops were recorded at different temperatures in the low temperature phases of the system. In the temperature dependent ZFC magnetization, the sample was cooled to lowest temperature in the absence of field, then the field was applied at the lowest temperature and the data were recorded on re-heating the sample. In the FC measurements, the sample was cooled in the applied field to lowest temperature and the data were recorded on re-heating the sample, keeping the field applied.

3.3.4 Magneto-dielectric Measurements

Magneto-dielectric measurements were carried out using a cryo-cooled closed cycle superconducting magnet capable of attaining a maximum field of 14 Tesla. The magnet consists of a single coil made from reacted multifilamentary Nb₃Sn wound on a stainless steel former and cast in epoxy resin to eliminate wire movement during

energisation. The coil is supplied with a superconducting persistent mode switch to connect in parallel across the whole magnet and wired to the main input/output current terminals. Resistive heaters wound into the the switch enable the switch to be either resistive or superconducting. The leads are of 2223 bismuth strontium calcium cuprate high temperature superconductor ($\text{Bi}_2\text{Sr}_2\text{Ca}_2\text{Cu}_3\text{O}_{10}$). The magnet can achieve a field up to 14 Tesla and consists of a room-temperature bore of 52 mm to carry out magneto-dielectric and other measurements from 20 to 350 K. Also, there is an optical window to carry out measurements under illumination with appropriate radiation.

In order to investigate the magnetoelectric coupling in these materials their dielectric responses were measured under different magnetic fields in the temperature range of 50 K – 300 K. The samples were mounted in a custom made sample holder. For the magneto-dielectric measurements the shielded two terminal cable configuration is used to connect the sample holder to HP 4294A Impedance analyzer. The sample holder is inserted in a 14 T cryo-cooled refrigeration system. In the present case the experiments were performed with a maximum magnetic field strength of 3.3 T. During the experiments the samples were cooled to 50 K and the dielectric properties were measured while warming up the samples with a rate of 1 °C per minute. At every temperature the samples were stabilized before recording the dielectric response in order to avoid any experimental artifact. Similarly, the dielectric responses were measured at several time intervals before and after applying the magnetic field to ensure that the observed response is originated from the application of the magnetic field and not from any possible temperature fluctuation that might be associated with increasing the magnetic field.

3.3.5 Heat Capacity measurement

Heat capacity (C_p) is the measure of heat energy required to increase the temperature of an object by 1 °C [8]. It is an extensive property because its value is proportional to the amount of material in the object; for example a bathtub of water has a greater heat capacity than a cup of water. Heat capacity is usually expressed in units of J/K. Heat capacity measurements of this thesis work were carried out using Physical Property Measurement System (Quantum Design, USA). The Quantum Design Heat Capacity measures the heat capacity at constant pressure,

$$C_p = (dQ/ dT)_p \quad (3.7)$$

As with other techniques for measuring heat capacity, the Quantum Design Heat capacity option controls the heat added to and removed from a sample while monitoring the resultant change in temperature. During a measurement, a known amount of heat is applied at constant power for a fixed time and then this heating period is followed by a cooling period of the same duration.

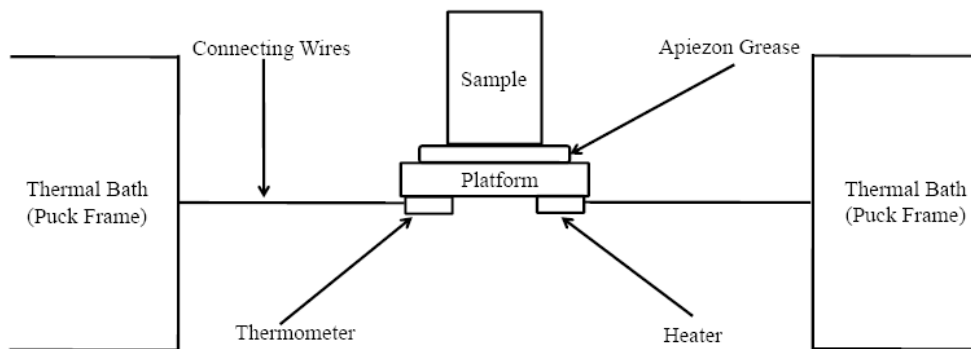


Fig. 3.9: Thermal connections to sample and sample platform in the heat capacity measurement

In the heat capacity measurement puck, a platform heater and platform thermometer are attached to the bottom side of the sample platform (Fig. 3.9). Small wires provide the electrical connection to the platform heater and platform thermometer and also provide the thermal connection and structural support for the platform. The sample is mounted to the platform by using a thin layer of apiezon grease, which provides the required thermal contact to the platform. Sufficient vacuum is created so that thermal conductance between the sample platform and the thermal bath is totally dominated by the conductance of the wires. This gives a reproducible heat link to the bath with a corresponding time constant large enough to allow both the platform and sample to achieve sufficient thermal equilibrium during the measurement.

Different measurement techniques [9] are optimized for different sample sizes and accuracy requirements. The Quantum Design Heat Capacity option uses a relaxation technique that combines the best measurement accuracy with robust analysis techniques. After each measurement cycle (which is a heating period followed by a cooling period), the heat capacity option fits the entire temperature response of the sample platform to a model that accounts for both the thermal relaxation of the sample platform to the bath temperature and the relaxation between the platform and the sample itself [10]. The effect of the relaxation between the sample platform and sample must be considered when the thermal connection shared by the sample and platform is poor. By modeling this effect, the software can report the correct heat capacity values despite such poor contact.

3.3.6 Non-linear optical experiments

Nonlinear optics describes the behavior of light in nonlinear media, that is, media in which the dielectric polarization P responds nonlinearly to the electric field E of the light. This nonlinearity is typically only observed at very high light intensities such as those provided by pulsed lasers. Second harmonic generation (SHG); also called frequency doubling is a nonlinear optical process, in which photons interacting with a nonlinear material are effectively combined to form new photons with twice the energy, and therefore twice the frequency and half the wavelength of the initial photons. Second harmonic generation occurs in two types. In one type, two photons having ordinary polarization while in the other orthogonal polarizations with respect to the crystal will combine to form one photon with double the frequency and extraordinary polarization. For a given crystal orientation, only one of these types of SHG occurs.

A number of nonlinear optical phenomena can be described as frequency-mixing processes. If the induced dipole moments of the material respond instantaneously to an applied electric field, the dielectric polarization (dipole moment per unit volume) $P(t)$ at time t in a medium can be written as a power series in the electrical field:

$$P(t) \propto \chi^{(1)} E(t) + \chi^{(2)} E^2(t) + \chi^{(3)} E^3(t) + \dots \quad (3.8)$$

Here, the coefficients $\chi^{(n)}$ are the n^{th} order susceptibilities of the medium. For any three-wave mixing process, the second-order term is crucial; it is only nonzero in media that have no inversion symmetry.

We have measured second order nonlinear optical intensity relative to quartz (Kurtz powder test) by employing a pulsed Q-switched Nd:YAG laser at a wavelength of 1064 nm. The pulse width of the laser is 8 ns and the repetition rate was 10 Hz. The backward scattered SHG light was collected using a spherical concave mirror and passed through a Czerny-Turner monochromator which transmits only 532 nm radiation.

3.3.7 Raman spectroscopy

Infrared (IR) and Raman spectroscopy are spectroscopic tools used in identifying the characteristic vibrational modes of the samples. In general atoms are known to vibrate in solids at frequencies of approximately 10^{12} to 10^{13} Hz. The vibrational modes, involving pairs or groups of bonded atoms, can be excited to higher energy states by absorption of radiation of appropriate frequency.

Raman spectroscopy is a spectroscopic technique used in condensed matter physics and chemistry to study vibrational, rotational and other low-frequency modes in a system. It relies on inelastic scattering or Raman scattering of monochromatic light, usually from a laser in the visible, near infrared or near ultraviolet range. The laser light interacts with phonons or other excitations in the system, resulting in the energy of the laser photons being shifted up or down. The shift in energy gives information about the phonon modes in the system. Infrared spectroscopy yields similar, but complementary information. Typically a sample is illuminated with a laser beam and the light from the illuminated spot is collected with a lens and sent through a monochromator. Wavelengths close to the laser line, due to elastic Rayleigh scattering, are filtered out while the rest of

the collected light is dispersed onto a detector. The Raman effect occurs when light impinges upon a molecule and interacts with the electron cloud of the bonds of that molecule. The incident photon excites one of the electrons into a virtual state. For the spontaneous Raman effect, the molecule will be excited from the ground state to a virtual energy state and relax into a vibrational excited state, which generates Stokes Raman scattering. If the molecule was already in an elevated vibrational energy state, the Raman scattering is then called anti-Stokes Raman scattering. A molecular polarizability change or amount of deformation of the electron cloud with respect to the vibrational coordinate is required for the molecule to exhibit the Raman effect. The amount of the polarizability change will determine the Raman scattering intensity, whereas the Raman shift is equal to the vibrational level that is involved.

3.3.8 Differential Thermal Analysis

Differential Thermal Analysis is a technique in which the temperature of a sample is compared with that of an inert reference material (Al_2O_3 in our measurements) during a programmed change of temperature [1]. The temperature of sample and reference should be the same until some thermal event, such as melting, decomposition or change in crystal structure occurs in the sample, in which case, the sample temperature either lags behind (if the change is endothermic) or leads (if the change is exothermic) the reference temperature. Polymorphic phase transitions may be studied easily and accurately by DTA. Since many physical or chemical properties of a particular sample may be modified or changed completely as a consequence of a phase transition, their study is extremely important. For example, it may be desired to prevent a transition from occurring in a

particular material or to modify the temperature at which the transition occurs. Instead of designing or looking for completely new materials it is often better to modify the properties of existing materials by the formation of solid solutions with certain additives. Phase transition temperatures often vary greatly with solid solution composition and hence DTA may provide a sensitive monitor of both the property and the composition of the material.

Examples are:

(a) Ferroelectric BaTiO_3 has a Curie temperature of $\sim 120^\circ\text{C}$ which may be determined by DTA; substitution of other ions for Ba^{2+} or Ti^{4+} causes the Curie temperature to vary.

(b) In refractories, transitions such as $\alpha \leftrightarrow \beta$ quartz or quartz \leftrightarrow cristobalite have a deleterious effect on silica refractories because volume changes associated with each transition reduce the mechanical strength of the refractory. These transitions, which should be prevented from occurring if possible, may be monitored by DTA.

Bibliography

1. A.R. West, Solid state chemistry and its applications. Wiley, Singapore, (1984).
2. B. Raveau, The perovskite history: More than 60 years of research from the discovery of ferroelectricity to colossal magnetoresistance via high T_C superconductivity, Prog. Solid State Chem. 35, 171 (2007)
3. B.D. Cullity, Elements of x-ray diffraction. Addison-Wesley, (1978).
4. M.H. Loretto, Electron beam analysis of materials. Chapman and Hall, New York, (1984).
5. J.I. Goldstein, and H. Yakowitz, Practical scanning electron microscopy, Plenum Press, New York, (1975).
6. Agilent Technologies, Inc., USA. Agilent basics of measuring the dielectric properties of materials, (2006).
7. Radiant Technologies, Albuquerque, NM 87106. Radiant technologies vision software manual version 3.1.0, (2002).
8. Quantum Design, San Diego, CA 92121, USA. Quantum Design. User manual of the physical property measurement system., 2 edition, (1999).
9. G.R. Stewart, Measurement of low-temperature specific heat, Rev. Sci. Instrum. **54**(1), 1 (1983).
10. J.S. Hwang, K.J. Lin, and C. Tien, Measurement of heat capacity by fitting the whole temperature response of a heat-pulse calorimeter, Rev. Sci. Instrum. **68**(1), 94 (1997).

4. RESULTS AND DISCUSSION

4.1 Studies of multiferroic nature of the manganites of YMnO_3

family

Summary*

Measurements of magnetic and dielectric properties of single crystalline ErMnO_3 establish the Néel and ferroelectric transition temperatures to be 77 K and 588 K respectively. The dielectric constant of ErMnO_3 shows an anomalous jump at T_N . At higher temperatures, the dielectric constant undergoes a significant decrease on application of magnetic fields. The study clearly exhibits multiferroic and magnetoelectric nature of ErMnO_3 . Similarly, magnetic and dielectric measurements on LuMnO_3 confirm its multiferroic nature. Raman Spectra of LuMnO_3 have been recorded in the 77 K - 800 K range covering both the antiferromagnetic transition at 90 K and the ferroelectric-paraelectric transition at 750 K. The changes in the phonon modes frequencies and band-widths indicate the presence of phonon-spin coupling in the antiferromagnetically ordered phase. The ferroelectric-paraelectric transition is accompanied by the broadening and disappearance of many of the phonon modes. Some of the phonon modes also show anomalies at the ferroelectric transition.

* Papers based on this study have appeared in *Materials Research Bulletin* (2009), *Solid State Sciences* (2009)

4.1.1 Single crystal studies of ErMnO_3

In order to determine the growth axis of the single crystals of ErMnO_3 , crystals were cut on both sides perpendicular to the length. The XRD pattern showed the (3 1 6) plane to be perpendicular to the growth direction (Fig. 4.1). The growth axis is [3 2 1] which subtends an angle of 52.32° with the c-axis. The parallel cut corresponds to the plane perpendicular to (3 1 6) plane, the crystallographic direction being [2 0 -1].

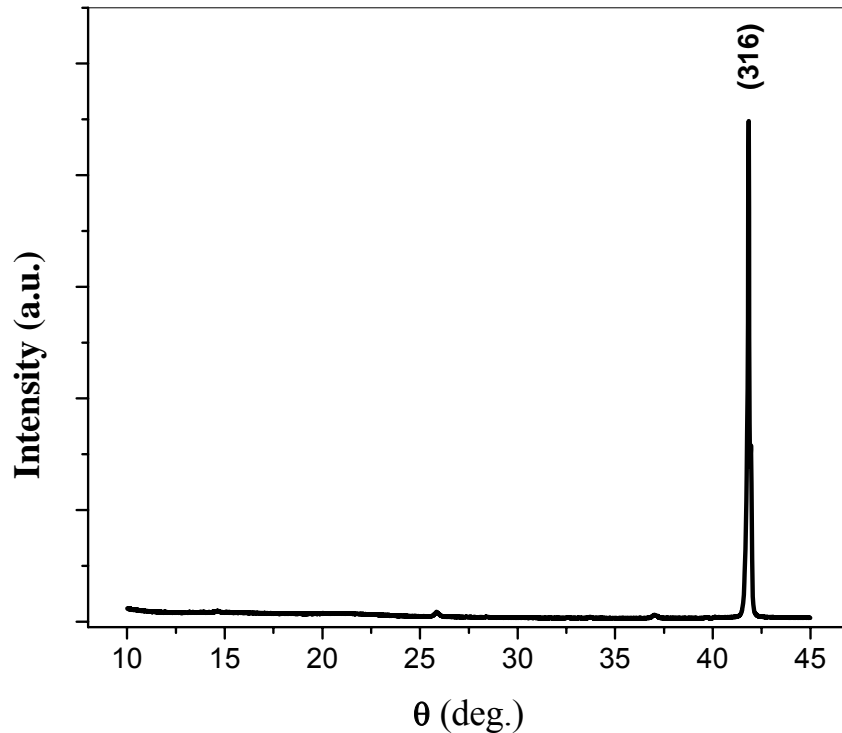


Fig. 4.1: XRD pattern of the ErMnO_3 single crystal

The powder of ErMnO_3 crushed from the single crystals gave an XRD pattern consistent with the $P6_3cm$ space group ($a = b = 6.1110 \text{ \AA}$, $c = 11.4029 \text{ \AA}$) [1]. DC magnetic susceptibility measurements showed only a weak anomaly at the Néel

temperature. The magnetic susceptibility data indicating AFM transition at 77 K agrees well with the neutron diffraction, thermal expansion and other measurements reported by Park et al. [2]. The derivative of the reciprocal of susceptibility clearly shows a peak at 77 K as can be seen from the inset in Fig. 4.2(a). As we do not see a distinct magnetic transition at the Néel temperature in the susceptibility data, we measured the specific heat capacity from 2 K to 160 K.

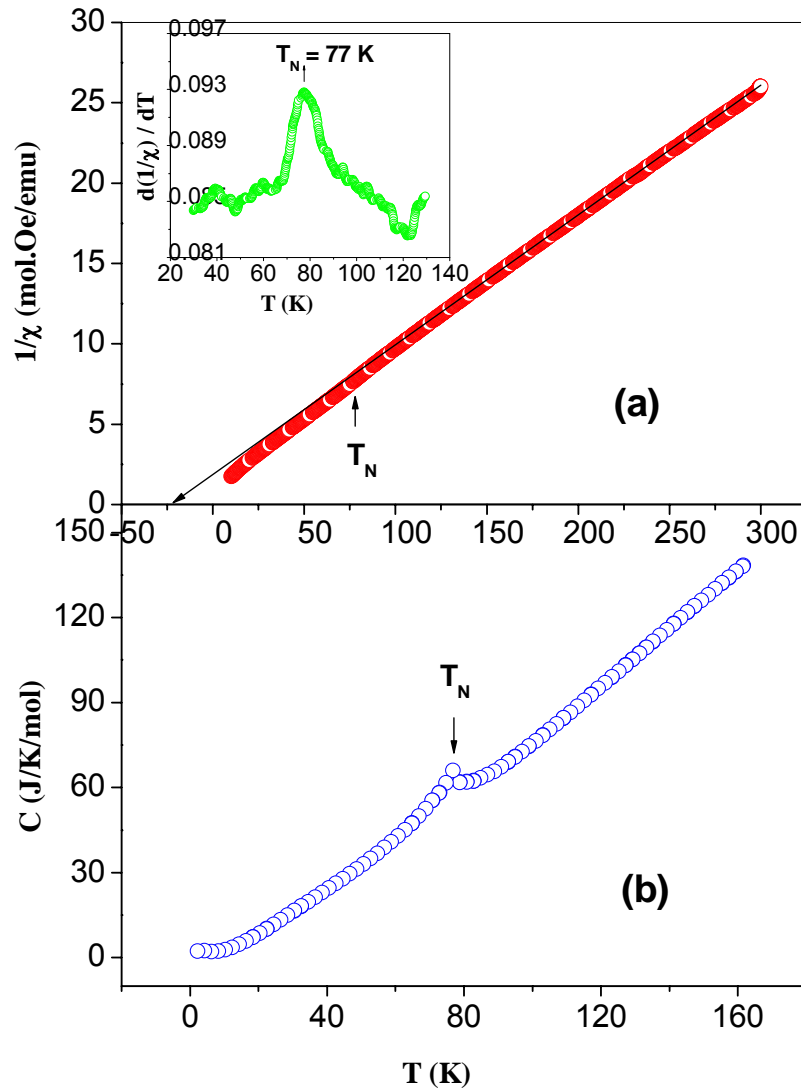


Fig. 4.2: Temperature variation of (a) reciprocal dc magnetic susceptibility and (b) specific heat of ErMnO₃ showing the antiferromagnetic transition temperature (T_N). Inset in (a) shows a plot of the derivative of reciprocal of magnetic susceptibility against temperature.

The data shown in Fig. 4.2(b) show a clear peak at 77 K indicating the onset of magnetic ordering. Below ~ 4 K, we observe a rise in heat capacity, probably due to the Er^{3+} moment ordering as reported earlier [3]. The magnetic susceptibility follows the Curie-Weiss law with a Curie-Weiss temperature (θ_{cw}) of 20 K and an effective magnetic moment, μ_{eff} , of $9.9 \mu_{\text{B}}$. This value of μ_{eff} is consistent with the theoretical value of $10.7 \mu_{\text{B}}$ calculated as $\mu_{\text{eff}} = [\mu_{\text{Er}}^2 + \mu_{\text{Mn}}^2]^{1/2}$, where μ_{Er} ($9.6 \mu_{\text{B}}$) and μ_{Mn} ($4.9 \mu_{\text{B}}$) are the effective magnetic moments of Er^{3+} and Mn^{3+} respectively. The ratio $f = \theta_{\text{cw}}/T_{\text{N}}$ which is a measure of geometric frustration [4] is around 10 for YMnO_3 . It is significantly reduced in ErMnO_3 .

We have measured the high temperature dielectric properties of ErMnO_3 along both the $[3\ 2\ 1]$ and $[2\ 0\ -1]$ directions of the crystal. The dielectric constant was recorded at various temperatures over a frequency of 100 Hz – 1 MHz range. In Fig. 4.3, the dielectric constant is plotted as a function of temperature at different frequencies. The curves are characterized by a maximum for each frequency, the maximum being broader for crystals along the $[2\ 0\ -1]$ direction compared to the $[3\ 2\ 1]$ direction. The maximum values of the dielectric constant observed at 100 kHz along the $[2\ 0\ -1]$ and $[3\ 2\ 1]$ directions are 157 and 312 respectively. The temperature corresponding to the maximum of the dielectric constant, T_{max} , shifts towards higher temperature with increase in frequency. In order to obtain the frequency-independent ferroelectric transition temperature (T_{FE}) below which frequency dispersion is appreciable [5], we have used the Curie – Weiss plots wherein the reciprocal of dielectric constant is plotted against

temperature. From these plots, we derive a T_{FE} of 590 K and 586 K for ErMnO_3 along the $[2\ 0\ -1]$ and $[3\ 2\ 1]$ directions respectively.

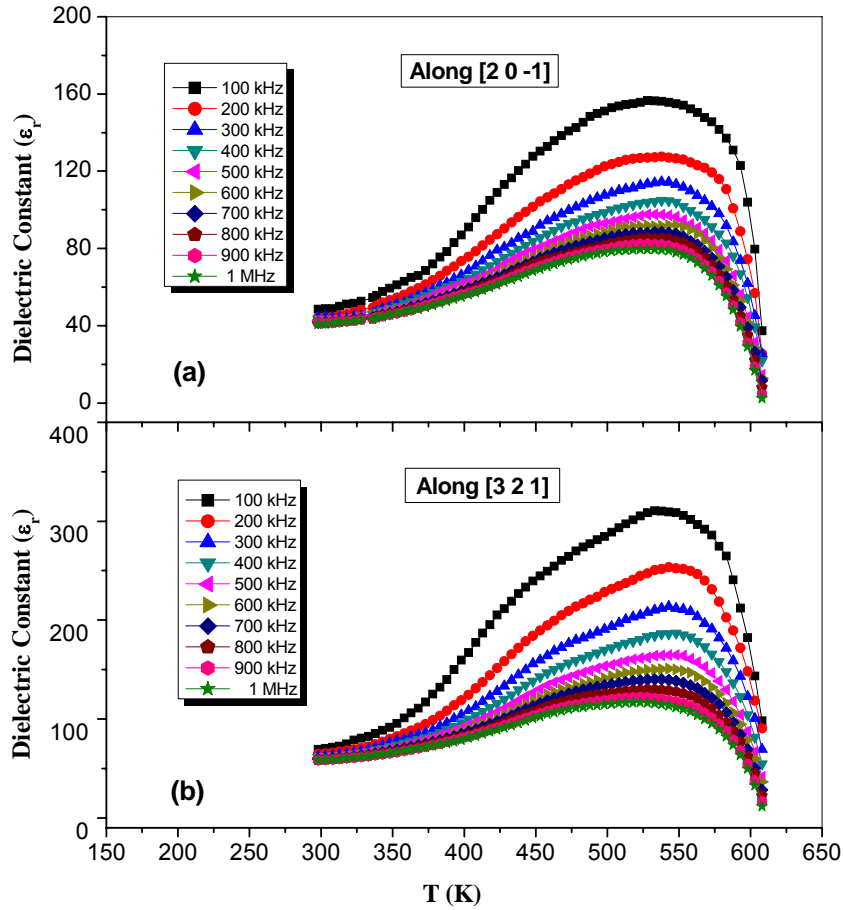


Fig. 4.3: Temperature dependence of the dielectric constant of ErMnO_3 over the 100 Hz – 1 MHz range along (a) $[2\ 0\ -1]$ and (b) $[3\ 2\ 1]$ directions of the crystal showing the ferroelectric transition.

In order to confirm the ferroelectric nature of ErMnO_3 , we carried out $P \sim E$ hysteresis measurements for both the crystal orientations at different voltages. We obtain hysteresis loops (Fig. 4.4) which do not exhibit saturation of polarization, indicating ErMnO_3 to be a leaky ferroelectric material [6]. Along the $[2\ 0\ -1]$ direction, the remnant polarization and coercive field are around $0.38\ \mu\text{C}/\text{cm}^2$ and $12\ \text{kV}/\text{cm}$ respectively at a frequency of 5 kHz at room temperature, corresponding to an applied voltage of 1600 V.

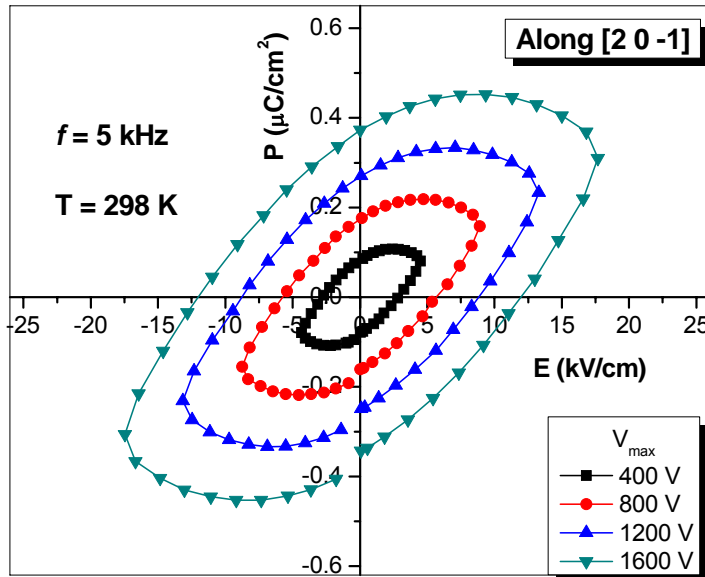


Fig. 4.4: Room temperature ferroelectric hysteresis loops ($P \sim E$ plots) along the $[2\ 0\ -1]$ direction at 5 kHz for various voltages.

We have investigated the dependence of the dielectric constant of ErMnO_3 at low temperatures with and without the application of magnetic fields. Figures 4.5 (a) and (b) show the plots of dielectric constant at 200 kHz for crystals along the $[2\ 0\ -1]$ and $[3\ 2\ 1]$ directions. In both the cases, there is a notable increase in the dielectric constant with the increase in temperature. Beyond ~ 250 K, the increase is significantly more rapid in the $[2\ 0\ -1]$ direction. The value of the dielectric constant at 310 K is 25 and 34 respectively for crystals along $[2\ 0\ -1]$ and $[3\ 2\ 1]$ directions. The most remarkable feature of the measurements in Fig. 4.5 is the anomaly at the Néel temperature (77 K) which establishes the presence of coupling between magnetic and ferroelectric order parameters. In order to illustrate the occurrence of the dielectric anomaly at T_N more prominently, we have plotted the derivative of the dielectric constant against temperature along the $[2\ 0\ -1]$ direction in the inset of Fig. 4.5(a). There are reports in the literature

wherein such an anomaly in the dielectric constant is observed at the magnetic transition in other members of the LnMnO_3 family [7-10].

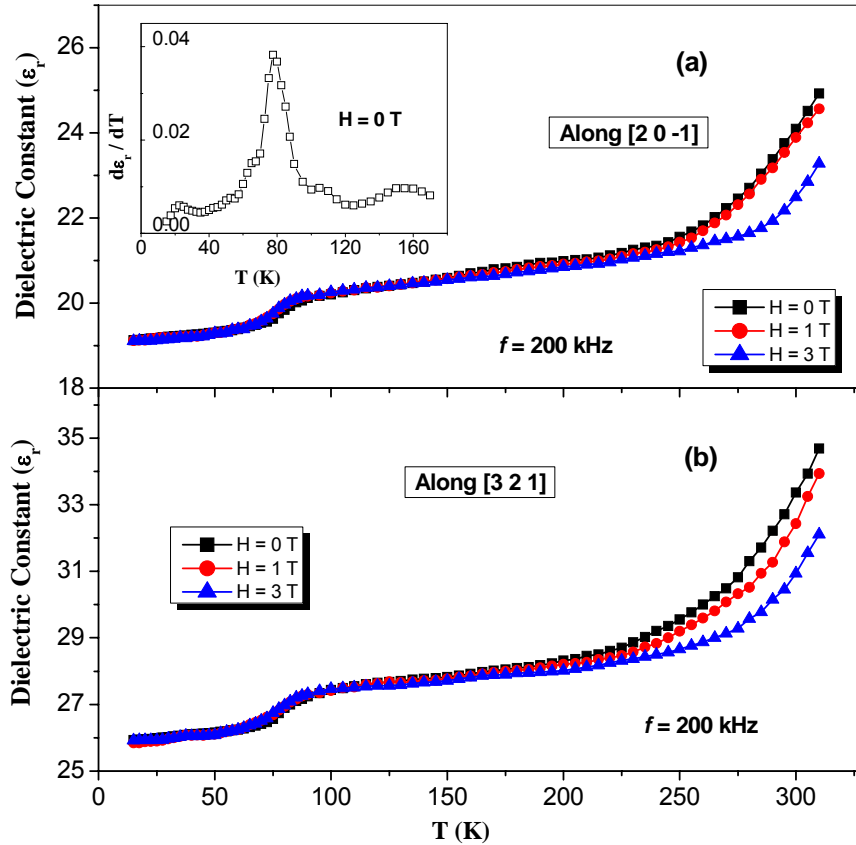


Fig. 4.5: Temperature variation of the dielectric constant at 200 kHz ($T < 300$ K) along the (a) $[2\ 0\ -1]$ and (b) $[3\ 2\ 1]$ directions of the ErMnO_3 crystal with and without the application of magnetic fields (1 T, 3 T). The inset in (a) shows the differential plot of the dielectric constant along the $[2\ 0\ -1]$ direction showing an anomaly at the Néel temperature.

The coupling between the ferroelectric and antiferromagnetic domain walls can be interpreted as a local magnetoelectric effect and is explained microscopically as a piezomagnetic interaction between the domain walls [11]. Hexagonal manganites like ErMnO_3 undergo an isostructural transition at T_N without breaking the $P6_3cm$ symmetry, simultaneously producing giant displacements of every atom in the unit cell [12]. The large magnetoelastic coupling is the origin of the multiferroic phenomenon in ErMnO_3 .

The magnetoelectric effect in ErMnO_3 is also evidenced by the effect of magnetic fields on the dielectric constant at high temperatures. We see from Fig. 4.5 that the response to the application of magnetic field of 1 T is less pronounced in the $[2\ 0\ -1]$ direction as compared to the $[3\ 2\ 1]$ direction. When subjected to a magnetic field of 3 T, it brings about a dramatic impact in the reduction of the dielectric constant.

4.1.2 A Raman study on multiferroic LuMnO₃

The XRD pattern of the sample confirmed the formation of single-phase LuMnO₃ in the hexagonal structure (P6₃cm) in agreement with the literature report ($a=6.039 \text{ \AA}$, $c=11.367 \text{ \AA}$) [13]. Fig. 4.6(a) shows the temperature variation of the zero-field-cooled (ZFC) and the field-cooled (FC) magnetization (at 100 Oe). The material is a canted antiferromagnet below the Néel temperature of 90 K. Previous reports of magnetic measurements [14] on single crystals of LuMnO₃ and thermal conductivity measurements on a polycrystalline sample [15] are in agreement with the present results. We notice a divergence between the FC and ZFC data below the 90 K which is characteristic of frustrated materials [16]. LuMnO₃ appears to be weakly ferromagnetic below 90 K as evidenced by the observation of magnetic hysteresis. The values of the remnant magnetization (M_r) and coercive field (H_c) are 26 emu/mol and 1080 Oe respectively. In Fig. 4.6(b), we show the temperature variation of the dielectric constant of LuMnO₃ at different frequencies. The value of the dielectric constant increases with temperature. Interestingly, the values for high frequencies are high, the curves converging near room temperature. The most notable feature of the dielectric constant plots is the anomaly seen at the Néel temperature (90 K) providing thereby evidence for coupling between magnetic and dipole moments. In order to illustrate the occurrence of the dielectric anomaly at T_N , we have plotted the derivative of the dielectric constant against temperature in the inset of Fig. 4.6(b). This plot shows a sharp peak at 90 K.

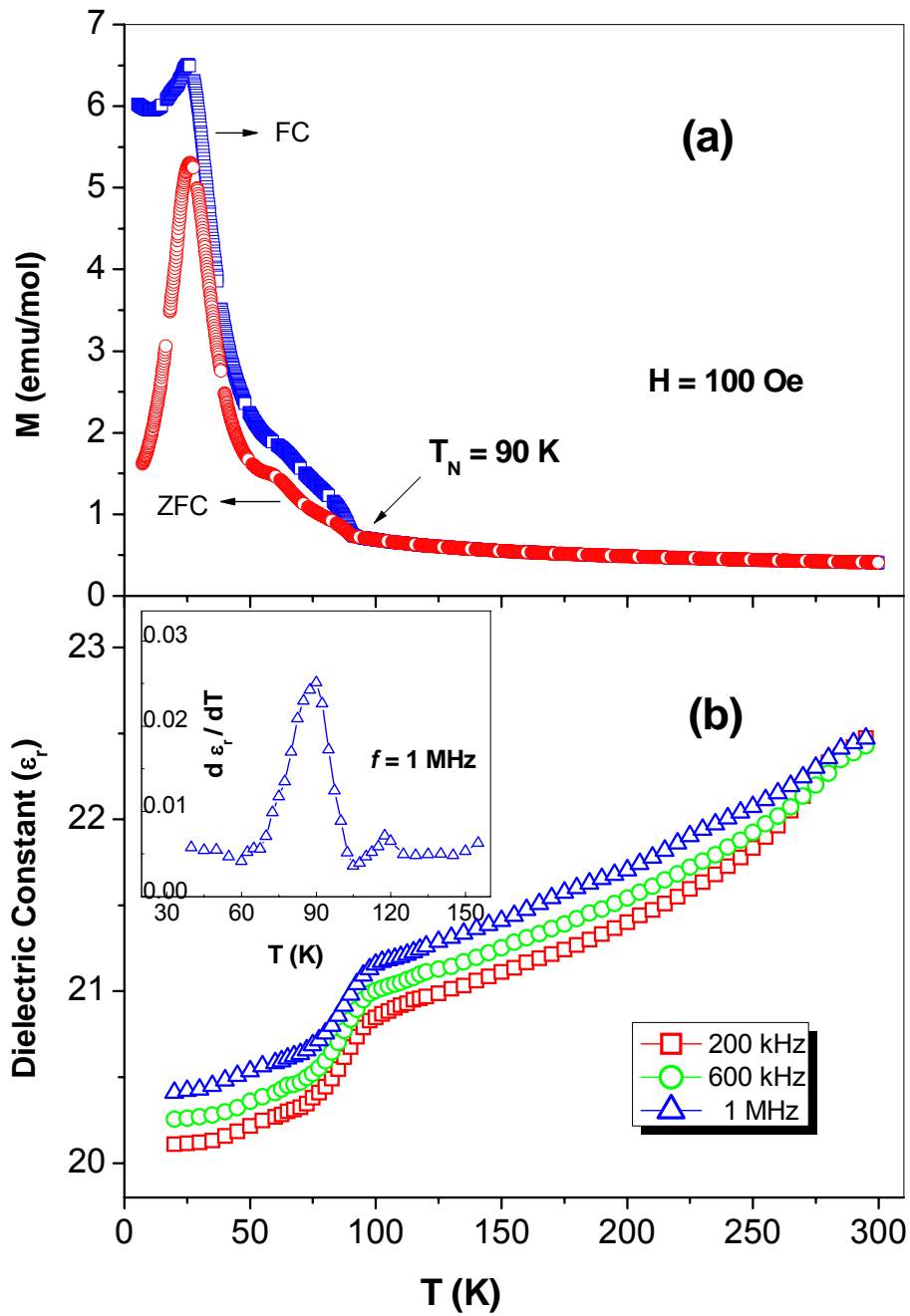


Fig. 4.6: Temperature-variation of (a) the magnetization and (b) the dielectric constant of LuMnO₃ in the low-temperature region. Inset in (b) shows the temperature variation of the derivative of the dielectric constant.

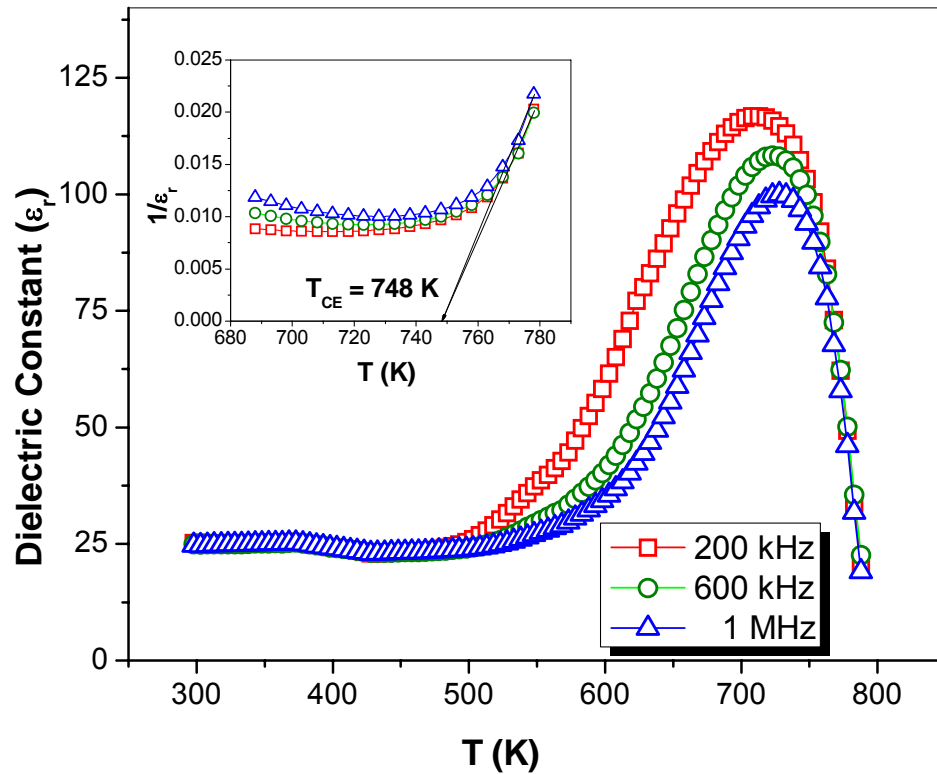


Fig. 4.7: Temperature-variation of the dielectric constant of LuMnO₃ in the 300-800 K region. The inset shows the Curie-Weiss plot.

We have measured the dielectric constant of LuMnO₃ as a function of temperature at various frequencies. The value of the dielectric constant decreases with increase in frequency. We also observe a transition around 740 K characterized by a dielectric constant maximum. We have obtained the ferroelectric transition temperature (T_{FE}) by employing the Curie-Weiss plot wherein the reciprocal of dielectric constant in the high temperature region is plotted against temperature (see inset of Fig. 4.7). The Curie-Weiss plot yields a frequency-independent T_{FE} of 748 K. Below this temperature, the dielectric constants show large dispersion, a behavior commonly observed in relaxor ferroelectrics [17].

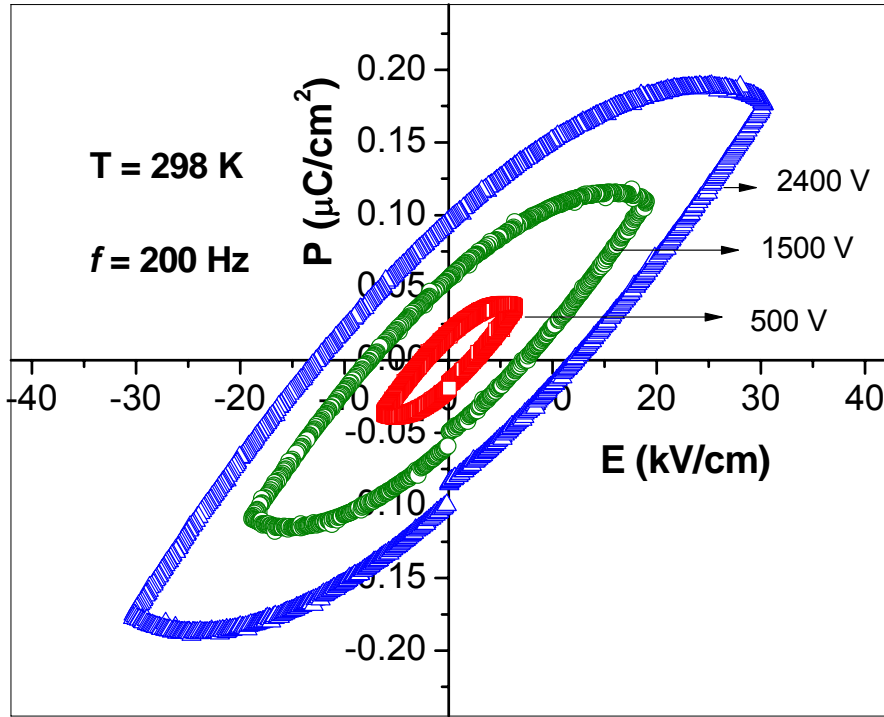


Fig. 4.8: Room temperature ferroelectric hysteresis loops of LuMnO₃ at 200 Hz for different voltages.

We have examined the ferroelectric hysteresis loop of LuMnO₃ at room temperature. In Fig. 4.8, we show the P~E curves at 200 Hz for applied voltages of 500, 1500 and 2400 V. We have not been able to observe saturation in the hysteresis loops due to the leaky nature of the sample. The leakage current in the sample is found to increase with voltage. Thus, at applied voltages of 500 V and 2400 V, the values of leakage current are 3.06×10^{-7} A and 1.31×10^{-5} A respectively corresponding to a sample area of 0.97 cm^2 . The values of maximum polarization, remnant polarization (P_r) and coercive field (E_c) at 2400 V are found to be $0.189 \text{ } \mu\text{C}/\text{cm}^2$, $0.096 \text{ } \mu\text{C}/\text{cm}^2$ and $12.13 \text{ kV}/\text{cm}$ respectively.

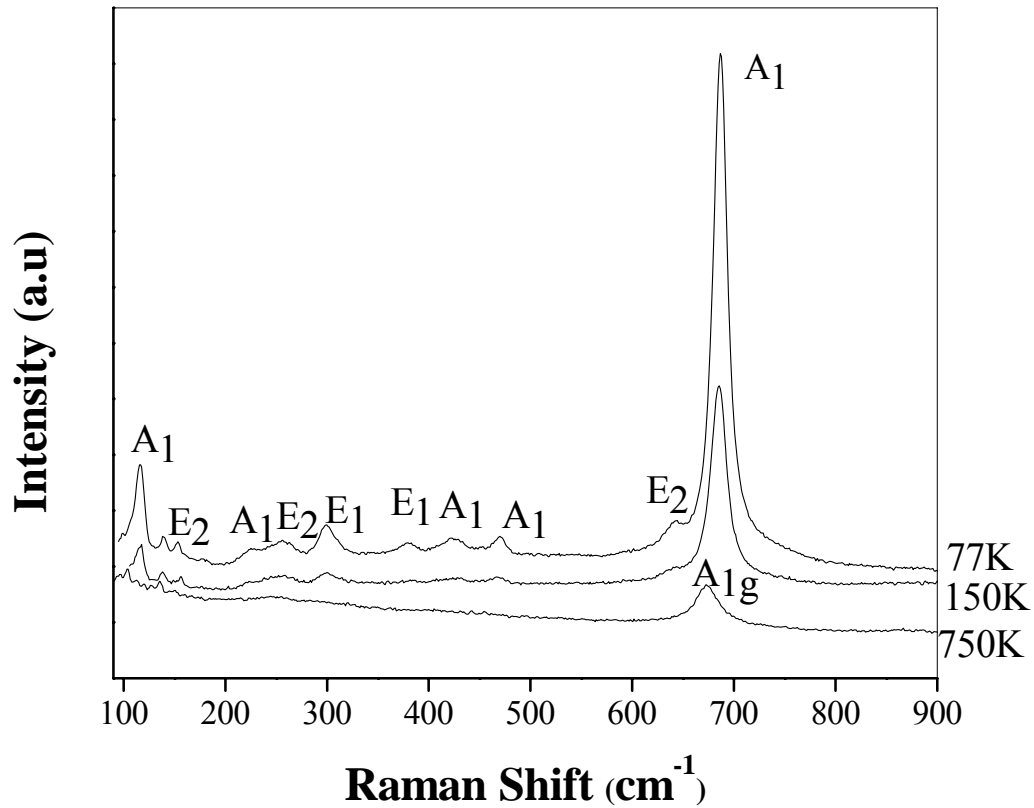


Fig. 4.9: Raman Spectra of LuMnO₃ at different temperatures.

Hexagonal LuMnO₃ in its ferroelectric phase (P6₃cm) contains six formula units and would have 38 Raman-active phonon modes (9A₁+14E₁+15E₂). The paraelectric phase with higher symmetry (P6₃/mmc) would have only two formula units and five phonon modes (A_{1g}+E_{1g}+3E_{2g}). The A₁ and E₁ modes may show LO-TO phonon splitting due to the induced dipole moment. In fig. 4.9, we show the Raman spectra of LuMnO₃ in the 77-750 K range covering both the magnetic and ferroelectric transition regimes.

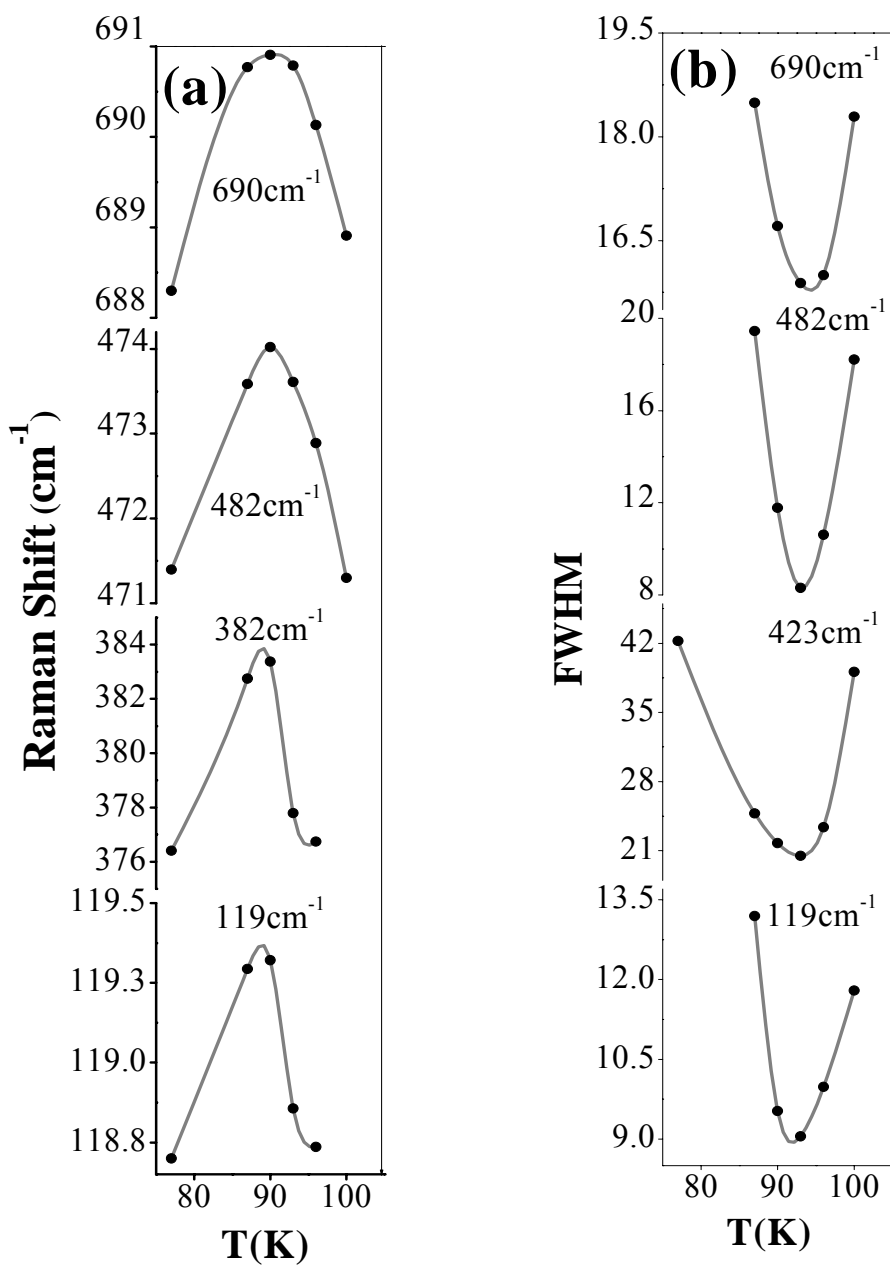


Fig. 4.10: Temperature- variation of (a) the phonon frequencies and (b) the full-widths at half maxima of LuMnO₃ across the Néel temperature (90 K).

We are able to observe close to 20 phonon modes in the ferroelectric phase at 77 K and we have indicated the assignments of some of the Raman bands in fig.4.9. Many of the phonon modes show substantial frequency shifts around 90 K which is the Néel temperature. These modes include those at 690 (A_1), 482 (A_1), 382 (E_1), 226(A_1) and 119(A_1) cm^{-1} . We show typical temperature variations of the phonon mode frequencies in fig. 4.10(a). We clearly see the frequency maxima around 90 K, accompanied by a decrease in the full width at half-maximum (FWHM) of the bands as shown in fig. 4.10(b). This behavior demonstrates the presence of spin-phonon coupling in the antiferromagnetically ordered phase. The low-frequency E_2 and A_1 modes both show anomalies at T_N indicating that the displacements of Mn and oxygen in the c-plane as well as of Lu ions along the c-axis may be involved due to mixing of the phonon modes or complex spin-phonon coupling.

At the high-temperature ferroelectric-paraelectric transition, the Raman bands became broader and fewer. There are significant changes in the phonon mode frequencies in this region as well. Many of them show minima around the ferroelectric transition temperature ($T_{FE} = 750$ K) as can be seen from fig. 4.11. The transition at 750 K is from the non-centrosymmetric $P6_3cm$ phase to the centrosymmetric $P6_3/mmc$ phase. The 682 cm^{-1} (A_1) mode transforms to an A_{1g} mode in the paraelectric phase. The change in this band shown in fig. 4.11 is probably due to such a transformation. The E_1 and E_2 modes in the 300-400 cm^{-1} region transform to the E_{1g} and E_{2g} modes in the paraelectric phase. The A_1 mode at 109 cm^{-1} related to the displacements of the Lu ions disappears in the paraelectric phase. These changes in the Raman Spectra are consistent with the polyhedral tilting mechanism of ferroelectricity in LuMnO_3 .

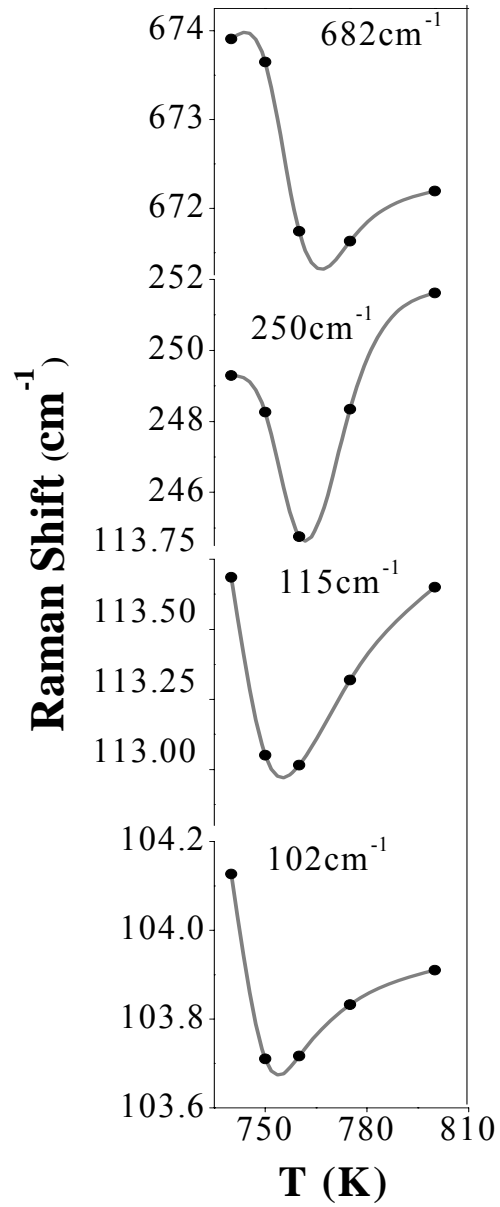


Fig. 4.11: Temperature-variation of the phonon frequencies of LuMnO_3 across the ferroelectric – paraelectric transition.

The Raman spectra of LuMnO₃ show the expected changes from that of YMnO₃ due to mass effect. There is anomalous variation of phonons in YMnO₃ as well, especially in the case of the 160 cm⁻¹ (A₁) phonon [18]. The present study shows a maximum in phonon frequencies at T_N, whereas in case of YMnO₃, sharp changes in the phonon frequencies are observed. At T_{FE}, our data clearly show band softening in the case of LuMnO₃ while in YMnO₃, only a change in slope is observed.

Conclusions

ErMnO₃ exhibits a ferroelectric transition temperature of around 588 K. It is clearly a multiferroic with an antiferromagnetic transition at 77 K (T_N). There is coupling between the electrical and magnetic order parameters since we observe a dielectric anomaly at T_N and magnetic field - induced decrease in the dielectric constant above 250 K. Dielectric and magnetic measurements establish the multiferroic nature of LuMnO₃. Variable temperature Raman spectra show marked changes at the Néel temperature as well as at the ferroelectric-paraelectric transition temperature. The changes in the spectra throw light on the nature of these phase transitions.

4.2 Raman evidence for orbiton-mediated multi-phonon scattering in multiferroic TbMnO₃

Summary*

Temperature-dependent Raman spectra of TbMnO₃ from 5 K to 300 K in the spectral range of 200 to 1525 cm⁻¹ show five first-order Raman allowed modes and two high frequency modes. The intensity ratio of the high frequency Raman band to the corresponding first order Raman mode is nearly constant and high (~ 0.6) at all temperatures, suggesting a orbiton-phonon mixed nature of the high frequency mode. One of the first order phonon modes shows anomalous softening below T_N (~ 46 K), suggesting a strong spin-phonon coupling.

* Paper based on this study has appeared in *J. Phys.: Condens. Matter* (2010)

Raman evidence for orbiton-mediated multiphonon scattering in multiferroic TbMnO₃

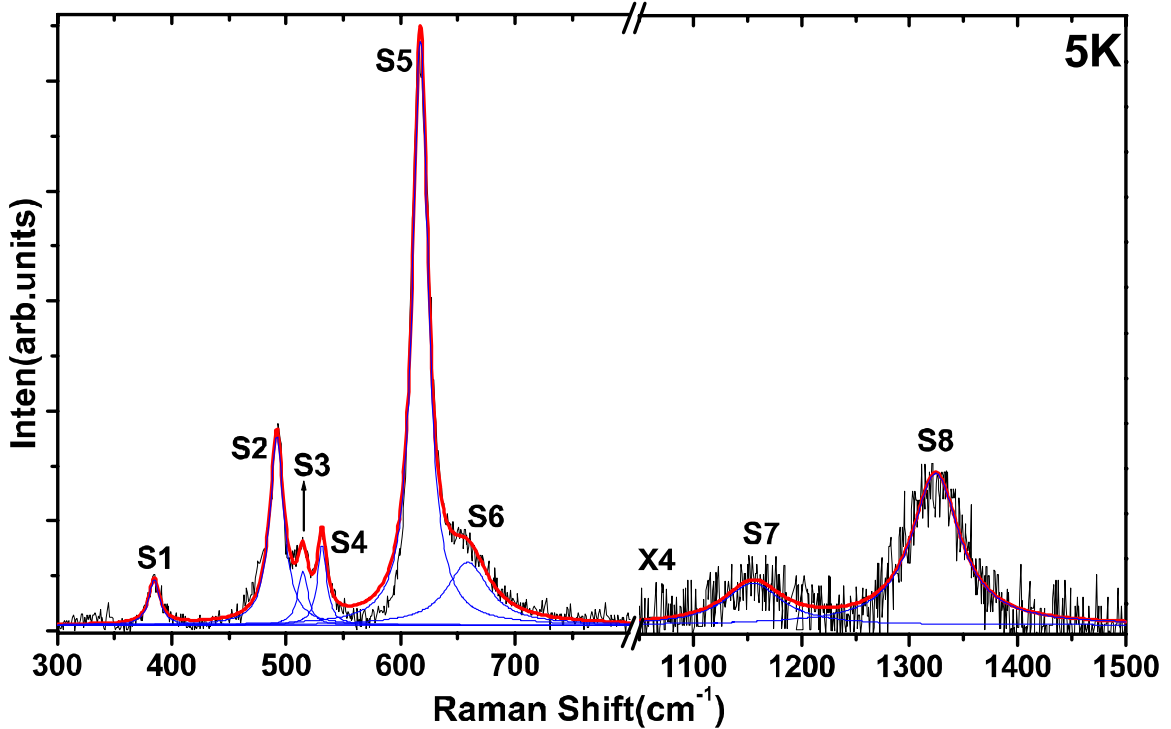


Fig. 4.12: Unpolarised-Raman spectra of TbMnO₃ measured at 5 K. Thick solid line shows the total fit, thin solid line show the individual Lorentzian fit.

Fig. 4.12 shows Raman spectrum at 5 K displaying 8 modes labeled as S1 to S8. The spectra are fitted to a sum of Lorentzian and the frequencies, linewidths and intensities so obtained are shown in Fig. 4.13 for the first order Raman modes and in Fig. 4.14 for the multiphonon modes S7 and S8. TbMnO₃ is orthorhombic (space group Pbnm), with 24 Raman active modes classified as $\Gamma_{\text{Raman}} = 7A_g + 5B_{1g} + 7B_{2g} + 5B_{3g}$ [19]. The assignment of low frequency modes S1- S5, given in Table 4.1, has been done following the work of Iliev et. al for TbMnO₃ [19]. The origin of mode S6 may be similar

to that of the 640 cm^{-1} mode observed in LaMnO_3 [20,21], attributed to the disorder-induced phonon density of states [22,23] or second order Raman scattering [20]. It can also be a disorder-induced infrared active phonon mode (transverse optic mode at 641 cm^{-1} and longitudinal optic mode at 657 cm^{-1}) observed in infrared studies of TbMnO_3 [24].

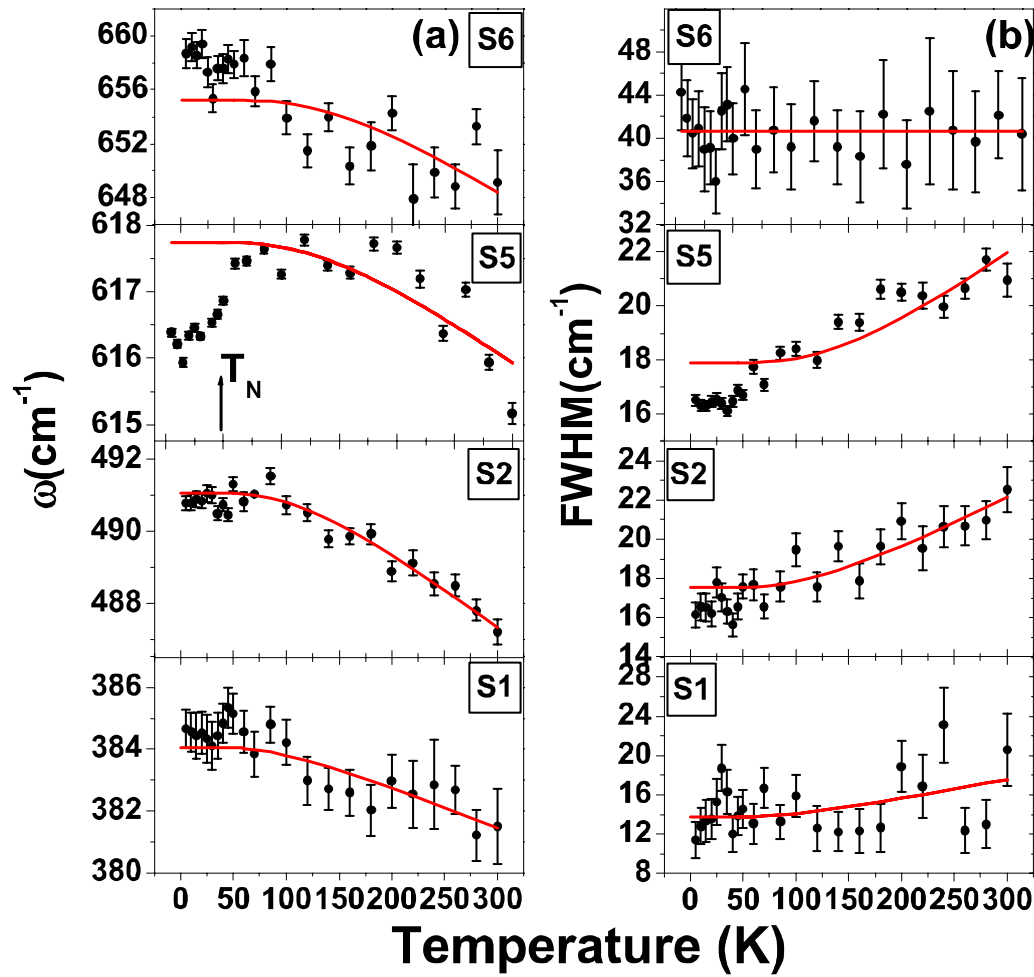


Fig. 4.13: Temperature dependence of the modes S1, S2, S5 and S6. The solid lines are the fitted curve as described in text.

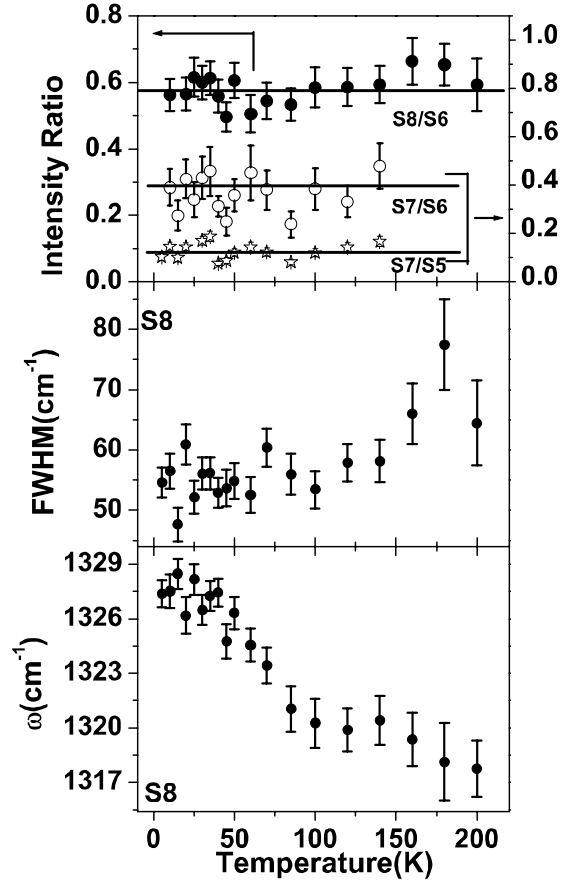


Fig. 4.14: Temperature dependence of the intensity ratio of the mode S8 to S6, S7 to S6 and S7 to S5 (Top Panel). Temperature dependence of the Frequency (Lower Panel) and Linewidth (Middle panel) of mode S8. Solid lines are guide to the eye.

Table 4.1: List of the experimental observed phonons frequencies and fitting parameters of a few phonons, fitted by equation (2) and (3) as described in text. Units are in cm^{-1} .

Assignment	Phonon ω (5 K)	Frequency ω (0)	C	$\Gamma(0)$	A
S1 (A_g)	384.9	386.1 ± 0.6	-4.1 ± 0.8	10.8 ± 2.7	5.9 ± 2.8
S2 (A_g)	491.9	495.3 ± 0.3	-8.5 ± 0.5	12.3 ± 0.9	10.4 ± 1.4
S3 (A_g)	514.5				
S4 (B_{2g})	531.3				
S5 (B_{2g})	616.2	620.8 ± 0.7	-6.2 ± 1.2	10.9 ± 1.2	14.1 ± 2.1
S6	658.4	668.8 ± 4.9	-27.2 ± 8.4	40.6 ± 3.2	0.09
S7 (Second order)	1157.1				
S8 (Overtone)	1327.4				

(A) Temperature dependence of the first order modes

We now discuss the temperature dependence of the modes S1 to S5 and S6. In general, the temperature dependent behavior of a phonon mode of frequency ‘ ω ’ is given as [25].

$$\omega(T) = \omega(0) + (\Delta \omega)_{\text{qh}}(T) + (\Delta \omega)_{\text{anh}}(T) + (\Delta \omega)_{\text{el-ph}}(T) + (\Delta \omega)_{\text{sp-ph}}(T) \quad (1)$$

$(\Delta \omega)_{\text{qh}}(T)$ corresponds to the change in phonon frequency due to a change in the lattice parameters of the unit cell, termed as quasi-harmonic effect. $\Delta \omega_{\text{anh}}(T)$ gives the intrinsic anharmonic contributions to the phonon frequency. The effect of renormalization of the phonon frequency ($(\Delta \omega)_{\text{el-ph}}(T)$) due to electron-phonon coupling is absent in insulating TbMnO₃. The last term, $\Delta \omega_{\text{sp-ph}}(T)$, represents the change in phonon frequency due to spin-phonon coupling, caused by the modulation of the exchange integral by lattice vibrations [25]. The change in phonon frequency of mode “ i ” due to the change in lattice parameters, i.e $(\Delta \omega)_{\text{qh}}(T)$, can be related to the change in volume if we know Grüneisen parameter $\gamma_i = - (B_0/\omega_i)(\partial \omega_i/\partial P)$, where B_0 is the bulk modulus and $\partial \omega_i/\partial P$ is the pressure-derivative of the phonon frequency. For a cubic crystal or isotropically expanded lattice, the change in phonon frequency due to change in volume is given as $(\Delta \omega)_i(T)_{\text{qh}}/\omega_i(0) = - \gamma_i(\Delta V(T)/V(0))$. The Grüneisen parameter calculated for RMnO₃ [R = Sm, Nd and Pr] is ~ 2 [26, 27]. The quasi harmonic contribution in TbMnO₃ can be neglected since the fractional change in volume is negligible [28], as has been done in earlier studies of rare earth manganites RMnO₃ (R = Gd, Eu, Pr, Nd, Sm, Tb, Dy, Ho, and Y) [29, 30].

In a cubic anharmonic process, a phonon of frequency $\omega(\vec{\kappa}=0)$ decays into two phonons $\omega_1(\vec{\kappa}_1)$ and $\omega_2(\vec{\kappa}_2)$, keeping energy and momentum conserved, i.e. $\omega = \omega_1 + \omega_2$, $\vec{\kappa}_1 + \vec{\kappa}_2 = 0$. Considering the simplest decay channel with $\omega_1 = \omega_2$, the temperature dependence of ω (T) and the full width at half maximum (Γ) can be expressed as [31]

$$\omega(T) = \omega(0) + C [1+2n(\omega(0)/2)] \quad (2)$$

$$\Gamma(T) = \Gamma(0) + A [1+2n(\omega(0)/2)] \quad (3)$$

where $n(\omega) = 1/(\exp(\hbar\omega/k_B T) - 1)$ is the Bose–Einstein mean occupation number and C and A are the self-energy parameters for a given phonon mode. We realize that below the phase transition temperature T_N , eqs (2) and (3) are not expected to hold good, as is obvious in the temperature dependence of S5 mode (see Fig. 4.13a). Therefore, we fit the data between 50 K to 300 K using eqs (2) and (3) and the theoretical curves are extrapolated below 50 K using the fitted parameters given in Table I (see solid lines in Fig. 4.13). Similar procedure has been adopted in earlier studies of manganites [29, 30]. We do not observe any significant signature, within the accuracy of our experiments, of the ferroelectric transition at T_{FE} (~ 27 K) in the temperature dependence of frequencies and linewidths. The fit of the data with Klemens model is modest. The fitting parameter C of mode S6 is very high as compared to the other modes, showing that this mode is much more anharmonic. The linewidths and frequencies of the modes S3 and S4 show normal temperature dependence and are not shown here.

An interesting observation is that the intense mode S5 shows anomalous temperature dependence: the mode shows softening near $T_N \sim 46$ K. Similar anomalous

temperature dependence has been observed for a few Raman modes in RMnO₃ where R = La [25] and Gd, Pr, Nd, Sm, Dy [29,30], which has been attributed to spin-phonon coupling [25]. This is understood as follows: if an ion is displaced from its equilibrium position by “*u*”, then the crystal potential is given as $U = 0.5 * (ku^2) + \sum_{ij} J_{ij}(u)S_iS_j$, where *k* in the first term represents the force constant and the second term arises from spin interactions between the Mn³⁺ spins. The phonon frequency is affected by the additional term $(\Delta \omega)_{\text{sp-ph}}(T) = \lambda \langle S_i S_j \rangle$, where $\lambda = (\partial^2 J_{ij}(u) / \partial u^2)$ is the spin-phonon coupling coefficient and $\langle S_i S_j \rangle$ is the spin-correlation function. The parameter λ can be positive or negative and can be different for different phonons. Below T_N, the spin correlations build up and hence the spin-phonon coupling becomes important at lower temperatures. The renormalization of the mode S5 frequency starts slightly above T_N (~ 46K), which can arise from spin fluctuations due to quantum and thermal effects [29].

(B) Orbiton-Phonon Coupling

We now discuss the two high energy excitations, S7 at (1156 cm⁻¹) and S8 at (1328 cm⁻¹). Fig. 4.14 shows temperature-dependence of the frequency and linewidth of S8 mode as well as the intensity ratio of S8 and S6 modes (S8/S6) in the temperature range from 5K to 200K. Above 200K, the mode S8 is too weak to be analyzed quantitatively as is the case for S7. Mode S7 can be assigned as the second order Raman mode involving a combination of S2 and S6 or S4 and S5 phonons and S8 as a overtone of S6 (658 cm⁻¹) mode. As the second order Raman scattering involves the phonons over the entire Brillouin zone, the frequencies of the observed second order phonons are not necessarily the double of first order phonons at the Γ - point (*q* = 0,0,0). The intensity

ratio of S8 to S6 is the most interesting, namely, it is ~ 0.6 at all temperatures. The intensity ratio of S7 to S5 is ~ 0.1 and S7 to S6 is ~ 0.4 in the temperature range of 5 K to 140 K. This anomalously large intensity ratio even at low temperatures can only be understood by invoking the mixing of the multiphonon modes with the orbitons [32-34]. Fig. 4.14 also shows temperature dependence of the frequency and the linewidth of the S8 mode which has yet to be understood quantitatively for the mixed multiphonon-orbiton mode. We hope our results will motivate further theoretical studies on this aspect.

Conclusions

In summary, we have carried out a detailed temperature dependence of the first and second order Raman modes in TbMnO_3 . The intensity ratio of the second-order phonon (S8) to its first-order counterpart (S6) is unusually high and it remains constant down to 5K. This anomalous temperature dependence of the intensity ratio is attributed to the mixing of the second-order phonon with the orbitons as theoretically predicted. Four first-order modes (S1, S2, S3 and S4) show normal behavior with temperature, whereas the S5 mode behaves anomalously below T_N probably arising from a strong spin-phonon coupling. We suggest that the present study brings out yet another example of orbiton-mediated multiphonon Raman scattering in the manganite family.

4.3 Multiferroic nature of rare-earth chromites

4.3.1 Rare-earth chromites, LnCrO_3 ($\text{Ln} = \text{Ho, Er, Yb, Lu}$)

Summary*

We have investigated the magnetic and dielectric properties of heavy rare earth chromites of the formula LnCrO_3 with $\text{Ln} = \text{Ho, Er, Yb, Lu}$. They have a structure similar to YCrO_3 and belong to the orthorhombic space group Pbnm . The magnetic characterization of these samples confirm the canted antiferromagnetic (CAF) behavior at low temperatures ($T_N = 113\text{-}140$ K). Magnetic ions Ln^{3+} and Cr^{3+} and the interactions between them is responsible for their magnetic behavior. Frequency and temperature dependent dielectric constant data show a dielectric anomaly in the temperature range 472-516 K. All the heavy rare earth chromites show the relaxor like transition in the dielectric data. The origin of ferroelectricity and relaxor like behavior is related to the local non-centrosymmetric nature of these chromites. As the ionic radius decreases from HoCrO_3 to LuCrO_3 their Neel temperature also decreases while dielectric transition temperature increases. These rare earth chromites are shown to be multiferroic.

* Paper based on this study has appeared in *Journal of Materials Chemistry* (2007)

Rare-earth chromites, LnCrO_3 (Ln = Ho, Er, Yb, Lu)

Several rare-earth chromites (LnCrO_3 , Ln = La, Nd, Ho, Er, Yb and Lu) were prepared by solid state reactions and characterized by X-ray diffraction. Fig. 4.15 shows typical X-ray diffraction patterns of LnCrO_3 . They were all found to belong to the orthorhombic system (Pbnm) as reported in the literature. The lattice parameters and so the cell volume decrease as we go towards higher atomic number from Ho to Lu. Table 4.2 gives the unit cell parameters of heavy rare earth chromites.

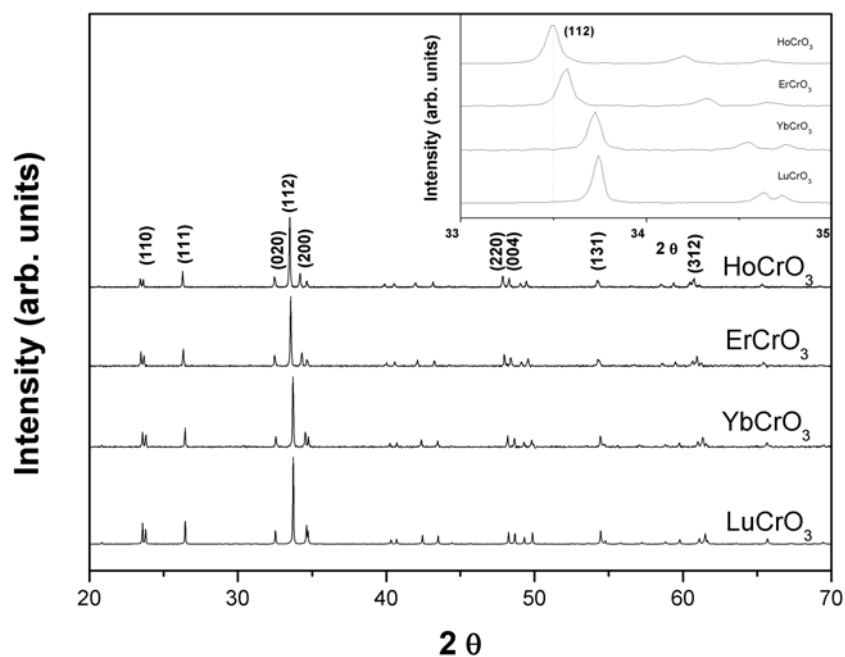


Fig. 4.15: The X-ray diffraction patterns of LnCrO_3 (Ln = Ho, Er, Yb and Lu), which belong to orthorhombic space group Pbnm.

Table 4.2: Unit cell parameters of the heavy rare earth chromites (space group Pbnm)

	a (Å)	b (Å)	c (Å)	V (Å ³)
HoCrO ₃	5.245	5.516	7.538	218.09
ErCrO ₃	5.226	5.517	7.522	216.87
YbCrO ₃	5.195	5.504	7.489	214.14
LuCrO ₃	5.178	5.500	7.480	213.02

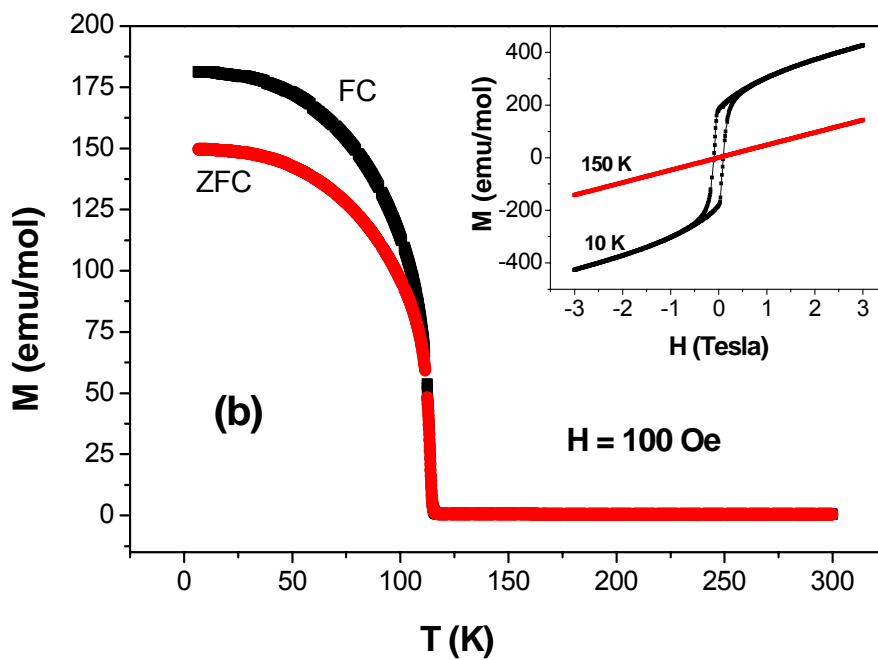
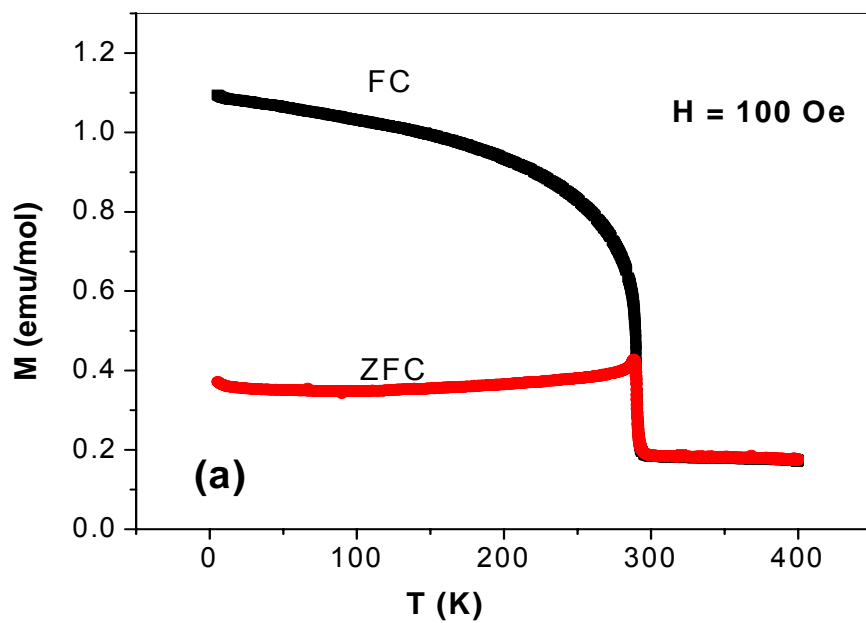


Fig. 4.16: Temperature variation of the magnetization of (a) LaCrO_3 and (b) LuCrO_3 under field-cooled and zero-field-cooled conditions ($H = 100 \text{ Oe}$). The inset in (b) shows the field-dependence of magnetization of LuCrO_3 at 10 K and 150 K.

Although these chromites are formally considered to be antiferromagnetic, low-temperature magnetic measurements show them to be CAFMs just as YCrO_3 . In Fig. 4.16, we show typical magnetization data of LaCrO_3 and LuCrO_3 . They exhibit a non-linear behavior of the magnetization with respect to the field below T_N as shown in the inset of Fig. 4.16(b). Detailed magnetic measurements have shown the weak ferromagnetic moment of the Cr^{3+} spins to be due to Dzyaloshinskii-Moriya (D-M) interaction in these chromites [35]. These chromites also show magnetic domain effects below T_N [35]. The exchange coupling between the Cr^{3+} nearest neighbors is predominantly antiferromagnetic and these ions order magnetically at Neel temperature (T_N); 113 K for LuCrO_3 and 287 K for LaCrO_3 . Below this temperature, they exhibit a weak ferromagnetic moment. There is some evidence for temperature-independent constant-canting-angle coupling in LuCrO_3 . Since the Lu^{3+} ions in LuCrO_3 are in a diamagnetic ground state, this compound's magnetic properties are dominated by the Cr spin system.

The rare earth orthochromites LnCrO_3 are paramagnetic at room temperature and magnetically ordered at low temperatures. They have two kinds of magnetic ions, Ln^{3+} and Cr^{3+} ; so they have three types of magnetic interactions, Cr^{3+} - Cr^{3+} , Cr^{3+} - Ln^{3+} and Ln^{3+} - Ln^{3+} . Generally each magnetic interaction consists of the isotropic, the antisymmetric and anisotropic-symmetric superexchange interactions. This inevitably makes the magnetic properties of LnCrO_3 complex. The interaction between Cr^{3+} is the 180 degree superexchange. The isotropic Cr^{3+} - Cr^{3+} exchange gives the first Neel temperature. As the temperature is lowered, the Ln^{3+} moment increases and spin reorientation occurs. The anisotropic parts of the magnetic interaction between Cr^{3+} and

Ln^{3+} spins, the antisymmetric and the anisotropic-symmetric exchange interactions, determine the spin reorientation temperature [36].

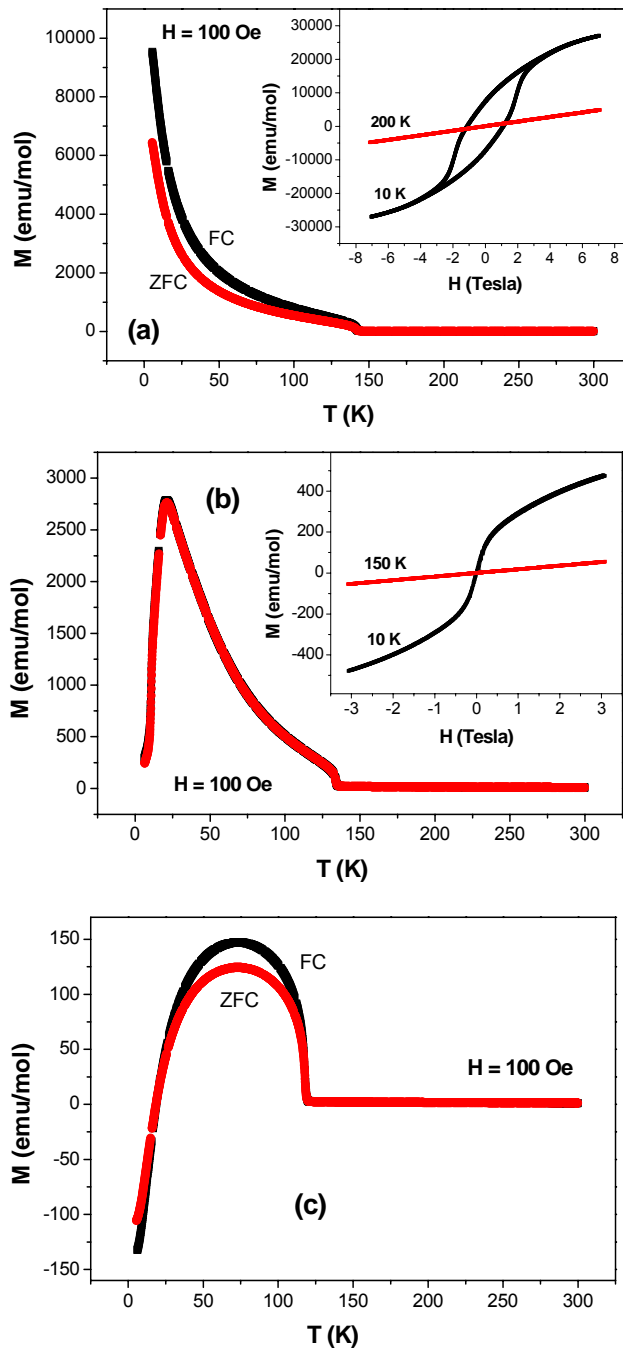


Fig. 4.17: Temperature variation of the magnetization of (a) HoCrO_3 , (b) ErCrO_3 and (c) YbCrO_3 under field-cooled and zero-field-cooled conditions ($H = 100$ Oe). The insets in (a) and (b) show the field-dependence of magnetization of HoCrO_3 and ErCrO_3 respectively.

In HoCrO_3 and ErCrO_3 , the antiferromagnetic transition occurs at 140 and 133 K respectively [Fig. 4.17(a) and (b)]. In these rare earth chromites the Ln^{3+} magnetic order is induced by the Cr^{3+} sublattice [37]. In ErCrO_3 , the Er^{3+} spins are oriented along the c axis by the effective field exerted by the ordered Cr^{3+} spins. Due to the interactions between Er^{3+} and Cr^{3+} spins, spin reorientation transition (T_{SR}) occurs at 15 K where the spin configuration changes from weak ferromagnetic phase to the antiferromagnetic phase below T_{SR} [38].

Magnetic data of YbCrO_3 shown in Fig. 4.17(c) is of special interest because of magnetization reversal at low temperatures. It shows an antiferromagnetic transition at Néel temperature 117 K. The magnetic moment of YbCrO_3 is negative below 17 K, which reveals that the induced magnetic moment of the Yb^{3+} spins couple antiparallel to the weak ferromagnetic moment of the Cr^{3+} spins [39]. The antisymmetric (Dzyaloshinskii-Moria) and the anisotropic-symmetric parts of the 3d-4f magnetic exchange interaction in YbCrO_3 are enormously stronger than those in other rare earth orthochromites, and these anisotropic parts of the 3d-4f exchange interaction induce the cooperative transition of a Cr^{3+} exciton and a Yb^{3+} spin flip [39].

Dielectric measurements show that the heavier rare-earth chromites (LnCrO_3 , Ln = Ho, Er, Yb and Lu) undergo a transition in the temperature range 439-485 K (T_{max}) accompanied by a maximum in the dielectric constant. In Fig. 4.18, we show the temperature variation of the dielectric constant in the case of LaCrO_3 and LuCrO_3 . We do not, however, find such a transition in the case of LaCrO_3 or NdCrO_3 as exemplified in the case of LaCrO_3 in the Fig. 4.18(a).

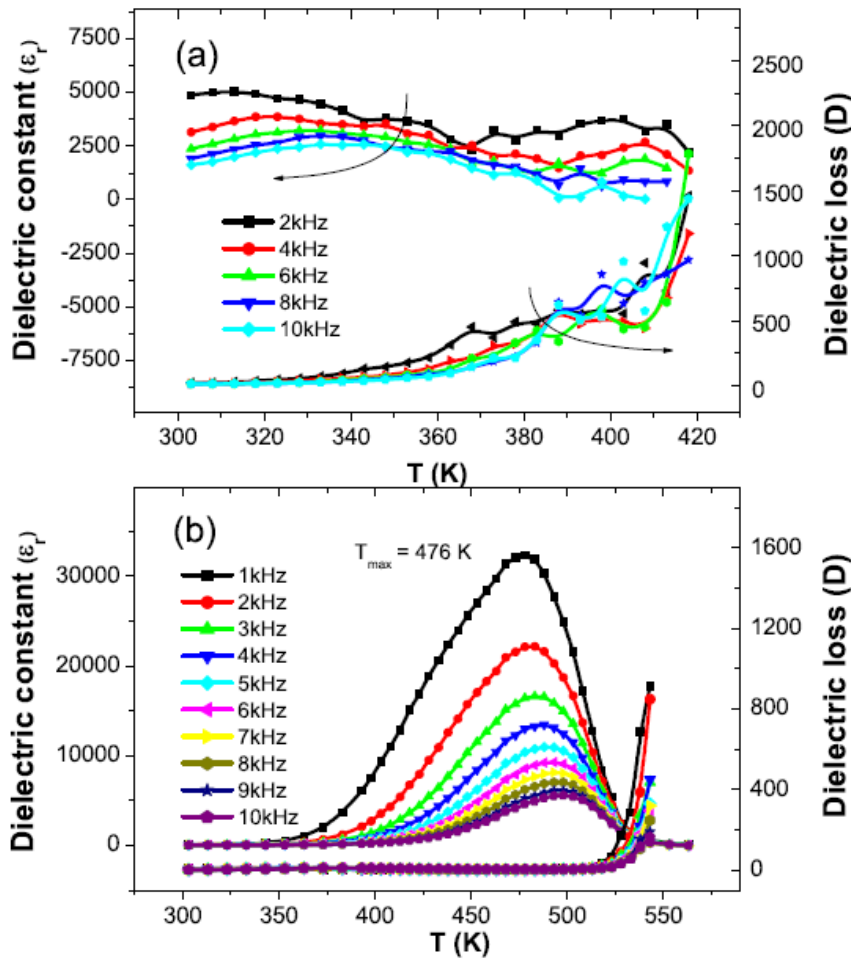


Fig. 4.18: Temperature variation of the dielectric constant and dielectric loss of (a) LaCrO_3 and (b) LuCrO_3 at different frequencies.

Temperature variation of the dielectric constant of HoCrO_3 , ErCrO_3 and YbCrO_3 is similar to that of LuCrO_3 as can be seen from the Fig. 4.19. We see from figures 4.18(b) and 4.19, that the T_{max} is frequency-dependent. In order to obtain the FE transition temperature, we employed the Curie-Weiss plot, wherein the reciprocal of dielectric constant in the high-temperature region ($T > T_{\text{max}}$) was plotted against temperature [5]. The Curie-Weiss plots yielded frequency-independent T_E values which are in the 472-516 K range for HoCrO_3 , ErCrO_3 , YbCrO_3 and LuCrO_3 . The dielectric constant of the rare earth chromites shows a large dispersion below T_E , but is frequency independent above T_E , a behavior commonly observed in relaxor ferroelectrics [17].

Local non-centrosymmetry is the the origin of this relaxor-like behavior. It is noteworthy that the value of dielectric constant increases as the size of rare-earth ion decreases.

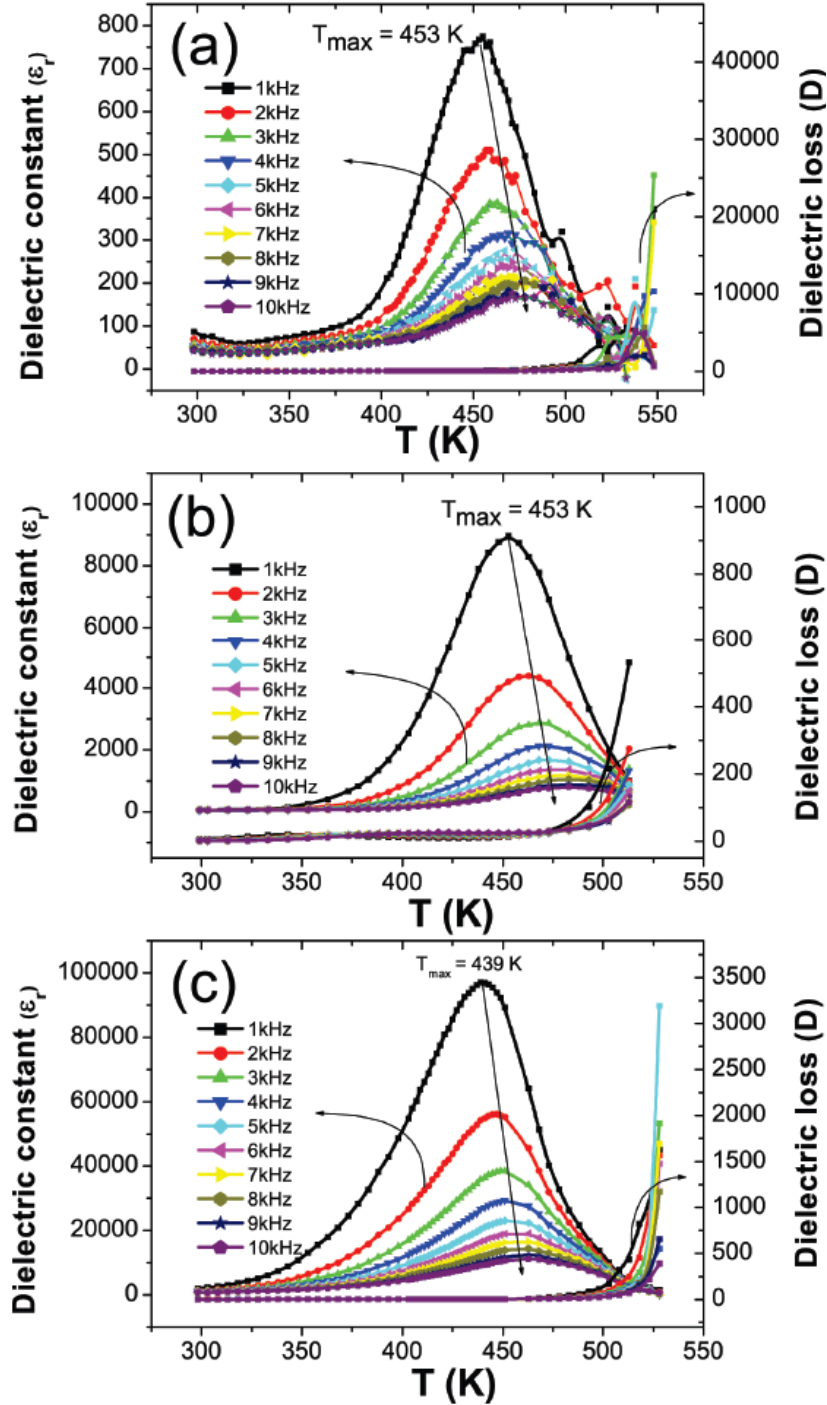


Fig. 4.19: Temperature variation of the dielectric constant of (a) HoCrO_3 , (b) ErCrO_3 and (c) YbCrO_3 at different frequencies.

The maximum value of the low frequency dielectric constant is around 5000 in LaCrO_3 and 32000 in LuCrO_3 . The polarization-electric field hysteresis loops of the heavier rare earth chromites are similar to those of leaky dielectrics and are comparable to the hysteresis loop in YCrO_3 [40]. Just as YCrO_3 , the heavy rare earth chromites show low values of the polarization and may, therefore, be considered to be weakly ferroelectric.

Based on the present findings, we can draw the phase diagram as shown in fig. 4.20, to describe the multiferroic properties of the heavy rare-earth chromites. The phase diagram demarcates three distinct regions: (CAFM, FE); (PM, FE) and (PM, PE), where PM and PE stand for the paramagnetic and the paraelectric regimes respectively. The T_N decreases with the decrease in the radius of the rare-earth ion while the T_E increases slightly with decrease in size.

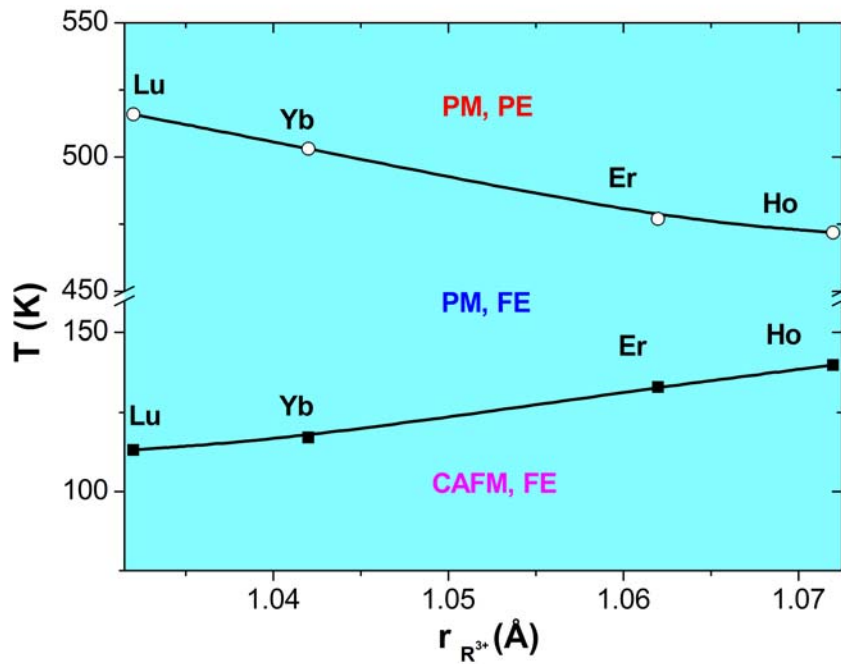


Fig. 4.20: Variation of the ferroelectric transition temperature T_E , and magnetic transition temperature, T_N , in the heavy rare-earth chromites.

Since the reported structures of the rare-earth chromites belong to the centrosymmetric orthorhombic system (Pbnm), it would be in order to comment on why ferroelectric manifests itself. We pointed out that ferroelectric materials could be locally non-centrosymmetric although they are globally centro-symmetric, as exemplified by YCrO_3 [40]. A detailed study of the pair distribution functions of YCrO_3 based on neutron diffraction data indicates that in the short distance range (1-6 Å), the data give the best fit to a non-centrosymmetric $P2_1$ space-group in the low-temperature FE phase [41]. In the high-temperature PE phase, however, the PDF data conform to the centrosymmetric structure in the same distance range. The PDF data over the entire distance range of 1-22 Å can be fitted reasonably well with the centrosymmetric structure.

We have employed first-principles calculations to determine the effects of magnetic ordering and the size of the A- cation on the ferroelectricity of the chromites, through the cases of LuCrO_3 which exhibits ferroelectricity and of LaCrO_3 which is paraelectric at all temperatures. Our calculations are based on density functional theory within a gradient corrected (PW91) local spin density approximation (LSDA), as implemented in the PWSCF package [42] with ultrasoft pseudopotentials [43] and plane-wave basis with energy cut-offs of 25 Ry and 150 Ry in representing Kohn-Sham wave-functions and electron densities respectively. In all our calculations, we have used experimental lattice parameters of the crystal unit cell as ferroelectricity is known to be sensitive to unit cell volume.

We determined Γ point ($\mathbf{k}=(000)$) phonons of LuCrO_3 and LaCrO_3 in the cubic perovskite structures (see Table 4.3) using the frozen phonon method. While LaCrO_3 has no Γ point instabilities in the PM form, it exhibits a weak ferroelectric instability upon ferromagnetic ordering. On the other hand, LuCrO_3 exhibits strong ferroelectric instabilities in both PM and FM orderings. We note that a change in magnetic ordering strongly affects the phonon frequencies, with a substantial softening upon FM ordering (relative to the PM phase) of the Γ_{25} mode which involves only the oxygen displacements. Since the modes of rotational instabilities belong to the subspace containing Γ_{25} , they are expected to behave similarly. Secondly, the softest polar (Γ_{15}) mode in both the chromites in the PM and FM phases involves A-cation off-centering, which softens upon FM ordering. In contrast, the hardest Γ_{15} mode is hardens further on FM ordering.

Table 4.3: Calculated phonon frequencies at gamma point $\Lambda(\text{cm}^{-1})$ (i is imaginary).

	LaCrO_3 (PM)	LaCrO_3 (FM)	LuCrO_3 (PM)	LuCrO_3 (FM)
Γ_{15} (polar)	538.09	579.28	623.53	715.83
Γ_{15} (polar)	338.68	231.75	327.95	224.37
Γ_{25} (nonpolar)	227.94	107.6	106.83	187.71 <i>i</i>
Γ_{15} (<i>A</i> off-center)	24.43	58.1 <i>i</i>	144.8 <i>i</i>	177.53 <i>i</i>

Since these chromites exhibit antiferromagnetism, we have determined the energetics of A-cation off-centering in the G-type antiferromagnetic ordering (involving two formula units per cell). As shown in Fig. 4.21, while the La displacement is stable at its high symmetry site, Lu exhibits a double energy well, with a tendency to be off-centered. It gains about 136 meV per formula unit due to off-centering by about 0.4 angstrom (comparable to the displacement of Pb in PbTiO_3). The frequency

of the unstable Γ_{15} mode corresponding to Lu-offcentering in the AFM ordered state is 64 cm^{-1} . The instabilities at the zone boundary are expected to compete with ferroelectric instabilities (we find more unstable modes, R_{25} (CrO_6 rotational mode) at $339i \text{ cm}^{-1}$ and R_{15} at $146i \text{ cm}^{-1}$ in AFM ordering) and the final ground state possibly involves a combination of these instabilities.

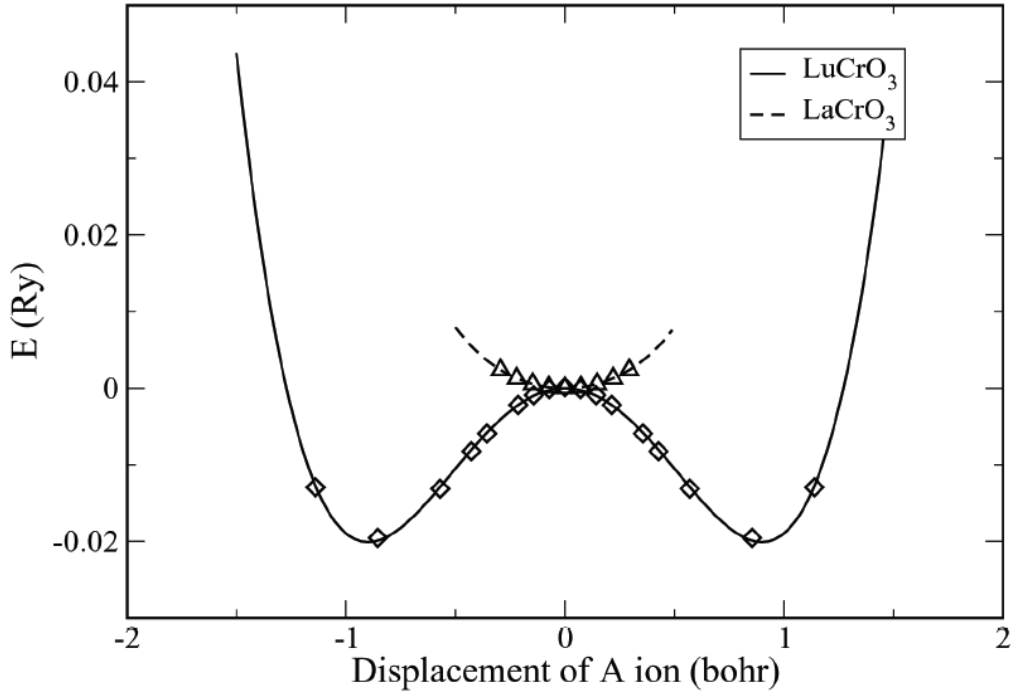


Fig. 4.21: Energy as a function of A-cation displacement along (100) direction from their high symmetry site in the cubic structure with G -type AF ordering.

We have investigated the possibility of broken inversion symmetry in LuCrO_3 with respect to the theoretical structure optimized with the Pbnm symmetry. The theoretical Pbnm structure exhibits less distorted CrO_6 octahedron and more distorted LuO_8 polyhedron in comparison with the experimental structure. We then broke the inversion symmetry by off-centering Lu atoms along each Cartesian direction by 1 % of the lattice constant and relaxing the structure with lower symmetry. This results in a

small gain in energy (of about 1 meV per formula unit) and correspondingly small polarization (less than $0.35 \mu\text{C}/\text{cm}^2$, computed from the Berry phase formula [44]) upon breaking the inversion symmetry along each of the three directions. These values are small and comparable to the magnitudes of computational errors. However, our results showing (a) the existence of a ferroelectric instability in the cubic structure, (b) its dependence on magnetic ordering and (c) the small but non-zero values of polarization support the occurrence of ferroelectricity in LuCrO_3 . It would appear that local magnetic ordering can induce local non-centrosymmetry and weak ferroelectric polarization in these materials.

Conclusions

Heavy rare-earth chromites HoCrO_3 , ErCrO_3 , YbCrO_3 , LuCrO_3 and YCrO_3 belong to a new family of multiferroics exhibiting canted antiferromagnetism at low temperatures. HoCrO_3 , ErCrO_3 , YbCrO_3 and LuCrO_3 show antiferromagnetic transitions at 140, 133, 117 and 113 K and ferroelectric transitions at 472, 477, 503 and 516 K respectively marking the decrease of antiferromagnetic transition temperature (T_N) and increase of ferroelectric transition temperature (T_E) with the decrease of rare-earth ionic radius. The members of the rare earth chromites family have three distinct regions: CAFM and FE at low temperatures, paramagnetic and paraelectric at high temperatures and paramagnetic and ferroelectric region in between. Further studies are necessary to fully understand the multiferroic properties of these chromites.

4.3.2 $\text{YCr}_{1-x}\text{Mn}_x\text{O}_3$ and $\text{LuCr}_{1-x}\text{Mn}_x\text{O}_3$ solid solutions

Summary*

The effect of Mn substitution on the multiferroic properties of YCrO_3 and LuCrO_3 has been investigated. Solid solutions of the type $\text{YCr}_{1-x}\text{Mn}_x\text{O}_3$ and $\text{LuCr}_{1-x}\text{Mn}_x\text{O}_3$ ($x = 0.0 - 0.3$) possess orthorhombic structures with Pnma and Pbnm space groups respectively. Both the series of materials show canted antiferromagnetic behavior with the T_N decreasing linearly with increasing x . The $x = 0.1$ and 0.2 compositions show an interesting magnetic phenomenon, negative value of magnetization below the compensation temperature. They also exhibit relaxor ferroelectricity similar to their parent compounds with the transition temperature decreasing linearly with increase in x .

* Paper based on this study has appeared in *Solid State Communications* (2008)

$\text{YCr}_{1-x}\text{Mn}_x\text{O}_3$ and $\text{LuCr}_{1-x}\text{Mn}_x\text{O}_3$ solid solutions

$\text{YCr}_{1-x}\text{Mn}_x\text{O}_3$ and $\text{LuCr}_{1-x}\text{Mn}_x\text{O}_3$ ($x = 0.0 - 0.3$) belong to the space groups Pnma and Pbnm respectively. Typical X-ray diffraction patterns indicating peak positions and (hkl) values are shown in Fig. 4.22.

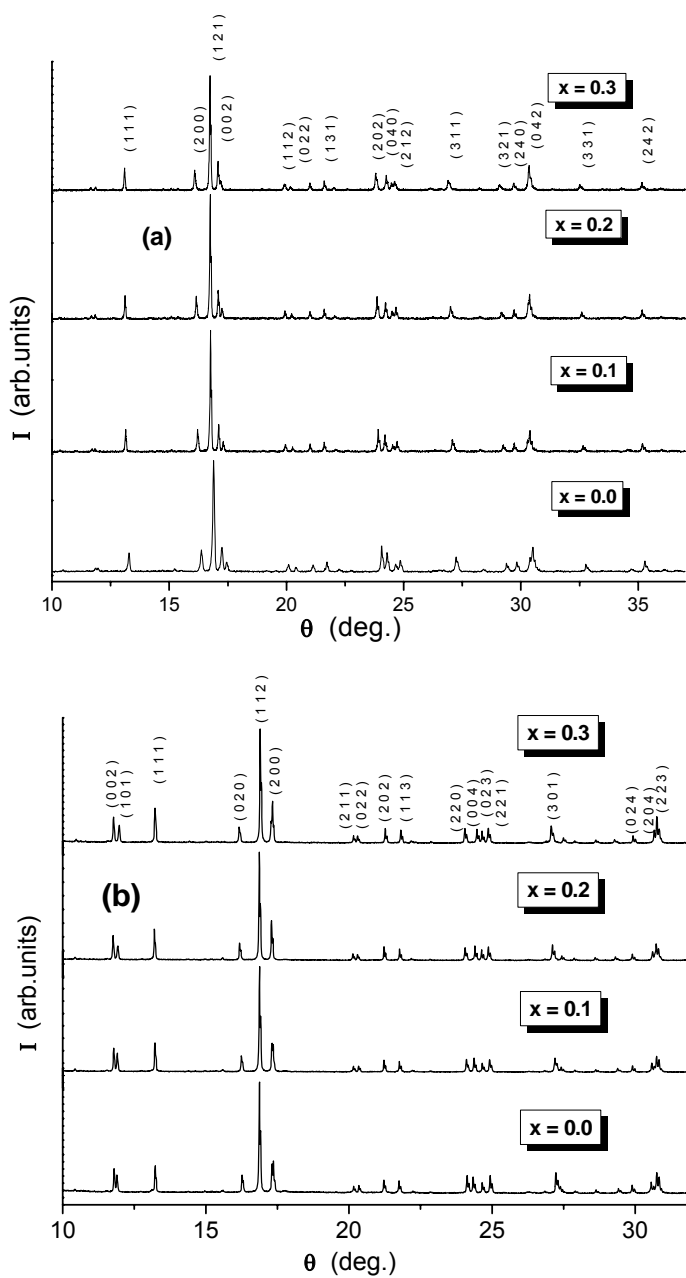


Fig. 4.22: The X-ray diffraction patterns of the series (a) $\text{YCr}_{1-x}\text{Mn}_x\text{O}_3$, (b) $\text{LuCr}_{1-x}\text{Mn}_x\text{O}_3$ ($x = 0.0 - 0.3$).

The unit cell parameters of these materials are listed in Table 4.4. The volume of the unit cell increases with Mn-doping in both the cases. The increase in volume with x is consistent with the relative ionic sizes.

Table 4.4

Unit cell parameters of Y(Lu)Cr_{1-x}Mn_xO₃ (x = 0.0-0.3)

x	YCr _{1-x} Mn _x O ₃ (Pnma)				LuCr _{1-x} Mn _x O ₃ (Pbnm)			
	a (Å)	b (Å)	c (Å)	V (Å ³)	a (Å)	b (Å)	c (Å)	V (Å ³)
0.0	5.52	7.53	5.24	217.80	5.17	5.50	7.48	212.69
0.1	5.53	7.52	5.24	217.91	5.18	5.51	7.47	213.21
0.2	5.54	7.51	5.24	218.01	5.18	5.53	7.46	213.69
0.3	5.56	7.50	5.24	218.81	5.19	5.54	7.44	213.92

Both YCr_{1-x}Mn_xO₃ and LuCr_{1-x}Mn_xO₃ exhibit transitions to a canted antiferromagnetic state at lower temperatures as evident from the Fig. 4.23, where magnetization has been shown for x = 0.0-0.3 measured with an applied field (H) of 100 Oe. The value of T_N monotonically decreases with x, which can be understood in connection with the continuous change of a Cr³⁺-O²⁻-Cr³⁺ angle governing the antiferromagnetic interaction between Cr³⁺. The field cooled (FC) and zero field cooled (ZFC) curves considerably deviate below T_N because of the irreversibility of the magnetic order. The members of these series corresponding to x = 0.2 exhibit distinct negative magnetization below a

temperature called compensation temperatures (T_{comp}) which is 95 K and 78 K for Y- and Lu- compositions respectively. Considering the fact that the present behavior is similar to that in GdCrO_3 [45], $\text{La}_{1-x}\text{Pr}_x\text{CrO}_3$ [46], this is plausibly attributed to the antiparallel coupling of the Y^{3+} (Lu^{3+}) moments and the canted Cr^{3+} and Mn^{3+} moments.

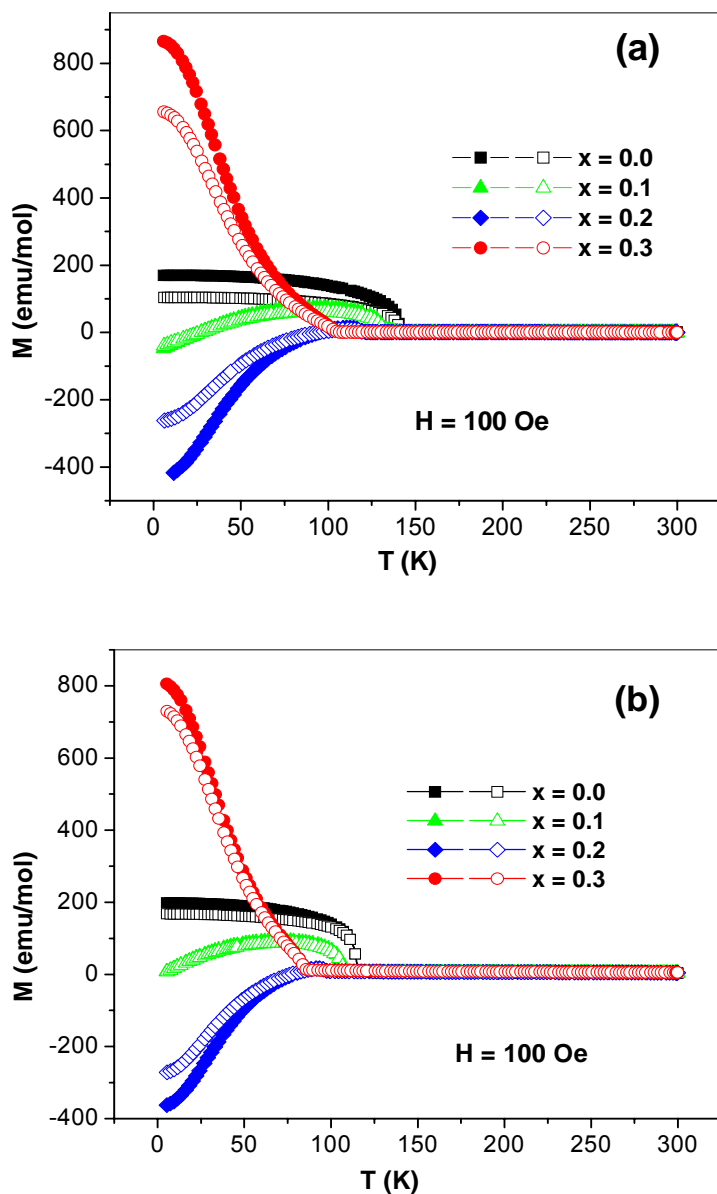


Fig. 4.23: The field cooled (FC) and zero field cooled (ZFC) magnetizations of (a) $\text{YCr}_{1-x}\text{Mn}_x\text{O}_3$, (b) $\text{LuCr}_{1-x}\text{Mn}_x\text{O}_3$ for $x = 0-0.3$ in an applied field of 100 Oe as a function of temperature. The solid symbols show FC data and open symbols show ZFC data.

Paramagnetic Curie-Weiss temperatures (θ) can be determined by plotting the reciprocal of susceptibility ($1/\chi$) as a function of temperature. In Table 4.5, we list the T_N and θ values of $YCr_{1-x}Mn_xO_3$ and $LuCr_{1-x}Mn_xO_3$ for all compositions. Both T_N and θ decrease linearly with increase in x (Fig. 4.24).

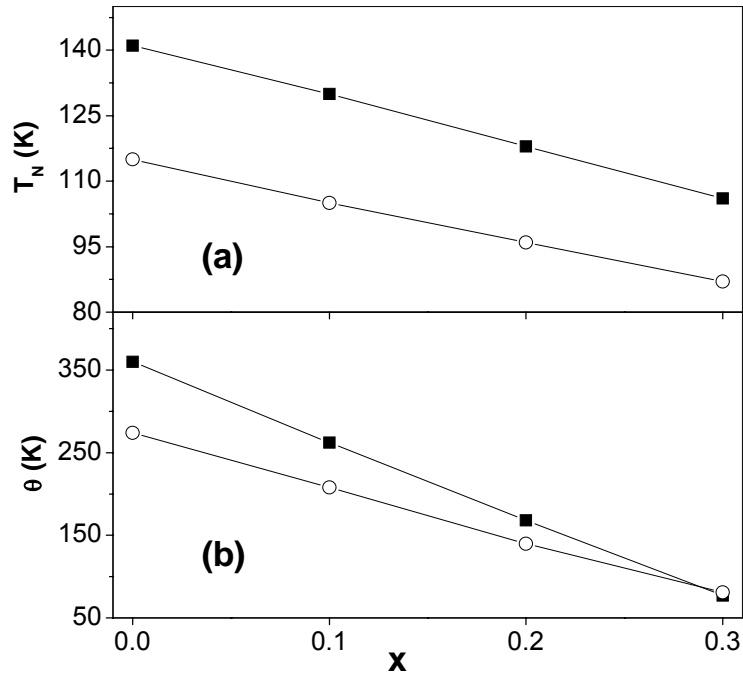


Fig. 4.24: The linear dependence of (a) T_N and (b) θ values with the compositions $x = 0.0-0.3$ for $YCr_{1-x}Mn_xO_3$ (shown by solid rectangles) and $LuCr_{1-x}Mn_xO_3$ (shown by open circles).

We have measured ferromagnetic hysteresis loops at 10 K for all compositions of $YCr_{1-x}Mn_xO_3$ and $LuCr_{1-x}Mn_xO_3$ (Fig. 4.25). The values of the remnant magnetization (M_r) and coercive field (H_C) data of the two series at 10 K are listed in Table 4.5. For reasons that are not clear, the $x = 0.1$ compositions show anomalously low values of M_r and H_C . The highest values of M_r are found for the $x = 0.3$ compositions.

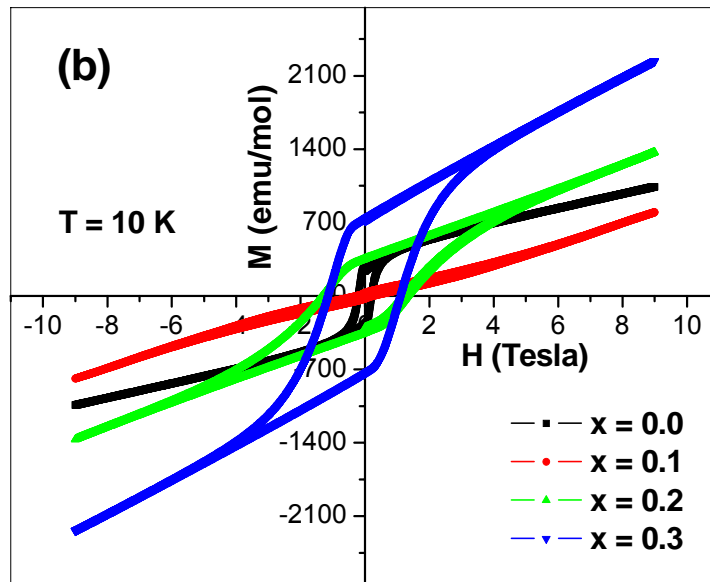
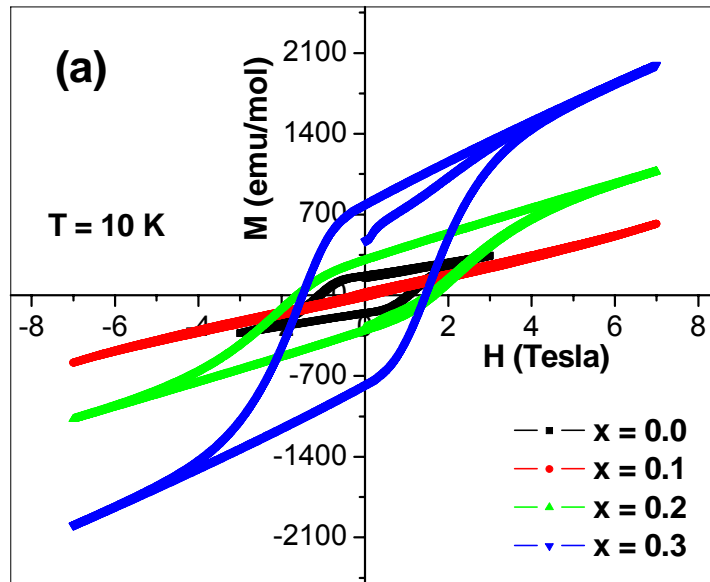


Fig. 4.25: The magnetic hysteresis loops of (a) $\text{YCr}_{1-x}\text{Mn}_x\text{O}_3$ and (b) $\text{LuCr}_{1-x}\text{Mn}_x\text{O}_3$ at 10 K.

Table 4.5Magnetic properties of Y(Lu)Cr_{1-x}Mn_xO₃ (x = 0.0-0.3)

x	YCr _{1-x} Mn _x O ₃				LuCr _{1-x} Mn _x O ₃			
	T _N (K)	(θ) (K)	M _r (emu/mol) (10 K)	H _C (Oe) (10 K)	T _N (K)	(θ) (K)	M _r (emu/mol) (10 K)	H _C (Oe) (10 K)
0.0	141	360	165	11000	115	274	268	2070
0.1	130	262	24	2350	105	208	31	2550
0.2	118	168	302	16355	96	140	353	13230
0.3	106	77	784	14770	87	81	738	11240

In fig. 4.26 (a)-(d), we have shown the temperature variation of dielectric constant for YCr_{1-x}Mn_xO₃ compositions at different frequencies over 200 Hz-1 MHz range. All of them exhibit relaxor ferroelectric kind of behavior with the dielectric constant maxima behaving dependently with frequency, the temperature corresponding to the maximum value of the dielectric constant, T_{max}, shifting towards higher temperature with values in the ranges 453-473 K, 486-494 K, 423-448 K and 378-393 K in the case of YCrO₃, YCr_{0.9}Mn_{0.1}O₃, YCr_{0.8}Mn_{0.2}O₃ and YCr_{0.7}Mn_{0.3}O₃ respectively. The Curie–Weiss plots yielded the frequency-independent transition temperature (T_E) as 477 K for YCrO₃, 470 K for YCr_{0.9}Mn_{0.1}O₃, 455 K for YCr_{0.8}Mn_{0.2}O₃ and 418 K for YCr_{0.7}Mn_{0.3}O₃. Thus the value of T_E was found to be decreasing with increase in x or the manganese concentration.

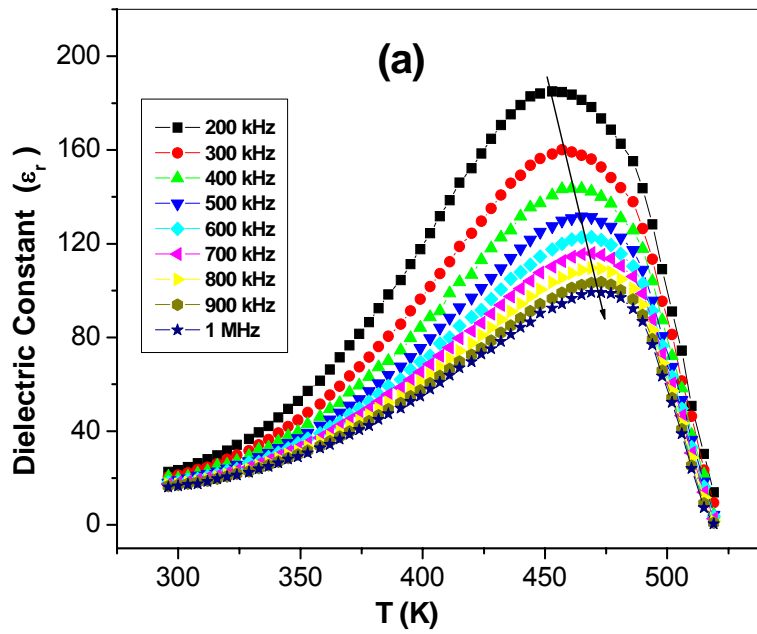


Fig. 4.26 (a): The variation of dielectric constant of YCrO_3 with temperature in 200 kHz-1 MHz range

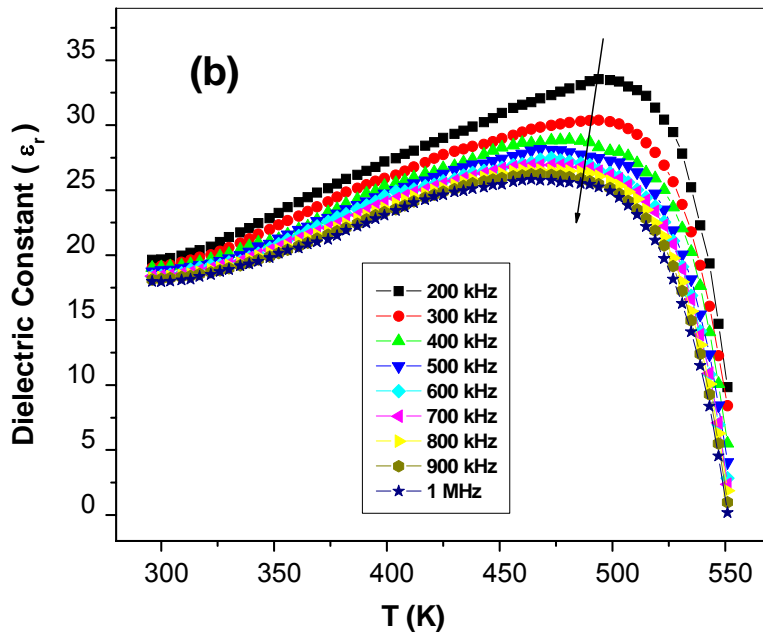


Fig. 4.26 (b): The temperature variation of dielectric constant of $\text{YCr}_{0.9}\text{Mn}_{0.1}\text{O}_3$ in 200 kHz-1 MHz range

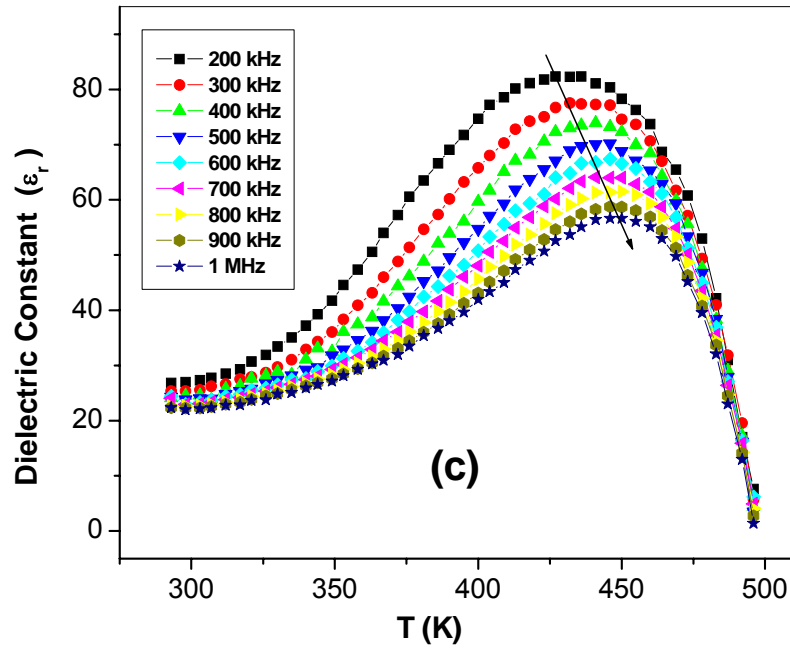


Fig. 4.26 (c): The temperature variation of dielectric constant of $\text{YCr}_{0.8}\text{Mn}_{0.2}\text{O}_3$ in 200 kHz-1 MHz range

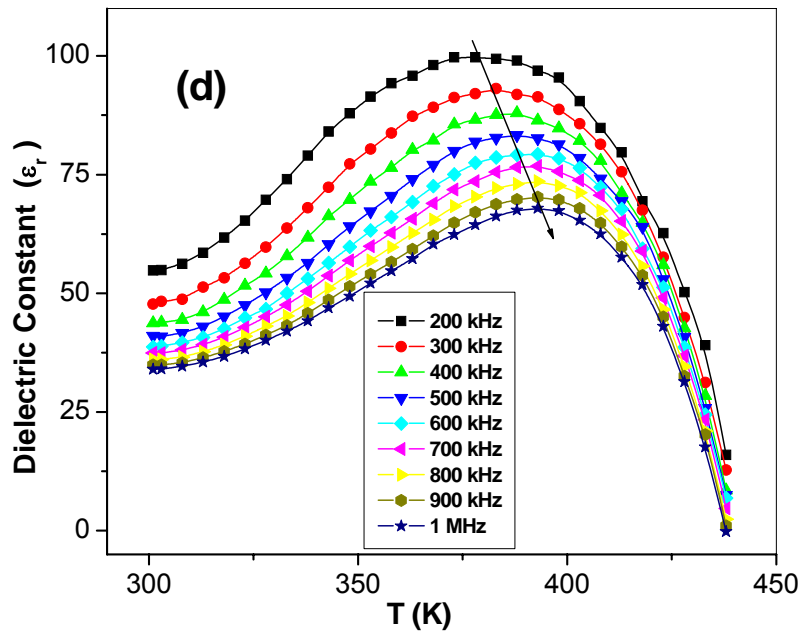


Fig. 4.26 (d): The temperature variation of dielectric constant of $\text{YCr}_{0.7}\text{Mn}_{0.3}\text{O}_3$ in 200 kHz-1 MHz range.

Similar observations were made on $\text{LuCr}_{1-x}\text{Mn}_x\text{O}_3$ compositions as shown in Fig. 4.27 (a)-(d) with T_{max} values in the ranges 467-482 K, 474-498 K, 459-465 K and 383-398 K and T_E values 523 K, 511 K, 482 K and 425 K respectively for $x = 0, 0.1, 0.2$ and 0.3 .

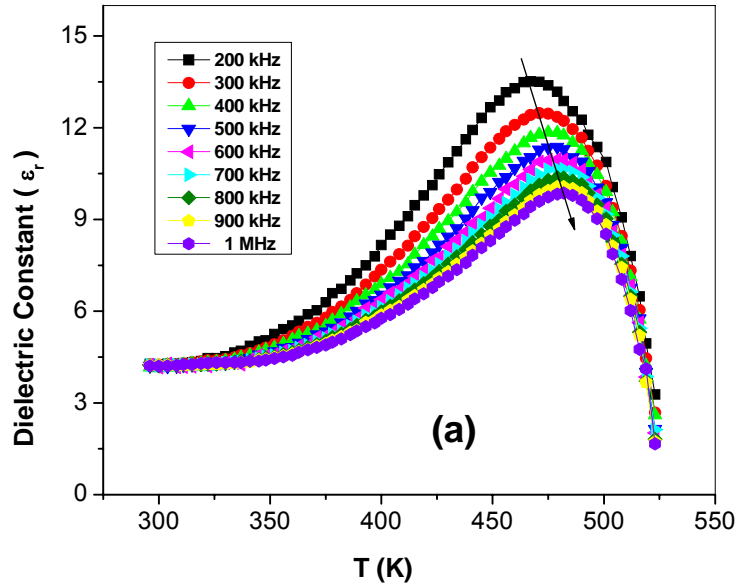


Fig. 4.27 (a): The variation of dielectric constant of LuCrO_3 with temperature in 200 kHz-1 MHz range

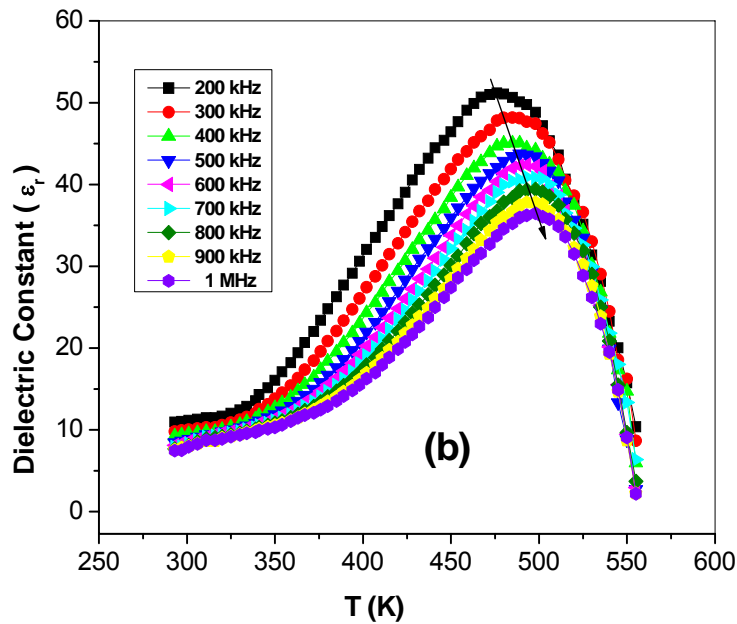


Fig. 4.27 (b): The temperature variation of dielectric constant of $\text{LuCr}_{0.9}\text{Mn}_{0.1}\text{O}_3$ in 200 kHz-1 MHz range

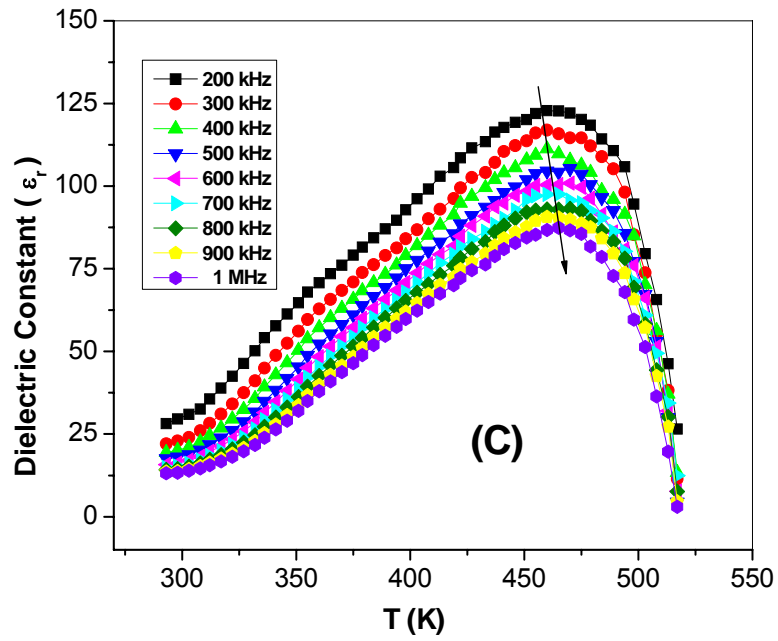


Fig. 4.27 (c): The temperature variation of dielectric constant of $\text{LuCr}_{0.8}\text{Mn}_{0.2}\text{O}_3$ in 200 kHz-1 MHz range

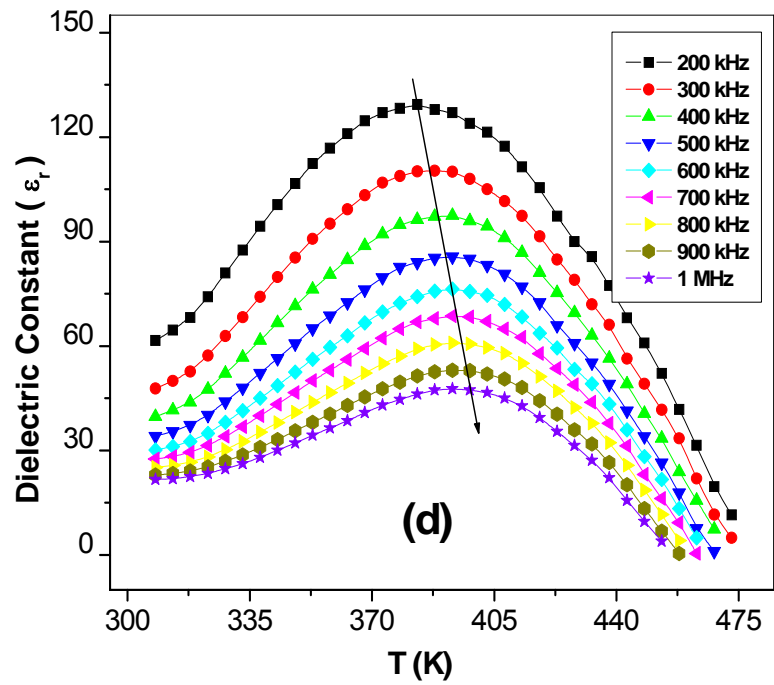


Fig. 4.27 (d): The temperature variation of dielectric constant of $\text{LuCr}_{0.7}\text{Mn}_{0.3}\text{O}_3$ in 200 kHz-1 MHz range

The values of T_E have been plotted in a schematic diagram (Fig. 4.28) to see the trend in its decrease with increase in x or manganese concentration for both the series.

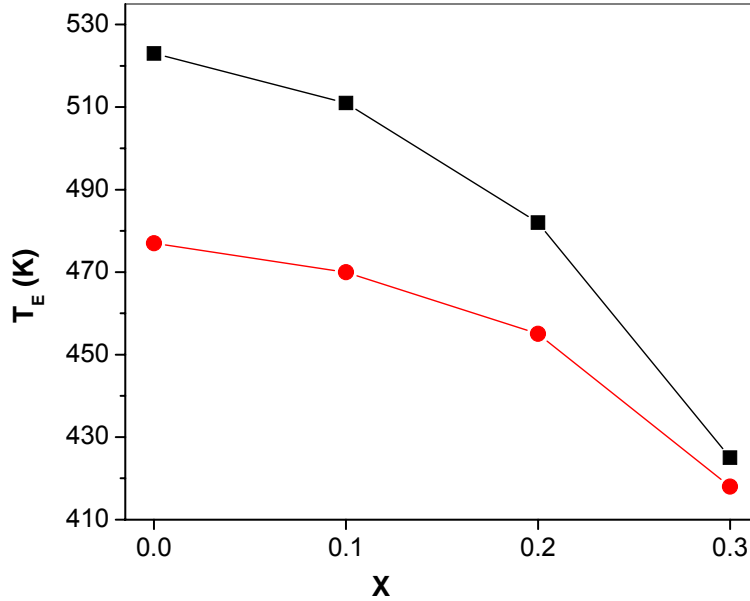


Fig. 4.28: The variation of ferroelectric transition temperature in $\text{YCr}_{1-x}\text{Mn}_x\text{O}_3$ (shown by red circles) and $\text{LuCr}_{1-x}\text{Mn}_x\text{O}_3$ (shown by black rectangles) ($x = 0.0-0.3$) as a function of composition.

Conclusions

In conclusion, the present study of the magnetic and dielectric properties of $\text{YCr}_{1-x}\text{Mn}_x\text{O}_3$ and $\text{LuCr}_{1-x}\text{Mn}_x\text{O}_3$ ($x = 0.0-0.3$) show that all the compositions exhibit canted antiferromagnetism and ferroelectricity with both the transition temperatures decreasing with x . The $x = 0.3$ compositions exhibit low T_N values but high values of the remnant magnetization and coercive field along with the ferroelectric transition in the more accessible temperature range. Preliminary studies reveal that these solid solutions do not exhibit magnetocapacitance.

4.4 Beneficial modification of the properties of multiferroic BiFeO₃ by cation substitution

Summary*

The effects of modifying the well-known multiferroic BiFeO₃ by substituting Fe by Mn and Bi by La have been investigated. It is shown that both the substitutions have a favorable effect on the multiferroic properties of BiFeO₃. Thus, both BiFe_{1-x}Mn_xO₃ and Bi_{1-x}La_xFeO₃ (x = 0.0-0.3) show increased magnetization accompanied by hysteresis loops as well as improved dielectric properties. The ferroelectric transition temperature is lower than that of BiFeO₃, but is in a more accessible range. In Bi_{1-x}La_xFeO₃, there is a change in structure at x = 0.2.

* Paper based on this study has appeared in *Solid State Sciences* (2007)

Beneficial modification of the properties of multiferroic BiFeO_3 by cation substitution

Fig. 4.29 shows the XRD patterns of $\text{BiFe}_{1-x}\text{Mn}_x\text{O}_3$ with $x = 0.0$ to 0.3 . All these materials belong to the space group $R\bar{3}c$ with the hexagonal structure (Table 4.6). Increase in the Mn content leads to a decrease in the unit cell volume with a significant decrease in both a and c parameters and a decrease in the c/a ratio from 2.486 for $x = 0.0$ to 2.478 for $x = 0.3$.

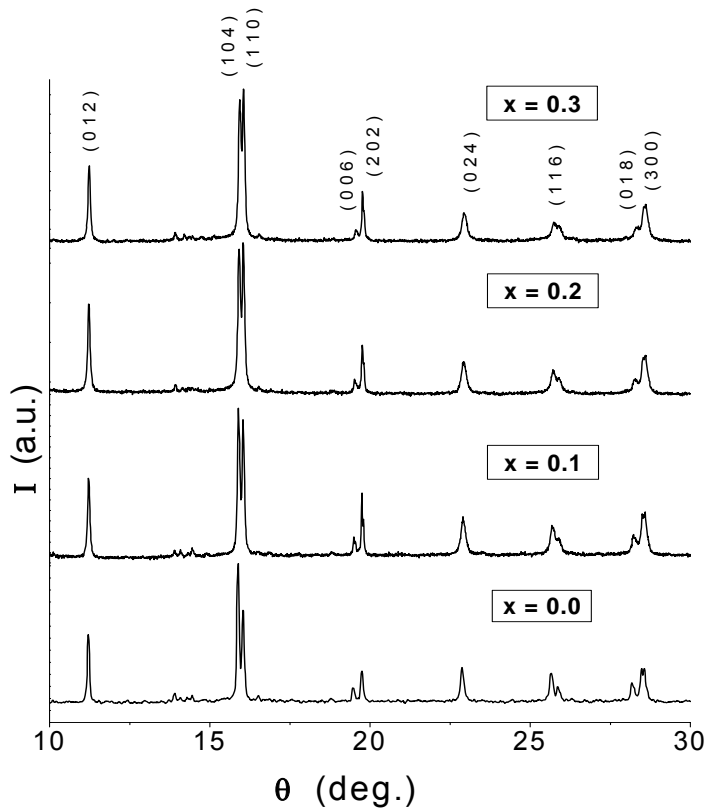


Fig. 4.29 : XRD patterns of $\text{BiFe}_{1-x}\text{Mn}_x\text{O}_3$ ($x = 0, 0.1, 0.2, 0.3$)

Table 4.6: Lattice Parameters of $\text{BiFe}_{1-x}\text{Mn}_x\text{O}_3$ ($x = 0.0-0.3$).

x	Space Group	a = b (Å)	c (Å)	c/a	V (Å ³)
0.0	R3c	5.578	13.868	2.486	373.727
0.1	R3c	5.575	13.844	2.483	372.668
0.2	R3c	5.573	13.831	2.482	371.942
0.3	R3c	5.570	13.801	2.478	370.853

Fig. 4.30 shows the variation of magnetization with temperature ($M \sim T$) in the temperature range 5-400 K at an applied magnetic field of 100 Oe for all the compositions. There is a steep increase in the magnetization at low temperatures with increase in x showing the feature of a canted antiferromagnet, the highest value being found for $\text{BiFe}_{0.7}\text{Mn}_{0.3}\text{O}_3$.

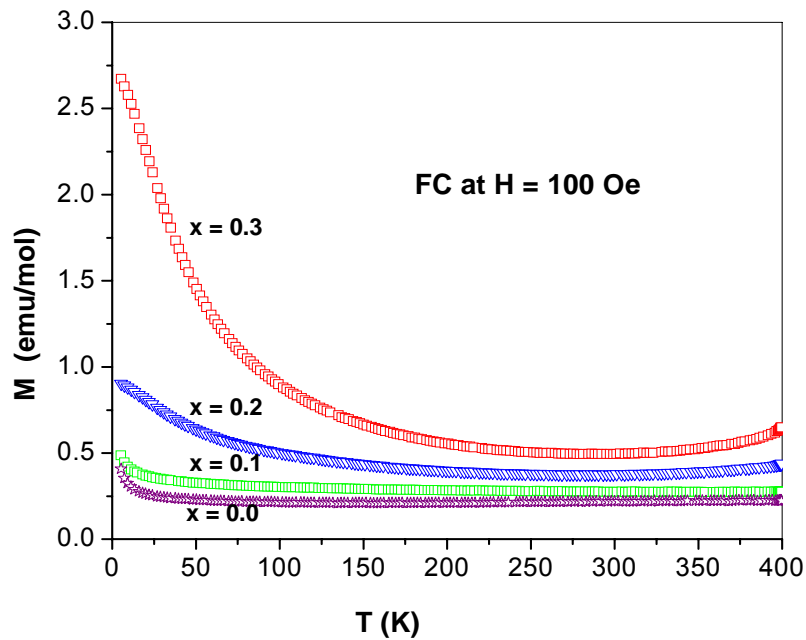


Fig. 4.30: Field-cooled (FC) magnetization curves at $H = 100$ Oe for $\text{BiFe}_{1-x}\text{Mn}_x\text{O}_3$ ($x = 0 - 0.3$).

We also observe a distinct magnetic hysteresis loop in the case of the $x = 0.3$ composition with a coercive field (H_C) of 1094 Oe and a remanent magnetization (M_r) of 24 emu/mol (Fig. 4.31). $\text{BiFe}_{0.8}\text{Mn}_{0.2}\text{O}_3$ also exhibits a hysteresis loop with an H_C of 686 Oe and an M_r of 5 emu/mol. No hysteresis loop was observed with the $x = 0.0$ and $x = 0.1$ compositions.

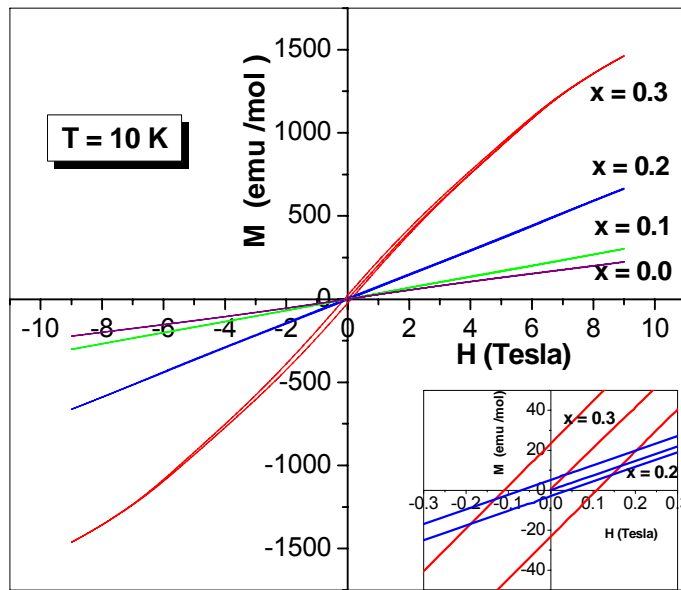


Fig. 4.31: Variation of magnetization of $\text{BiFe}_{1-x}\text{Mn}_x\text{O}_3$ with magnetic field at $T = 10$ K. The inset shows the enlarged ferromagnetic hysteresis observed for $x = 0.2$ and 0.3 .

DTA curves of $\text{BiFe}_{1-x}\text{Mn}_x\text{O}_3$ compositions are shown in fig. 4.32. The DTA curve of BiFeO_3 shows a prominent peak at 1106 K due to the ferroelectric transition and an additional anomaly at 1036 K which is not clearly understood. Such additional peaks have been reported by other workers as well [47]. We see a shift in the DTA peak position to lower temperatures in $\text{BiFe}_{1-x}\text{Mn}_x\text{O}_3$ with increase in x . Thus, when $x = 0.3$,

the DTA peak due to the ferroelectric transition occurs at 933 K. The inset in fig. 4.32 clearly reveals a regular decrease in the ferroelectric transition temperature with the increase in the Mn content.

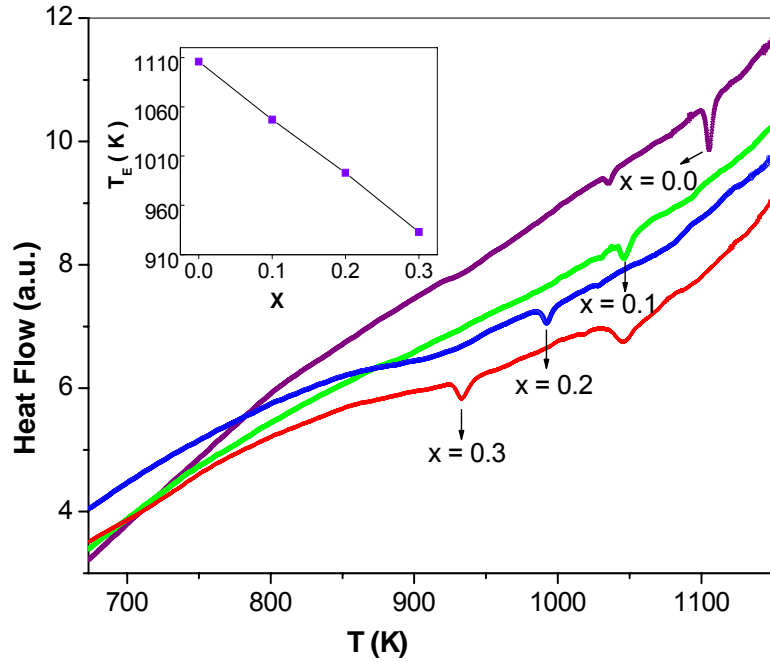


Fig. 4.32: DTA curves showing ferroelectric transitions in $\text{BiFe}_{1-x}\text{Mn}_x\text{O}_3$. The inset shows the linearity of the ferroelectric transition temperature (T_E) with Mn-content.

Fig. 4.33 shows the variation of the dielectric constant as a function of frequency in the range 100 Hz to 1 MHz at room temperature for $\text{BiFe}_{1-x}\text{Mn}_x\text{O}_3$. All the samples exhibit dielectric dispersion. A notable feature is that with the increase in Mn doping, the dielectric constant increases to a high value, reaching values above 10000 at 100 Hz for the $x = 0.3$ composition. The value of the dielectric constant is high at low frequencies and decreases with the increase in frequency and is nearly constant at high frequencies. The dissipation factor, $\tan \delta$, which is the dielectric loss follows the same trend as the

dielectric constant over the whole frequency range of 100 Hz-1 MHz. From these results, we conclude that Mn substitution in the Fe site has beneficial effect with respect to the dielectric properties.

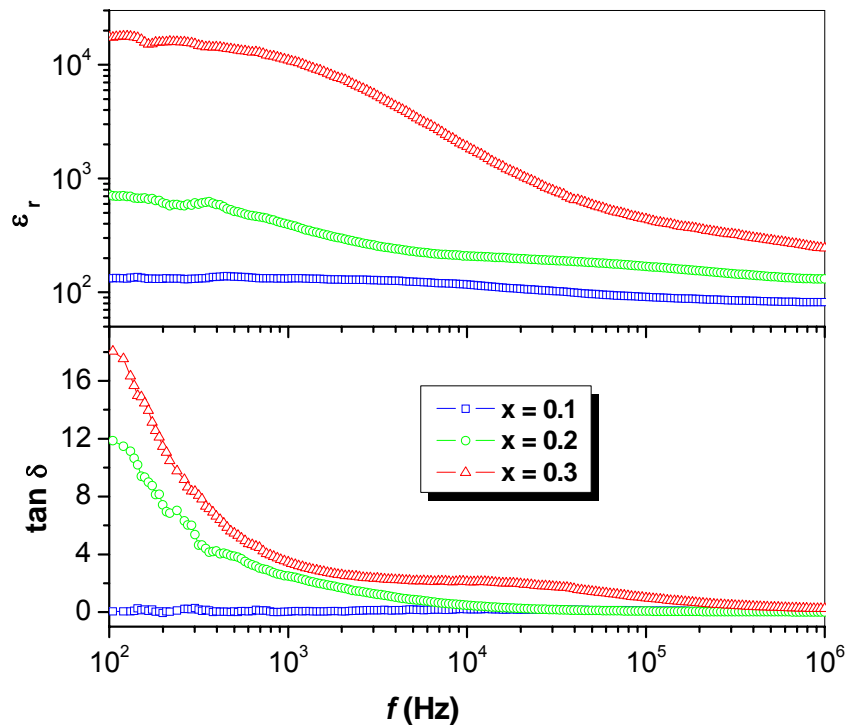


Fig. 4.33: Dielectric behavior of Bi(Fe, Mn)O₃ as a function of frequency (100Hz -1 MHz).

Fig. 4.34 shows the XRD patterns for the samples of the compositions Bi_{1-x}La_xFeO₃ (x = 0.1, 0.2, 0.3). When x = 0.1, the material has the same hexagonal structure as BiFeO₃ with the space group of R3c. However, when x ≥ 0.2, the symmetry becomes C222 with the orthorhombic structure. The lattice parameters of the various compositions are given in table 4.7.

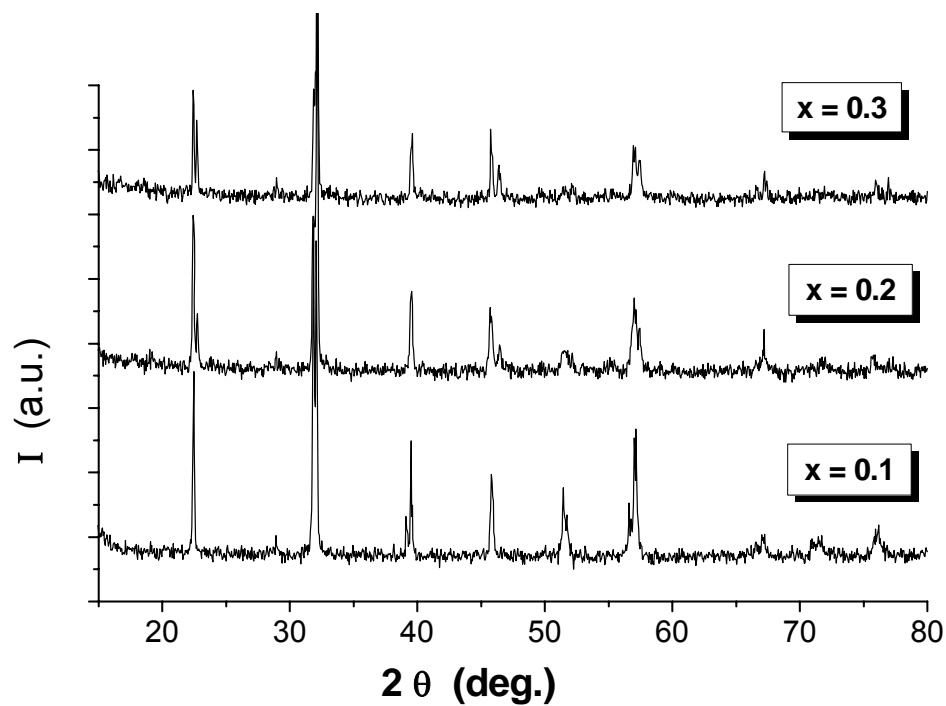


Fig. 4.34: XRD patterns of $\text{Bi}_{1-x}\text{La}_x\text{FeO}_3$ ($x = 0.1, 0.2, 0.3$)

Table 4.7: Lattice Parameters of $\text{Bi}_{1-x}\text{La}_x\text{FeO}_3$ ($x = 0.1 - 0.3$)

x	Space Group	a (Å)	b (Å)	c (Å)
0.1	R3c	5.581	5.581	13.809
0.2	C222	5.59	5.62	3.91
0.3	C222	5.60	5.61	3.91

We now focus our attention on the influence of the La substitution in BiFeO_3 upon the magnetic properties. In fig. 4.35, the variation of the field-cooled magnetization for $\text{Bi}_{1-x}\text{La}_x\text{FeO}_3$ is shown over the 5 - 400 K range at an applied magnetic field of 1000 Oe. There is a marked increase in the magnetization value with the increase in the La content. The transition temperature due to canted antiferromagnetism is observed at 329 K (T_N) for the $x = 0.3$ composition.

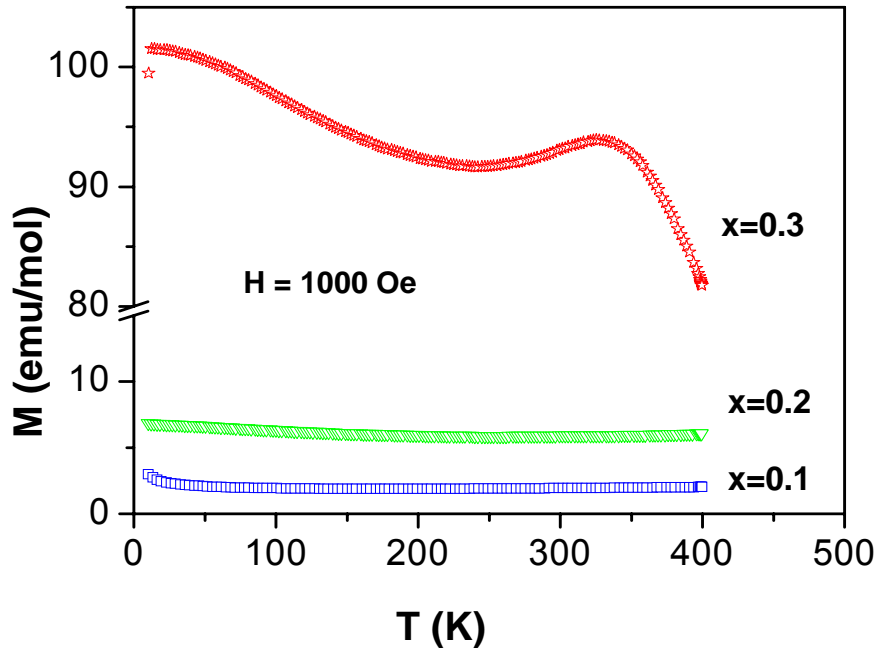


Fig. 4.35: FC magnetization plots of $\text{Bi}_{1-x}\text{La}_x\text{FeO}_3$ at $H=1000$ Oe.

We observe magnetic hysteresis at room temperature for all the samples with $x > 0.0$ whereas we don't observe hysteresis for $x = 0.1$ at 10 K (Fig. 4.36). The values of the coercive field (H_C) at 300 K are 1089 Oe, 7357 Oe and 1102 Oe for $x = 0.1$, 0.2 and 0.3 respectively. The corresponding values of the remnant magnetization are 5, 62 and 86 emu/mol suggesting increased ferromagnetic interactions with increasing La

content in $\text{Bi}_{1-x}\text{La}_x\text{FeO}_3$. But these values don't undergo substantial changes at low temperature.

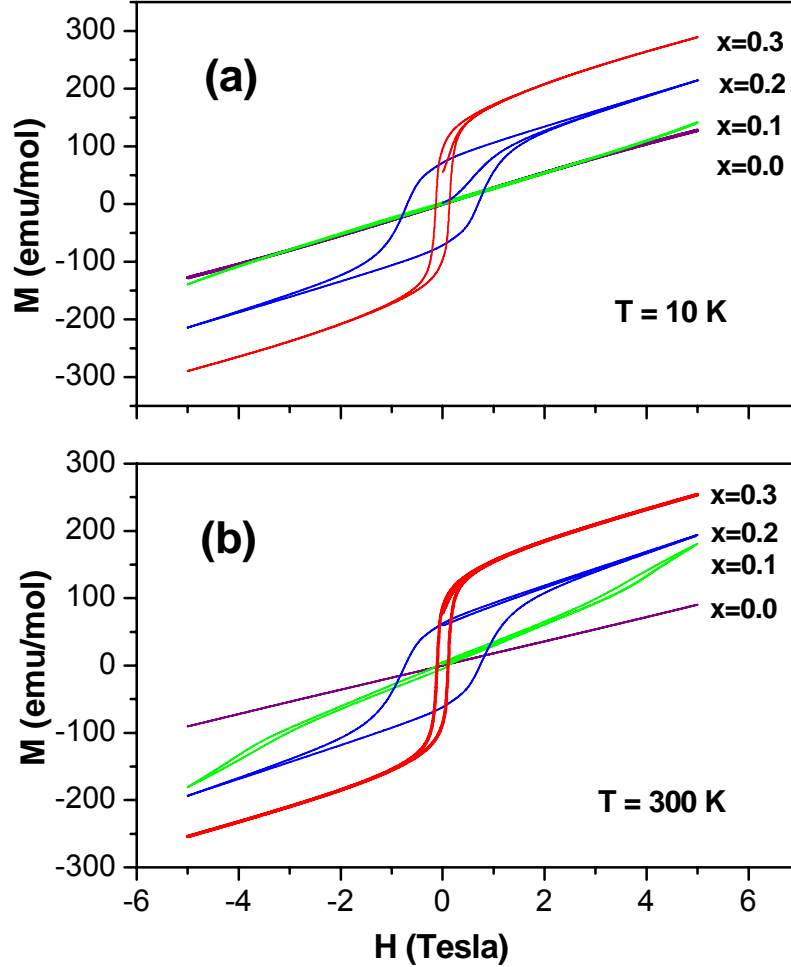


Fig. 4.36: M vs H plots for $\text{Bi}_{1-x}\text{La}_x\text{FeO}_3$ at (a) 10 K and (b) 300 K respectively.

The ferroelectric transitions in $\text{Bi}_{1-x}\text{La}_x\text{FeO}_3$ were examined by DTA measurements (Fig. 4.37). We observe endothermic peaks due to the ferroelectric transition at 875 K and 624 K for the $x = 0.1$ and $x = 0.3$ compositions respectively. We have measured P-E curves of $\text{Bi}_{0.7}\text{La}_{0.3}\text{FeO}_3$ at 298 K and obtained the hysteresis loop shown in the inset of fig. 4.37.

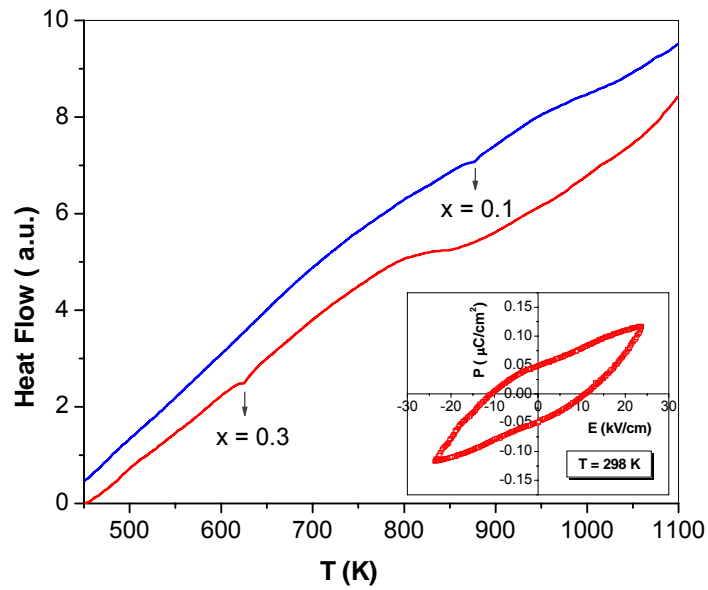


Fig. 4.37: DTA curves showing the ferroelectric transitions in $\text{Bi}_{1-x}\text{La}_x\text{FeO}_3$. Inset shows the $P \sim E$ loop of $\text{Bi}_{0.7}\text{La}_{0.3}\text{FeO}_3$ at $T = 298 \text{ K}$.

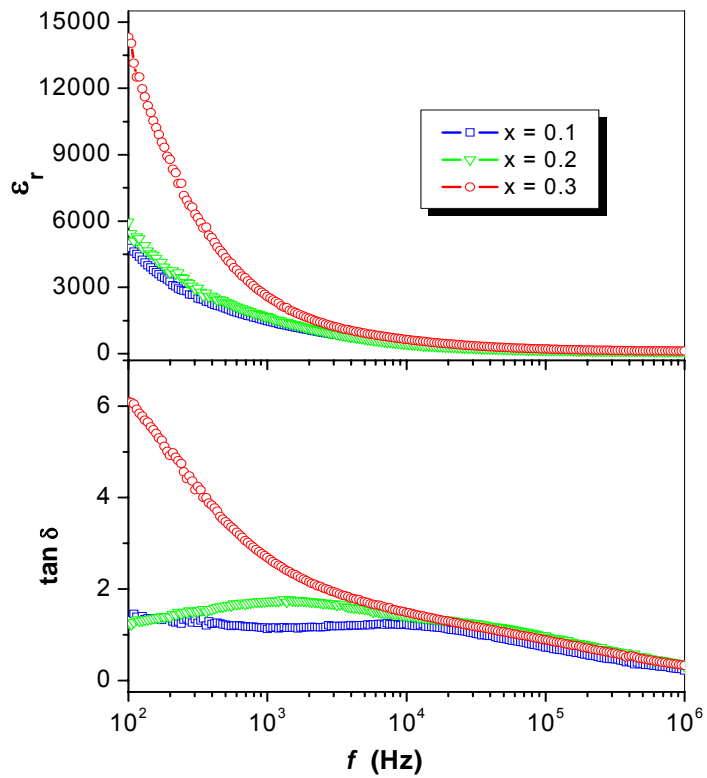


Fig. 4.38: Dielectric properties of $(\text{Bi}, \text{La})\text{FeO}_3$ in the frequency range 100 Hz-1 MHz.

The frequency-dependent dielectric behavior of $\text{Bi}_{1-x}\text{La}_x\text{FeO}_3$ is similar to that of $\text{BiFe}_{1-x}\text{Mn}_x\text{O}_3$ with the dielectric constant increasing with the La content, the maximum value being 14100 at 100 Hz for the $x = 0.3$ composition (Fig. 4.38). With the increase in frequency, the dielectric constant registers a decrease and remains almost constant beyond 10^5 Hz. The dissipation factor decreases appreciably with frequency over the whole range of frequency taken i.e. 100 Hz-1 MHz.

Conclusions

The present investigation of $\text{BiFe}_{1-x}\text{Mn}_x\text{O}_3$ and $\text{Bi}_{1-x}\text{La}_x\text{FeO}_3$ has revealed that cation substitutions in the Fe site by Mn and in the Bi site by La have beneficial effects on the multiferroic properties. We have not been able to obtain satisfactory samples of the compounds where Bi and Fe are substituted by La and Mn respectively, but even one of the substitutions seems to be sufficient, improving the properties of BiFeO_3 for possible applications.

4.5 Charge-ordered multiferroic rare-earth ferrites, LnFe_2O_4

Summary*

We synthesized a series of rare earth ferrites by sealed tube and reducing atmosphere method. Electronic and magnetic properties of YFe_2O_4 , ErFe_2O_4 , $\text{Lu}_{0.5}\text{Y}_{0.5}\text{Fe}_2\text{O}_4$ and YbFe_2O_4 have been investigated to establish the magnetodielectric effect in them. All the rare earth ferrites show a ferrimagnetic transition around 250 K. They also show a divergence between the zero field cooled and field cooled data indicating the possible existence of magnetic domains. Frequency and temperature dependent dielectric constant data show a sudden increase in the dielectric constant near the magnetic transition temperature. Most of the rare earth ferrites show a magnetodielectric effect on the application of magnetic field. YFe_2O_4 shows a positive magnetocapacitive effect while $\text{Lu}_{0.5}\text{Y}_{0.5}\text{Fe}_2\text{O}_4$ shows a weak negative magnetocapacitive effect around the magnetic transition temperature. ErFe_2O_4 shows negative magnetocapacitive effect at $T < T_N$ and a positive magnetocapacitive effect above T_N . The dielectric dispersion of LnFe_2O_4 can be understood qualitatively on the basis of the charge frustration of the iron ions in the two-dimensional triangular lattice, where the electrons hop between Fe^{2+} and Fe^{3+} ions. The origin of ferroelectricity is basically related to the charge-ordering transition arising from strong electron correlation.

* Paper based on this study has appeared in *J. Appl. Phys.* (2008)

Charge-ordered multiferroic rare-earth ferrites, LnFe_2O_4

Polycrystalline samples of rare earth ferrites LnFe_2O_4 ($\text{Ln} = \text{Y}, \text{Er}, \text{Lu}_{0.5}\text{Y}_{0.5}$ and Yb) were prepared by sealed tube and reducing atmosphere method discussed earlier in experimental section. They were found to be in a single phase with the rhombohedral R-3m structure. The lattice parameters of these rare earth ferrites are given in table 4.8.

Table 4.8: Unit cell parameters of the rare earth ferrites (space group R-3m)

	a = b (Å)	c (Å)
YFe_2O_4	3.524	24.787
ErFe_2O_4	3.491	24.924
$\text{Lu}_{0.5}\text{Y}_{0.5}\text{Fe}_2\text{O}_4$	3.468	25.132
YbFe_2O_4	3.473	25.201

The FC and ZFC magnetic measurements were carried out at 100 Oe magnetic field in the temperature range 5-300 K. Magnetization data of YFe_2O_4 , ErFe_2O_4 , $\text{Lu}_{0.5}\text{Y}_{0.5}\text{Fe}_2\text{O}_4$ and YbFe_2O_4 as a function of temperature is shown in fig. 4.39 (a), (b), (c) and (d) respectively. The magnetic behaviors of YFe_2O_4 and $\text{Lu}_{0.5}\text{Y}_{0.5}\text{Fe}_2\text{O}_4$ are similar while ErFe_2O_4 and YbFe_2O_4 behave in a similar way with a rise in the magnetization at low temperature which may be attributed to the ordering of f-electrons. We observe the occurrence of ferrimagnetic transition around 240 K for YFe_2O_4 which slightly increases with the decrease in the size of the A-site ions for other members. As the Fe ions have an

average valence of 2.5+, an equal amount of the Fe^{2+} and Fe^{3+} ions coexist on the same lattice. Strong magnetic interactions between the localized Fe moments give rise to ferrimagnetic ordering below Neel temperatures [48]. The discrepancy between the FC and ZFC curves suggest the existence of short-ranged magnetic clusters [49].

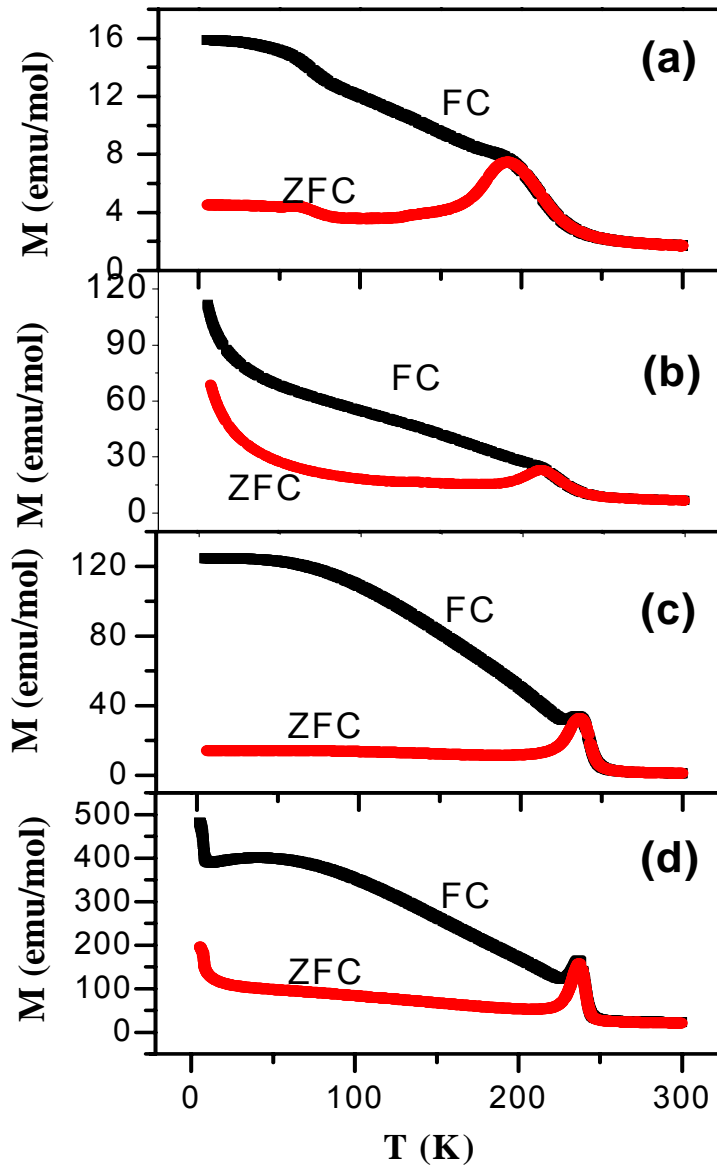


Fig 4.39: Temperature dependence of magnetization for (a) YFe_2O_4 , (b) ErFe_2O_4 (c) $\text{Lu}_{0.5}\text{Y}_{0.5}\text{Fe}_2\text{O}_4$ and (d) YbFe_2O_4 at 100 Oe. The black squares denote FC and red circles denote ZFC data.

We measured the capacitance and dielectric loss from 100 Hz to 1 MHz in the temperature range 50-300 K with 5 K interval between each two measurements. Frequency and the temperature dependent dielectric constant data of YFe_2O_4 are shown in fig. 4.40(a) for a few selected frequencies. Figure 4.40(b) shows the dielectric loss with respect to temperature for the same set of frequencies.

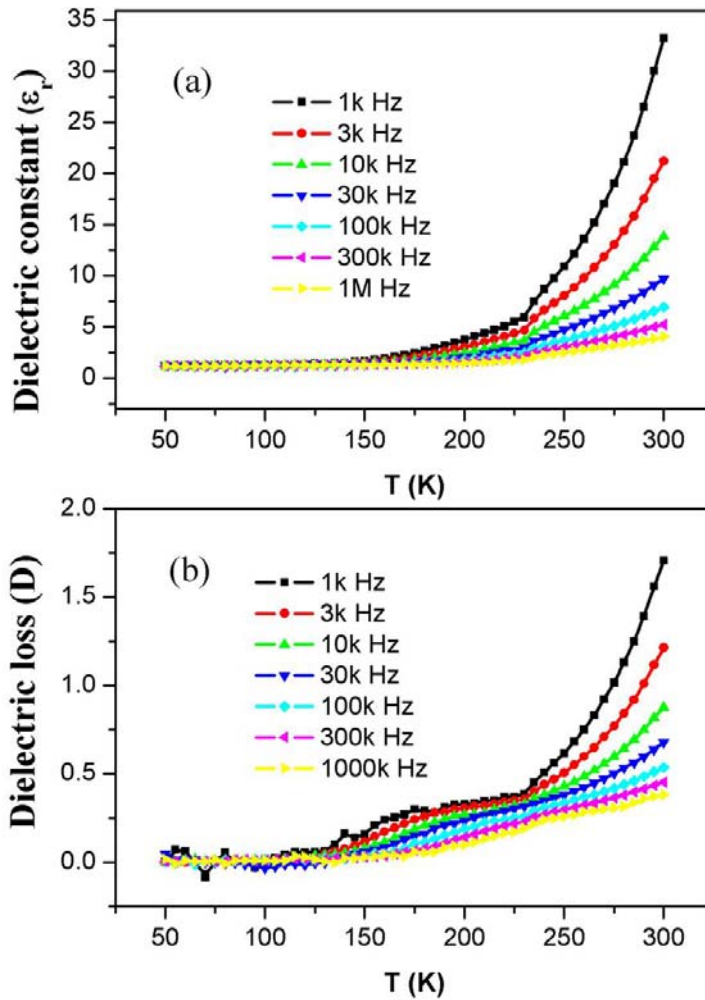


Fig. 4.40: (a) Dielectric constant (ϵ_r) and (b) Dielectric loss (D) plotted against the temperature for YFe_2O_4 at different frequencies.

We observed a marked increase in the dielectric constant near the magnetic transition temperature. Since the unit cell of electric polarization and ferromagnetic polarization is same, a strong correlation exists between the spin and the charge orderings of the Fe ions [50]. So, we would expect the dielectric properties to change at the magnetic transition. To investigate the magneto-dielectric behavior, we measured the dielectric properties at 0, 1 T and 2 T magnetic fields. Figure 4.41 demonstrates the magnetocapacitance behavior of the YFe_2O_4 in a heating cycle.

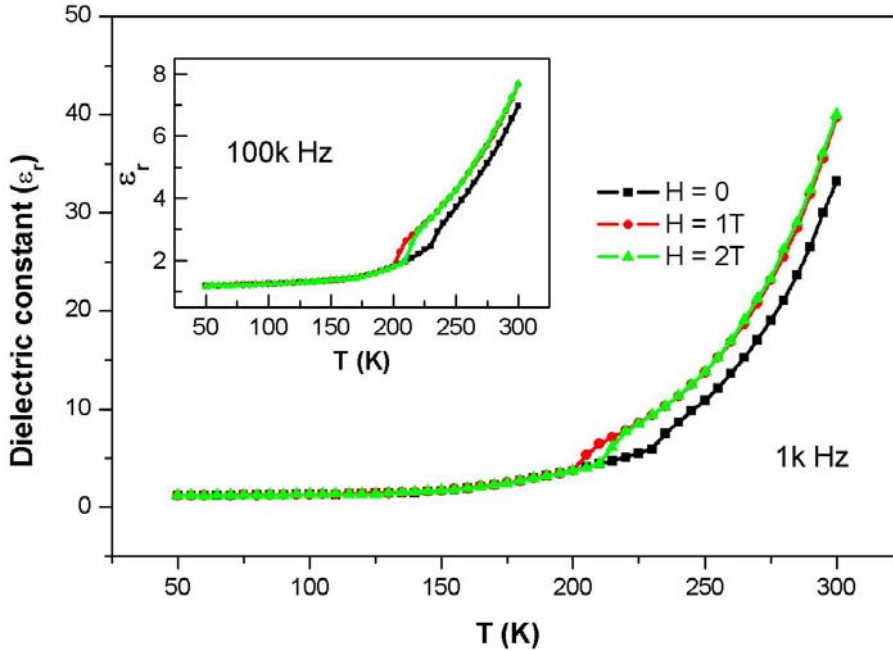


Fig. 4.41: Dielectric constant (ϵ_r) versus temperature of YFe_2O_4 measured at 0, 1 and 2 T for the frequency 1 kHz. The inset shows the the data for 100 kHz.

From the fig. 4.41, it is clear that YFe_2O_4 shows a positive magnetocapacitive effect above the magnetic transition temperature. It is noteworthy that the measurement at 2 T does not show any significant change from that of 1 T indicating the saturation of magneto-dielectric effect. Although the observed large change in the dielectric

permittivity can be correlated with a nonzero value of the magnetoelectric susceptibility, it is an indirect indication of the magnetoelectric coupling under a static magnetic field condition. The static charge structure in YFe_2O_4 can be affected by the application of an external magnetic field in the non-magnetic phase as in the case of LuFe_2O_4 . The room-temperature magnetoelectric effect in this multiferroic system is a direct result of the field affecting the static charge order [51].

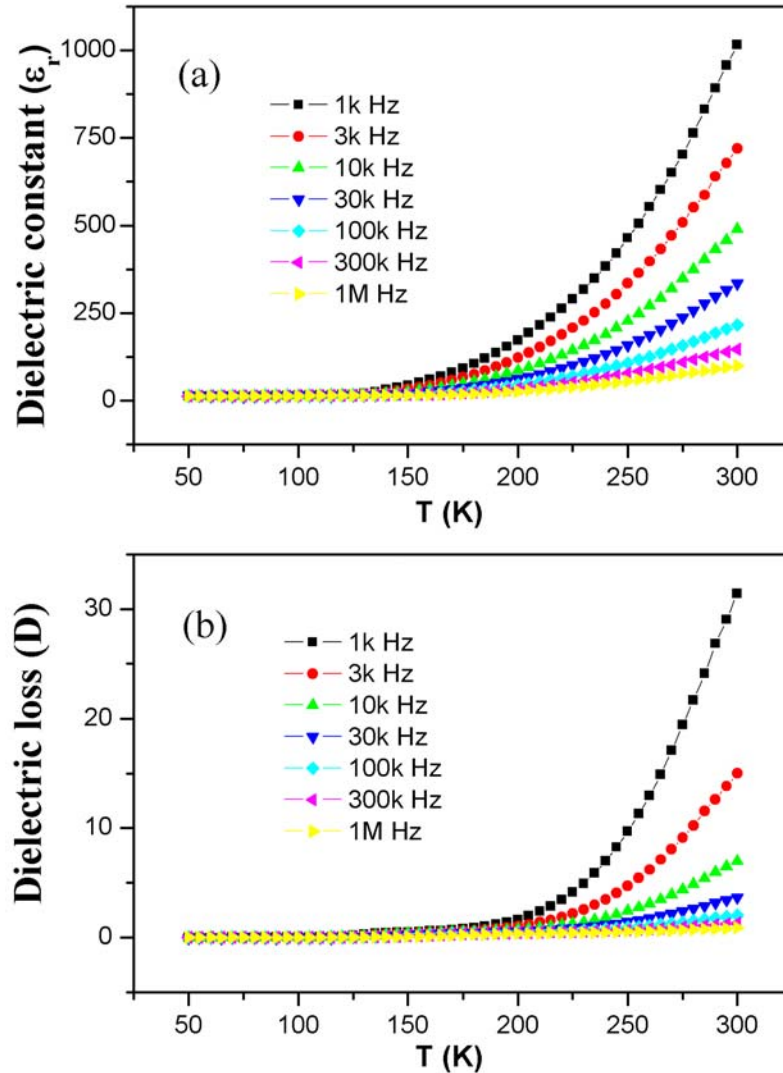


Fig. 4.42: (a) Dielectric constant (ϵ_r) and (b) Dielectric loss (D) plotted against the temperature for $\text{Lu}_{0.5}\text{Y}_{0.5}\text{Fe}_2\text{O}_4$ at different frequencies.

Data of dielectric constant for $\text{Lu}_{0.5}\text{Y}_{0.5}\text{Fe}_2\text{O}_4$ is shown in figure 4.42(a) while that of dielectric loss is shown in figure 4.42(b). The dielectric dispersion of $\text{Lu}_{0.5}\text{Y}_{0.5}\text{Fe}_2\text{O}_4$ is similar to that of parent compounds LuFe_2O_4 and YFe_2O_4 . Fig. 4.43 shows the magnetocapacitive effect in $\text{Lu}_{0.5}\text{Y}_{0.5}\text{Fe}_2\text{O}_4$. This particular compound shows weak negative magneto-dielectric behavior. This may be because of the fact that LuFe_2O_4 shows a significant negative magnetocapacitive effect while YFe_2O_4 shows positive one. Thus the behavior of $\text{Lu}_{0.5}\text{Y}_{0.5}\text{Fe}_2\text{O}_4$ falls in between the two extreme compositions.

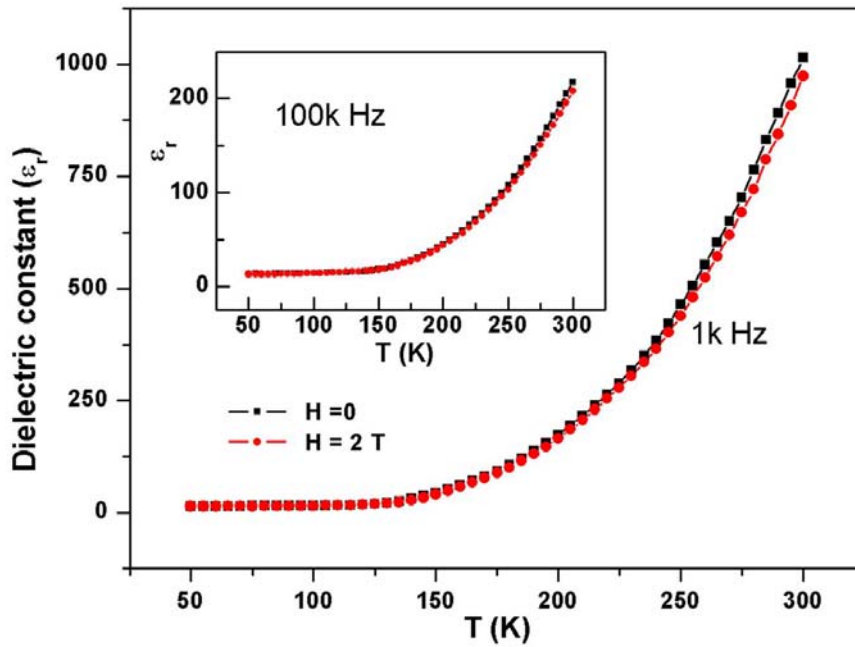


Fig. 4.43: Dielectric constant (ϵ_r) versus temperature of $\text{Lu}_{0.5}\text{Y}_{0.5}\text{Fe}_2\text{O}_4$ measured at 0 and 2 T for 1 kHz. The inset shows the the data for 100 kHz.

Figures 4.44 (a) and (b) show the temperature variation of the dielectric constant and dielectric loss at different frequencies for YbFe_2O_4 . In the case of YbFe_2O_4 , we did not observe appreciable magnetocapacitance.

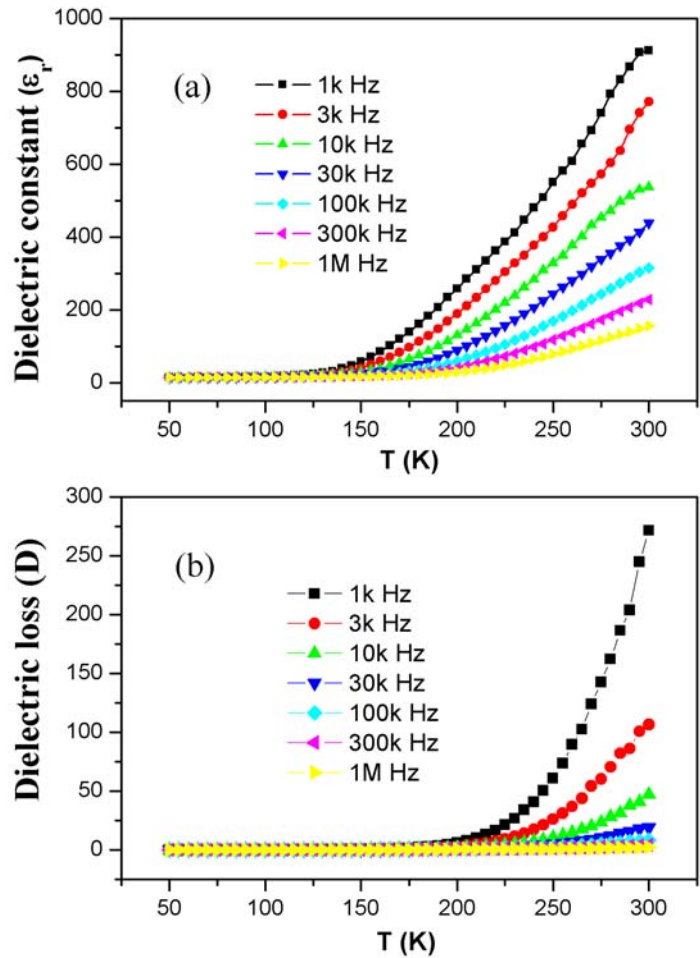


Fig. 4.44: (a) Dielectric constant (ϵ_r) and (b) Dielectric loss (D) plotted against the temperature for YbFe_2O_4 at different frequencies.

Fig. 4.45 shows the temperature variation of the dielectric constant and dielectric loss at different frequencies for ErFe_2O_4 . A large dielectric relaxation, of the order of 10^4 , is observed in the magnetically ordered state in ErFe_2O_4 . We observe a definitive dielectric constant maximum near the magnetic transition temperature (T_N) in the case of ErFe_2O_4 , as can be seen in fig. 4.45 (a). The very high dielectric constant of this ferrite at T_N is noteworthy. In the case of ErFe_2O_4 , the position of the dielectric maximum at T_N shifts to higher temperatures on the application of magnetic fields, as shown in fig. 4.46. Accordingly, ErFe_2O_4 shows negative magnetocapacitive effect at $T < T_N$ and a positive magnetocapacitive effect above T_N .

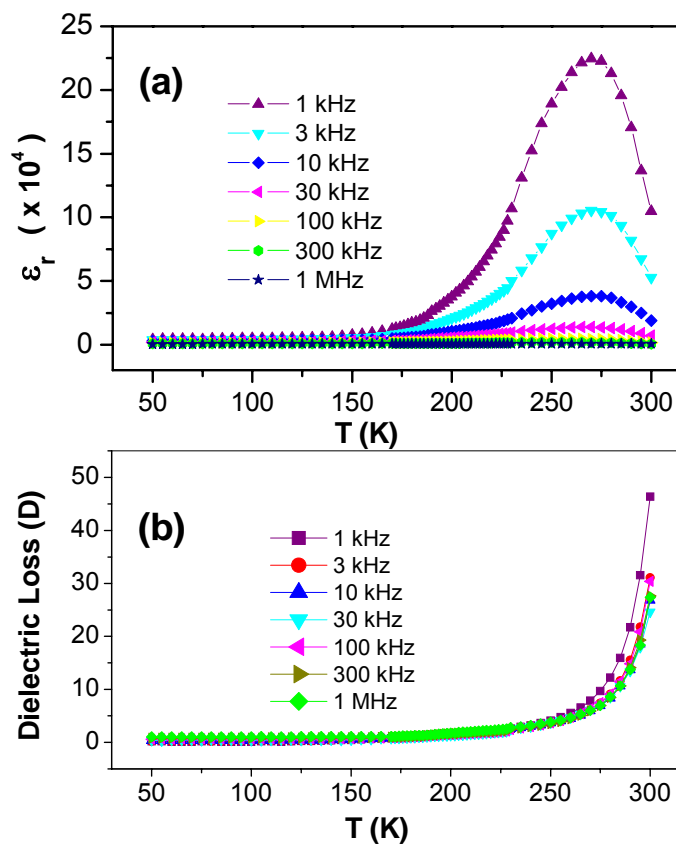


Fig. 4.45: (a) Dielectric constant (ϵ_r) and (b) Dielectric loss (D) plotted against the temperature for ErFe_2O_4 at different frequencies.

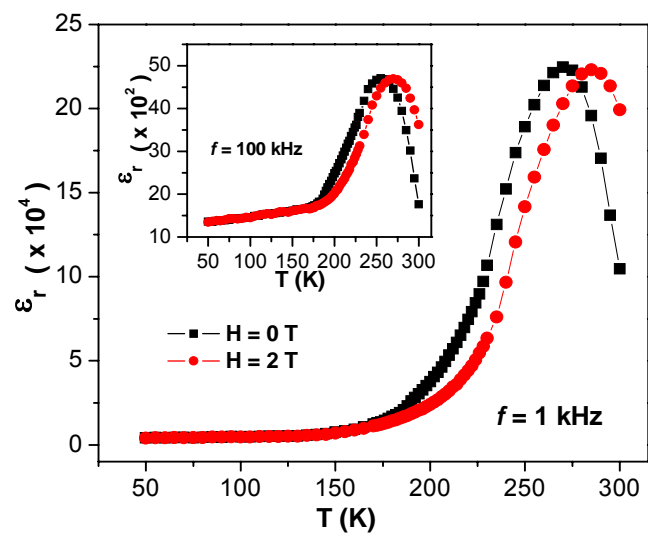


Fig. 4.46: Dielectric constant vs temperature of ErFe_2O_4 measured at 0 and 2 T for the frequency 1 kHz. The inset shows the data for 100 kHz.

We observe a sudden increase in dielectric constant near the magnetic transition temperature in all the ferrites. However, the difference in dielectric behavior of the ferrites with different rare earth ions may be attributed to the change in the ionic size and related polyhedral distortions. Electron hopping expected between Fe^{2+} and Fe^{3+} ions within the layer leads to high electrical conductivity. So it is not possible to carry out the direct measurement of electric polarization by P-E hysteresis loop. The superstructure formed by the Fe^{2+} and Fe^{3+} ions supports electric polarization since the centers of Fe^{2+} and Fe^{3+} ions do not coincide [52-54]. The dielectric dispersion of LnFe_2O_4 can be understood qualitatively on the basis of the charge frustration of the iron ions in the two-dimensional triangular lattice, where the electrons hop between Fe^{2+} and Fe^{3+} ions [55-57] and the origin of ferroelectricity is basically related to the charge-ordering transition arising from strong electron correlation [57,58], even without a pairing of anion and cation which is the case of usual off-centering ferroelectrics. Thus, rare earth ferrites belong to “electronic ferroelectrics” that originate from electron correlations rather than from the covalency between anions and cations. The polarization of the ordered electrons is originated from the competitive coulomb interactions between charges [55].

Conclusions

In conclusion, we have been able to demonstrate that several members of the rare earth ferrite family are magneto-dielectric because of the presence of cation charge-ordering. All the rare earth ferrites, YFe_2O_4 , ErFe_2O_4 , $\text{Lu}_{0.5}\text{Y}_{0.5}\text{Fe}_2\text{O}_4$ and YbFe_2O_4 show a ferrimagnetic transition around 250 K. Frequency and temperature dependent dielectric constant data show a sudden increase in the dielectric constant near the magnetic

transition temperature. YFe_2O_4 shows a positive magnetocapacitive effect while $\text{Lu}_{0.5}\text{Y}_{0.5}\text{Fe}_2\text{O}_4$ shows a weak negative magnetocapacitive effect around the magnetic transition temperature. ErFe_2O_4 shows negative magnetocapacitive effect at $T < T_N$ and a positive magnetocapacitive effect above T_N whereas YbFe_2O_4 does not exhibit magnetocapacitance. The coupling between the electric and magnetic order parameters in the rare earth ferrites can be exploited technologically in memory devices, recording and other applications.

4.6 Charge-ordered manganites

4.6.1 $\text{Ln}_{1-x}\text{A}_x\text{MnO}_3$ (Ln = Rare earth, A = Alkaline earth)

Summary*

We have investigated the magnetic properties, dielectric properties and magneto-dielectric properties of charge-ordered rare earth Manganites $\text{Nd}_{0.5}\text{Ca}_{0.5}\text{MnO}_3$, $\text{Pr}_{0.6}\text{Ca}_{0.4}\text{MnO}_3$, $\text{Y}_{0.6}\text{Ca}_{0.4}\text{MnO}_3$, $\text{Y}_{0.5}\text{Ca}_{0.5}\text{MnO}_3$ and $\text{Y}_{0.55}\text{Ca}_{0.45}\text{MnO}_3$ which have comparable radii of the A-site cations. These rare earth manganites show antiferromagnetic transition in the 130-170 K region and exhibit charge-ordering in the 220-240 K region. They are all found to exhibit dielectric constant anomalies around the charge-ordering or the antiferromagnetic transition temperatures. Magnetic fields have a marked effect on the dielectric properties, indicating the presence of coupling between the magnetic and electrical order parameters. The observation of magnetoferroelectricity in these manganites is in accord with the recent theoretical predictions of Khomskii and co-workers predicted for rare earth manganites of the formula $\text{Ln}_{1-x}\text{A}_x\text{MnO}_3$ [59].

* Paper based on this study has appeared in *Solid State Communications* (2009), *AIP Proceedings* (2008)

$\text{Ln}_{1-x}\text{A}_x\text{MnO}_3$ (Ln = Rare earth, A = Alkaline earth)

The X-ray diffraction patterns of rare earth manganites showed that all the compounds are found to be in single phase belonging to orthorhombic space group Pbnm. The A-site cationic radius, variance and lattice parameters are shown below in table 4.9.

Table 4.9: Structural details of $\text{Ln}_{1-x}\text{Ca}_x\text{MnO}_3$ (Ln = Nd, Gd, Y)

Compounds	$\langle r_A \rangle$ (Å)	σ^2 ($\times 10^{-3} \text{Å}^2$)	Lattice parameters (Å)		
			a	b	c
$\text{Nd}_{0.5}\text{Ca}_{0.5}\text{MnO}_3$	1.1715	0.072	5.378	5.399	7.590
$\text{Gd}_{0.5}\text{Ca}_{0.5}\text{MnO}_3$	1.1435	1.332	5.433	5.437	7.489
$\text{Y}_{0.5}\text{Ca}_{0.5}\text{MnO}_3$	1.1275	2.756	5.304	5.466	7.435
$\text{Y}_{0.55}\text{Ca}_{0.45}\text{MnO}_3$	1.1223	2.725	5.301	5.492	7.436
$\text{Y}_{0.6}\text{Ca}_{0.4}\text{MnO}_3$	1.117	2.646	5.299	5.53	7.436
$\text{Pr}_{0.6}\text{Ca}_{0.4}\text{MnO}_3$	1.1794	0.566	5.435	5.446	7.606

We have measured the magnetic properties of rare earth manganites from 5 K to 300 K in different magnetic fields. $\text{Nd}_{0.5}\text{Ca}_{0.5}\text{MnO}_3$ exhibits a charge-ordered transition at 240 K (T_{CO}), an anti-ferromagnetic transition at 140 K (T_{N}) and another transition to a canted antiferromagnetic state around 50 K as evident at a magnetic field of 100 Oe [60]. The antiferromagnetic transition around 140 K, seen as a shoulder at low magnetic fields, cannot be easily discerned at higher fields [Fig. 4.47]. The transition around 50 K is also wiped out at high fields, the difference between the zero-field-cooled and field-cooled data becoming negligible.

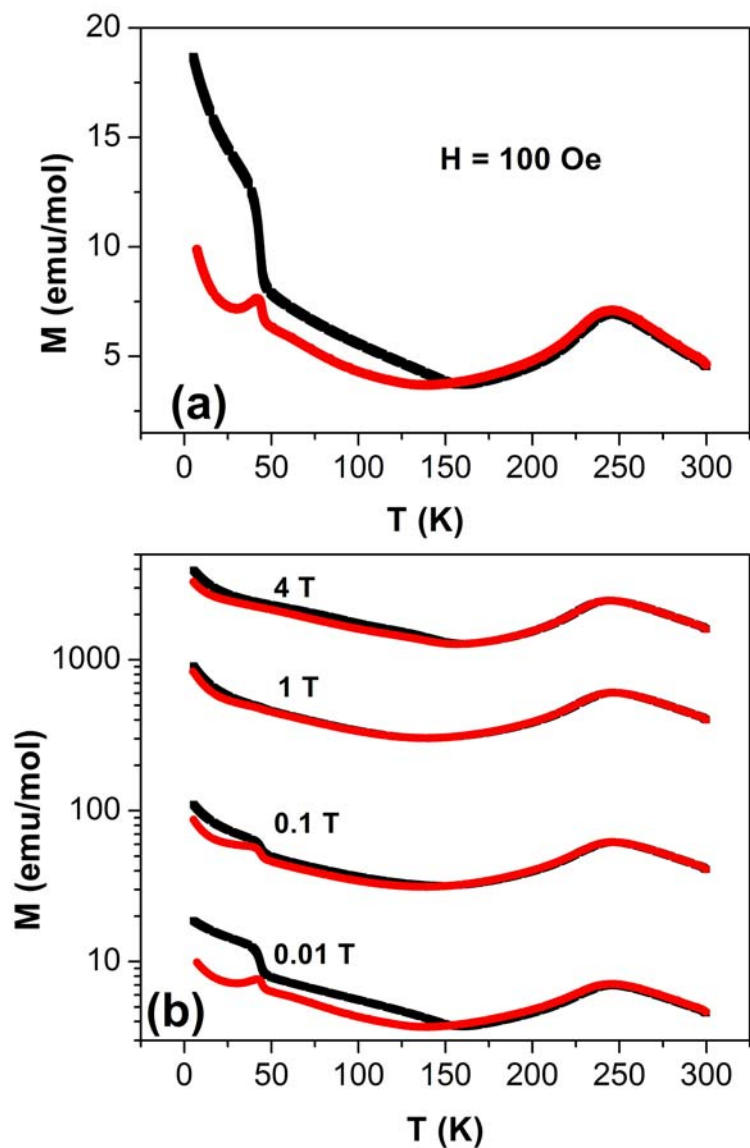


Fig. 4.47: Effect of magnetic fields on the magnetization behavior of $\text{Nd}_{0.5}\text{Ca}_{0.5}\text{MnO}_3$ at (a) 100 Oe (0.01 T) and (b) 0.01 T, 0.1 T, 1 T and 4 T. The black squares indicate field cooled (FC) and red circles indicate zero field cooled (ZFC) data.

The frequency and the temperature dependent dielectric constant data of $\text{Nd}_{0.5}\text{Ca}_{0.5}\text{MnO}_3$ are shown in fig. 4.48. The dielectric constant of $\text{Nd}_{0.5}\text{Ca}_{0.5}\text{MnO}_3$ increases substantially in the region of T_{CO} and T_{N} showing a broad maximum, reaching a value of 500 or above. To investigate the magneto-dielectric properties we measured the dielectric constant in the presence of magnetic field. Application of a magnetic field of

3.3 T has a significant effect on the dielectric constant as seen from fig. 4.49. $\text{Nd}_{0.5}\text{Ca}_{0.5}\text{MnO}_3$ shows a colossal magneto-dielectric effect below T_N . This demonstrates that there is coupling between the electrical and magnetic order parameters in $\text{Nd}_{0.5}\text{Ca}_{0.5}\text{MnO}_3$.

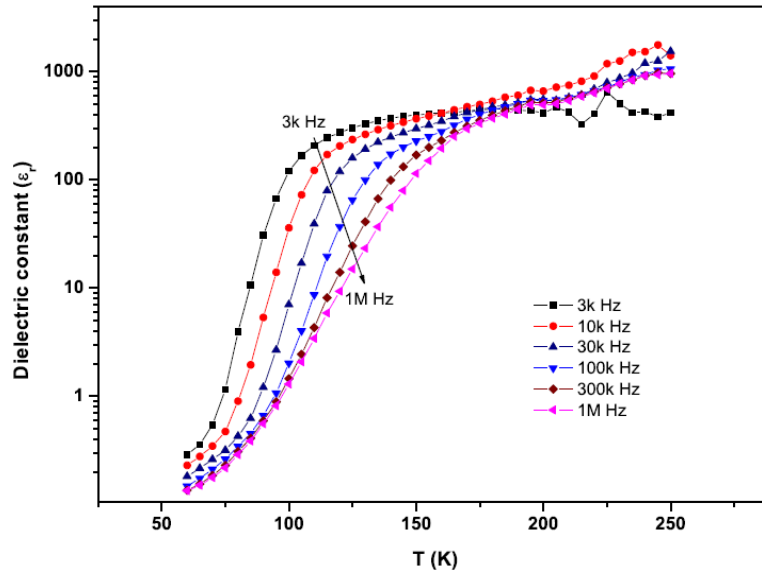


Fig 4.48: Temperature variation of dielectric constant (ϵ_r) of $\text{Nd}_{0.5}\text{Ca}_{0.5}\text{MnO}_3$ at different frequencies.

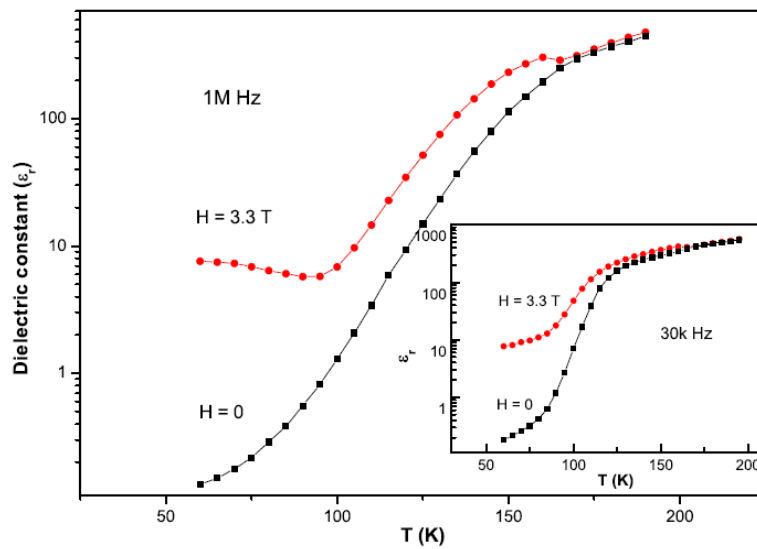


Fig. 4.49: Temperature variation of the dielectric constant (1M Hz) of $\text{Nd}_{0.5}\text{Ca}_{0.5}\text{MnO}_3$ in the absence and presence of a magnetic field ($H = 3.3 \text{ T}$). The inset shows data at 30k Hz.

The case of $\text{Pr}_{0.6}\text{Ca}_{0.4}\text{MnO}_3$ is of special interest because of the presence bond-centered charge ordering (BCO). This manganite exhibits a T_{CO} of 240 K and T_{N} of 170 K [61]. There is an additional magnetic transition around 40 K [Fig. 4.50(a)]. From the fig. 4.50(b) it is clear that with increasing field, the low-temperature transition is affected significantly, the material bearing exhibitory greater ferromagnetic interactions. The dielectric constant of $\text{Pr}_{0.6}\text{Ca}_{0.4}\text{MnO}_3$ shows a broad maximum around T_{N} and the value is also high (Fig. 4.51). Application of a magnetic field of 2 T markedly affects the dielectric properties as shown in figure 4.51.

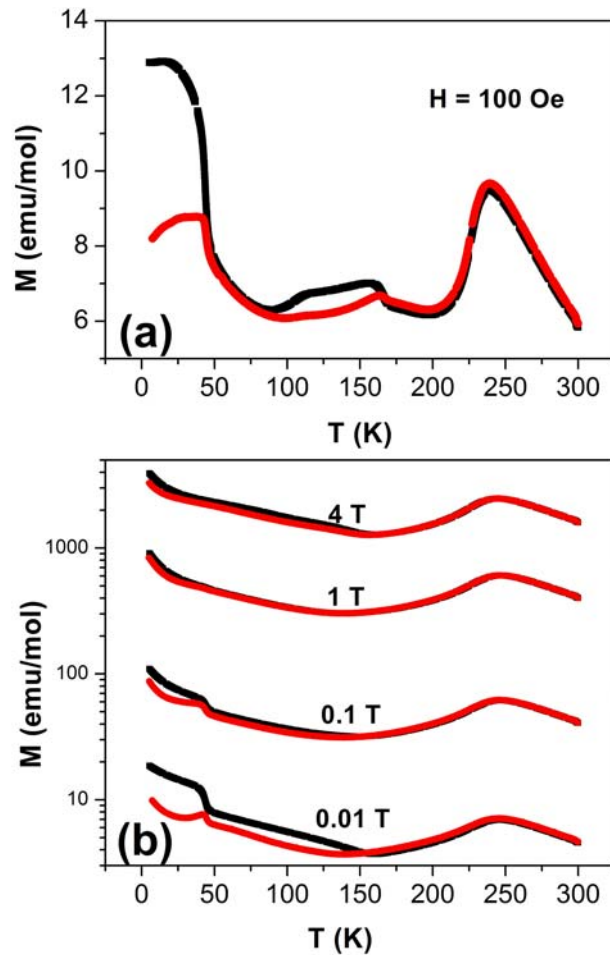


Fig. 4.50: Effect of magnetic fields on the magnetization behavior of $\text{Pr}_{0.6}\text{Ca}_{0.4}\text{MnO}_3$ (a) at 100 Oe (0.01 T) and (b) for 0.01 T, 0.1 T, 1 T and 4 T. The black squares indicate field cooled (FC) and red circles indicate zero field cooled (ZFC) data.

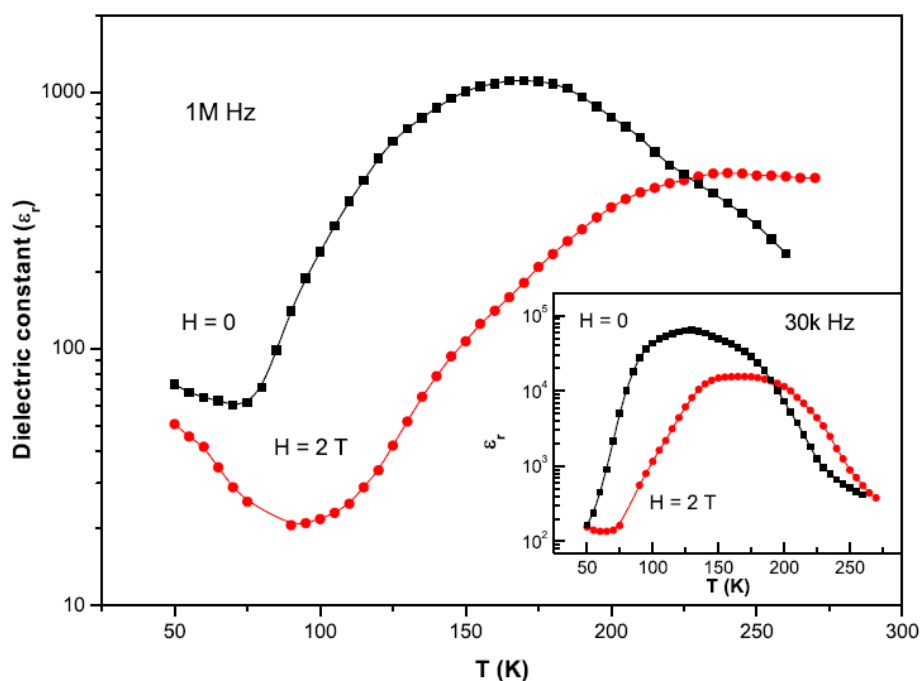


Fig. 4.51: Temperature variation of the dielectric constant (1M Hz) of $\text{Pr}_{0.6}\text{Ca}_{0.4}\text{MnO}_3$ in the absence and presence of a magnetic field ($H = 2$ T). The inset shows data at 30k Hz.

The sign of the magnetocapacitive effect changes with temperature, being negative near T_N and positive near T_{CO} . We observe a crossing of the dielectric constant curves around a temperature between T_{CO} and T_N . The magnetoelectric behavior of this manganite is somewhat different from that of the $\text{Nd}_{0.5}\text{Ca}_{0.5}\text{MnO}_3$. The results, however, demonstrate the presence of magnetoelectricity in all the charge-ordered manganites studied by us as predicted by Khomskii and coworkers [59].

$\text{Gd}_{0.5}\text{Ca}_{0.5}\text{MnO}_3$, with a slightly larger $\langle r_A \rangle$ than $\text{Y}_{0.5}\text{Ca}_{0.5}\text{MnO}_3$ exhibits a T_{CO} of 290 K [62], T_N of 120 K (Fig. 4.52). It shows a ferromagnetic hysteresis loop at low temperature (~ 5 K) with M_r and H_C values of 17.6 emu/mol and 44 Oe respectively.

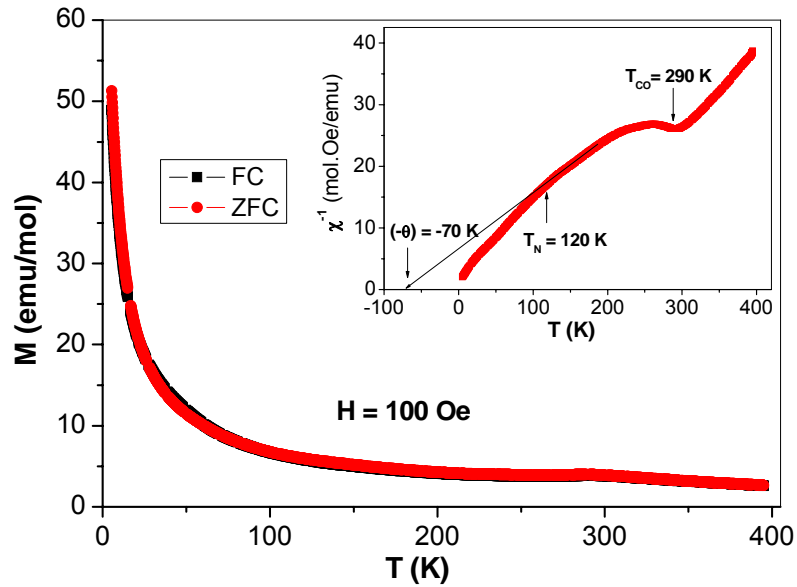


Fig. 4.52: Variation of magnetization of $\text{Gd}_{0.5}\text{Ca}_{0.5}\text{MnO}_3$ with temperature at 100 Oe. Inset shows the temperatures marking the onset of charge-ordering, canted antiferromagnetism and Curie-Weiss temperature.

In fig. 4.53(a), we have shown the temperature variation of dielectric constant for $\text{Gd}_{0.5}\text{Ca}_{0.5}\text{MnO}_3$ at different frequencies. The temperature corresponding to the maximum value of the dielectric constant shifts towards the higher temperature from 250 to 265 K over the frequency range 1 kHz-10 kHz. The maximum value of the dielectric constant is 6.2×10^3 at 10 kHz. The Curie-Weiss plots in the high temperature region ($T > T_{\text{max}}$) yields the ferroelectric transition temperature, T_{FE} , equal to 290 K which is close to the value of T_{CO} . There is a marked decrease observed in the value of dielectric constant when magnetic field is applied, showing the maximum at a relatively lower temperature [Fig. 4.53(b)]. Fig. 4.54 shows the P-E loops of $\text{Gd}_{0.5}\text{Ca}_{0.5}\text{MnO}_3$ at 70 K and 300 Hz corresponding to various values of the voltage in the 500-1500 V range. There is no saturation and the maximum polarization found at 1500 V is $0.328 \mu\text{C}/\text{cm}^2$. The observed values of P_r and E_c at 1500 V are $0.172 \mu\text{C}/\text{cm}^2$ and 4.025 kV/cm respectively.

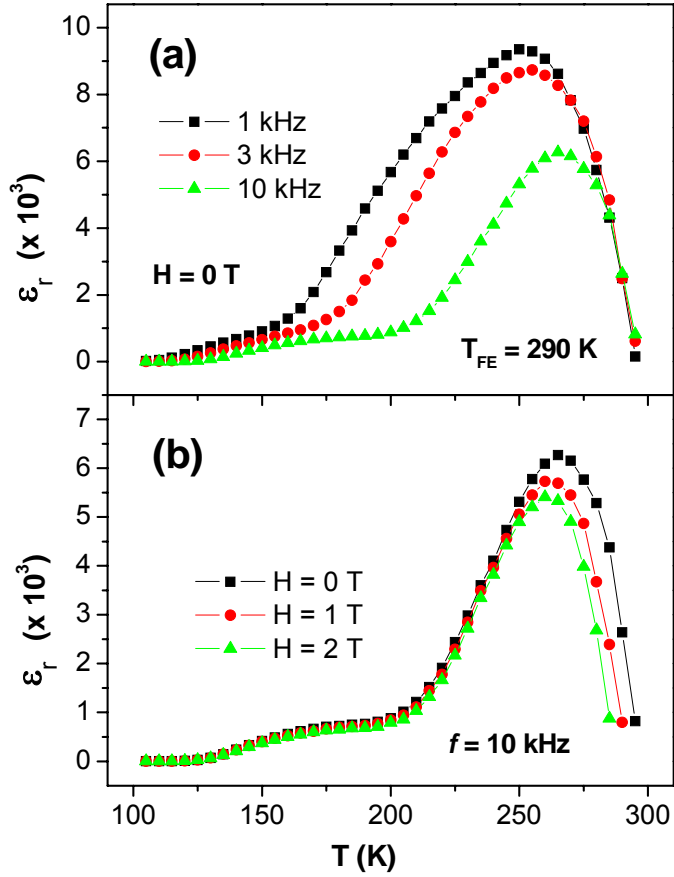


Fig. 4.53: (a) Frequency dependence and (b) magnetic-field dependence (10 kHz) of the dielectric constant of $\text{Gd}_{0.5}\text{Ca}_{0.5}\text{MnO}_3$ varying with temperature.

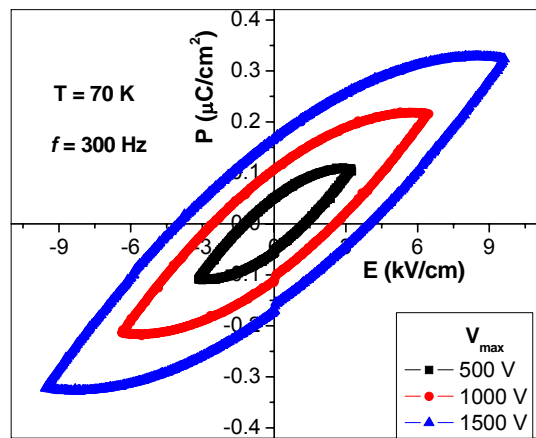


Fig. 4.54: Ferroelectric hysteresis loops of $\text{Gd}_{0.5}\text{Ca}_{0.5}\text{MnO}_3$ (at 300 Hz, 70 K) for various voltages.

$Y_{0.5}Ca_{0.5}MnO_3$, with a slightly smaller $\langle r_A \rangle$ than $Gd_{0.5}Ca_{0.5}MnO_3$, exhibits a charge-ordering transition at 275 K (T_{CO}) and an antiferromagnetic transition at 110 K (T_N) [63] [Fig. 4.55]. Ferromagnetic interactions are manifested at low temperatures due to electronic phase separation [64, 65]. Magnetic hysteresis is observed at $T < 50$ K, the values of remnant magnetization (M_r) and coercive field (H_C) at 5 K being 35 emu/mol and 489 Oe respectively.

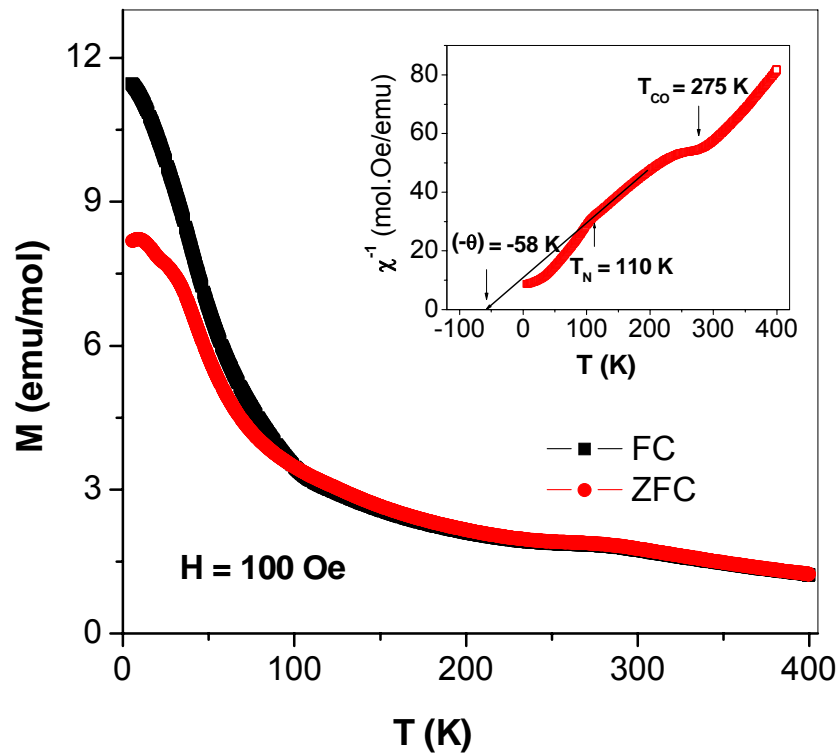


Fig. 4.55: Variation of magnetization of $Y_{0.5}Ca_{0.5}MnO_3$ with temperature at 100 Oe. Inset shows the inverse susceptibility plot marking the onset of charge-ordering, canted antiferromagnetism and Curie-Weiss temperature.

In Fig. 4.56 (a), we have plotted the dielectric constant as a function of temperature for various frequencies. The dielectric constant exhibits a maximum in the 225-240 K range. On increasing the frequency, the dielectric constant decreases markedly

with the maximum shifting to slightly higher temperatures. At 10 kHz, the maximum value of the dielectric constant is 2×10^4 , high compared to other rare-earth manganites. This would be expected considering the robust charge-ordered state and the small size of the yttrium ion. The ferroelectric transition temperature (T_{FE}) derived from the inverse Curie-Weiss plot of dielectric constant is close to T_{CO} . Application of a magnetic field of 1 T has a significant effect on the dielectric constant causing a shift of the dielectric constants maximum to a lower temperature as can be seen in Fig. 4.56 (b).

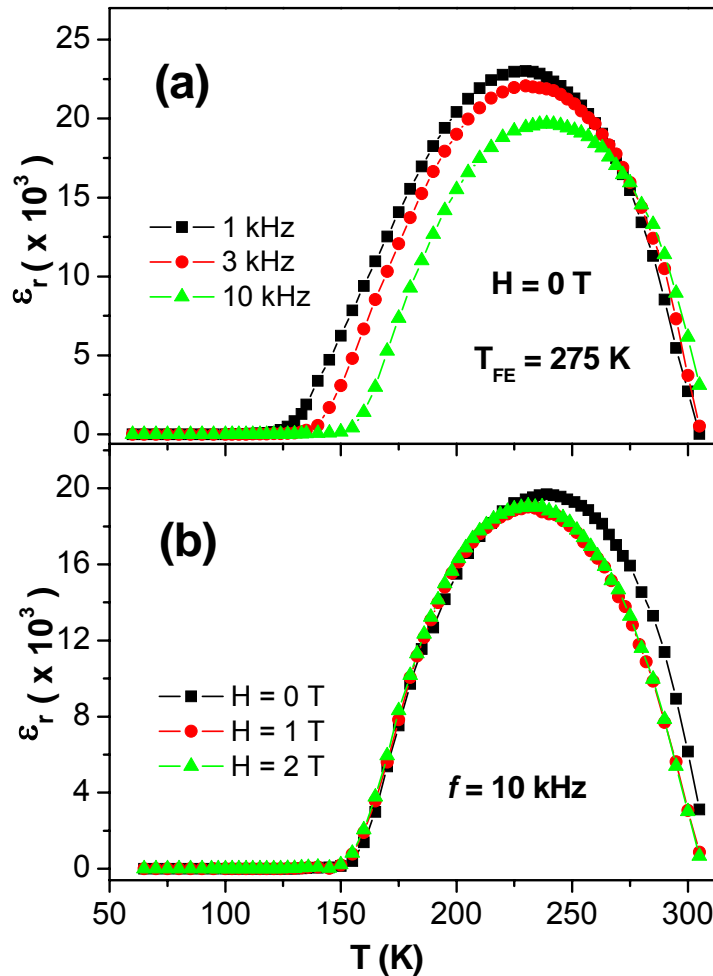


Fig. 4.56: (a) Temperature-dependence of the dielectric constant of $Y_{0.5}Ca_{0.5}MnO_3$ for different frequencies. (b) Effect of magnetic fields on the dielectric behavior of $Y_{0.5}Ca_{0.5}MnO_3$ at 10 kHz.

The magnetocapacitive effect is genuine which is not due to the magneto-resistance, since we do not observe any change in resistance on the application of magnetic fields up to 15 T. In fig. 4.57, we show the polarization (P) - electric field (E) hysteresis in $Y_{0.5}Ca_{0.5}MnO_3$ at 100 K and 200 Hz in applied voltage range of 500 – 1500 V. There is no saturation and the maximum polarization found at 1500 V is $0.355 \mu C/cm^2$. The remanent polarisation (P_r) and coercive field (E_c) are $0.182 \mu C/cm^2$ and 5.215 kV/cm respectively at 1500 V.

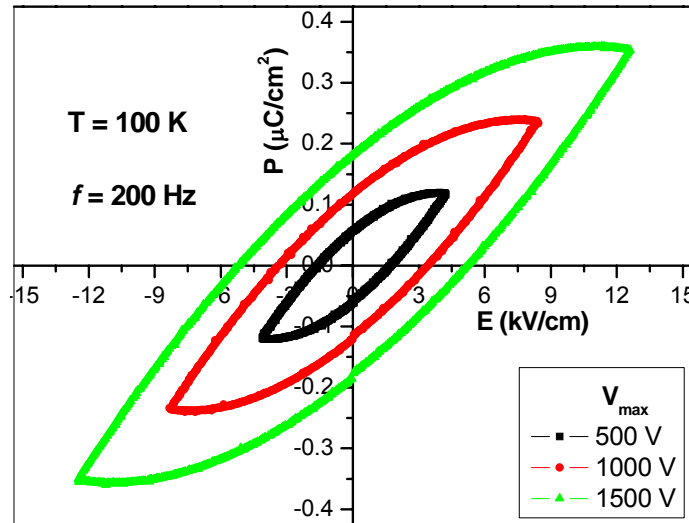


Fig. 4.57: Ferroelectric hysteresis loops of $Y_{0.5}Ca_{0.5}MnO_3$ (at 100 K, 200 Hz) for various voltages.

$Y_{0.6}Ca_{0.4}MnO_3$, with bond-centered charge ordering, shows divergence in the FC and ZFC magnetization curves with possible short-range ferromagnetism below 84 K (Fig. 4.58). We have examined the ferromagnetic hysteresis loop of $Y_{0.6}Ca_{0.4}MnO_3$ at 5 K and found M_r and H_c values of 277 emu/mol and 891 Oe respectively (Fig. 4.59).

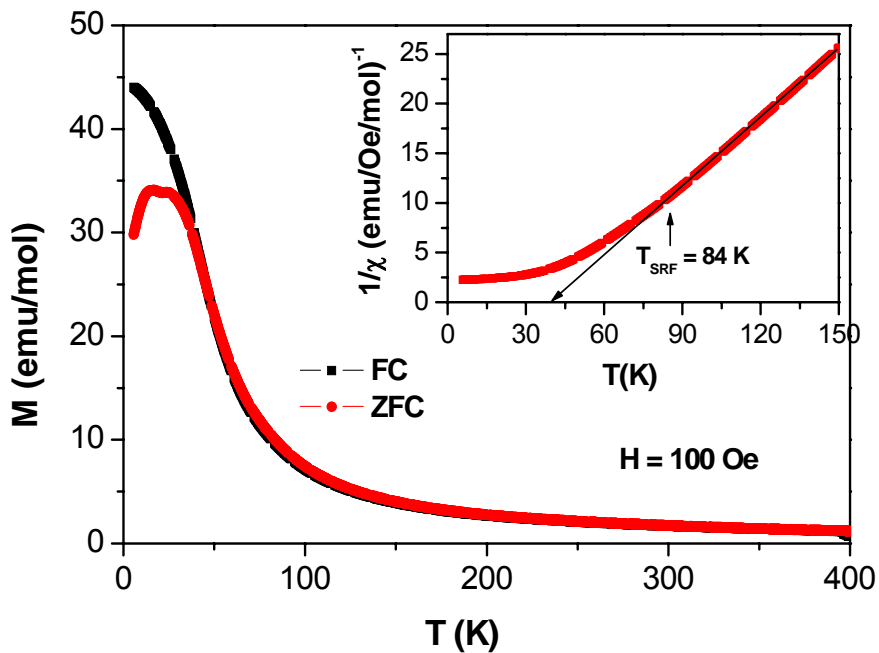


Fig. 4.58: Variation of magnetization of $Y_{0.6}Ca_{0.4}MnO_3$ with temperature at 100 Oe. Inset shows the occurrence of short-range ferromagnetism at 90 K.

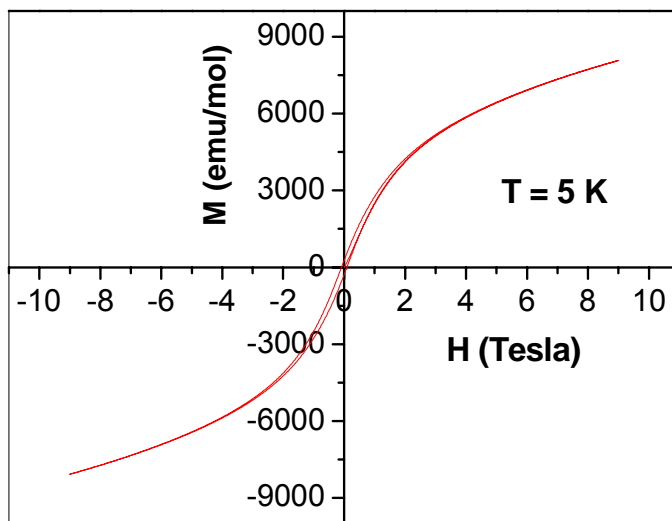


Fig. 4.59: Ferromagnetic hysteresis loop of $Y_{0.6}Ca_{0.4}MnO_3$ at 5 K.

The dielectric constant shows a maximum with the T_{\max} shifting from 227 K to 247 K in 1 kHz-10 kHz range as shown in fig. 4.60(a). The maximum value of dielectric constant at 10 kHz is around 10^5 which is larger than that in $Y_{0.5}Ca_{0.5}MnO_3$. The ferroelectric transition temperature, T_{CE} , is found to be 300 K from the plot of reciprocal dielectric constant versus temperature. Fig. 4.60(b) shows the effect of magnetic fields on the dielectric constant at 10 kHz.

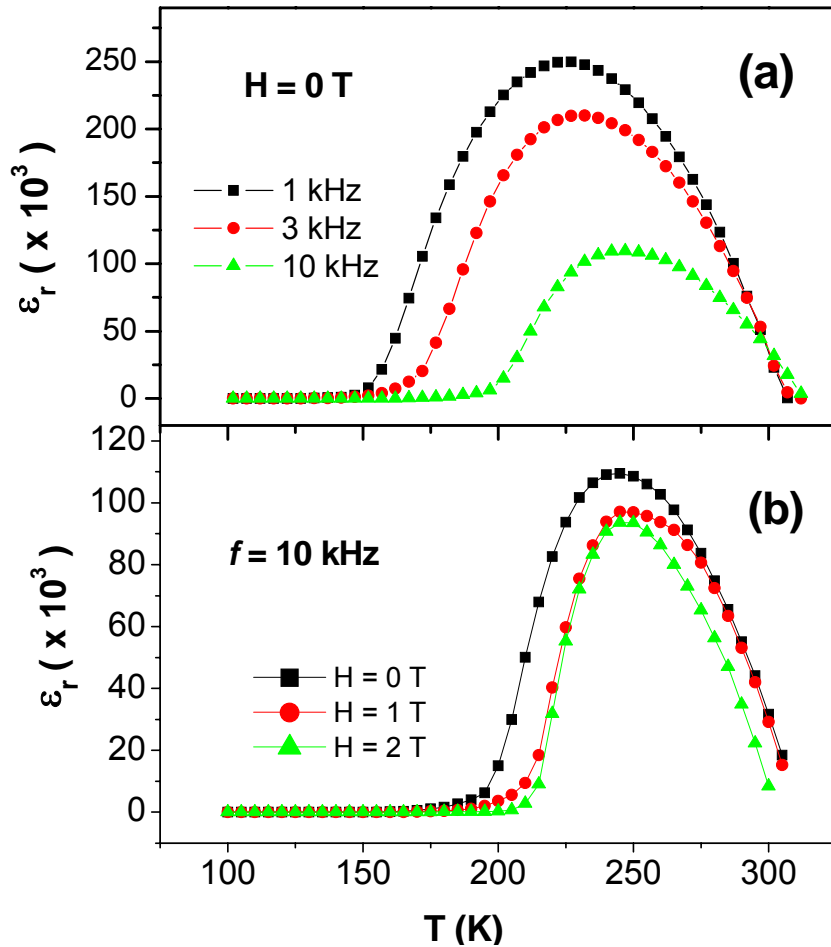


Fig. 4.60: (a) Temperature-dependence of the dielectric constant of $Y_{0.6}Ca_{0.4}MnO_3$ for different frequencies. (b) Effect of magnetic fields on the dielectric behavior of $Y_{0.6}Ca_{0.4}MnO_3$ at 10 kHz.

Investigation of the ferroelectric hysteresis yielded the values $0.145 \mu\text{C}/\text{cm}^2$ and $3.503 \text{ kV}/\text{cm}$ for P_r and E_c respectively at 125 K and 1 kHz corresponding to 1500 V (Fig. 4.61). The maximum polarization found at 1500 V is $0.336 \mu\text{C}/\text{cm}^2$.

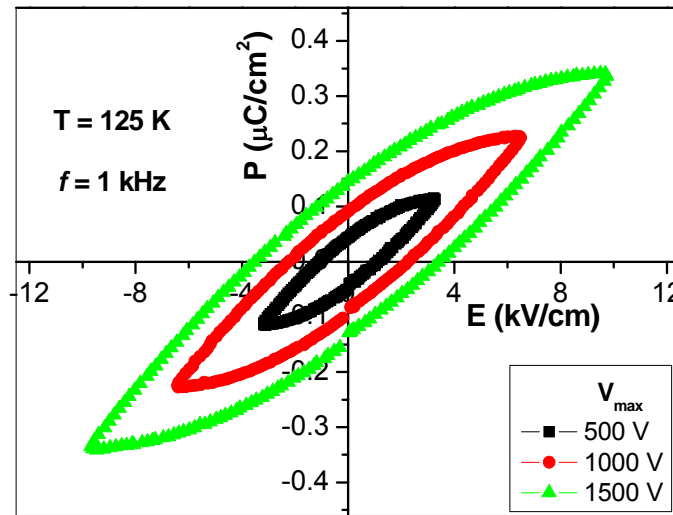


Fig. 4.61: Ferroelectric hysteresis loops of $\text{Y}_{0.6}\text{Ca}_{0.4}\text{MnO}_3$ (at 125 K , 1 kHz) for various voltages.

Magnetic measurements on $\text{Y}_{0.55}\text{Ca}_{0.45}\text{MnO}_3$ show evidence for charge ordering at 275 K which is same as that of $\text{Y}_{0.5}\text{Ca}_{0.5}\text{MnO}_3$ and weak ferromagnetic interactions with a short-range ferromagnetic order below around 50 K (Fig. 4.62). It exhibits magnetic hysteresis loop at low temperatures, the values of M_r and H_C at 5 K being $45 \text{ emu}/\text{mol}$ and 502 Oe respectively. We show the temperature variation of the dielectric constant for $\text{Y}_{0.55}\text{Ca}_{0.45}\text{MnO}_3$ in Fig. 4.63(a). Based on the Curie-Weiss plot, we estimate T_{CE} to be 326 K which is much higher than that of $\text{Y}_{0.5}\text{Ca}_{0.5}\text{MnO}_3$. The maximum value of dielectric constant observed at 10 kHz is 3.3×10^4 . The effect of magnetic field on the dielectric constants is shown in Fig. 4.63(b). The data show clear evidence for magnetocapacitance.

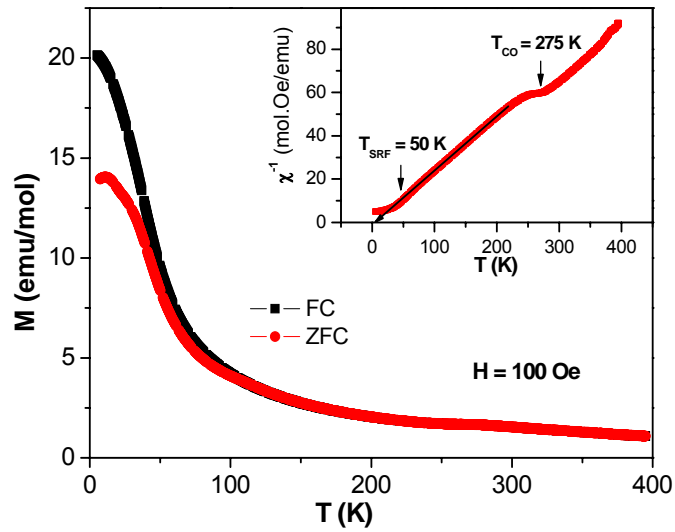


Fig. 4.62: Variation of magnetization of $Y_{0.55}Ca_{0.45}MnO_3$ with temperature at 100 Oe. Inset shows the inverse susceptibility plot marking the onset of charge-ordering, short-range ferromagnetic order.

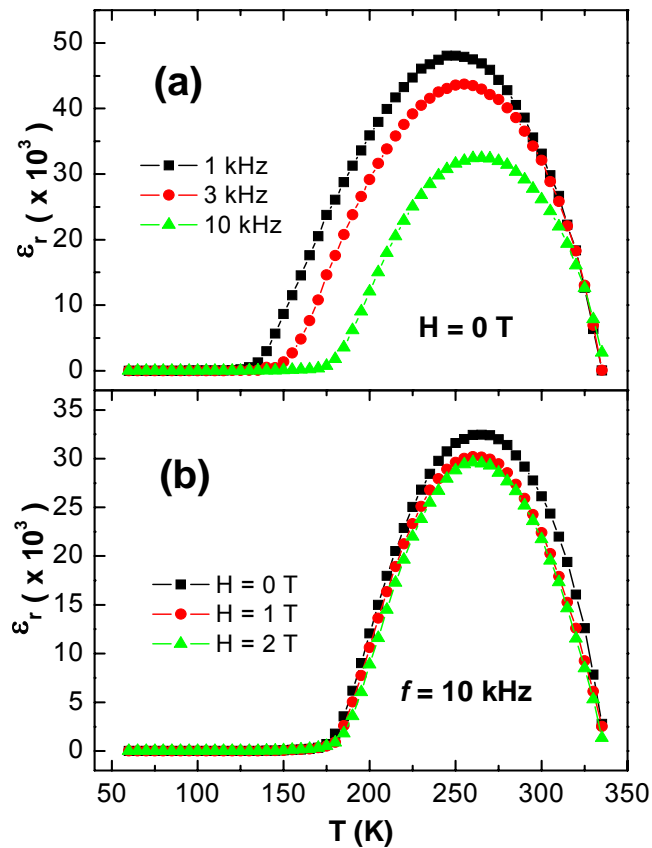


Fig. 4.63: (a) Temperature-dependence of the dielectric constant of $Y_{0.55}Ca_{0.45}MnO_3$ for different frequencies. (b) Effect of magnetic fields on the dielectric behavior of $Y_{0.55}Ca_{0.45}MnO_3$ at 10 kHz.

The ferroelectric hysteresis loops exhibited by most of the rare-earth manganites are similar to those of leaky dielectrics [6]. The dielectric hysteresis loop of a very thin sample (thickness $\sim 180 \mu\text{m}$) of $\text{Y}_{0.55}\text{Ca}_{0.45}\text{MnO}_3$ recorded by us showed a maximum polarization of around $0.43 \mu\text{C}/\text{cm}^2$ and a remnant polarization of $0.25 \mu\text{C}/\text{cm}^2$ at 900 V (Fig. 4.64).

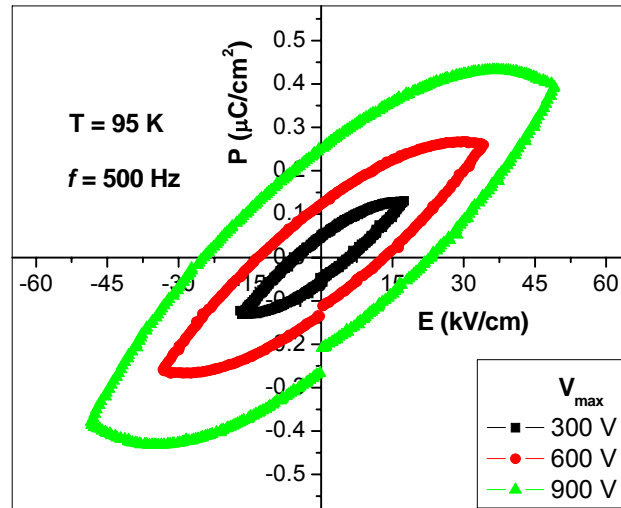


Fig. 4.64: Ferroelectric hysteresis loops of $\text{Y}_{0.55}\text{Ca}_{0.45}\text{MnO}_3$ (at 95 K, 500 Hz) for various voltages.

In view of the unreliability of dielectric hysteresis loops [6], we have carried out second harmonic generation (SHG) of polycrystalline $\text{Y}_{1-x}\text{Ca}_x\text{MnO}_3$ samples with $x = 0.45$ and 0.4 . The SHG responses of $\text{Y}_{0.55}\text{Ca}_{0.45}\text{MnO}_3$ and $\text{Y}_{0.6}\text{Ca}_{0.4}\text{MnO}_3$ were found to be 1.25 and 0.79 times that of quartz respectively. These measurements establish that charge-ordered rare-earth manganites do, indeed, possess non-linear properties and polarization features of ferroelectrics. All these observations establish that among the charge-ordered rare earth manganites, $\text{Y}_{1-x}\text{Ca}_x\text{MnO}_3$ compositions are multiferroic.

It is important to note some of the important characteristics of the charge-ordered manganites studied by us in order to fully understand their ferroic properties. The most important feature is that all the manganites exhibit electronic phase separation at low temperatures ($T < T_{CO}$) [66]. Application of electric fields also causes a significant decrease in the resistivity of the manganites [67, 68]. On the application of electric fields, the manganites show magnetic response [69,70]. Such electric field-induced magnetization may also be taken as evidence for coupling between the electric and magnetic order parameters in the manganites. This would be expected since the metallic state created by the electric field should necessarily be ferromagnetic according to the double exchange mechanism. It is likely that grain boundaries between the different electronic phases have a role in determining the dielectric behavior. The importance of grain boundaries in giving rise to high dielectric constants has indeed been recognized [71, 72]. In spite of the complexity of their electronic structure, the present study shows that the charge-ordered rare earth manganites possess multiferroic and magnetoelectric properties. These observations are consistent with the predictions of Efremov et al. [59].

Conclusions

The magnetocapacitive behavior is likely to reflect the electronic phase-separation that could be present in the material. Charge-ordered and ferromagnetic regimes or domains of different sizes would be present in such a manganite. The magnetocapacitance exhibited by these manganites is genuine since we do not observe any change in resistance on the application of magnetic fields upto 4 T in these manganites. Charge-ordered rare earth manganites of the general formula $Ln_{1-x}A_xMnO_3$

exhibit dielectric constant anomalies around the charge-ordering or the antiferromagnetic transition temperature. $\text{Gd}_{0.5}\text{Ca}_{0.5}\text{MnO}_3$ shows negative magnetocapacitance progressively with the ferroelectric transition shifting to a relatively lower temperature. $\text{Y}_{1-x}\text{Ca}_x\text{MnO}_3$ compositions show ferroelectric transition around room temperature with leaky ferroelectric hysteresis. The compounds $\text{Nd}_{0.5}\text{Ca}_{0.5}\text{MnO}_3$ shows a positive magnetocapacitive effect below T_N and the charge ordering temperatures, while $\text{Pr}_{0.6}\text{Ca}_{0.4}\text{MnO}_3$ shows a negative magnetocapacitive effect near T_N and positive effect near T_{CO} . $\text{Y}_{1-x}\text{Ca}_x\text{MnO}_3$ compositions show invariably negative magnetocapacitive effect. Magnetic fields have a marked effect on the dielectric properties of these compounds, indicating the presence of coupling between the magnetic and electrical order parameters enabling them for device applications.

4.6.2 Magnetoelectric effect in binary rare-earth manganite systems

Summary

We have synthesized the binary rare earth manganites like $(\text{La}_{0.7}\text{Ca}_{0.3})_{1-x}(\text{Y}_{0.5}\text{Ca}_{0.5})_x\text{MnO}_3$, $(\text{La}_{0.5}\text{Sr}_{0.5})_{1-x}(\text{Y}_{0.5}\text{Ca}_{0.5})_x\text{MnO}_3$, $(\text{La}_{0.7}\text{Ca}_{0.3}\text{MnO}_3)_{1-x}(\text{Y}_{0.5}\text{Ca}_{0.5}\text{MnO}_3)_x$, $(\text{La}_{0.5}\text{Sr}_{0.5}\text{MnO}_3)_{0.75}(\text{Y}_{0.5}\text{Ca}_{0.5}\text{MnO}_3)_{0.25}$ and $(\text{Pr}_{0.5}\text{Sr}_{0.5}\text{MnO}_3)_{1-x}(\text{Pr}_{0.6}\text{Ca}_{0.4}\text{MnO}_3)_x$ through two different ways and studied the modification of ferromagnetic behavior of the compounds like $\text{La}_{0.7}\text{Ca}_{0.3}\text{MnO}_3$, $\text{La}_{0.5}\text{Sr}_{0.5}\text{MnO}_3$ and $\text{Pr}_{0.5}\text{Sr}_{0.5}\text{MnO}_3$ on one hand and ferroelectric behavior of $\text{Y}_{0.5}\text{Ca}_{0.5}\text{MnO}_3$ and $\text{Pr}_{0.6}\text{Ca}_{0.4}\text{MnO}_3$ on the other by combining them in various proportions like 25, 50 and 75 percents. $(\text{La}_{0.7}\text{Ca}_{0.3})_{1-x}(\text{Y}_{0.5}\text{Ca}_{0.5})_x\text{MnO}_3$ exhibits lowering of magnetization value as well as cusp temperature in ZFC curve as we approach $\text{Y}_{0.5}\text{Ca}_{0.5}\text{MnO}_3$. For $x = 0.25$, there is appreciable magnetoelectric effect, whereas for higher x values, the effect is less realized. $(\text{La}_{0.7}\text{Ca}_{0.3}\text{MnO}_3)_{1-x}(\text{Y}_{0.5}\text{Ca}_{0.5}\text{MnO}_3)_x$ show similar kind of magnetic properties like $(\text{La}_{0.7}\text{Ca}_{0.3})_{1-x}(\text{Y}_{0.5}\text{Ca}_{0.5})_x\text{MnO}_3$. A peak is observed at 230 K for $x = 0.25$, which is found to shift towards higher temperature for higher compositions approaching T_{CO} of $\text{Y}_{0.5}\text{Ca}_{0.5}\text{MnO}_3$. For $x = 0.25$, positive magnetocapacitance was observed, whereas for others, it is negative. $(\text{La}_{0.5}\text{Sr}_{0.5})_{1-x}(\text{Y}_{0.5}\text{Ca}_{0.5})_x\text{MnO}_3$ exhibits the same trend in magnetic characteristics like $(\text{La}_{0.7}\text{Ca}_{0.3})_{1-x}(\text{Y}_{0.5}\text{Ca}_{0.5})_x\text{MnO}_3$. Again, the magnetic properties of $(\text{La}_{0.5}\text{Sr}_{0.5})_{0.75}(\text{Y}_{0.5}\text{Ca}_{0.5})_{0.25}\text{MnO}_3$ and $(\text{La}_{0.5}\text{Sr}_{0.5}\text{MnO}_3)_{0.75}(\text{Y}_{0.5}\text{Ca}_{0.5}\text{MnO}_3)_{0.25}$ are similar. $(\text{La}_{0.5}\text{Sr}_{0.5}\text{MnO}_3)_{0.75}(\text{Y}_{0.5}\text{Ca}_{0.5}\text{MnO}_3)_{0.25}$ shows a decrease in dielectric constant above 200 K on the application of 1 or 3 T magnetic field. The $x = 0.5$ and 0.75 compositions in $(\text{La}_{0.5}\text{Sr}_{0.5})_{1-x}(\text{Y}_{0.5}\text{Ca}_{0.5})_x\text{MnO}_3$ show broad maxima in the dielectric constant at higher

temperatures. $x = 0.5$ shows remarkable response to higher magnetic field. In $(\text{Pr}_{0.5}\text{Sr}_{0.5}\text{MnO}_3)_{1-x}(\text{Pr}_{0.6}\text{Ca}_{0.4}\text{MnO}_3)_x$, $x = 0.5$ and 0.75 compositions exhibit ferromagnetic transitions with the transition temperatures at 250 K and 215 K respectively. All the compositions possess maxima in dielectric constant curves which are found to shift to higher temperatures with the application of magnetic field. $x = 0.5$ shows a dramatic impact of magnetic field on its dielectric constant. $x = 0.5$ and 0.75 compositions exhibit magneto-dielectric effect in the paramagnetic regime.

Magnetoelectric effect in binary rare-earth manganite systems

Magnetization data of $\text{La}_{0.7}\text{Ca}_{0.3}\text{MnO}_3$ and $\text{Y}_{0.5}\text{Ca}_{0.5}\text{MnO}_3$ as a function of temperature at 100 Oe magnetic field are shown in fig. 4.65. $\text{La}_{0.7}\text{Ca}_{0.3}\text{MnO}_3$ is a ferromagnetic (FM) metal below the Curie temperature ($T_C \sim 247$ K) and a paramagnetic insulator above T_C . $\text{Y}_{0.5}\text{Ca}_{0.5}\text{MnO}_3$ exhibits a charge-ordering transition at 275 K (T_{CO}) and an antiferromagnetic transition at 110 K (T_N) [63] as seen in the inset of fig. 4.65. Ferromagnetic interactions are manifested in $\text{Y}_{0.5}\text{Ca}_{0.5}\text{MnO}_3$ at low temperatures due to electronic phase separation [64, 66].

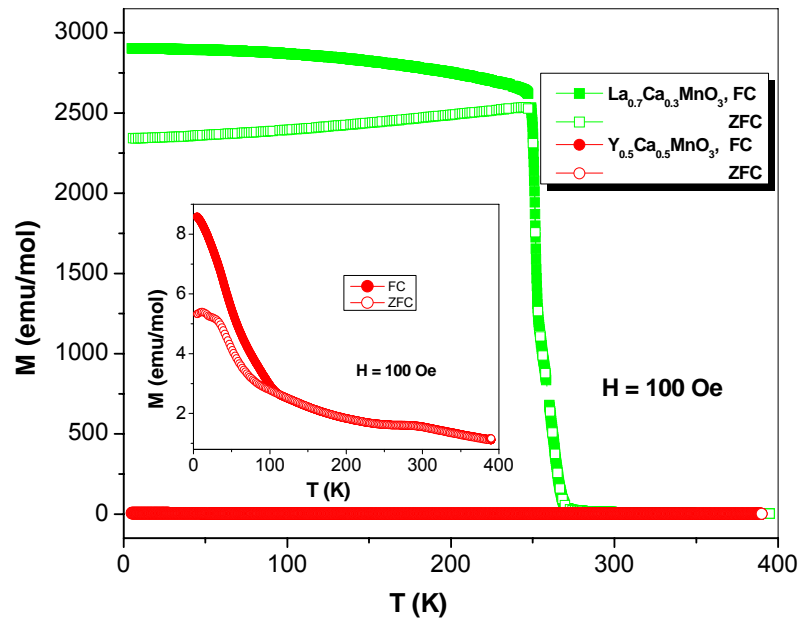


Fig. 4.65: A comparative picture of the magnetization curves for $\text{La}_{0.7}\text{Ca}_{0.3}\text{MnO}_3$ and $\text{Y}_{0.5}\text{Ca}_{0.5}\text{MnO}_3$, FC and ZFC data shown by solid and open symbols respectively. The inset gives the exact appearance of the curves for $\text{Y}_{0.5}\text{Ca}_{0.5}\text{MnO}_3$.

Typical magnetization data of the series $(\text{La}_{0.7}\text{Ca}_{0.3})_{1-x}(\text{Y}_{0.5}\text{Ca}_{0.5})_x\text{MnO}_3$ are shown in fig. 4.66. All the three compositions show a cusp in zero field cooled data at a

temperature which is found to decrease with the increase in composition. The values of the cusp temperature was observed to be 46 K, 39 K and 36 K respectively for $x = 0.25$, 0.5 and 0.75 respectively. With increase in x , the value of magnetization decreases systematically, being the lowest for $x = 0.75$ composition. They all exhibit characteristic hysteresis loops. $(\text{La}_{0.7}\text{Ca}_{0.3})_{0.5}(\text{Y}_{0.5}\text{Ca}_{0.5})_{0.5}\text{MnO}_3$, for example, has a remnant magnetization of 880 emu/mol and coercive field of 1400 Oe (Fig. 4.67).

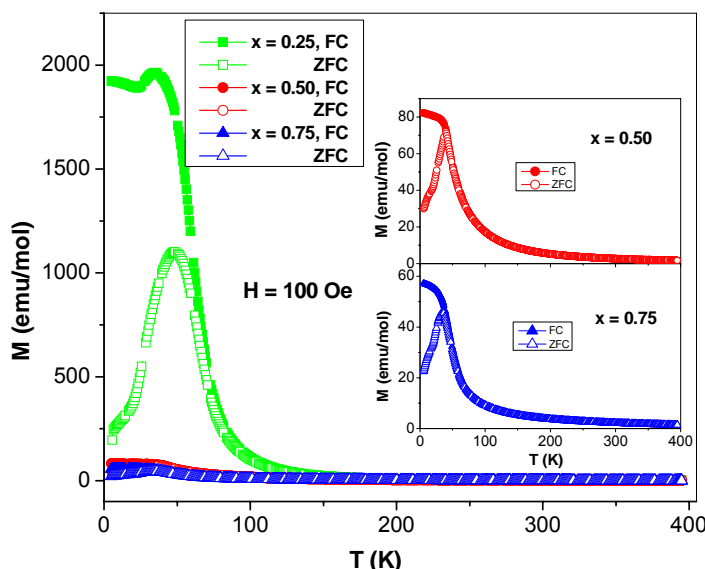


Fig. 4.66: The field-cooled (FC) and zero-field-cooled (ZFC) magnetization curves for $(\text{La}_{0.7}\text{Ca}_{0.3})_{1-x}(\text{Y}_{0.5}\text{Ca}_{0.5})_x\text{MnO}_3$. The insets show the enlarged view of the curves corresponding to $x = 0.5$ and $x = 0.75$ compositions.

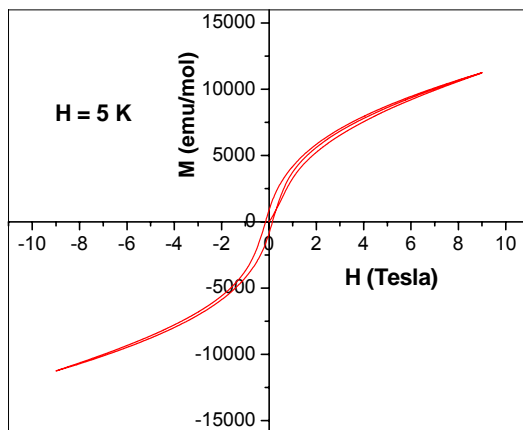


Fig. 4.67: Ferromagnetic hysteresis of $(\text{La}_{0.7}\text{Ca}_{0.3})_{0.5}(\text{Y}_{0.5}\text{Ca}_{0.5})_{0.5}\text{MnO}_3$ at 5 K.

In fig. 4.68, we show the magneto-electric effect in $(La_{0.7}Ca_{0.3})_{1-x}(Y_{0.5}Ca_{0.5})_xMnO_3$ at 100k Hz frequency. Dielectric data for $x = 0.25$ show two humps around 110 K and 150 K. The composition $x = 0.5$ shows increase in dielectric constant above 150 K while $x = 0.75$ show a broad maxima around 200-250 K. Application of 1 T magnetic field has a significant effect on the dielectric behavior of the $x = 0.25$ composition. Similar behavior is also observed in a 3 T magnetic field.

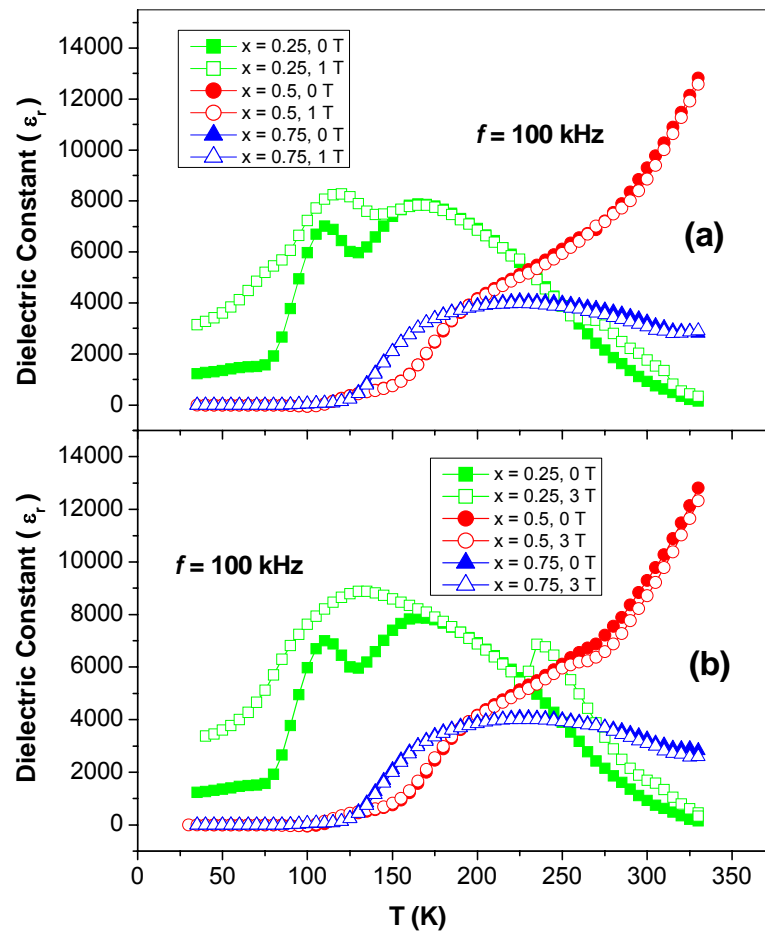


Fig. 4.68: The effect of magnetic field of (a) 1 T and (b) 3 T on the dielectric constant of $(La_{0.7}Ca_{0.3})_{1-x}(Y_{0.5}Ca_{0.5})_xMnO_3$ compounds. The solid and open symbols indicate the data without and with magnetic field respectively.

The magnetoelectric effect is small for $x = 0.5$ and 0.75 , for both the applied fields. Thus, we find the magnetoelectric effect only at small values of x , where for $x = 0.5$ and 0.75 , the highly insulating component due to incorporation of Y causes a small magnetoelectric effect.

We examine the properties of $(\text{La}_{0.7}\text{Ca}_{0.3}\text{MnO}_3)_{1-x}(\text{Y}_{0.5}\text{Ca}_{0.5}\text{MnO}_3)_x$ prepared by mixing the parent compounds followed by sintering of the pellet at high temperatures. Fig. 4.69 shows the magnetization data for $(\text{La}_{0.7}\text{Ca}_{0.3}\text{MnO}_3)_{1-x}(\text{Y}_{0.5}\text{Ca}_{0.5}\text{MnO}_3)_x$ which are similar to those of $(\text{La}_{0.7}\text{Ca}_{0.3})_{1-x}(\text{Y}_{0.5}\text{Ca}_{0.5})_x\text{MnO}_3$. This shows that the properties are independent of the methods of preparation of this binary manganite system.

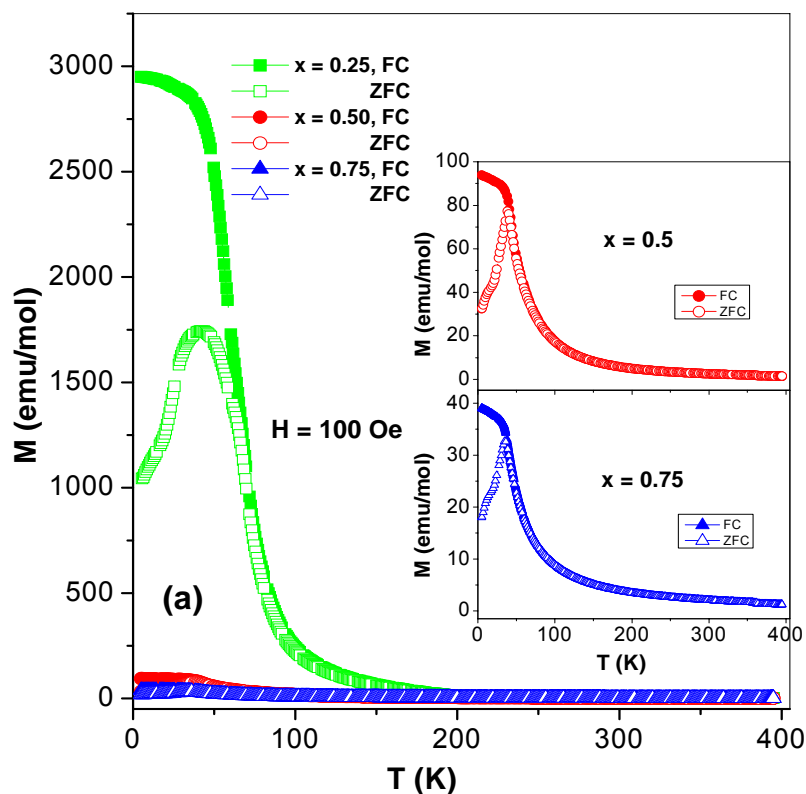


Fig. 4.69: The field-cooled (FC) and zero-field-cooled (ZFC) magnetization curves for $(\text{La}_{0.7}\text{Ca}_{0.3}\text{MnO}_3)_{1-x}(\text{Y}_{0.5}\text{Ca}_{0.5}\text{MnO}_3)_x$. The insets show the enlarged view of the curves corresponding to $x = 0.5$ and $x = 0.75$ compositions.

We show the variation of dielectric constant with temperature for different compositions of $(\text{La}_{0.7}\text{Ca}_{0.3}\text{MnO}_3)_{1-x}(\text{Y}_{0.5}\text{Ca}_{0.5}\text{MnO}_3)_x$ at 100 kHz frequency in fig. 4.70. All the compositions show dielectric constant maxima around 125 K which is believed to have arisen due to canted antiferromagnetic type behavior of $\text{Y}_{0.5}\text{Ca}_{0.5}\text{MnO}_3$. One more peak is observed at 230 K which shifts towards higher temperature approaching the T_{CO} of $\text{Y}_{0.5}\text{Ca}_{0.5}\text{MnO}_3$ as the composition of $\text{Y}_{0.5}\text{Ca}_{0.5}\text{MnO}_3$ is increased from $x = 0.25$ to $x = 0.75$.

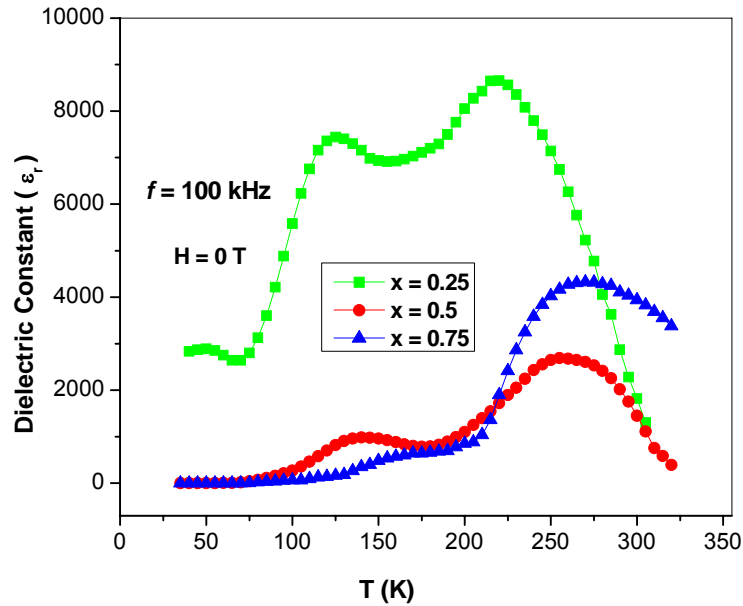


Fig. 4.70: Variation of dielectric constant of $(\text{La}_{0.7}\text{Ca}_{0.3}\text{MnO}_3)_{1-x}(\text{Y}_{0.5}\text{Ca}_{0.5}\text{MnO}_3)_x$ compositions with temperature for 100 kHz.

Application of magnetic field of 1 T has a marked effect on the $x = 0.25$ composition as it leads to increase in dielectric constant, while almost no effect on 0.5 and 0.75 compositions is observed [Fig. 4.71 (a)]. However, magnetic field of 3 T has appreciable effect on the dielectric constant of all the compositions as shown in fig. 4.71 (b), the $x = 0.5$ and 0.75 compositions showing negative magnetoelectric effect.

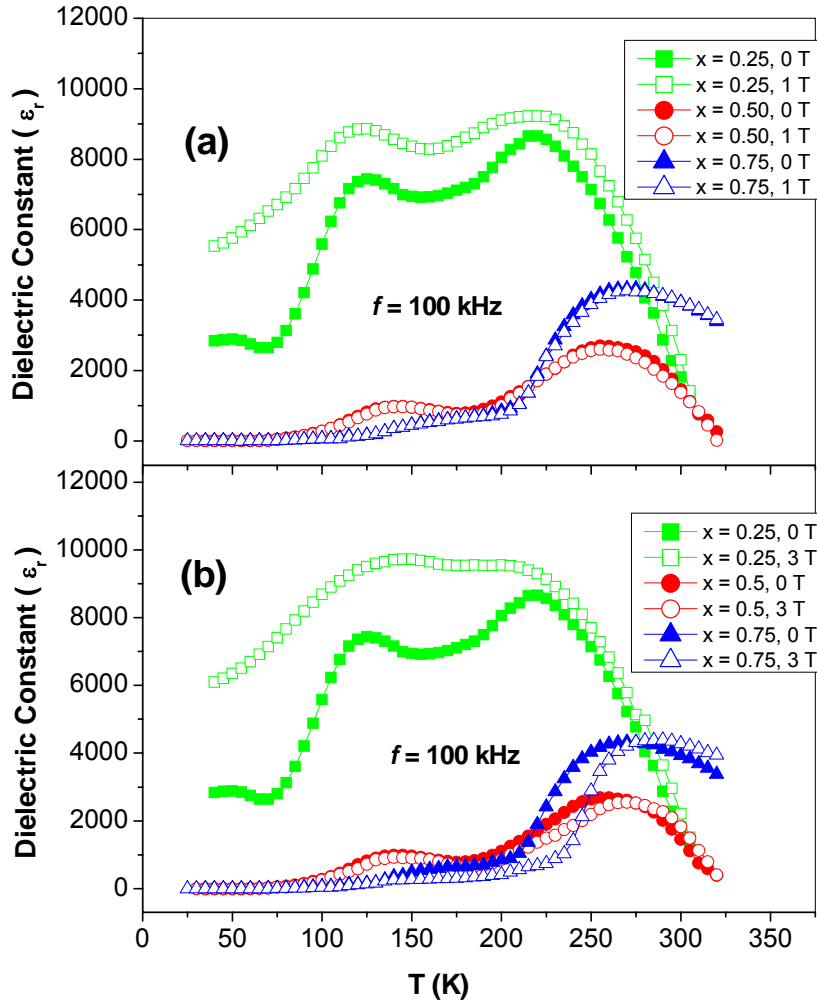


Fig. 4.71: The effect of magnetic field of (a) 1 T and (b) 3 T on the dielectric constant of $(\text{La}_{0.7}\text{Ca}_{0.3}\text{MnO}_3)_{1-x}(\text{Y}_{0.5}\text{Ca}_{0.5}\text{MnO}_3)_x$ compounds. The solid and open symbols indicate the data without and with magnetic field respectively.

Fig. 4.72 shows the magnetization data for the compound $\text{La}_{0.5}\text{Sr}_{0.5}\text{MnO}_3$, undergoing a ferromagnetic transition (T_C) at 330 K. $\text{La}_{0.5}\text{Sr}_{0.5}\text{MnO}_3$ is metallic both in the FM and paramagnetic states. Fig. 4.73 (a) shows the magnetic data for the series $(\text{La}_{0.5}\text{Sr}_{0.5})_{1-x}(\text{Y}_{0.5}\text{Ca}_{0.5})_x\text{MnO}_3$. These compounds do not show ferromagnetism, but there

is a broad magnetic transition around 200 K in the $x = 0.25$ composition. The value of the magnetization as well as the temperature corresponding to the divergence FC and ZFC curves decrease for $x = 0.5$ and 0.75 compositions similar to $(\text{La}_{0.7}\text{Ca}_{0.3})_{1-x}(\text{Y}_{0.5}\text{Ca}_{0.5})_x\text{MnO}_3$ series discussed earlier.

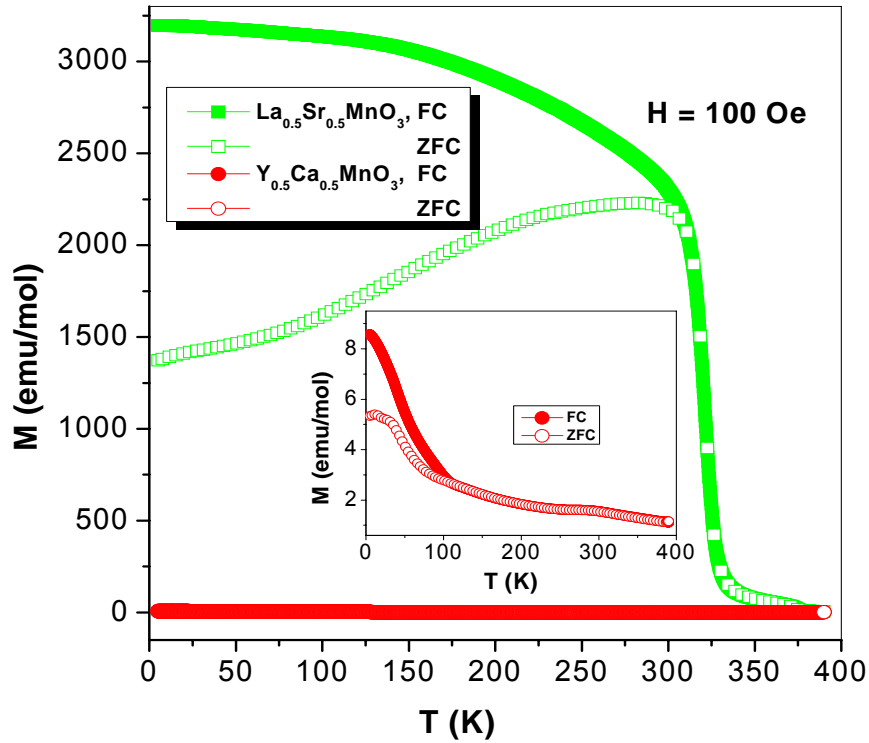


Fig. 4.72: A comparative picture of the magnetization curves for $\text{La}_{0.5}\text{Sr}_{0.5}\text{MnO}_3$ and $\text{Y}_{0.5}\text{Ca}_{0.5}\text{MnO}_3$, FC and ZFC data shown by solid and open symbols respectively. The inset gives the exact appearance of the curves for $\text{Y}_{0.5}\text{Ca}_{0.5}\text{MnO}_3$.

All the compounds of $(\text{La}_{0.5}\text{Sr}_{0.5})_{1-x}(\text{Y}_{0.5}\text{Ca}_{0.5})_x\text{MnO}_3$ series exhibit characteristic hysteresis loops. $(\text{La}_{0.5}\text{Sr}_{0.5})_{0.75}(\text{Y}_{0.5}\text{Ca}_{0.5})_{0.25}\text{MnO}_3$, for example, has a remnant magnetization of 2900 emu/mol and coercive field of 210 Oe [Fig. 4.73 (b)]. Magnetisation curve approaches towards saturation after 1.5 T.

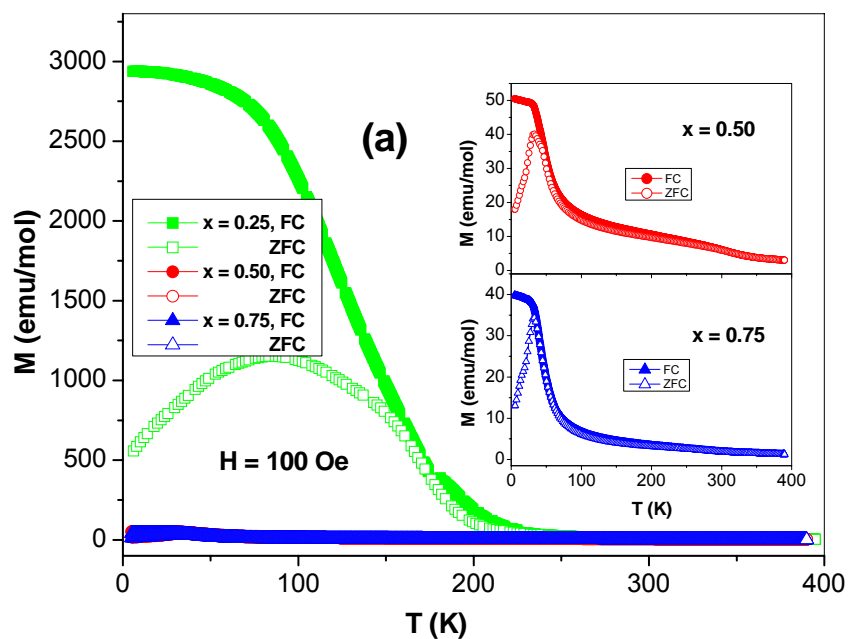


Fig. 4.73 (a): The field-cooled (FC) and zero-field-cooled (ZFC) magnetization curves for $(\text{La}_{0.5}\text{Sr}_{0.5})_{1-x}(\text{Y}_{0.5}\text{Ca}_{0.5})_x\text{MnO}_3$. The insets show the enlarged view of the curves corresponding to $x = 0.5$ and $x = 0.75$ compositions.

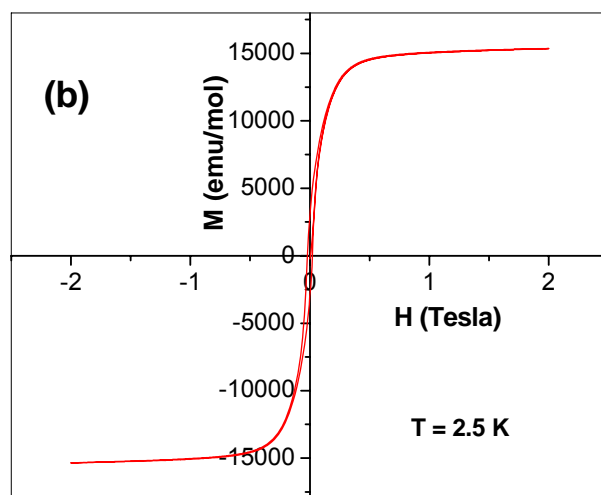


Fig. 4.73 (b): Ferromagnetic hysteresis of $(\text{La}_{0.5}\text{Sr}_{0.5})_{0.75}(\text{Y}_{0.5}\text{Ca}_{0.5})_{0.25}\text{MnO}_3$ at 2.5 K .

In fig. 4.74, dielectric data of $(\text{La}_{0.5}\text{Sr}_{0.5})_{1-x}(\text{Y}_{0.5}\text{Ca}_{0.5})_x\text{MnO}_3$ are shown. We do not see dielectric constant maxima in $x = 0.25$, nor any significant magnetoelectric effect. The $x = 0.5$ and 0.75 compositions show broad maxima in the dielectric constant at higher temperatures. $x = 0.5$ shows remarkable response to higher magnetic field.

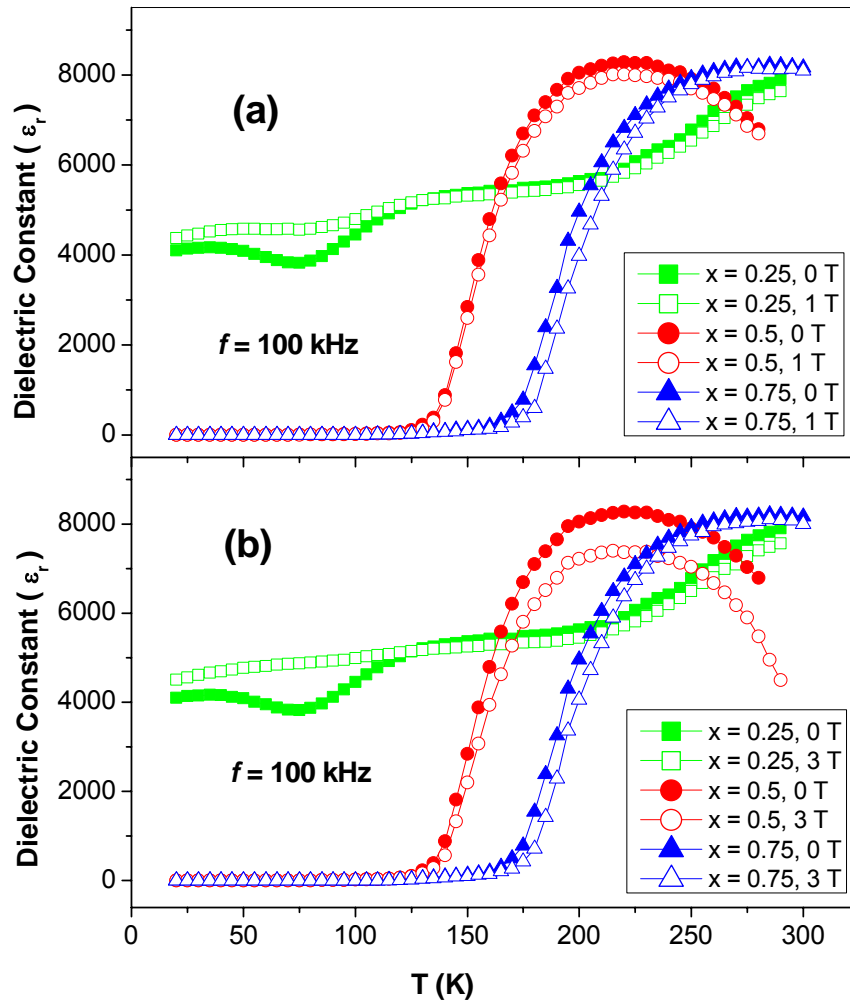


Fig. 4.74: The effect of magnetic field of (a) 1 T and (b) 3 T on the dielectric constant of $(\text{La}_{0.5}\text{Sr}_{0.5})_{1-x}(\text{Y}_{0.5}\text{Ca}_{0.5})_x\text{MnO}_3$ compounds. The solid and open symbols indicate the data without and with magnetic field respectively.

The magnetic behaviors of mechanically mixed $(\text{La}_{0.5}\text{Sr}_{0.5}\text{MnO}_3)_{0.75}$ $(\text{Y}_{0.5}\text{Ca}_{0.5}\text{MnO}_3)_{0.25}$ are similar to $(\text{La}_{0.5}\text{Sr}_{0.5})_{0.75}(\text{Y}_{0.5}\text{Ca}_{0.5})_{0.25}\text{MnO}_3$ [Fig. 4.75 (a) & (b)]. It possesses a remnant magnetization of 2700 emu/mol and coercive field of 220 Oe.

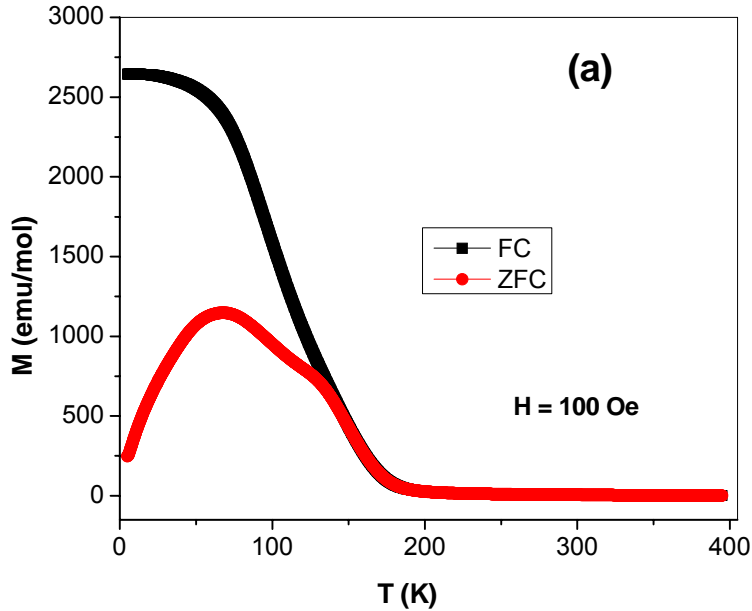


Fig. 4.75 (a): The field-cooled (FC) and zero-field-cooled (ZFC) magnetization curves for $(\text{La}_{0.5}\text{Sr}_{0.5}\text{MnO}_3)_{0.75}(\text{Y}_{0.5}\text{Ca}_{0.5}\text{MnO}_3)_{0.25}$ at 100 Oe.

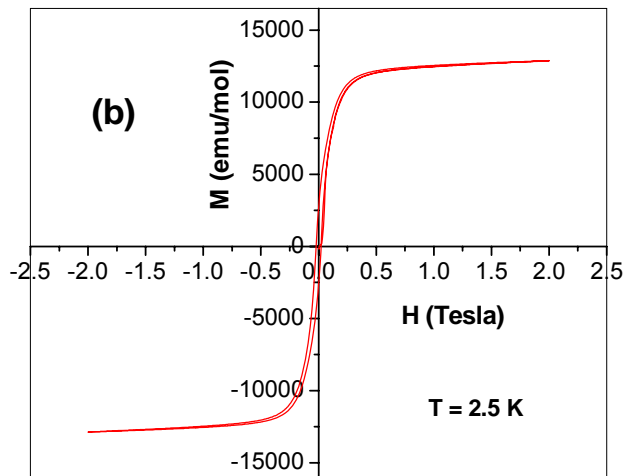


Fig. 4.75 (b): Ferromagnetic hysteresis of $(\text{La}_{0.5}\text{Sr}_{0.5}\text{MnO}_3)_{0.75}(\text{Y}_{0.5}\text{Ca}_{0.5}\text{MnO}_3)_{0.25}$ at 2.5 K.

Magnetic fields of 1 and 3 T cause a decrease in the dielectric constant below the maxima. $(\text{La}_{0.5}\text{Sr}_{0.5}\text{MnO}_3)_{0.75}(\text{Y}_{0.5}\text{Ca}_{0.5}\text{MnO}_3)_{0.25}$ shows a broad dielectric constant maximum around 200 K as shown in fig. 4.76(a). There is a small decrease in dielectric constant on the application of 1 or 3 T magnetic field above around 200 K [fig. 4.76(b)].

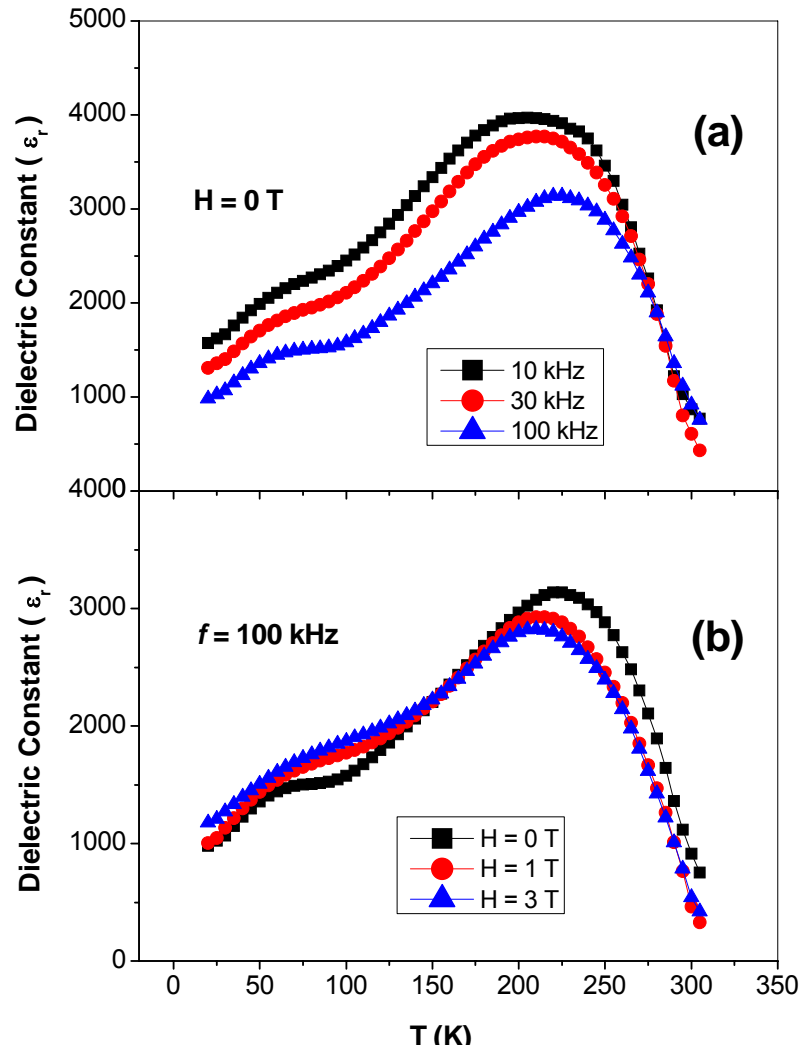


Fig. 4.76: Variation of dielectric constant of $(\text{La}_{0.5}\text{Sr}_{0.5}\text{MnO}_3)_{0.75}(\text{Y}_{0.5}\text{Ca}_{0.5}\text{MnO}_3)_{0.25}$ with temperature (a) for various frequencies and (b) for various magnetic fields at 100 kHz.

Fig. 4.77 shows the magnetization curves for the series $(\text{Pr}_{0.5}\text{Sr}_{0.5}\text{MnO}_3)_{1-x}(\text{Pr}_{0.6}\text{Ca}_{0.4}\text{MnO}_3)_x$ with $x = 0, 0.25, 0.5$ and 0.75 . $\text{Pr}_{0.5}\text{Sr}_{0.5}\text{MnO}_3$ shows a ferromagnetic transition at 270 K followed by a first order phase transition from an FM metal to AFM nonmetal at 140 K [73]. $\text{Pr}_{0.6}\text{Ca}_{0.4}\text{MnO}_3$ is a bond-centered charge-ordered insulator with a T_{CO} of 240 K and T_{N} of 170 K exhibiting evidence for electronic phase separation at low temperatures [60]. For $x = 0.25$, the behavior is similar to that of $\text{Pr}_{0.5}\text{Sr}_{0.5}\text{MnO}_3$. However for $x = 0.5$ and 0.75 , we see ferromagnetic transitions at 250 K and 215 K respectively.

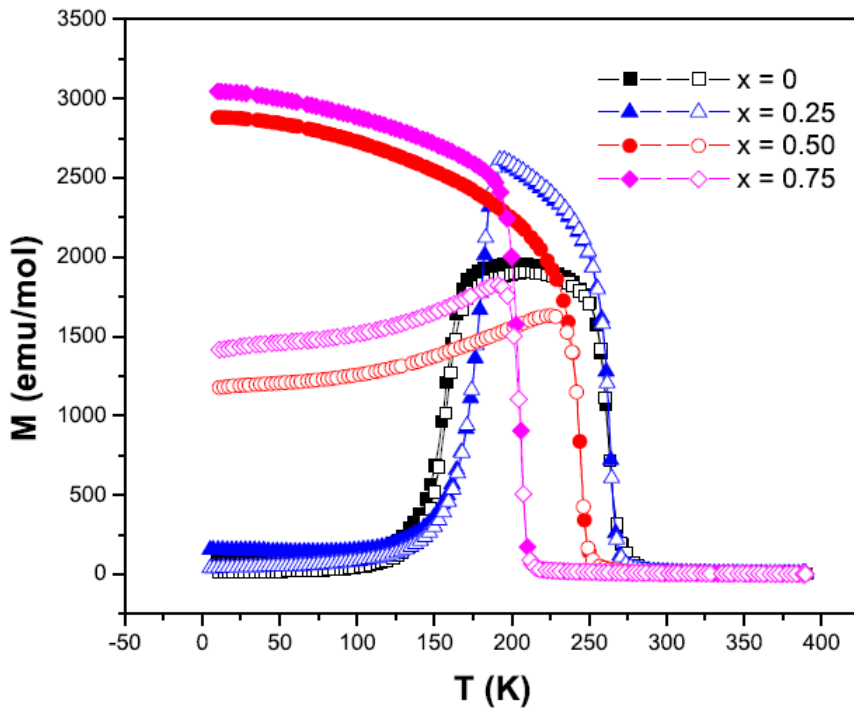


Fig. 4.77: The field-cooled (FC) and zero-field-cooled (ZFC) magnetization of the series $(\text{Pr}_{0.5}\text{Sr}_{0.5}\text{MnO}_3)_{1-x}(\text{Pr}_{0.6}\text{Ca}_{0.4}\text{MnO}_3)_x$ with $x = 0, 0.25, 0.5$ and 0.75 in an applied field of 100 Oe as a function of temperature. The solid symbols show FC data and open symbols ZFC data.

Dielectric data for all the three compositions are given in fig. 4.78. The dielectric data show a maximum around 150 K for $x = 0.25$ which is shifted on application of a magnetic field of 1 T or 2 T. We see a significant decrease in dielectric constant on the application of magnetic fields in $x = 0.5$ composition above 200 K, while $x = 0.75$ shows positive and negative magnetoelectric effects alternatively over the entire temperature range. It's noteworthy that both these compositions show magneto-dielectric effect above the FM transition temperatures in the paramagnetic regime.

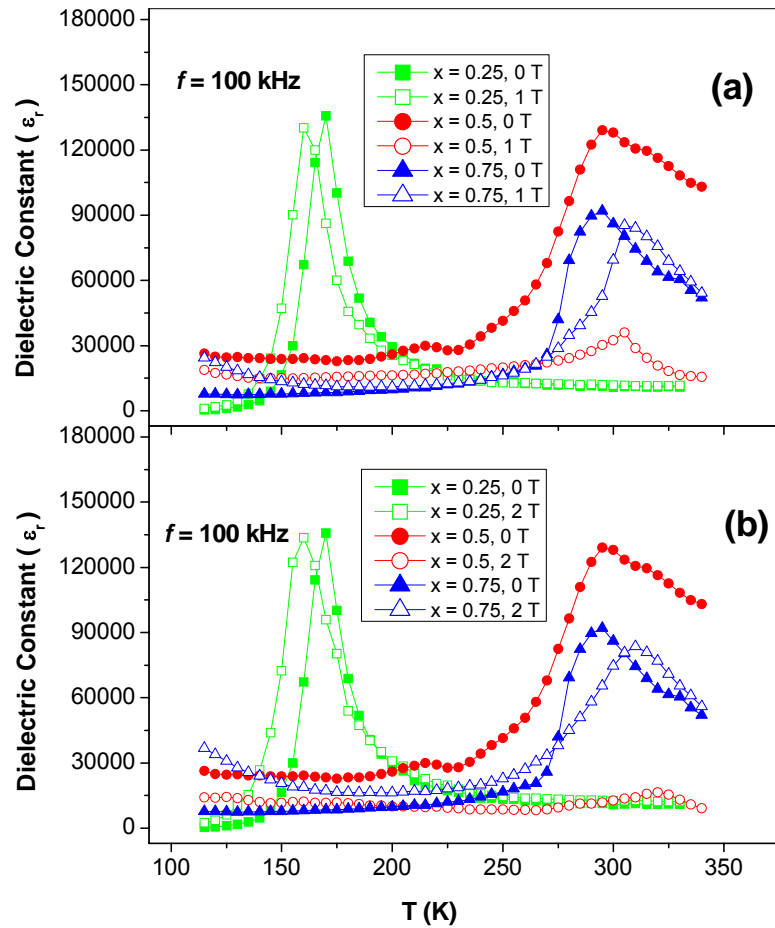


Fig. 4.78: Temperature-dependence of the dielectric constant of the series $(\text{Pr}_{0.5}\text{Sr}_{0.5}\text{MnO}_3)_{1-x}(\text{Pr}_{0.6}\text{Ca}_{0.4}\text{MnO}_3)_x$ with $x = 0, 0.25, 0.5$ and 0.75 for 100kHz frequency (a) at $H = 1$ T and (b) $H = 2$ T.

Conclusions

We observe interesting features in the magnetic, dielectric properties in all the binary manganites with respect to the behavior in their parent compounds. $(La_{0.7}Ca_{0.3})_{1-x}(Y_{0.5}Ca_{0.5})_xMnO_3$ exhibits lowering of magnetization value as well as cusp temperature in ZFC curve as we approach $Y_{0.5}Ca_{0.5}MnO_3$. For $x = 0.25$, there is appreciable magnetoelectric effect, whereas for higher x values, the effect is less realized. $(La_{0.7}Ca_{0.3}MnO_3)_{1-x}(Y_{0.5}Ca_{0.5}MnO_3)_x$ show similar kind of magnetic properties like $(La_{0.7}Ca_{0.3})_{1-x}(Y_{0.5}Ca_{0.5})_xMnO_3$. A peak is observed at 230 K for $x = 0.25$, which is found to shift towards higher temperature for higher compositions approaching T_{CO} of $Y_{0.5}Ca_{0.5}MnO_3$. For $x = 0.25$, positive magnetocapacitance was observed, whereas for others, it is negative. $(La_{0.5}Sr_{0.5})_{1-x}(Y_{0.5}Ca_{0.5})_xMnO_3$ exhibits the same trend in magnetic characteristics like $(La_{0.7}Ca_{0.3})_{1-x}(Y_{0.5}Ca_{0.5})_xMnO_3$. Again, the magnetic properties of $(La_{0.5}Sr_{0.5})_{0.75}(Y_{0.5}Ca_{0.5})_{0.25}MnO_3$ and $(La_{0.5}Sr_{0.5}MnO_3)_{0.75}(Y_{0.5}Ca_{0.5}MnO_3)_{0.25}$ are similar. $(La_{0.5}Sr_{0.5}MnO_3)_{0.75}(Y_{0.5}Ca_{0.5}MnO_3)_{0.25}$ shows a decrease in dielectric constant above 200 K on the application of 1 or 3 T magnetic field. The $x = 0.5$ and 0.75 compositions in $(La_{0.5}Sr_{0.5})_{1-x}(Y_{0.5}Ca_{0.5})_xMnO_3$ show broad maxima in the dielectric constant at higher temperatures. $x = 0.5$ shows remarkable response to higher magnetic field. In $(Pr_{0.5}Sr_{0.5}MnO_3)_{1-x}(Pr_{0.6}Ca_{0.4}MnO_3)_x$, $x = 0.5$ and 0.75 compositions exhibit ferromagnetic transitions with the transition temperatures at 250 K and 215 K respectively. All the compositions possess maxima in dielectric constant curves which are found to shift to higher temperatures with the application of magnetic field. $x = 0.5$ shows a dramatic impact of magnetic field on its dielectric constant.

Bibliography

1. B.B. van-Aken, A. Meetsma, T.T.M. Palstra, Hexagonal ErMnO_3 , *Acta Crystallogr. E* **57**, i38 (2001)
2. J. Park, U. Kong, S.I. Choi, J. -G Park, C. Lee, W. Jo, Magnetic structure studies of ErMnO_3 , *Appl. Phys. A* **74** [Suppl.], S802-S804 (2002)
3. M. Fiebig, C. Degenhardt and R.V. Pisarev, Interaction of Frustrated Magnetic Sublattices in ErMnO_3 , *Phys. Rev. Lett.* **88**, 027203 (2002)
4. A.P. Ramirez, Geometrical Frustration, *Handbook of Magnetic Materials Vol. 13*, (2001) edited by K. H. J. Buschow (North-Holland, Amsterdam)
5. L.E. Cross, Relaxor ferroelectrics: An overview, *Ferroelectrics*, **151**, 305 (1994)
6. J.F. Scott, Ferroelectrics go bananas, *J. Phys.: Condens. Matter* **20**, 021001 (2008)
7. Z.J. Huang, Y. Cao, Y.Y. Sun, Y.Y. Xue and C.W. Chu, Coupling between the ferroelectric and antiferromagnetic orders in YMnO_3 , *Phys. Rev. B* **56**, 2623 (1997)
8. D.G. Tomuta, S. Ramakrishnan, G.J. Nieuwenhuys and J.A. Mydosh, The magnetic susceptibility, specific heat and dielectric constant of hexagonal YMnO_3 , LuMnO_3 and ScMnO_3 , *J. Phys.: Condens. Matter* **13**, 4543 (2001)
9. H. Sugie, N. Iwata and K. Kohn, Magnetic ordering of rare earth ions and magnetic-electric interaction of hexagonal RMnO_3 ($R = \text{Ho, Er, Yb or Lu}$), *J. Phys. Soc. Jpn.* **71**, 1558 (2002)
10. N. Iwata and K. kohn, Dielectric anomalies at magnetic transitions of hexagonal rare earth manganese oxides RMnO_3 , *J. Phys. Soc. Jpn.* **67**, 3318 (1998)

11. M. Fiebig, Th. Lottermoser, Th. Lonkai, A.V. Goltsev and R.V. Pisarev, Magnetolectric effects in multiferroic manganites, *J. Magnetism and Magn. Mater.* **290-291**, 883 (2005)
12. S. Lee, A. Pirogov, M. Kang, K.-H. Jang, M. Yonemura, T. Kamiyama, S.-W. Cheong, F. Gozzo, N. Shin, H. Kimura, Y. Noda and J.-G. Park, Giant magneto-elastic coupling in multiferroic hexagonal manganites, *Nature* **451**, 805 (2008)
13. B.B. van Aken, A. Meetsma, and T.T.M. Palstra, Hexagonal LuMnO₃ revisited, *Acta Crystallogr., Sect.E: Struct. Rep. Online* **57**, i101 (2001)
14. T. Katsufuji, S. Mori, M. masaki, Y. Moritomo, N. Yamamoto and H. Takagi, Dielectric and magnetic anomalies and spin frustration in hexagonal RMnO₃ (R = Y, Yb, and Lu), *Phys. Rev. B* **64**, 104419 (2001)
15. P. A. Sharma, J.S. Ahn, N. Hur, S. Park, S.B. Kim, S. Lee, J.G. Park, S. Guha and S-W. Cheong, Thermal Conductivity of Geometrically Frustrated, Ferroelectric YMnO₃: Extraordinary Spin-Phonon Interactions, *Phys. Rev. Lett.* **93**, 177202 (2004)
16. A. Munoz, J.A. Alonso, M.J. Martinez-Lope, M.T. Casais, J.L. Martinez and M.T. Fernandez-Diaz, Magnetic structure of hexagonal RMnO₃ (R = Y, Sc): Thermal evolution from neutron powder diffraction data, *Phys. Rev. B* **62**, 9498 (2000)
17. L.E. Cross, Relaxor ferroelectrics, *Ferroelectrics* **76**, 241 (1987)
18. H. Fukumura, S. Matsui, H. Harima, K. Kisoda, T. Takahashi, T. Yoshimura and N. Fujimura, Raman scattering studies on multiferroic YMnO₃, *J. Phys.: Condens. Matter* **19**, 365239 (2007)

19. M.N. Iliev, M.V. Abrashev, J. Laverdiere, S. Jandl, M.M. Gospodinov, Y.Q. Wang and Y. Y. Sun, Distortion-dependent Raman spectra and mode mixing in RMnO₃ perovskites (R = La, Pr, Nd, Sm, Eu, Gd, Tb, Dy, Ho, Y) Phys. Rev. B **73**, 064302 (2006)
20. V.B. Podobedov, A. Weber, D.B. Romero, J.P. Rice and H.D. Drew, Effect of structural and magnetic transitions in La_{1-x}M_xMnO₃ (M = Sr, Ca) single crystals in Raman scattering, Phys. Rev. B **58**, 43 (1998).
21. M.V. Abrashev, A.P. Litvinchuk, M.N. Iliev, R.L. Meng, V.N. Popov, V.G. Ivanov, R. A. Chakalov and C. Thomsen, Comparative study of optical phonons in the rhombohedrally distorted perovskites LaAlO₃ and LaMnO₃, Phys. Rev. B **59**, 4146 (1999)
22. M.N. Iliev, V.G. Hadjiev, A.P. Litvinchuk, F. Yen, Y.Q. Wang, Y.Y. Sun, S. Jandl, J. Laverdiere, V.N. Popov and M.M. Gospodinov, Multiple-order Raman scattering from rare-earth manganites: Oxygen isotope and rare-earth substitution effects, Phys. Rev. B **75**, 064303 (2007)
23. M.N. Iliev, M.V. Abrashev, V.N. Popov and V.G. Hadjiev, Role of Jahn-Teller disorder in Raman scattering of mixed-valence manganites, Phys. Rev. B **67**, 212301 (2003)
24. P. Kumar, S. Saha, C.R. Serrao, A.K. Sood and C.N.R. Rao, Temperature-dependent infrared reflectivity studies of multiferroic TbMnO₃: Evidence for spin-phonon coupling, Pramana-J. Phys. **74**, 281 (2010), Pramana J. Phys. (arXiv:0905.3092).

25. E. Granado, A. Garcia, J.A. Sanjurjo, C. Rettori, I. Torriani, F. Prado, R.D. Sanchez, A. Caneiro and S. B. Oseroff, Magnetic ordering effects in the Raman spectra of $\text{La}_{1-x}\text{Mn}_{1-x}\text{O}_3$, *Phys. Rev. B* **60**, 11879 (1999)
26. R. Choithrani, N.K. Gaur and R.K. Singh, Study of calcium doping effect on thermophysical properties of some perovskite Manganites, *J. Alloys and Compounds*. **480**, 727 (2009)
27. R. Choithrani, N.K. Gaur and R.K. Singh, Thermodynamic properties of SmMnO_3 , $\text{Sm}_{0.55}\text{Sr}_{0.45}\text{MnO}_3$ and $\text{Ca}_{0.85}\text{Sm}_{0.15}\text{MnO}_3$, *J. Phys.: Condens. Matter* **20**, 415201 (2008).
28. D. Meier, N. Aliouane , D.N. Argyriou , J.A. Mydosh and T. Lorenz, New features in the phase diagram of TbMnO_3 , *New J. Phys.* **9**, 100 (2007)
29. J. Laverdiere, S. Jandl, A.A. Mukhin, V. Yu. Iyanov, V.G. Iyanov and M.N. Iliev, Spin-phonon coupling in orthorhombic RMnO_3 (R=Pr, Nd, Sm, Eu, Gd, Tb, Dy, Ho, Y): A Raman study, *Phys. Rev. B* **73**, 214301 (2006)
30. W.S. Ferreira, J.A. Moreira, A. Almeida, M.R. Chaves, J.P. Araujo, J.B. Oliveira, J. M. Machado Da Silva, T.M. Sa, T.M. Mendonca, P.S. Carvalho, J. Kreisel, J.L. Riberio, L.G. Vieira, P.B. Tavares and S. Mendonca, Spin-phonon coupling and magnetoelectric properties: EuMnO_3 versus GdMnO_3 , *Phys. Rev. B* **79**, 054303 (2009).
31. P.G. Klemens, Anharmonic Decay of Optical Phonons, *Phys. Rev.* **148**, 845 (1966)
32. P.B. Allen and V. Perebeinos, Self-Trapped Exciton and Franck-Condon Spectra Predicted in LaMnO_3 , *Phys. Rev. Lett.* **83**, 4828 (1999)

33. V. Perebeinos and P.B. Allen, Multiphonon resonant Raman scattering predicted in LaMnO_3 from the Franck-Condon process via self-trapped excitons Phys. Rev. B **64**, 085118 (2001)
34. Light Scattering in solids II, Topics in Applied Physics vol. 50, edited by M. Cardona (Springer-Verleg, Berlin, 1982).
35. R.M. Hornreich, S. Shtrikman, B.M. Wanklyn, and I. Yaeger, Magnetization studies in rare-earth orthochromites. VII. LuCrO_3 , Phys. Rev. B **13**, 4046 (1976).
36. T. Yamaguchi, Theory of spin reorientation in rare earth orthochromites and orthoferrites, J. Phys. Chem. Solids **35**, 479 (1974).
37. N. Shamir, H. Shaked, and S. Shtrikman, Magnetic structure of some rare earth orthochromites, Phys. Rev. B **24**, 6642 (1981).
38. T. Morishita and K. Tsushima, Susceptibility of the weak ferromagnets ErCrO_3 and YCrO_3 near the critical anomaly, Phys. Rev. B **24**, 341 (1981).
39. N. Kojima, Bound state of an exciton-magnon system under high magnetic fields. II. YbCrO_3 , Phys. Rev. B **47**, 15091 (1993).
40. C.R. Serrao, A.K. Kundu, S.B. Krupanidhi, U.V. Waghmare and C.N.R. Rao, Biferroic YCrO_3 , Phys. Rev. B, 2005, **72**, 220201(R).
41. K. Ramesha, A. Llobet, T. Profen, C.R. Serrao and C.N.R. Rao, Observation of local non-centrosymmetry in weakly biferroic YCrO_3 , J. Phys.: Condens. Matter **19**, 102202 (2007)
42. S. Baroni, A.D. Corso, S. de Gironcoli, P. Giannozzi, C. Cavazzoni, G. Ballabio, S. Scandolo, G. Chiarotti, P. Focher, A. Pasquarello, K. Laasonen, A. Trave, R. Car, N. Marzari and A. Kokalj, <http://www.pwscf.org/>.

43. D. Vanderbilt, Soft self-consistent pseudopotentials in a generalized eigenvalue formalism, *Phys. Rev. B* **41**, 7892 (1990).
44. R. D. King-Smith and D. Vanderbilt, Theory of polarization of crystalline solids, *Phys. Rev. B* **47**, 1651(1993).
45. K. Yoshii, Magnetic properties of perovskite GdCrO_3 , *J. Solid State Chem.* **159**, 204 (2001).
46. K. Yoshii, A. Nakamura, Y. Ishii, and Y. Morii, Magnetic properties of $\text{La}_{1-x}\text{Pr}_x\text{CrO}_3$, *J. Solid State Chem.* **162**, 84 (2001).
47. W. Kaczmarek, Z. Pajak and M. Polomska, Differential thermal analysis of phase transitions in $(\text{Bi}_{1-x}\text{La}_x)\text{FeO}_3$ solid solution, *Solid State Commun.*, **17**, 807 (1975)
48. K. Yoshii, N. Ikeda, Y. Matsuo, Y. Horibe, and S. Mori, Magnetic and dielectric properties of RFe_2O_4 , RFeMO_4 , and RGaCuO_4 ($\text{R}=\text{Yb}$ and Lu , $\text{M}=\text{Co}$ and Cu), *Phys. Rev. B: Condens. Matter* **76**, 024423 (2007).
49. J.Y. Park, J.H. Park, Y.K. Jeong, and H.M. Jang, Dynamic magneto-electric coupling in "electronic ferroelectric" LuFe_2O_4 , *Appl. Phys. Lett.* **91**, 152903 (2007).
50. N. Ikeda, Ferroelectric properties of triangular charge-frustrated LuFe_2O_4 , *J. Phys.: Condens. Matter* **20**, 434218 (2008).
51. J. Wen, G. Xu, G. Gu and S.M. Shapiro, Magnetic-field control of charge structures in the magnetically disordered phase of multiferroic LuFe_2O_4 , *Phys. Rev. B* **80**, R20403 (2009).
52. N. Ikeda, H. Ohsumi, K. Ohwada, K. Ishii, T. Inami, K. Kakurai, Y. Murakami, K. Yoshii, S. Mori, Y. Horibe and H. Kito, Ferroelectricity from iron valence ordering in the charge-frustrated system LuFe_2O_4 , *Nature* **436**, 1136 (2005).

53. A. Nagano, M. Naka, J. Nasu and S. Ishihara, Electric polarization, magneto- electric effect and orbital state of a layered iron oxide with frustrated geometry, *Phys. Rev. Lett.* **99**, 217202 (2007).
54. N. Ikeda, S. Mori and K. Yoshii, Ferroelectricity from valence ordering in RFe_2O_4 , *Ferroelectrics* **348**, 38 (2007).
55. N. Ikeda, S. Mori, and K. Kohn, Charge Ordering and dielectric dispersion in mixed valence oxides RFe_2O_4 , *Ferroelectrics* **314**, 41 (2005).
56. N. Ikeda, K. Kohn, N. Myouga, E. Takahashi, H. Kito, and S. Takekawa, Charge frustration and dielectric dispersion in $LuFe_2O_4$, *J. Phys. Soc. Jpn.* **69**, 1526 (2000).
57. N. Ikeda, K. Kohn, H. Kito, J. Akimitsu and K. Siratori, Anisotropy of dielectric dispersion in $ErFe_2O_4$ single crystal, *J. Phys. Soc. Jpn.* **64**, 1371 (1995).
58. Y. Yamada, S. Nohdo and N. Ikeda, Incommensurate charge ordering in charge-frustrated $LuFe_2O_4$ system, *J. Phys. Soc. Jpn.* **66**, 3733 (1997).
59. D.V. Efremov, J. van den Brink and D.I. Khomskii, Bond-versus site-centred ordering and possible ferroelectricity in manganites, *Nat. Mater.* **3**, 853 (2004).
60. P. Murugavel, C. Narayana, A. K. Sood, S. Parashar, A.R. Raju, and C.N.R. Rao, Magnetic excitations in charge-ordered $Nd_{0.5}Ca_{0.5}MnO_3$: A Brillouin scattering study, *Europhys. Lett.* **52**, 461 (2000).
61. Y. Tomioka, A. Asamitsu, H. Kuwahara, Y. Moritomo, and Y. Tokura, Magnetic-field-induced metal-insulator phenomena in $Pr_{1-x}Ca_xMnO_3$ with controlled charge-ordering instability, *Phys. Rev. B* **53**, R1689 (1996).

62. T. Terai, T. Sasaki, T. Kakeshita, . Fukuda, T. Saburi, H. Kitagawa, K. Kindo and M. Honda, Electronic and magnetic properties of $R_{0.5}A_{0.5}MnO_3$ compounds ($R = Gd, Dy, Ho, Er; A = Sr, Ca$), Phys. Rev. B **61**, 3488 (2000)
63. A. Arulraj, R. Gundakaram, A. Biswas, N. gayathri, A. K. Raychaudhuri and C. N. R. Rao, The nature of the charge-ordered state in $Y_{0.5}Ca_{0.5}MnO_3$ with a very small average radius of the A-site cations, J. Phys.: Condens. Matter **10**, 4447 (1998).
64. V. B. Shenoy and C. N. R. Rao, Electronic phase separation and other novel phenomena and properties exhibited by mixed-valent rare-earth manganites and related materials, Phil. Trans. R. Soc. A **366**, 63 (2008).
65. C. N. R. Rao, A. K. Kundu, M. M. Seikh and L. Sudheendra, Electronic phase separation in transition metal oxides, Dalton Transactions (Feature article), 3003 (2004)
66. V.B. Shenoy, D.D. Sarma and C.N.R. Rao, Electronic phase separation in correlated Oxides: The phenomenon, its present status and future prospects, ChemPhysChem **7**, 2053 (2006)
67. C.N.R. Rao, Charge, spin, and orbital ordering in the perovskite manganates, $Ln_{1-x}A_xMnO_3$ ($Ln = \text{Rare Earth}, A = Ca \text{ or } Sr$), J. Phys. Chem. B **104**, 5877 (2000).
68. S. Parashar, L. Sudheendra, A.R. Raju and C.N.R. Rao, Current-induced phase control in charged-ordered $Nd_{0.5}Ca_{0.5}MnO_3$ and $Pr_{0.6}Ca_{0.4}MnO_3$ crystals, J. Appl. Phys. **95**, 2181 (2004).
69. A. Guha, N. Khare, A.K. Raychaudhuri and C.N.R. Rao, Magnetic field resulting from nonlinear electrical transport in single crystals of charge-ordered $Pr_{0.63}Ca_{0.37}MnO_3$, Phys. Rev. B **62**, R11941 (2000).

70. H. Sakai and Y. Tokura, Current-induced persistent magnetization in a relaxorlike manganite, *Appl. Phys. Lett.* **92**, 102514 (2008).
71. P. Lunkenheimer, V. Bobnar, A.V. Pronin, A.I. Ritus, A.A. Volkov and A. Loidl, Origin of apparent colossal dielectric constants, *Phys. Rev. B* **66**, 521051 (2002).
72. L. Sudheendra, and C.N.R. Rao, Electronic phase separation in the rare-earth manganates $(\text{La}_{1-x}\text{Ln}_x)_{0.7}\text{Ca}_{0.3}\text{MnO}_3$ ($\text{Ln} = \text{Nd, Gd and Y}$), *J. Phys.: Condens. Matter* **15**, 3029 (2003).
73. Y. Tomioka, A. Asamitsu, Y. Moritomo, H. Kuwahara and Y. Tokura, Collapse of a Charge-Ordered State under a Magnetic Field in $\text{Pr}_{1/2}\text{Sr}_{1/2}\text{MnO}_3$, *Phys. Rev. Lett.* **74**, 5108 (1995)